

---

Electronic Thesis and Dissertation Repository

---

3-21-2019 2:00 PM

## Advances in Design Methodology in Swelling Shale Rock in Southern Ontario

Thomas R.A. Lardner  
*The University of Western Ontario*

Supervisor

El Naggari, Hesham

*The University of Western Ontario* Co-Supervisor

Lo, K.Y.

*The University of Western Ontario*

Graduate Program in Civil and Environmental Engineering

A thesis submitted in partial fulfillment of the requirements for the degree in Doctor of Philosophy

© Thomas R.A. Lardner 2019

Follow this and additional works at: <https://ir.lib.uwo.ca/etd>



Part of the [Computational Engineering Commons](#), [Geotechnical Engineering Commons](#), and the [Mechanics of Materials Commons](#)

---

### Recommended Citation

Lardner, Thomas R.A., "Advances in Design Methodology in Swelling Shale Rock in Southern Ontario" (2019). *Electronic Thesis and Dissertation Repository*. 6152.

<https://ir.lib.uwo.ca/etd/6152>

This Dissertation/Thesis is brought to you for free and open access by Scholarship@Western. It has been accepted for inclusion in Electronic Thesis and Dissertation Repository by an authorized administrator of Scholarship@Western. For more information, please contact [wlsadmin@uwo.ca](mailto:wlsadmin@uwo.ca).

# Abstract

As infrastructure requirements increase in southern Ontario, excavations within swelling rock formations will become more frequent and larger. The objective of this study is to advance design capability for structures in swelling rock through three aspects: i) developing a practical swelling model for design engineers, ii) investigate two crushable/compressible materials for the mitigation of swelling rock effects, and iii) observe and analyze the behaviour of swelling rock to current excavation techniques.

A swelling rock constitutive model has been developed. The swelling parameters include the horizontal and vertical free swell potential, threshold stress, and critical stress as well as a “pseudo-Poisson’s ratio” effect that allows the practicing engineer to explore the interaction between orthogonal suppression pressures without the need for advanced testing. The model has been verified through analysis of swell tests and well documented case studies.

Extruded polystyrene foams and light-weight cellular grouts were tested at monotonic low strain rates mimicking the loading behaviour of swelling rock to identify their potential as well mitigation materials. Results show low strain rates affect the yield strengths and elastic moduli. Cellular grout test results indicate it behaves as three-phase material in stress and groundwater conditions typical for infrastructure projects.

Two case studies were investigated, monitored, and analyzed. The Zone 1 Water Main project was located in the Halton Region, Ontario and the Billy Bishop Pedestrian Tunnel was located in Toronto, Ontario Results were analyzed to investigate the effect of excavation technique and shape on the elastic and time-dependent deformations of the rock mass.

## Keywords

Swelling shale, tunneling, constitutive modelling, time-dependent deformation, cellular grout

## Acknowledgments

The creation of this work is due solely to the amazing support that I received during my studies.

The love and support that I received from my family was a lifeline throughout this process. I cannot thank Katie, Ben, and Teddy enough. My loving parents and siblings provided much needed encouragement and support.

I relied heavily on a wonderful team at Western. The lab technicians, Wilbert, Melodie, and Caitlyn, provided critical guidance and support. My fellow graduate students helped me clarify my ideas. The administration support by Stephanie, Sandra, Cindy, and Kristen smoothed away any issues that I encountered. This thesis wouldn't exist if it wasn't for the incredible support and encouragement from my supervisor, Dr El Naggar. Dr K.Y. Lo is the reason I came back to study my PhD. He is an inspiration and has provided incredible mentorship throughout a majority of my professional and academic life. Thank you Dr Lo for your amazing gifts.

A major personal requirement for my studies was to be involved in industry problems. I was lucky to develop connections over the course of my studies. Brian Isherwood of Isherwood Geotechnical Engineers is a wonderful mentor. Tony and Joey DiMillo, Mike McFarlane, and Dave Marsland of Technicore Underground taught me more about tunneling than any textbook ever could. Stan Gonsalves of EXP Services Inc has supported my work through my studies. The team at RV Anderson was incredibly supportive during my study of the Zone 1 Water Main project. The success at the Zone 1 Water Main project wouldn't be possible without the help of Chris Fost and the team at C&M McNally.

Finally, I would like to thank my grandparents, Bill and Ruth Lardner, who have passed. Without a doubt, I would not be where I am without the love, encouragement, and incredible support I received from them. Bill's influence on my personal and professional life choices and growth cannot be understated. I dedicate this work to his memory.

# Table of Contents

Abstract .....	i
Acknowledgments.....	ii
Table of Contents .....	iii
List of Tables .....	vii
List of Figures .....	ix
List of Appendices .....	xv
Notations .....	xvi
Chapter 1 .....	1
1 Introduction .....	1
1.1 Background .....	1
1.2 Objectives .....	3
1.3 Organization of the thesis .....	5
1.4 Unique contributions.....	6
Chapter 2.....	9
2 Literature review .....	9
2.1 Introduction.....	9
2.2 Swelling rock formations and mechanism in southern Ontario.....	9
2.3 Swelling tests and the Lo and Hefny model .....	10
2.4 Swelling constitutive models .....	13
2.4.1 Anagnostou model .....	13
2.4.2 Wittke model.....	14
2.4.3 Kramer and Moore model.....	16
2.4.4 Hawlader model .....	17
2.4.5 Carvalho model.....	18

2.4.6	Lee model.....	19
2.5	Case histories .....	19
2.6	Compressible/crushable material .....	22
2.6.1	Expanded polystyrene foam.....	22
2.6.2	Cellular grout .....	24
2.7	Figures.....	26
Chapter 3	.....	34
3	Development of a constitutive model for time-dependent deformation of shaly rock in southern Ontario.....	34
3.1	Introduction.....	34
3.2	Constitutive model for swelling rock.....	35
3.2.1	Constitutive swelling relationships .....	35
3.2.2	Numerical procedure.....	38
3.3	Model verification.....	44
3.4	Case study – Heart Lake Road.....	47
3.5	Summary and conclusions .....	52
3.6	Acknowledgments.....	54
3.7	Figures.....	55
Chapter 4	.....	72
4	Investigation of swell mitigating material.....	72
4.1	Introduction.....	72
4.1.1	Purpose of this research .....	73
4.2	Experimental program .....	73
4.2.1	EPS foam .....	73
4.2.2	Cellular Grout .....	76
4.2.3	Sample preparation .....	76

4.2.4	Unconfined compression strength tests .....	77
4.2.5	Cellular grout triaxial tests.....	78
4.3	Summary and discussion.....	83
4.3.1	Design recommendations.....	86
4.4	Figures.....	88
Chapter 5	.....	107
5	Case study of circular excavations in swelling rock – Zone 1 Water Main Project ..	107
5.1	Introduction.....	107
5.2	Geotechnical investigation.....	108
5.2.1	Line Drilling and rock core logging.....	109
5.2.2	Laboratory testing conducted for this study.....	110
5.2.3	Additional laboratory and in-situ testing .....	113
5.3	Monitoring program.....	114
5.3.1	Shaft monitoring .....	115
5.3.2	Tunnel monitoring .....	117
5.4	Interpretation and analysis of shaft monitoring .....	118
5.5	Analysis of tunnel monitoring .....	119
5.5.1	Swelling rock constitutive model.....	119
5.5.2	Tunnel analysis .....	122
5.6	Summary and conclusions .....	125
5.7	Acknowledgements.....	127
5.8	Figures.....	129
Chapter 6	.....	147
6	Case study of rectangular shaft in swelling rock – Billy Bishop Pedestrian Tunnel Project .....	147
6.1	Construction history.....	147

6.2 Purpose of chapter.....	148
6.3 Geotechnical investigation.....	148
6.3.1 Site and laboratory work conducted outside of this study .....	149
6.3.2 Laboratory work conducted for this study .....	150
6.4 Monitoring program.....	152
6.4.1 Inclinometers.....	152
6.4.2 Precision survey monitoring .....	153
6.4.3 Extensometers .....	154
6.5 Shaft modeling.....	156
6.5.1 Geotechnical parameters.....	156
6.5.2 Model details and phases .....	159
6.5.3 Phase 2 – Long-term stresses on shaft structure .....	161
6.6 Discussion and conclusions .....	166
6.6.1 Phase 1 – Model calibration and comparison with mainland shaft monitoring.....	168
6.7 Acknowledgements:.....	169
6.8 Figures.....	170
Chapter 7.....	198
7 Summary and conclusions .....	198
7.1 Development of a swelling constitutive model.....	198
7.2 Swell mitigation material.....	200
7.3 Analysis of case studies .....	201
7.4 Future work recommendations .....	204
References.....	206
Appendices.....	217
Curriculum Vitae .....	263

## List of Tables

### Chapter 3

Table 3.1. Finite element calculation process in host program.....	40
Table 3.2. List of input and output variables provided by the host program. ....	41
Table 3.3. Swelling constitutive model input parameters.....	41
Table 3.4. Baseline parameters for verification testing. ....	45
Table 3.5 Input parameters for the Heart Lake Road analysis.....	49
Table 3.6. Section details.....	51

### Chapter 4

Table 4.1. Results of compression tests on EPS foams. ....	74
Table 4.2. Triaxial Set #1 test results.....	79
Table 4.3. Triaxial Set #2 test results.....	81
Table 4.4. Triaxial Set #3 test results.....	82



## Chapter 5

Table 5.1. Swell test summary at Zone 1 Water Main.....	113
Table 5.2. Checksum averages and Standard Deviations of inclinometer readings. ....	116
Table 5.3. Swelling parameters used in finite element analysis. ....	121
Table 5.4. Soil and rock parameters.....	124
Table 5.5 Spring line convergence over 120 days from excavation. ....	125
Table 5.6. Bending moments in steel liner after 75 years.....	125

## Chapter 6

Table 6.1. Lo and Hefny swelling model parameters for the BBPT (Micic et al 2016).....	150
Table 6.2. Uniaxial compression test results on Georgian Bay siltstone.....	151
Table 6.3. Uniaxial compression test results on horizontal Georgian Bay shale samples...	152
Table 6.4. Variable parameters used in calibration analysis.....	159
Table 6.5. Initial soil and rock parameters for finite element analysis. ....	160
Table 6.6. Effect of EPS 39 on bending moments of foundation wall due to swelling rock. .....	164

## List of Figures

### Chapter 2

Figure 2.1. Queenston and Georgian Bay Formations, modified from Armstrong and Carter 2006.....	26
Figure 2.2. Stress – swell potential relationship from Lo and Hefny 1996. ....	27
Figure 2.3. Example of a FST sample with measurement points. ....	27
Figure 2.4. Schematic of a free swell test deformation gauge. ....	28
Figure 2.5. Schematic of a semi-confined swell test. ....	29
Figure 2.6. Schematic of a null swell test. ....	30
Figure 2.7. Swelling model using 3 Kelvin units as per Kramer and Moore 2004. ....	31
Figure 2.8. Rock mass strength envelope in 2D principal stress space showing Excavation Damage Zone theory (Perras et al. 2015). ....	32
Figure 2.9. Typical EPS geofam uniaxial compression results. ....	33

### Chapter 3

Figure 3.1. Flow chart of swelling rock constitutive model. ....	55
Figure 3.2. First Time Step input. ....	56
Figure 3.3 Typical mesh and boundary conditions for model verification.....	57
Figure 3.4. Effect of meshing on constitutive model behaviour.....	58
Figure 3.5. Effect of First Time Step input on the behaviour of the constitutive model. ....	59
Figure 3.6. Swelling results using a First Time Step value of 10 days.....	60

Figure 3.7. Verification of free swell potentials, with constant $\epsilon_{fh}$ .....	61
Figure 3.8. Effects of applied stress on swelling potential selected by model. ....	62
Figure 3.9. Model verification of PPR values.....	63
Figure 3.10. Vertical swell potential Lo and Hefny model derived from Yuen (1979). ....	64
Figure 3.11. Heart Lake Tunnel mesh and boundary conditions. ....	65
Figure 3.12. Initial uniform horizontal stress of 4 MPa in Georgian Bay Formation.....	66
Figure 3.13. Horizontal deformations due to swelling after 10 years at Chainage 136+20. .	67
Figure 3.14. Deformed tunnel after 10 years at Chainage 136+20.....	68
Figure 3.15. Axial and bending forces after 10 years.....	69
Figure 3.16. Tangential stress at springline over 10 years.....	70
Figure 3.17. Variation of radial stress with distance from interface over time. ....	71
 Chapter 4	
Figure 4.1. Results of uniaxial compression tests with variable strain rate on EPS22 geofoam. .....	88
Figure 4.2. Results of uniaxial compression tests with variable strain rate on EPS39 geofoam. .....	89
Figure 4.3. Deformation modulus based on strain rate in post-elastic zone. ....	90
Figure 4.4. Results of ASTM UCS tests on cellular grout.....	91
Figure 4.5. Typical pre (a) and post failure (b) UCS test results. ....	92
Figure 4.6. UCS test results for strain rate of 0.17 %/min.....	93
Figure 4.7. UCS test results for strain of 0.034 %/min.....	94

Figure 4.8. UCS test results for strain rate of 0.007 %/min.....	95
Figure 4.9. Ultimate strength and $E_{50}$ modulus from variable strain rate UCS tests. ....	96
Figure 4.10. Typical triaxial samples (a), test set-up (b), and post-test results (c).....	97
Figure 4.11. Deviatoric stresses for Set #1. ....	98
Figure 4.12. Volume change during shearing in Set #1.....	99
Figure 4.13. Mohr's circles for residual strength in Set #1. ....	99
Figure 4.14. Post-test sample showing crushed zone. ....	100
Figure 4.15. Deviatoric stresses for Set #2. ....	101
Figure 4.16. Volume change during shearing in Set #2.....	102
Figure 4.17. Mohr's circles for residual strength in Set #2. ....	102
Figure 4.18. Test #8 with a crushed portion of cylinder due to cell pressure of 500 kPa....	103
Figure 4.19. Deviatoric stresses for test set #3. ....	104
Figure 4.20. Volume change during shearing in test set #3.....	105
Figure 4.21. Effective stress Mohr Circles for test set #3.....	105
Figure 4.22. Maximum shear stresses per backpressure.....	106
 Chapter 5	
Figure 5.1. Zone 1 water main tunnel location in Burlington and Oakville, Ontario.....	129
Figure 5.2. Excavated tunnel showing the McNally support system.....	130
Figure 5.3. Plan view of shaft and inclinometer location (dimensions are in mm). ....	131
Figure 5.4. Entry shaft section. ....	132

Figure 5.5. Monitoring section in tunnel showing borehole and tape extensometer layout (Dimensions are in mm).....	133
Figure 5.6. RQD with depth from borehole inclinometer drilling.....	134
Figure 5.7. UCS test results for Queenston shale. ....	135
Figure 5.8. UCS test pre (a) and post (b) failure.....	136
Figure 5.9. Free swell test results at Zone 1 Water Main .....	137
Figure 5.10. Semi-confined swell test results.....	138
Figure 5.11. Summary of null swell tests. ....	138
Figure 5.12. Lo and Hefny (1996) swelling model.....	139
Figure 5.13. Lo-Hefny swelling characteristics for vertical and horizontal swell potentials. ....	139
Figure 5.14. Select inclinometer results from the main shaft. ....	140
Figure 5.15. All inclinometer results from the main shaft.....	140
Figure 5.16. Deformation over time at main shaft at two Elevations.....	141
Figure 5.17. Select readings from East extensometer.....	141
Figure 5.18. Select readings from West borehole extensometer. ....	142
Figure 5.19. Tape extensometer readings. ....	143
Figure 5.20. Shaft analysis comparing calculated and observed deformations. ....	144
Figure 5.21. Comparison of swelling constitutive model with free swell test results .....	145
Figure 5.22. Constitutive model results at varying confining stresses. ....	145
Figure 5.23. Springline convergence over 75 years.....	146

## Chapter 6

Figure 6.1. Billy Bishop Pedestrian Tunnel mainland shaft. ....	170
Figure 6.2. Billy Bishop Pedestrian Tunnel typical section (Dimensions in mm). ....	171
Figure 6.3. Billy Bishop Pedestrian Tunnel mainland shaft section (Elevations in m). ....	172
Figure 6.4. Shaft structure at section (Elevations in m).....	173
Figure 6.5. Measured horizontal (a) and vertical (b) swell potentials (Micic et al 2016). ..	174
Figure 6.6. Square UCS test sample. ....	175
Figure 6.7. Results from USC test 1. ....	176
Figure 6.8. Results from USC test 2. ....	177
Figure 6.9. Results from USC test 3. ....	178
Figure 6.10. Results from USC test 4. ....	179
Figure 6.11. Horizontal UCST results from Sample 5.....	180
Figure 6.12. Horizontal UCST results from Sample 6.....	181
Figure 6.13. Inclinator results from the north wall at BBPT. ....	182
Figure 6.14. Deformation and excavation over time recorded by Inclinator 8.....	183
Figure 6.15. Example of pile survey results at north wall. ....	184
Figure 6.16. East wall extensometer readings. ....	185
Figure 6.17. West wall extensometer readings. ....	186
Figure 6.18. Numerical model connectivity plot showing mesh and boundary conditions. ....	187
Figure 6.19. RQD with depth at the mainland shaft. ....	188

Figure 6.20. FE results compared to Inclinometer BH01 readings at the end of active excavations.....	189
Figure 6.21. FE results compared to Inclinometer 8 readings at end of active excavation.	190
Figure 6.22. FE comparison to Inclinometer 8 movement over construction period. ....	191
Figure 6.23. Detail of EPS foam in FEA. ....	192
Figure 6.24. Principal strains in EPS 39 foam after 50 years of swelling. ....	193
Figure 6.25. Normal stress and bending moments for Case 1. ....	194
Figure 6.26. Horizontal deformations at end of shaft construction. ....	195
Figure 6.27. Foundation wall rotations at end of shaft construction. ....	195
Figure 6.25. Normal stress and bending moments for Case 2. ....	196
Figure 6.25. Normal stress and bending moments for Case 3. ....	197

## List of Appendices

Appendix A: Fortran Code for Swelling Subroutine .....	217
Appendix B: Zone 1 Water Main borehole logs .....	226



## Notations

Notations are limited to those used in the scope of this thesis.

Notation	Units	Description
$\bar{B}$		Strain interpolation matrix
CID		Isotropic consolidated drained triaxial test
CSP		Stiffness parameter
$\bar{D}^e$	kPa	Elastic stiffness matrix
$e$		Error per iteration
$e_{tolerated}$		Tolerated error per iteration
$E_r$	MPa	Elastic rock modulus
$E_{50}$	MPa	Intact rock modulus
EPS		Extruded polystyrene
$f'_c$	MPa	28 day compressive strength of concrete or grout
$f'_t$		28 day tensile strength of concrete or grout
$f(\bar{\sigma}^{tr})$		Yield function
$\bar{f}$	kN	Force vector
$\bar{f}_{ex}$	kN	External force vector
$\bar{f}_{in}$	kN	Internal force vector
$G$		associated flow function

Notation	Units	Description
$G$	MPa	Shear modulus
$l$		Step number
$j$		Iteration number
$\bar{\bar{K}}$		Stiffness matrix
$PPR$		Pseudo-Poisson's ratio
$\bar{\bar{R}}$		Rotation matrix
$r_{app}$		Applied free swell reduction
$r_m$		Reduction in free swell potential
$r_{max}$		Maximum free swell potential reduction amongst three orthogonal directions
$TBM$		Tunnel boring machine
$T_0$ or $t_0$	Days	Time at beginning of calculation step
$\Delta T$ or $\Delta t$	Days	Time increment of calculation step
$\bar{v}$		Displacement vector
$\gamma$	kN/m <sup>3</sup>	unit weight
$\bar{\epsilon}$		Strain vector
$\bar{\bar{\epsilon}}_{p,tdd}$		Swelling strain matrix in principal stress space
$\dot{\epsilon}$	Strain/log cycle of time	Swell potential

Notation	Units	Description
$\dot{\epsilon}_{free}$	Strain/log cycle of time	Free swell potential
$\dot{\bar{\epsilon}}_{free}$	Strain/log cycle of time	Free swell potential matrix
$\dot{\bar{\epsilon}}_{pot}$	Strain/log cycle of time	Swell potential matrix
$\sigma_i$	kPa	Applied stress
$\sigma_{th}$	kPa	Threshold stress
$\bar{\bar{\sigma}}_{th}$		Threshold stress matrix
$\sigma_c$	kPa	Critical stress or suppression stress
$\bar{\bar{\sigma}}_c$	kPa	Critical stress or suppression stress matrix
$\bar{\sigma}_c$	kPa	Stress vector
$\bar{\bar{\sigma}}_{c,tda}$	kPa	Swelling stresses in Cartesian space
$\bar{\sigma}^{tr}$	kPa	Iteration stress vector
$\bar{\mu}_i$		Directional vector of principal stress $i$
$\nu$		Poisson's ratio
$\phi$	Degrees	Friction angle
$\psi$	Degrees	Dilation angle

# Chapter 1

## 1 Introduction

### 1.1 Background

The issue of swelling rock in southern Ontario and the negative effects on buried structures has been known for decades, with one of the earliest known cases being the Wheel Pit at the Niagara Power Plant (Lee and Lo 1976). Research on this phenomenon conducted at the Geotechnical Research Centre at the University of Western Ontario has identified the mechanisms driving the swelling behaviour (Lee and Lo 1993) and developed series of Laboratory tests (Lo et al. 1982, Lo and Lee 1990) that have become standard for rock excavations in southern Ontario. Along-side this research, practical applications of the theory were employed in tunnel and excavation projects (Lo and Lukajic 1984, Lo et al. 1987, and Trow and Lo 1989). This work resulted in design recommendations that persist today. The two major design recommendations are: i) to allow the rock to swell for a period of time (typically 90 days) prior to installation of the permanent structure, and ii) if such a wait period is not permissible in the construction schedule, a crushable/compressible material should be placed between the swelling rock and the permanent structure. An alternative design option is to resist the strains and stresses due to swelling. This may be uneconomical as the stresses can reach 1.0 to 3.0 MPa and likely would be anisotropic. For a reinforced concrete structure, the results would be a thick, heavily reinforced liner, potentially requiring a larger excavation to accommodate the thicker liner. New design tools, such as numerical methods, are beginning to be employed. The

It is important to discuss the historical conditions of the historical design recommendations. At the time, most tunnel excavations occurred using the “drill and blast” method, employing explosives to excavate the rock. This excavation style typically results in extensive damage to the rock mass immediately surrounding the excavation, causing a decrease in rock mass competency and an increase in hydraulic conductivity. This damage typically aids the swelling mechanisms, resulting in an increase in swelling deformations over a shorter period of time, and allowing the swelling to occur throughout more of the rock mass.

Since the 1980's, advances have been made in rock excavation tools and techniques. Now, the predominant method for tunnel excavation is using Tunnel Boring Machines – essentially large, flat-faced, low-impact drills that excavate a circular tunnel with minimal damage to the surrounding rock mass. Other techniques include Tunnel Excavation Machines, which are typically composed of a large mechanical base with a hammer or rotomiller attached to a long excavation arm. Both of these excavation techniques result in a less damaged rock mass after excavation compared to the drill and blast method. This aids in resisting the swelling mechanism through reducing the intrusion of fresh water into the rock mass, lower in-situ stress reduction, and higher rock mass stiffness.

In general, drill and blast has fallen out of favour. Urban areas dislike the method for noise and vibration issues. Safety and regulation concerns also make it an unappealing choice when excavating in the soft shales known to swell.

The development of advanced excavation tools and techniques has not been matched by an advancement in the engineering tools and capabilities. Initial design tools included closed-form analytical analyses (Lo and Yuen 1981) and a more advanced version (Lo and Hefny 1996). The Lo and Yuen model is still a useful tool for “back of the envelope” design, but consistently provides conservative results due to the assumptions required for the solution. Several attempts have been made to create a constitutive model for numerical method solutions (Hawlder 2005, Kramer and Moore 2005, Carvalho 2015). To date, a constitutive model in a widely used commercial finite element program does not exist that sufficiently estimates the swelling behaviour of shales in southern Ontario.

Growth in the urban areas will drive the requirement for advanced understanding of swelling rock in southern Ontario and better engineering tools. Infrastructure development in southern Ontario, specifically within the Greater Toronto Area, spanning east to west from Oshawa to Burlington, and north to south from Newmarket to Lake Ontario, is undergoing tremendous growth. The Ontario Government estimates 33.5 % growth in the GTA between 2017 and 2041 (Ministry of Finance 2018). The population of Region of Halton alone is expected to increase by 35% in 15 years. To account for this growth, The Ontario Ministry of Infrastructure is investing \$190 billion in infrastructure by 2030 (Ministry of Infrastructure 2017). Much of

this infrastructure involves construction of tunnels and pipelines in swelling shale formations of southern Ontario such as Queenston shale and the Georgian Bay Shale.

## 1.2 Objectives

The work conducted for this thesis was done to advance the engineering tools and design capability for structures built in swelling rock. The following three aspects of design advancement have been considered:

1. Development of a constitutive model for swelling rock based on the behavior of swelling shales in southern Ontario that can be implemented in a widely used, commercially available finite element model program.
2. Explore the engineering behaviour of crushable/compressible materials for the purpose of mitigating the effects of swelling strains on buried structures.
3. Investigate the swelling behavior of rock due to a variety of modern excavation techniques.

The main objective of this study is to develop a swelling rock constitutive model for calculating the stresses and strains due to time-dependent deformation of rock mass and its effect on buried structures. The model couples the Lo and Hefney (1996) swelling model for shale rocks with a linear-elastic perfectly-plastic behaviour using the Mohr-Coulomb yield criteria. The model also incorporates a “pseudo-Poisson’s ratio” effect, similar to what was described in Lee and Lo (1993).

The main objective of this research is achieved through the development of a constitutive swelling model that provides practising engineers with a simplified and practical method for estimating the stresses and strains from swelling rock affecting buried structures due to complex excavations. The model accurately follows the state-of-the-art theoretical knowledge on swelling rock. This development is timely as many infrastructure projects involve excavation within swelling shales in southern Ontario are under consideration, especially in urban areas experiencing significant growth. As these infrastructure projects involve complex and expensive structures, there is a need for design tool that is capable of estimating the

swelling behaviour of shales and the interaction between the rock, structure, and any swell mitigating materials that may be used.

The model inputs are standard parameters of swelling rocks that are measured from well established swell tests widely used in the industry. This model also incorporates the “pseudo-Poisson’s ratio” effect by reducing the swelling potentials in the three principal stress directions to that of the lowest swell potential experienced. This simplification allows practising engineer to explore the “pseudo-Poisson's ratio” effects in a simplified manner, and eliminates the need for complicated and unreliable testing. The constitutive model has been implemented in the finite element computer program, PLAXIS (Brinkgreve 2016) that is widely used in industry.

The second objective is to identify and characterize the behavior of crushable/compressible materials for the use of swell strain mitigation. The two materials investigated were Extruded Polystyrene foam boards and cellular grout with high porosity. The original design recommendations were broadly defined and lacked actionable details (Section 1.1). From the author’s own experience, the definition of these materials has included everything from loosely placed sand to 15 MPa of compressive strength sand grout.

This objective aims to describe the behaviour of the two materials under low strain rates. The effect of low strain rates on EPS foam yield strength, elastic modulus, and post yield behaviour has not been researched. Cellular grout with a void ratio of 75 % is poorly understood, as the majority of studies concentrate on void ratios of 35 % or less. The effects of confinement on the behaviour have been studied.

Testing was conducted on both materials in order to evaluate their mechanical properties and determine their engineering parameters required for design purposes. Consequently, recommendations are made for testing and specifications in contractual works.

The third objective was to observe and analyze the effects of modern excavations on the swelling behavior of shales in southern Ontario. This was done by monitoring rock deformations due to shaft and tunnel excavations at two construction projects. The first project, excavated in the Queenston Formation, was the Zone 1 Water Main project, located in the Halton Region. The second was the Billy Bishop Pedestrian Tunnel project located in Toronto,

Ontario. The excavation was in the Georgian Bay Formation. Of interest was the behavior based on excavation type (shaft and tunnel depths and shapes) and excavation methods (hydraulic hammers, roto-millers, and tunnel boring machines). In each case study, the geotechnical investigation is reviewed, the monitoring system is described, the construction sequence is summarized, and the results of the monitoring are analyzed and used to predict future behavior.

### 1.3 Organization of the thesis

This thesis is organized into seven (7) chapters. Chapter 1 is an introduction to the problem and the proposed research to address the observed issues.

Chapter 2 is a literature review that covers the topics of this research. Included in the literature review are: i) a review of the geological conditions in southern Ontario, specifically the sedimentary rocks that experience swelling; ii) a detailed description of the swelling phenomenon and the tests developed at the Geotechnical Research Centre to measure the swelling behavior; iii) a review of the Lo and Hefny (1996) swelling model and previous constitutive models that have been developed to analyze swelling rocks; iv) case studies of recent excavations in swelling rock, and v) known behavior of extruded polystyrene foams and light weight cellular grout.

Chapter 3 presents the constitutive model developed for this research. It details the equations used to develop the numerical procedure for the three-dimensional swelling effect, how the swelling and elasto-plastic behavior is integrated, and how the swelling constitutive model fits within the host program. The model behavior is verified through a series of analyses mimicking well known swelling behavior in laboratory testing. Further verification is done through the analysis of the Heart Lake Tunnel project, a well documented case study.

Chapter 4 presents the results from laboratory testing of Extruded Polystyrene Foams and light-weight cellular grout. These materials were studied to evaluate their ability to mitigate the strains from swelling rock on buried structures. Tests included relevant industry accepted standard testing as well as low-strain rate uniaxial strength tests and unconsolidated-drained, low strain rate triaxial tests. Results are presented and interpreted to identify the relevant engineering behaviours and parameters.



Chapter 5 presents the first case study – the Zone 1 Water Main tunnel project. The main shaft was located near the south-west corner of the Burloak and Highway 403 intersection. The circular shaft was approximately 13 m in diameter and 42 m deep. The tunnel was excavated with a 2.6 m diameter main beam tunnel boring machine. Geotechnical investigation of the host Queenston shale included borehole logging, strength and strain property testing, and testing for swelling parameters. Monitoring included a series of inclinometers to observe shaft behavior, and tape and borehole extensometers in the tunnel to observe the time-dependent deformation behavior. The shaft monitoring results were analyzed to estimate the in-situ horizontal stress and the tunnel results were used to validate the model and predict the long-term swelling effect on the buried steel pipe.

Chapter 6 presents the case study of the Billy Bishop Pedestrian Tunnel project, located at the end of Bathurst Street at Lake Ontario in Toronto, Ontario. The tunnel was approximately 10 m across and 7.5 m high and connects the mainland to the Toronto Island airport. The mainland shaft was a rectangular excavation 33 m long, 14 m wide, and 35 m deep. The geotechnical investigation of the host Georgian Bay shale is summarized including borehole log and laboratory results. Monitoring included a series of inclinometers to observe shaft behavior, and tape and borehole extensometers in the tunnel to observe the swelling behavior. The shaft monitoring results were used to conduct a calibration analysis. The results of the analysis are used to predict the long-term effects of the swelling rock – compressible material – concrete structure interaction. Excavation technique and tools and bedrock behavior, including swelling, are analyzed and discussed.

Chapter 7 includes a summary of the work conducted for this research, conclusions derived from the results, discussion in regards to design of structures in swelling rock in southern Ontario, and recommendations for future work.

## 1.4 Unique contributions

The research conducted for this study has resulted in several unique contributions, each aligning to one or more of the objectives stated in Section 1.2.

The constitutive model developed for this research is one of the major unique contributions. The need for a swelling rock constitutive model that can be readily adapted for industrial use

with a minimal complexity was identified and addressed in this research. The model adapts the Lo and Hefny (1996) swelling model in a finite element host program. The swelling behaviour requires seven inputs, six of which are derived from tests developed at the University of Western Ontario in the Geotechnical Research Centre. The seventh parameter, the “pseudo-Poisson’s ratio”, was developed to address two issues. The first was to eliminate the need for advanced and often unsuccessful testing by implementing the “pseudo-Poisson’s ratio” as a sensitivity parameter that a practicing engineer can vary and study the effects on excavation and buried structures. The second development with the “pseudo-Poisson’s ratio” was to limit the influence of orthogonal suppression pressures, preventing conservative reductions in swelling potentials. See Section 3.2.2.2 for details. The programmed model differentiates itself from existing models in three key ways:

1. The model relies only on established swelling tests for inputs.
2. The model fully incorporates the anisotropic swelling behaviour described by vertical and horizontal Lo and Hefny swelling models.
3. The model works fully in three dimensions at all stages of swelling calculations.

Testing of compressible/crushable materials for the mitigation of swelling strains and stresses provides unique contributions on the behaviour of materials. For the study of EPS foams, the unique aspect of this research was the effect on material properties due to low strain rates. The low, monotonic strain rates the EPS samples were tested at represent the swelling behaviour. Testing of EPS foam boards is fairly extensive, as will be discussed in Section 2.6.1. However, no previous works were discovered during the literature review that dealt with the type of loading as seen in swelling rock conditions.

Cellular grouts are another established and well researched building material, as will be discussed in Section 2.6.2. This work on cellular grouts is unique due to studying cellular grouts with a high porosity (75%) and low density (approximately 400 kg/m<sup>3</sup>). Cellular grout with these properties were chosen as a readily crushable, strain softening material to address the issues of swelling rocks. There is a lack of research on cellular grouts with these properties and this work provides valuable insight into the material behaviour under confined and saturated/partially-saturated conditions.

The research also presents two case studies of recent excavations in swelling rocks in southern Ontario. For each case study, the results of the geotechnical and laboratory investigation are provided; the excavation methodology and construction sequence is detailed; the rock support and structural information is detailed; the monitoring program to observe rock mass behaviour in shafts and tunnels is described, with results presented and analyzed; the structures were analyzed using the programmed constitutive model described above and the effects of EPS foams and cellular grouts on the final stresses experienced by the buried structures were explored.

## Chapter 2

### 2 Literature review

#### 2.1 Introduction

This chapter provides a review of information relevant to the research and work conducted for this thesis and contains six sections. Section 2.2 contains a review of the geological conditions in southern Ontario and the swelling mechanism of shales is provided. Section 2.3 section discusses the Lo and Hefny (1996) swelling model and the swelling laboratory tests developed at the Geotechnical Research Centre to provide the inputs of the model and describe the stress-dependent swelling behaviour are detailed. In Section 2.4, previous swelling models are discussed. Section 2.5 reviews recent case studies of excavations in swelling shales in southern Ontario. Section 2.6 reviews the behaviour of extruded polystyrene foams and light-weight cellular grout.

#### 2.2 Swelling rock formations and mechanism in southern Ontario

Within southern Ontario, the two major formations that experience swelling behaviour are the Queenston Formation and Georgian Bay Formation, both composed mainly of shale. Both formations are shown in Figure 2.1, and are within the Appalachian Basin, which is overlain by the Michigan Basin and overlays the Canadian Shield (Armstrong and Carter 2006). The mineralogy of these shales from multiple studies (Lo et al. 1978, Lo et al. 1987, Lee and Lo 1993) indicate that the shale rocks contain minimal amounts of swelling clay minerals and negligible amounts of other minerals known to cause swelling such as anhydrite and pyrite. Lee and Lo (1993) conducted a thorough test regime on Queenston shale samples and found that the driving mechanism for time-dependent swelling is the exchange of cations between the salt-rich pore water and ambient freshwater. Lee and Lo (1993) proposed that it is the action of cations leaving the sample (diffusion) and freshwater entering the sample (osmosis) that propels the formation of micro and macrocracks, which become saturated, resulting in an increase in volume. The chemical process of diffusion and the movement of water into the rock are both time-dependent behaviours, resulting in the observed time-dependent swelling.

Calcite content within the rock is known to affect the swelling potential (Lo et al. 1978) by acting as a cementing agent and reducing the swelling by resisting the growth of microcracks. Although calcite is the most common bonding agent observed in southern Ontario shales, other cementitious minerals are known, such as quartz and other silicates, and iron oxides. Calcite binds the shale minerals, preventing the growth of microcracks. However, access to fresh water and atmospheric conditions can lead to the dissolution of calcite over time. Calcite acting as a limiting factor on the swelling behaviour of rock has been noted by Lo (1989), who observed swelling in rocks with calcite contents less than 12%. Al-Maamori et al (2016) observed calcite contents as high as 37% in swelling Queenston shale samples taken from the Milton, Ontario region.

The Geotechnical Research Centre at Western University has studied the phenomena over the last 40 years. Lee and Lo's (1993) work on the Queenston shale highlighted the stress dependency of the swelling potential and illustrated the salt water gradient between the rock pore water and fresh groundwater as the driving mechanism of the swelling phenomenon. Lee and Lo (1993) also provided the following conditions required to initiate swelling:

- i. The relief of initial stresses which serves as an initiating mechanism;*
- ii. The accessibility to water; and*
- iii. And outward salt concentration gradient from the pore fluid of the rock to the ambient fluid.*

In Lee and Lo's work the relief of initial stresses was considered to be the initiating mechanism for swelling. Negative porewater pressures are generated as the rock experiences relaxation from the stress relief. This negative porewater pressure drives the water into the sample, initiating the swelling process.

## 2.3 Swelling tests and the Lo and Hefny model

Lo et al. (1978) developed a test procedure and tools to measure the deformation of rock core samples over time with unrestrained samples (Free Swell Test) and samples confined in a single direction (Semi-Confined Swell Test). Further refinement occurred over the decades,

including more advanced tests (Lo and Lee 1990) and the addition of the Null Swell Test (Lo and Hefny 1999), which measures the applied stress that suppresses swelling in the direction of the applied stress.

Free Swell Tests (FST) measure the strain in three orthogonal directions over time of a cylindrical sample cut from a rock core, providing the determination of the free swell potentials. FST are conducted using the methodology developed by Lo et al. (1978). Samples for FST are cleaned, measured, and weighed. The centre of each horizontal face is marked, as well as four points along the mid-section each 90 degrees apart. Measurement points are fixed to these locations to measure deformation in three orthogonal directions. An example FST sample is shown in Figure 2.3. Once prepared, the samples are kept at constant temperature and 100% humidity. Readings are taken over a 100-day period using a deformation gauge device developed by the Geotechnical Research Centre, as shown in Figure 2.4. The test results are plotted as log-time vs strain and the free swell potential is defined as the swelling strains based on the best-fit line from the data points between 10 and 100 days.

Semi-confined swell tests (SCST) measure the swelling strain in a single direction due to an applied pressure. Semi-confined swell tests are conducted using the methodology described in Lo et al. (1978). After cutting, samples are cleaned, measured, and weighed. Samples are placed in an open-top cylindrical container and a load cap was placed on top of the sample. The container is then placed in the load application device shown in Figure 2.5. The container is then filled with tap water and the desired load was applied directly on the load frame or through the lever arm for higher pressures. Deformation measurements are recorded over 100 days. The test results are plotted as log-time vs strain and the swell potential is defined as the swelling strains based on the best-fit line from the data points between 10 and 100 days.

The FST and SCST results are used to evaluate the stress dependent swelling potential. The swelling potential is defined as the rate at which the rock is swelling and is given in strain per log cycle of time.

Null swell tests (NST) measure the suppression pressure in a single direction exerted by the swelling sample when deformations are controlled to near zero. Null swell tests are conducted using the methodology described in Lo et al. (1978) and Lo and Hefny (1996). After cutting, samples are cleaned, measured, and weighed. Samples are placed in an open-top cylindrical

container and a load cap is placed on top of the sample. The sample is placed in a compression device developed by the Geotechnical Research Centre as shown in Figure 2.6. A load cell is placed on the sample and the deformation gauges are initialized. A sitting load of 5 % or less of the expected load is placed on the sample and then tap water is added to the container. Measurements are taken daily, with additional load being placed on the sample to control deformation to within 0.01 % strain. Pressures typically stabilize to the null swell pressure within 5 to 30 days. Test results are typically plotted as pressure over linear time, with the stress at which no swelling occurs, or critical stress, being obtained by the stabilized pressure.

The swell tests are conducted on vertical rock cores, or horizontally oriented samples re-cored from the borehole sample. The applied stresses and measured swelling strains are always oriented parallel or orthogonal to the bedding planes. It is assumed that the stress-swell potential relationships measured in the orthogonal directions are the principal values.

Results from the Lo et al. (1978) and Lo and Lee (1990) studies clearly indicated that the swelling potential is stress dependent. The relationship between confining stress and swell potential can be characterized by the swelling tests described above. The Free Swell Test (FST) provides a maximum swelling potential, and the Null Swell Test (NST) provides a stress limit to the swelling behaviour. The Semi-Confined Swell Test (SCST) provides the stress-swell behaviour between the two extremes. The relationship between the confining stress and the swelling potential can be plotted as shown in Figure 2.2, and forms the stress – swell potential relationship described in Hefny et al. (1996). Three values can identify each relationship:

$\epsilon_{\text{free}}$  = free swell potential, derived from free swell tests,

$\sigma_{\text{th}}$  = threshold stress, the value at which stress dependency begins,

$\sigma_{\text{c}}$  = critical stress, the stress at which the swelling is fully suppressed.

Lo et al. (1978), Lee and Lo (1993), and others noted that the swelling potentials and critical stresses are anisotropic. In general, free swell potentials and critical stresses are greater in the vertical direction. Lo et al. (1978) noted that the bedding and fabric of the sedimentary rocks were a likely cause of this anisotropy.

Lo and Lee (1990) discovered that the applied stress in one direction not only reduced time-dependent deformation in that direction but also reduced deformation in the orthogonal directions. This effect has become known as the “pseudo-Poisson’s ratio” (PPR) effect. The number of tests reported that measured the PPR are limited and no general relationships for the reduction magnitude due to the PPR are available. It is known that the reduction does not follow a 1:1 ratio. Lo and Lee found a PPR of approximately 0.3 during testing of Queenston shale.

## 2.4 Swelling constitutive models

Swelling rock behaviour occurs in multiple formations throughout the world and has been a known engineering issue for decades. In southern Ontario, the swelling shales were observed to cause damage over a 75 year monitoring period beginning in 1905 (LO SAB). Internationally, Wittke-Gattermann and Wittke (2004) and Anagnostou (1993) have worked on tunnels in swelling rock in Germany. Models have been created to address various swelling mechanisms with emphasis on different variables. This section provides a non-exhaustive summary of swelling models.

### 2.4.1 Anagnostou model

Anagnostou (1993) proposed a coupled hydraulic-mechanical model for rock swelling. This model considers the effects of pore water and flow through the rock mass and relates the swelling potentials to the orientation of the bedding planes as opposed to the principal stresses. The model assumes swelling is predominantly linked to the effects of pore water pressure and mean effective stress, which can lead to abnormal behaviour with anisotropic stress states. Swelling parameters are derived from a multistage triaxial tests. The first stage is equivalent to a Null Swell Tests. The second stage requires gradual reduction in confining stresses and measuring the volumetric strain and resulting effective stresses. The model requires a large number of input parameters, including the elastic properties, rock strength, volumetric and directional swelling potentials, and hydraulic conductivity of the rock mass. The model is incorporated in a computer code developed by the author, but not available to practicing engineers for their design. Although this model was one of the first comprehensive swelling rock constitutive models and has provided important insights on how to analyze the



phenomenon, the non-standard and in-situ testing inputs required to measure the values make it difficult to implement.

## 2.4.2 Wittke model

A constitutive swelling model has been developed by Wittke-Gattermann and Wittke (2004) and Hosseinzadeh (2012) and was incorporated in the commercially available program PLAXIS. The model incorporates the swelling behaviour described by Grob (1972), which is similar to the stress - swell potential relationship proposed by Hefny et al. (1996), and Anagnostou's work in that it relates the swelling behaviour to the bedding plane orientation.

The model considers an elasto-plastic rock mass with anisotropic elastic moduli based on its bedding. The model incorporates a linear-elastic perfectly-plastic “Mohr-Coulomb” yield criteria, with isotropic parameters for the cohesion, friction angle, dilatancy angle, and tensile strength. Swelling behaviour follows Grob's (1972) relationship, with the swelling rates being adjusted by the volumetric strain history. It evaluates the total strain ( $\epsilon_{tot}$ ) at each time step as the sum of the elastic ( $\epsilon_{el}$ ), visco-plastic ( $\epsilon_{vp}$ ), and time-dependent (swelling) ( $\epsilon_q$ ) strains, i.e.,

$$\epsilon_{tot}(t) = \epsilon_{el}(t) + \epsilon_{vp}(t) + \epsilon_q(t) \quad [2.1]$$

All strains are considered to be a function of time due to the nature of swelling rock. The resulting stresses are then calculated based on the calculated strains.

The time-dependent swelling function is given by (Kiehl 1990):

$$\dot{\epsilon}_i^q = \frac{1}{\eta_q} [k_q(\log \sigma_i(t) - \log \sigma_0) - \epsilon_i^q(t)] \text{ for } i = 1,2,3 \quad [2.2]$$

Where:

$\dot{\epsilon}_i^q$  = the swelling potential in principal direction  $i$ ,

$\frac{1}{\eta_q}$  = the swelling time parameter, which controls the strain rate of swelling behaviour,

$k_q(\log \sigma_i(t) - \log \sigma_0)$  = is the final strain expected in the principal direction  $i$ ,

$\epsilon_i^q(t)$  = the swelling strain at time  $t$ .

The rate at which swelling occurs is controlled by the parameter  $1/\eta_q$ , which in turn is a function of the strain history. Recognizing that the swelling behaviour is controlled by access to water, the model assumes a relationship between the swell potential and hydraulic conductivity, which is affected by the volumetric strain history. As the strains increase, the hydraulic conductivity should decrease along with the swelling rate. The model accounts for these changes over time with the following equation:

$$\frac{1}{\eta_q} = a_0 + a_{el0} \cdot \varepsilon_{v0}^{el} + a_{vp} \cdot \varepsilon_v^{vp}(t) \quad [2.3]$$

Where:

$a_0$  = the threshold swelling parameter,

$a_{el0}$  = the elastic volumetric strain parameter,

$a_{vp}$  = the visco-plastic volumetric strain parameter.

The  $a_0$  parameter represents the initial swelling conditions. The second term of Eq. 2.3 represents the elastic volumetric strains before swelling initialization. The third term represents the visco-plastic volumetric strains as a result of dilatancy. The model has a maximum cut-off value of  $\varepsilon_{vp}^v$ , which represents a strain magnitude and the corresponding permeability at which no further increase in the swelling rate is expected as the maximum amount of water the system can absorb is supplied.

In practice,  $1/\eta_q$  is obtained through curve fitting of observed data, which affects the rate at which the maximum swelling strain is reached. The volumetric strain parameters ( $a_0$ ,  $a_{el0}$ , and  $a_{vp}$ ) cannot be derived from any standardized swell test and their ranges reported in literature are empirically established from a small number of case studies. Hosseinzadeh (2012) modelled a series of laboratory swell tests and noted that  $a_0$  has the largest effect on the swelling rate while  $a_{el0}$  has a minimal effect on the results. Meanwhile, increasing  $a_{vp}$  resulted in a sudden reduction in the  $1/\eta_q$  value after yielding had occurred. Hosseinzadeh (2012) models were based on laboratory results of small samples, and there was no discussion of suitable volumetric strain parameters for project scale problems.

Even though the model requires 18 engineering parameters, including the volumetric strain parameters discussed above, it does not account for the effect of PPR on swell potential reduction from orthogonal stresses. The volumetric strain parameters cannot be measured. Since they are volume based, curve fitting laboratory sample results may not reflect project scale problems. The model is incorporated in a commercial finite element product, but has limited use in practice because of the above mentioned limitations.

The Wittke model was used by Al-Maamori et al (2018) to conduct a study on the effects of different lubricant fluids for micro-tunneling applications in swelling rock. The paper presents a strong model verification process through modeling results of Free Swell Tests, Semi-Confined Swell Tests, and Null Swell Tests. Further model verification was done on known case studies. The results of the micro-tunnel modelling presented stresses and strains acting on the buried structures that matched known and expected material behaviour. However, the paper is silent on the volumetric strain inputs described above. The paper does not list what the values were or how they affect the results. It would be of interest to see the sensitivity of the modeling to variations of these input parameters.

### 2.4.3 Kramer and Moore model

Kramer and Moore (2005) developed a constitutive model for swelling rocks based on the characteristics of shales from southern Ontario. The constitutive model is based on the work by Hefny et al. (1996) and was implemented in the finite element program AFENA. It assumes that the behaviour of swelling shale can be estimated using a system of three Kelvin units in series, as shown in Figure 2.7. The elastic and plastic strains are calculated using the elastic stress-strain matrix ( $\bar{D}_E$ ) and combined yield function ( $f(\bar{\sigma})$ ) and plastic potential ( $g(\bar{\sigma})$ ). The swelling strain is calculated using the sum of three Kelvin units composed of the elastic stress strain matrices ( $\bar{D}_{TDD,i}$ ) and the viscosity matrix ( $\bar{\eta}_{TDD,i}$ ). The swelling parameters are anisotropic and input as vertical and horizontal values, which are rotated to the principal stresses during evaluation of the swelling strains.

The nonlinear, visco-elasto-plastic constitutive model uses a Mohr-Coulomb yield criterion and anisotropic swelling parameters. It does not consider the effects of the pseudo-Poisson's ratio. In addition, obtaining the swelling input parameters are difficult due to the required testing duration.

#### 2.4.4 Hawlader model

Hawlader et al. (2003) and (2005) developed a constitutive model based on the swelling characteristics of shales from southern Ontario, and is incorporated in AFENA. Unlike the Kramer and Moore model, the Hawlader model evaluates the swell potentials based on the free swell potential being reduced through the effects of the three-dimensional stress condition using the stress-swell potential relationship proposed by Hefny et al. (1996), which is shown in Figure 2.2. The model accounts for the “pseudo-Poisson’s ratio” effect, but is linear-elastic and does not consider the effects of plasticity. In addition, the threshold stress and critical stress are considered equal in the horizontal and vertical directions. The free swell potentials are input separately for the vertical and horizontal directions.

The general methodology outlined by Hawlader (2005) has been used as a foundational work by this study and others to be discussed later in this research. Hawlader recognized the impact of three-dimensional stress on the formulation of swelling strains and the importance of performing the calculations in principal stress orientation.

The formulation of swelling strains in the principal stress directions by Hawlader (2005) is conducted over six steps. The first is to transform the free swell potentials from the horizontal and vertical direction with following simple equation:

$$\dot{\epsilon}_{free,i} = \dot{\epsilon}_{free,x} \cos \alpha_{pi} + \dot{\epsilon}_{free,y} \sin \alpha_{pi} \quad [2.4]$$

Where  $\dot{\epsilon}_{free,i}$  is the free swell potential in the  $i^{\text{th}}$  principal stress direction,  $\dot{\epsilon}_{free,a}$  is the free swell potential in either the horizontal ( $a = x$ ) or vertical direction ( $a = y$ ), and  $\alpha_{pi}$  is the angle between the major principal stress orientation and the x-direction.

The applied stress is then calculated for each principal stress direction. The effect of the PPR is applied as a pseudo-stress derived from orthogonal stresses. The pseudo-stresses from orthogonal directions are added to the stress acting in the principal direction being calculated, as shown in Equation 2.5.

$$\sigma_i^{TS} = \sigma_i + \sum \sigma_{th} 10^{[R_{ij} \log(\sigma_c / \sigma_{th})]} \quad [2.5]$$

Where  $\sigma_i^{TH}$  is the confining stress used to determine the swelling potential in the direction of interest,  $\sigma_i$  is the confining stress in the direction of interest,  $\sigma_{th}$  is the threshold pressure in the orthogonal directions,  $R_{ij}$  is the percent reduction from the free swell potential in the orthogonal directions multiplied by the PPR value,  $\sigma_c$  is the critical stress in the orthogonal direction.

Thus, the applied stress in any principal direction is a function of the stresses in all three directions. In each principal direction, the applied stress is the sum of the initial stress plus the two pseudo-stresses from the orthogonal directions reduced by the PPR.

The applied stresses, which have been increased due to the PPR calculations, are used to determine the swell potentials in principal stress state. These potentials are then rotated back to Cartesian (x, y, z) space. Finally, the swelling strains and resulting stresses are calculated.

This model provides a strong foundation for the models that followed. It provided a framework for the interaction of swelling potentials and confining stresses in terms of the three-dimensional stress state.

#### 2.4.5 Carvalho model

Carvalho (2015) developed a swelling constitutive model and incorporated it in a finite difference program. The model assumes linear-elastic perfectly plastic behaviour with the Mohr-Coulomb yield criteria for the rock and adopts the swelling model of Hefny et al. (1996), hence it requires six parameters: stress – swelling potential relationship: free swell potential, threshold stress, and suppression stress for vertical and horizontal directions. In addition, it accounts for the “pseudo-Poisson’s ratio” effect. In general, the model is a simplified version of the Hawlader model. Similar to the other models discussed above, it calculates the swelling potentials and swelling strains in the principal stress directions by rotating the parameters from the vertical and horizontal directions into principal stress orientation.

Carvalho simplifies the approach to the PPR implementation from Hawlader et al. (2005) work. For each principal stress direction, the ratio between the calculated swelling potential and the free swell potential,  $r_i$ , is calculated as shown in Equation 2.6.

$$r_i = 1 - R_i \quad [2.6]$$

Where:

$$R_i = \log \frac{(\sigma_i/\sigma_{th})}{(\sigma_c/\sigma_{th})} \quad [2.7]$$

The swell potential in any principal stress direction is then calculated by Equation 2.8, below.

$$\dot{\epsilon}_i = \dot{\epsilon}_{i \text{ free}} \times r_i \times (r_{ij} \times PPR) \times (r_{ik} \times PPR) \quad [2.8]$$

Thus, the swell potential is reduced by a function of the confining stress in the direction of interest, and by the ratio of the confining stresses and PPR values in the orthogonal directions ( $r_{ij}$  and  $r_{ik}$ ).

#### 2.4.6 Lee model

Lee (2017) developed a swelling constitutive model, based on Hawlader's and incorporated it in a finite difference program. It considers the free swell potential, threshold stress, and suppression stress as the main input for swelling behaviour. The model also incorporates the "pseudo-Poisson's ratio" effect and simulates the rock as linear-elastic perfectly plastic material utilizing the Mohr-Coulomb yield criteria. However, the model is not clearly described. It appears that only one suppression stress is used for both the horizontal and vertical directions, which could lead to poor results depending on the values chosen. The difference between the vertical and horizontal in-situ stresses in southern Ontario tend to be large: 100's of kPa vertically near surface compared to 2 to 8 MPa horizontal stress measured in downtown Toronto (Trow and Lo 1989). The ratio between vertical and horizontal suppression stress is typically around 3V:1H. It is very difficult to propose a single suppression stress that accommodates all of the rock characteristics.

## 2.5 Case histories

Tunneling projects in Ontario face the unique challenge of long-term design for swelling rock. The swelling phenomena is well documented in terms of case studies (Lo and Yuen 1981, Lo and Lukajic 1984, Lo et al. 1987) and material behaviour (Lo et al. 1978, Lo and Lee 1990). Much of the research on the effect of swelling rock occurred in the 1980's and 1990's, with blasting being a major factor in excavation (Lo et al. 1979, Lo and Lukajic 1984).

A recent excavation in swelling rock in southern Ontario was the Niagara Tunnel project, a 14.4 m diameter, 10.1 km long water diversion tunnel for the Sir Adam Beck power plant. Excavation of the tunnel began in September 2006 with the Tunnel Boring Machine (TBM) breaking through in March 2011. The majority of the excavation occurred in the Queenston Formation, with significant overbreak ranging between 2 and 4 m deep at the crown. Analysis of the tunnel by Perras (2009) and Perras et al. (2015) identified several key parameters in the rock mass response to excavation. Perras (2009) explored the role of layer thickness and anisotropic rock mass strength and strain properties. The study noted the importance of using an anisotropic constitutive model for tunnel analysis in order to properly capture the bedded rock mass behaviour. Bedding layer thickness was found to influence failure modes when considering the ratio between layer thickness and tunnel radius. The ratio between horizontal in-situ stress and intact Elastic Modulus had some effect as well. The results of the rock mass anisotropy and bedding plan thickness study show strong correlation with the overbreak observed in Niagara Tunnel Project and match failure modes in other tunnels observed by the author. Perras et al. (2015) expanded on the analysis by incorporating Excavation Damage Zone theory for brittle rock (Diederichs 2007), shown in Figure 2.8. Although the authors identified the sedimentary rocks at the Niagara Tunnel Project as likely “shear failure” type rocks (upper right corner of Figure 2.8), the detailed numerical analysis highlighted the ability of incorporating the Crack Initiation, CI, and Crack Damage, CD, input values to provide analyses that reflect the complex rock behaviour more accurately.

Recently published studies on excavations in the Georgian Bay Shale include a series of shafts in the Toronto area by Aglawe and Sinclair (2002), a summary of tunnels in the Georgian Bay Formation by Cushing et al. (2015), and the excavation for the Shangri-La mixed use condominium in downtown Toronto (Isherwood et al. 2014). Aglawe and Sinclair (2002) and Cushing et al. (2015) discuss shaft and tunnel excavation in the Georgian Bay shales respectively. Aglawe and Sinclair discussed the typical design consideration for structures in swelling rock: allow the rock to expand over a period of time and measure the rock mass deformations. Once the rate of deformations reaches an acceptably low amount, installation of the final structure may begin. Cushing et al. (2002) provided time-dependent deformation monitoring results from select projects throughout the Toronto area. Two shafts showed swelling deformations, while two TBM excavated tunnels showed negligible deformations

over 80 days or more, indicating orientation and excavation methodology may play a role in the development of swelling strains. Isherwood et al. (2014) did not discuss the role of swelling behaviour of Georgian Bay shale, but addressed several of the practical challenges of excavating within the Formation. These include limiting the elasto-plastic rock deformation to prevent undesired movement of foundations, rock face protection, ground water, and support for the two prominent near vertical joint families – the major family strikes roughly east-west and the minor family strikes roughly north south.

Most tunnels and vertical shafts that experienced damage from swelling rock were constructed using drill and blast excavation, such as the Heart Lake Tunnel (Lo and Yuen 1981) and the Darlington nuclear power plant intake tunnel (Lo and Lukajic 1984). Only a portion of the Heart Lake Tunnel was constructed using drill and blast excavation, with another portion being constructed using cut-and-cover and the majority of the tunnel being excavated with a TBM. The drill and blast section suffered significant damage that progressed upstream into the TBM section.

A non-circular configuration such as the Thorold underpass (Bowen et al 1976) and a recently constructed sewer system (Carvalho 2015) may lead to damage from swelling rock. Both the Thorold underpass and the sewer system had vertical cuts with the main structure connected to the rock via concrete. Both structures suffered damage that affected their serviceability and required remediation/replacement. Drill and blast excavation leads to varying amounts of overbreak, causes significant damage to the surrounding rock resulting in discontinuities, causes significant expansion of micro and macro fractures, increases hydraulic conductivity, and decreases the mass modulus. All these consequences would exacerbate the swelling condition and lead to higher deformations. The Darlington tunnel was adequately designed for the swelling strains, but experienced up to 4 mm of displacement at the springline. The Heart Lake Tunnel project did not include any measurement of deformations during construction, but experienced significant damage from the swelling rock in the tunnel section that was constructed employing drill and blast.

Research is being conducted on shale formations that may experience time-dependent deformations for the purpose of low-grade nuclear waste storage. The need for extremely stringent safety conditions for the storage of nuclear waste requires intimate knowledge of how



rock behaves due to excavation and construction over a very long time period. Current design of deep nuclear waste storage facilities consider sedimentary formations as the preferred location, and their swelling behaviour is considered a very important factor. Researchers are concerned with how the rock swell affects the hydrological properties of the rock mass over the lifespan of the facility (Bluming et al 2007, Laynon et al 2011). Current research indicates that swelling in the Excavation Damaged Zone (EDZ) causes a decrease in the hydraulic conductivity of the rock mass, resulting in an improved condition for the waste storage (Bluming et al 2007). This reduced hydraulic conductivity potentially limits the access to water over time and would in theory reduce the swelling effects.

## 2.6 Compressible/crushable material

Initial design recommendations for buried structures in swelling rock (Lo et al 1987) including installation of a compressible/crushable material between the buried structure and the swelling rock if the construction schedule prevents waiting for the swelling strains to abate. The definition of such a material has not been well established in the tunneling industry. Two potential materials have been investigated as part of this study. The first is Extruded Polystyrene foam and the second is light-weight cellular grout. This section will discuss known behavior and previous testing conducted on these materials.

### 2.6.1 Expanded polystyrene foam

Expanded Polystyrene (EPS) foam has favourable properties such as high strength to weight ratio, ease of installation, low cost, thermal insulation, moisture resistance, and acoustic and dynamic absorption. In addition, EPS foams are recyclable and can represent a green building material. EPS foam products are used as building material in applications such as insulated concrete moulds and Structurally Insulated Panels. They are also used in geotechnical applications such as lightweight fill for embankment stability.

EPS foam material properties are well documented. In general, density controls its mechanical properties; an increase in the density of EPS foam results in proportional increase in its stiffness and strength. The compression and tensile strength of the EPS foam can be determined following standard tests (i.e., ASTM D6817, ASTM D1621, ASTM C203). ASTM D6817 provides typical values of stress and strain at 1%, 5%, and 10% strain, as well as other

properties for various densities of EPS. ASTM D1621 specifies the load testing up to maximum strain of 10%. This range encompasses the elastic portion and the yield point, but does not capture the post-yield behaviour. Figure 2.9 shows the typical stress-strain behaviour of foam subjected to uniaxial compression loading up to 80% strain. The response curve displays three distinct segments: an elastic segment that typically extends from start of loading up to 5% - 10% strain; a near perfect plastic segment; and a final segment that typically depicts drastic strain-hardening behaviour.

Several studies evaluated the engineering parameters of EPS foams. Elragi (2000) found that the strength at 5% and 10% strain were relatively independent of sample size or strain rate. However, the stiffness was affected by both. Gnip et al. (2007a) also reported that values of the elastic modulus from the loading test are influenced by the sample width and height. Elragi discussed the potential end effects on the testing results, but neither reference made recommendations on sample size requirements.

The Gnip et al. (2007b) and Smakosz and Tejchman (2014) concluded that the tensile strength of EPS foam determined from tensile testing is a function of the sample size. They also reported that brittle failure occurs in pure tension, and the ultimate load occurs at approximately 3% strain.

There are no applicable standard tests to evaluate creep in EPS foams, albeit their creep behaviour has been widely investigated. Elragi (2000) and Srirajan et al. (2006) conducted load tests on EPS specimens with different sizes and densities and reported that creep behaviour is dependent on sample size. Nugessey (2007) presented observations of settlement and creep from a case study, which indicated that laboratory tests underpredict elastic modulus and overpredict creep values. The findings present problems for practical engineering applications.

Chen et al. (2015) and Mohamed et al. (2017) studied the effect of strain rate on the measured mechanical properties of EPS foam, considering strain rates ranging from 2% strain/min up to dynamic load rates of 3,000,000% strain/min. Mohamed et al. (2017) evaluated the behaviour at varying strain rates from 2% strain/min to 400% strain/min and found that, generally, the elastic modulus and yield point increased as the strain rate increased. Similarly, Chen et al (2015) reported that the response of EPS foams to dynamic loading depends on the strain rate,

with an increase in the measured compressive strength as the strain rate increases, while the measured elastic modulus increased slightly.

## 2.6.2 Cellular grout

Cellular grout is a mixture of cement, sand, foaming agent, and some other additives. It is used in geotechnical applications such as backfill material for retaining walls, bridge abutments and approaches. The density, strength and elastic modulus of the grout are highly dependent on the selection of the foaming agent, foam preparation, and mixing method with the grout. The density of cellular grout varies between 500 to 2000 kg/m<sup>3</sup> and its strength varies between 0.5 and 90 MPa.

Kearsley and Wainwright (2002) investigated the relationship between the cellular grout porosity (defined as percentage of voids volume per total volume) and its compressive strength, considering porosity range from 31.7 to 62.6% voids. They reported that the compressive strength is a function of the grout porosity and maturity time, i.e.:

$$f_c = 39.6(\ln(t))^{1.174}(1 - p)^{3.6} \quad [2.9]$$

Where:  $f_c$  = compressive strength of cellular grout (MPa);  $t$  = maturity time (days);  $p$  = porosity at 1 year.

Ramamurthy et al. (2009) reviewed the published research on cellular grout covering a range of its properties including: drying shrinkage, density, compressive and tensile strengths, modulus of elasticity, sulphate resistance, thermal insulation, acoustical properties, and fire resistance. Of particular interest is the finding that for low density foam the volume controls the strength more than the cement and/or filler properties. Ameer et al. (2015) explored the effect of void shape and void size on the cellular grout mechanical properties. Their findings indicate that reducing void size and limiting void interconnectedness result in higher strength at the desired air content.

Tiwari et al. (2017) evaluated the cellular grout properties to examine its suitability for use as backfill in mechanically stabilised walls. They measured the compressive strength, elastic modulus, coefficient of lateral pressure at rest, and settlement characteristics for grout samples with density ranging from 300 to 750 kg/m<sup>3</sup>. The grout effective strength parameters obtained

from the direct shear tests were friction angle of  $35^\circ$  and cohesion of 36 kPa. Meanwhile, their consolidated drained and undrained triaxial tests yielded effective strength parameters of friction angle of  $34^\circ$  and cohesion of 78 kPa. Nehdi et al. (2002) conducted a series of triaxial tests on cellular grout with density ranging from 710 and  $1560 \text{ kg/m}^3$ . Based on the obtained results, they evaluated the plastic behaviour of the cellular grout under a range of confining pressure. They reported post-peak behaviour in terms of decrease in cohesion and not friction angle.

Swelling behaviour is typically monotonic, with very low strain rates. Behaviour under such conditions of either EPS or light weight cellular grout has not been investigated. Typical light-weight cellular grouts have a density of 750 to  $2000 \text{ kg/m}^3$ . For swelling mitigation, the use of cellular grout with a density of  $500 \text{ kg/m}^3$  or less is proposed. Little is known about the behaviour of such a material.

## 2.7 Figures

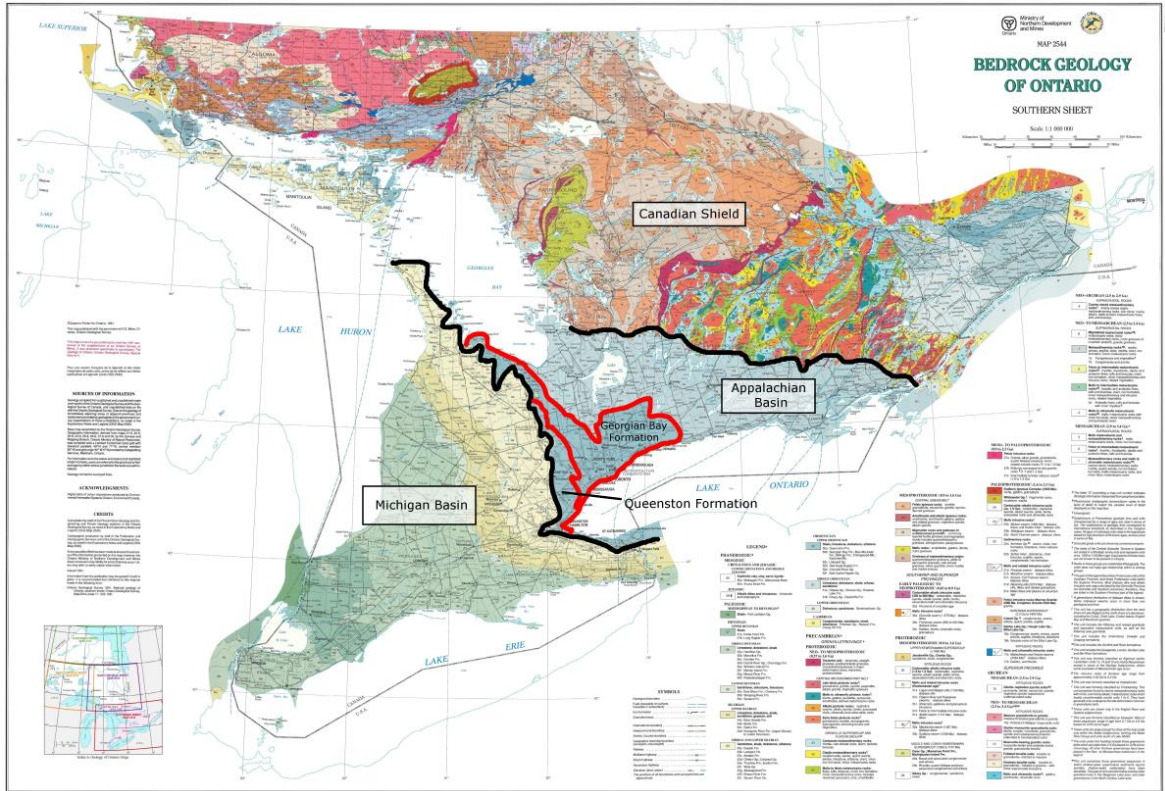


Figure 2.1. Queenston and Georgian Bay Formations, modified from Armstrong and Carter 2006.

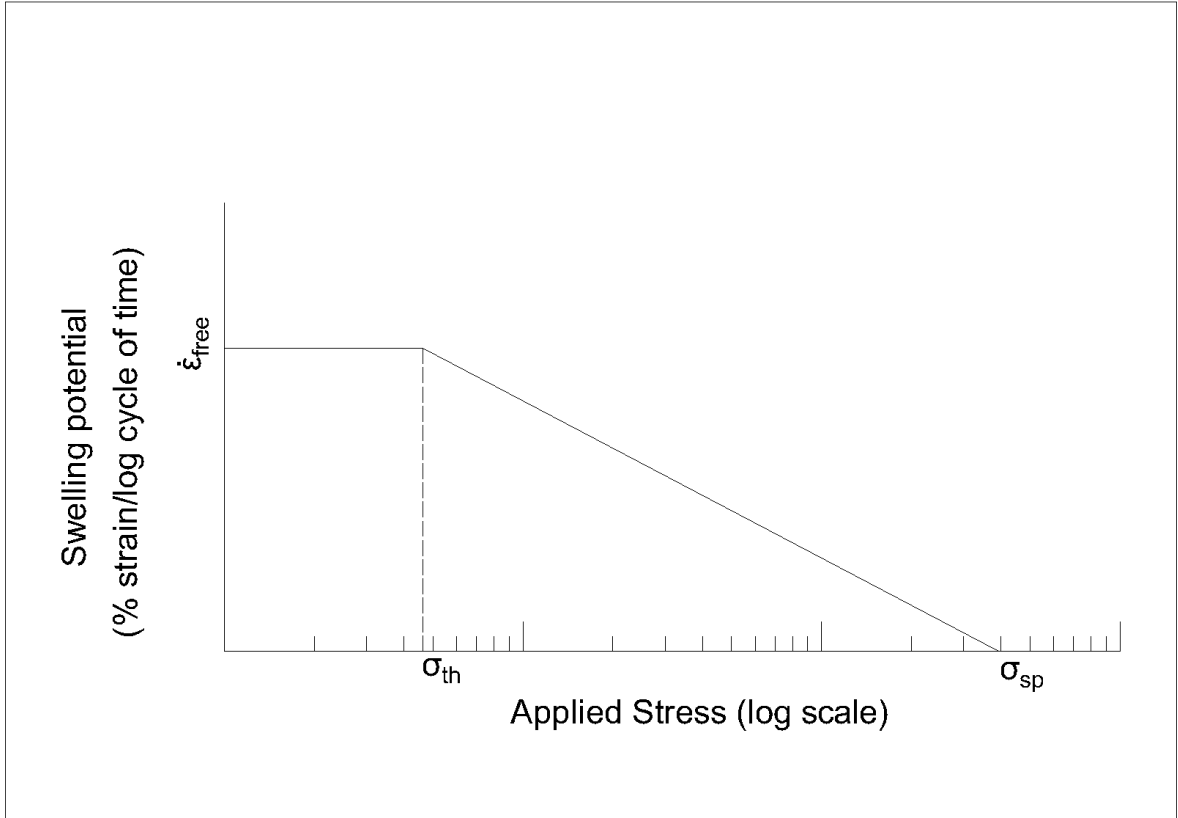


Figure 2.2. Stress – swell potential relationship from Lo and Hefny 1996.



Figure 2.3. Example of a FST sample with measurement points.

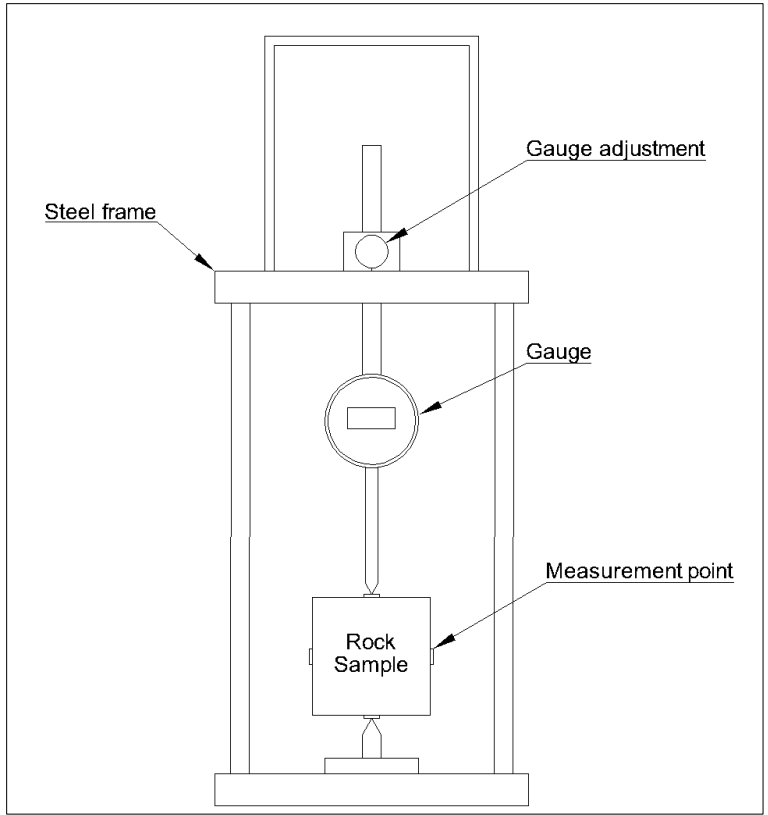


Figure 2.4. Schematic of a free swell test deformation gauge.

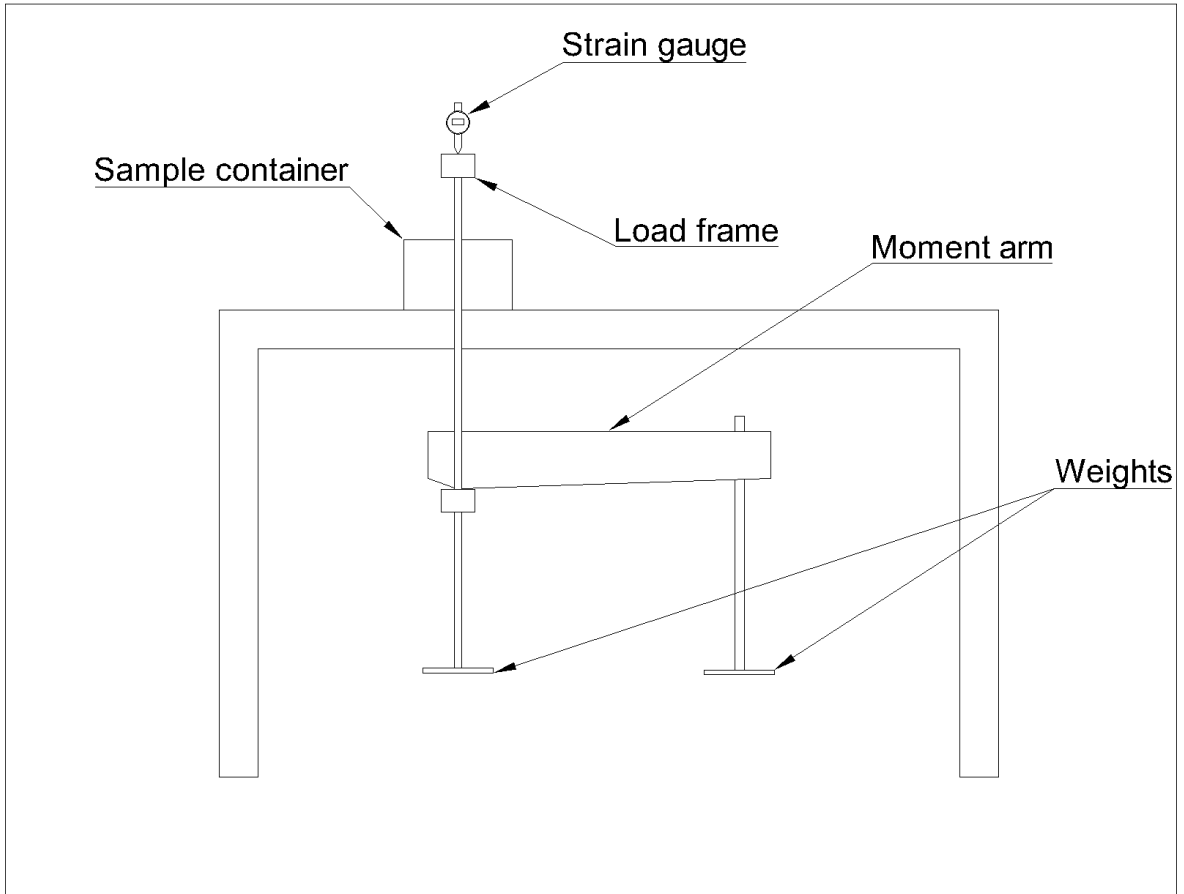


Figure 2.5. Schematic of a semi-confined swell test.



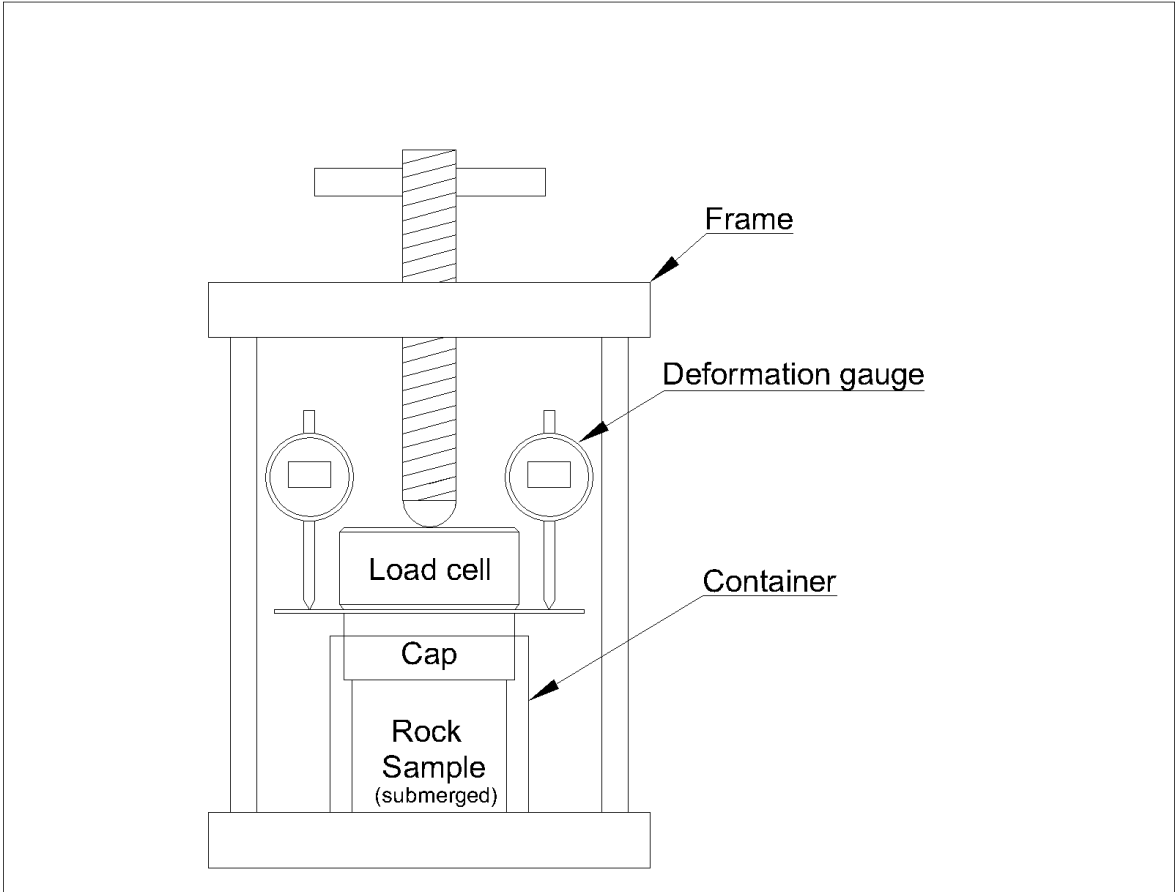


Figure 2.6. Schematic of a null swell test.

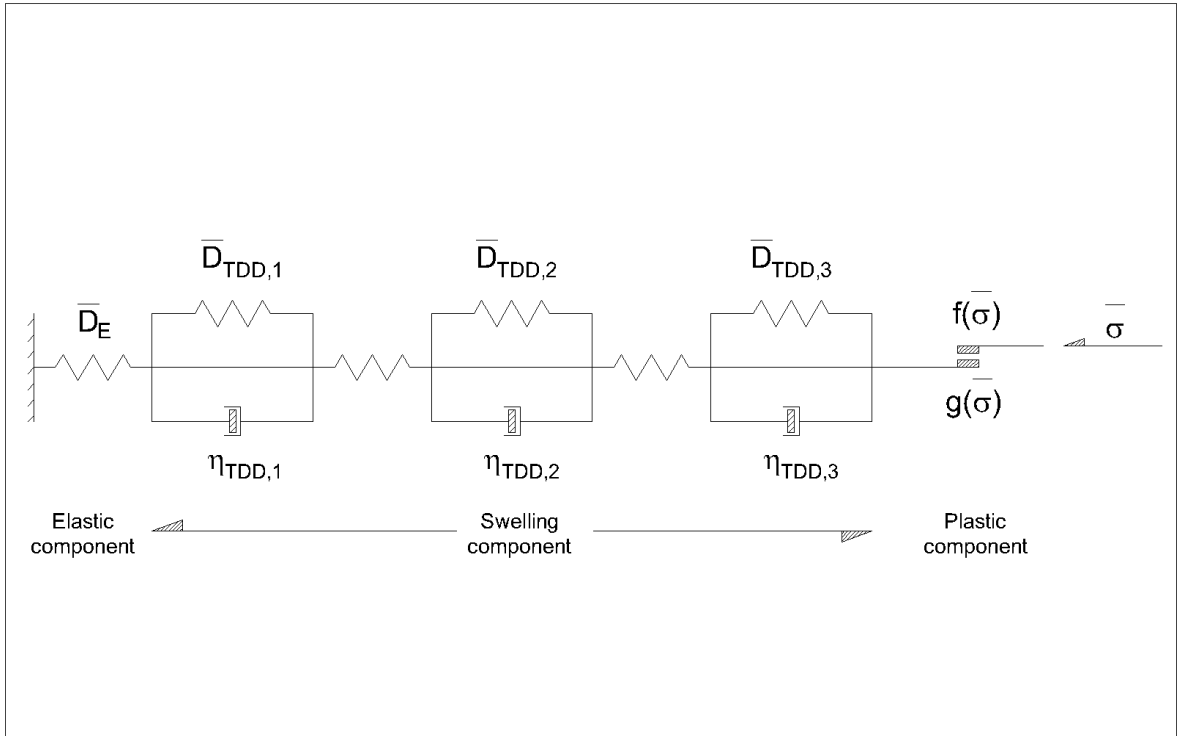


Figure 2.7. Swelling model using 3 Kelvin units as per Kramer and Moore 2004.

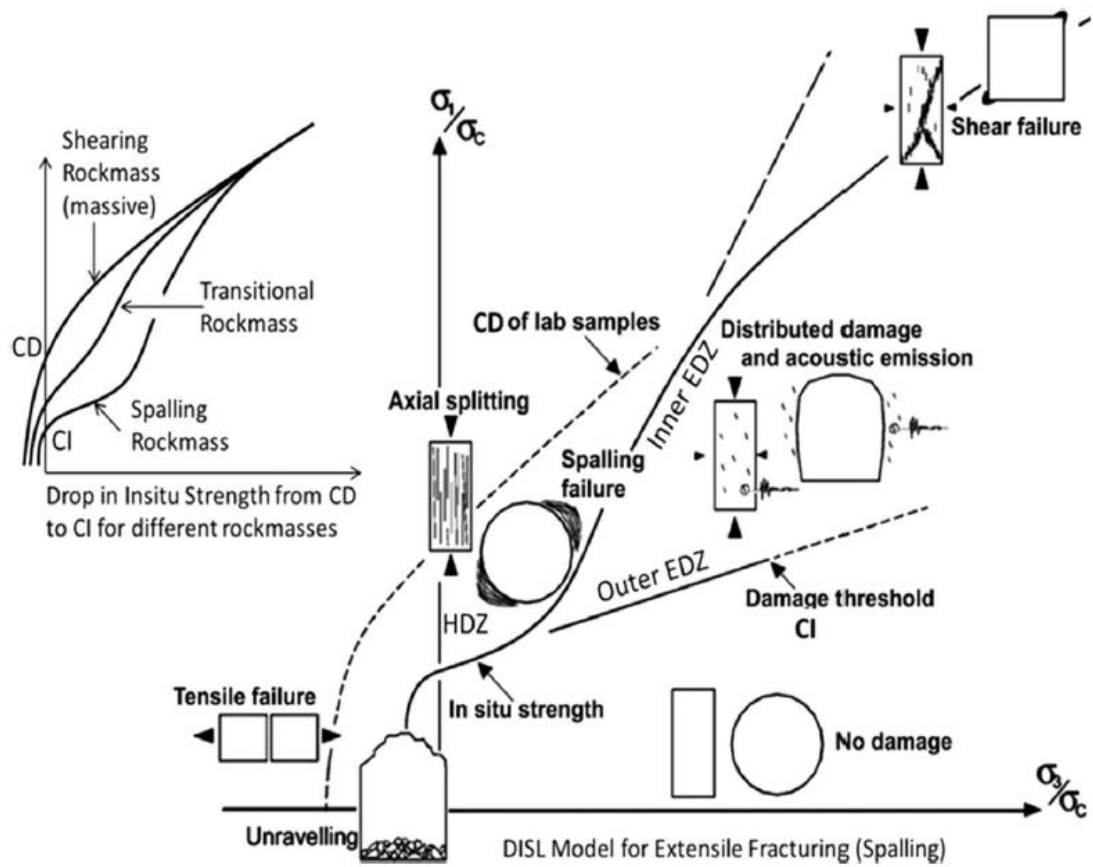


Figure 2.8. Rock mass strength envelope in 2D principal stress space showing Excavation Damage Zone theory (Perras et al. 2015).

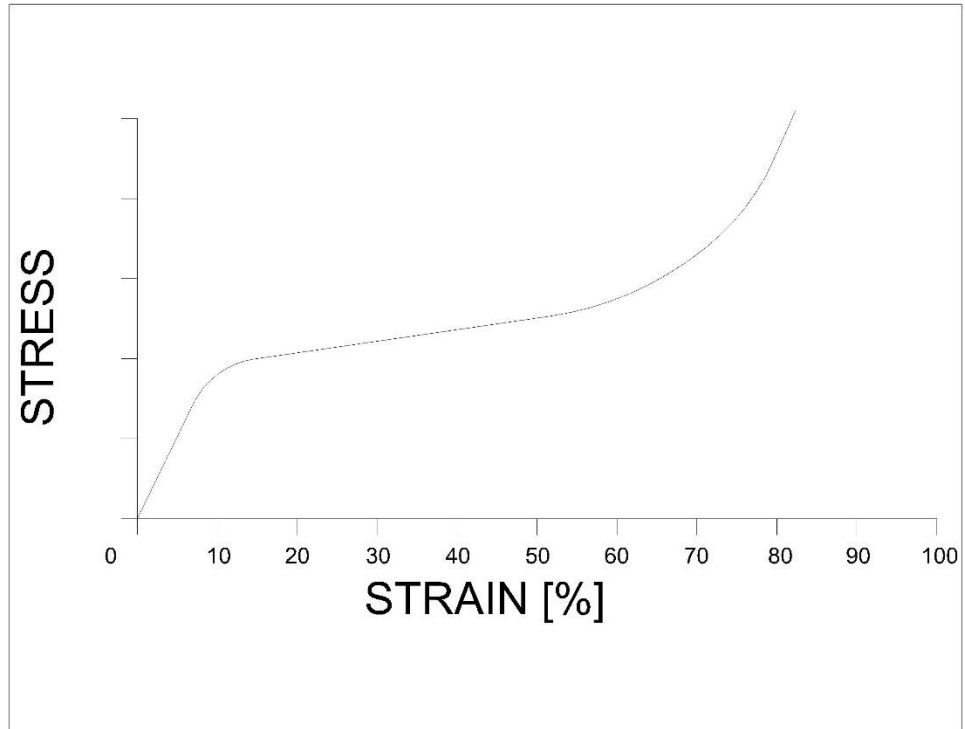


Figure 2.9. Typical EPS geofoam uniaxial compression results.

## Chapter 3

### 3 Development of a constitutive model for time-dependent deformation of shaly rock in southern Ontario

#### 3.1 Introduction

Time-dependent deformation of shale rocks in southern Ontario is a well-known phenomenon. Evidence of structures experiencing the detrimental effects has been discussed as early as Lee and Lo's (1976) analysis of the rock deformations and shaft deformations at the Niagara Falls power plant wheel pit, where the movement had been occurring for over 50 years. More recently, Carvalho (2015) discussed the significant damage experienced by a pre-cast sewer pipe, where the pipe was placed in a trench cut out of swelling rock. A cast-in-place concrete saddle allowed for direct connection between the swelling rock and the spring line of the pipe and lead to shear failure.

Lo and Yuen (1981) provided a closed-form solution for circular excavations in swelling rock. Inputs are derived from free swell and semi-confined swell tests as described in Lo et al. (1978). Their solution considered initial stress in the rock formation, the rock/structure interface, and the time-dependent behaviour of the rock and lining as well as the time lapst between excavation and lining installation. The solution provided the stresses and strains in both the rock surrounding the excavation and within the structure. Results from the studying the solution indicated that the critical stresses within the structure are tensilte stresses located at the tunnel springline, which matches observed damage in tunnels. In practice, the Lo and Yuen solution provides conservative results, although the approach has been used successfully for many tunnels for a long time.

Current design practices are to provide 90 to 100 days between excavation and construction of the final structure. Providing a waiting period allows for the early part of swelling behaviour to occur without transferring strains to the structure. Past approximately 100 days, the swelling strains are modest and could be absorbed by most structures. When construction schedules prevent or prohibit a waiting period, a crushable/compressible material may be placed between

the rock and the structure. Lo et al. (1987) provided a case study using both spray-in-place and preformed polyurethane foam to protect the tunnel and shaft structures.

## 3.2 Constitutive model for swelling rock

This section discusses the constitutive relationships governing the swelling behaviour observed in southern Ontario shales. The swelling behaviour in this model is controlled by time step and confining stress. A brief overview of the implementation of the model in finite element software PLAXIS is provided. Finally, the step-by-step numerical process is explained.

### 3.2.1 Constitutive swelling relationships

The swelling potential of rock is stress dependent and anisotropic. This is because the volume increase over time is controlled by diffusion and osmosis, resulting in swelling magnitudes being time-dependent and non-linear. Hefny et al. (1996) provided a rock behavioural model encompassing the effects of time and stress on the deformation of a rock mass undergoing swelling. This section describes the relationships between swelling potential, representing the amount of strain over a log-cycle of time, to the confining stress in a single direction.

Considering the swelling behaviour in a single direction, the relationship between the swelling potential and confining stress can be represented by a straight line between a point provided by the free swell potential and the threshold stress and a point provided by zero swelling potential and the suppression stress in semi-log space. This means that as the confining stress acting along a single direction increases from the threshold stress to the suppression stress, the swelling potential decreases from the theoretical maximum (Free Swell conditions) to zero (no swelling).

Swelling potential is then described in three different conditions: applied stress is less than the threshold stress; applied stress is between the threshold stress and suppression stress; and applied stress is greater than the suppression stress. The swelling potential to be used at any given stress condition can be described as follows (Lo and Hefny 1996, Carvahlo 2015):

$$\dot{\epsilon} = \begin{cases} \epsilon'_{free} & \text{for } \sigma_i \leq \sigma_t \\ \epsilon'_{free} \times \frac{\log(\sigma_i/\sigma_c)}{\log(\sigma_t/\sigma_c)} & \text{for } \sigma_t < \sigma_i < \sigma_c \\ 0 & \text{for } \sigma_i \geq \sigma_c \end{cases} \quad [3.1]$$

Where:  $\epsilon$  is the swelling potential,

$\epsilon_{\text{free}}$  is the free swell potential,

$\sigma_i$  is the applied stress,

$\sigma_t$  is the threshold stress, and

$\sigma_c$  is the suppression stress.

Since the swelling behaviour is anisotropic, the input parameters ( $\epsilon_{\text{free}}$ ,  $\sigma_t$ , and  $\sigma_s$ ) will differ for the horizontal and vertical directions. Lo et al. (1978) and Lo and Lee (1990) indicated that the horizontal free swell potentials, measured in two orthogonal directions in the Free Swell Test, do not show significant differences in magnitudes. Since the horizontal swelling potentials are oriented parallel to the bedding plane and orthogonal to the minor in-situ principal stress (vertical stress), an acceptable assumption is that the swelling behaviour is isotropic in the horizontal plane. This important assumption allows for the reduction of input parameters from three orientations to two – the vertical and horizontal directions. This greatly simplifies the problem for implementation in a 2D finite element solution, which renders the constitutive model to be efficient, and easy to use in engineering applications. However, it does not reduce the applicability of the model to address three-dimensional problems.

The “pseudo-Poisson’s ratio” effect has been addressed in several different ways by researchers. Hawlader et al. (2005) considered the effects of PPR as an applied stress from the orthogonal directions acting to reduce the swelling potential in the desired orientation while Carvahlo (2015) utilized the PPR as a reduction in the free swell potential based on stress ratios further reduced by the PPR effect. Both models considered the reduction in swell potential as a function of all three confining stresses. Consequently, the swelling potential can be drastically reduced by the PPR effect. This effect can lead to non-conservative designs, as a greatly reduced swelling potential will result in smaller strains and stresses, especially when complex three-dimensional stress regimes are considered.

The methodology created for this study simplifies the calculations for the PPR effect. In this approach, the PPR effect is accounted for through a reduction of the swelling potentials in the

orthogonal directions of the maximum reduction experienced. For example, if the maximum reduction in free swell potential is in the vertical direction, then the PPR effect would reduce the swelling potentials in the horizontal directions. The PPR effect methodology is described below.

For each principal direction, the percentage reduction in free swell potential is calculated. Considering Equation 3.1, depending on the value of the applied stress relative to the threshold stress and suppression stress, the reduction in free swell potential is given by:

$$r_m = \frac{\log(\sigma_m/\sigma_s)}{\log(\sigma_t/\sigma_s)} \quad \text{for } \sigma_t < \sigma_i < \sigma_c$$

$$r_m = 1 \quad \text{for } \sigma_i < \sigma_t \quad [3.2]$$

$$r_m = 0 \quad \text{for } \sigma_i \geq \sigma_c$$

The maximum reduction amongst each of the three principal directions is  $r_{max}$ . In the orthogonal directions to  $r_{max}$ , the reduction from free swell potential is then calculated with the following equation:

$$r_{app} = r_m - PPR \times (r_m - r_{max}) \quad [3.3]$$

Where:  $r_{app}$  is the applied reduction to the free swell potential, and  $r_m$  is the reduction based on the stress acting in the  $m^{\text{th}}$  principal direction.

Thus, the reduction in any principal direction is limited to the maximum reduction experienced amongst the three directions, which eliminates the possibility for unsafe reductions in swelling potential based on orthogonal stress conditions. Lo and Lee (1990) found that a typical PPR value is 0.3. In this methodology, the reduction in swelling due to a PPR of 0.3 would result in a further reduction of 30% of the difference between the maximum swelling reduction and the direction of interest.

Al-Maamori et al. (2018) observed a significant reduction in rock strength and stiffness after soaking. A base assumption for swelling is contact with fresh water at all locations where swelling occurs. This implies that soaking leads to reduction in both elastic modulus and



compressive strength due to the swelling behaviour. This reduction of strength and stiffness with time is not considered in the constitutive model. Rather, the proposed constitutive model assumes the rock behaves as an elasto-plastic material following the Mohr-Coulomb yield criteria based on its intact stiffness and strength parameters.

### 3.2.2 Numerical procedure

The step-by-step procedure and relevant equations will be described in this section. The procedure includes aspects of the host program (PLAXIS). Detailed descriptions of the swelling portion of the constitutive model and how it fits into the host program's numerical procedure are provided.

#### 3.2.2.1 Host program general procedure

Plaxis program is widely used in the design of geotechnical problems. It has a user-friendly interface and allows user defined soil models, and other customization is supported by the developer. In order to facilitate employing the proposed swelling constitutive model in practise, a succinct description of the host program procedure is provided herein and further details are given in Brinkgreve et al. (2016).

PLAXIS v2016 used in the current analysis is a two-dimensional, finite element program. It can solve geotechnical problems related to stresses and strains in soil and rock bodies, the interaction between structures constructed in or on the soil and rock, and the effects of ground water. The program uses finite element approximation of soil/rock domain to solve a series of governing equations written at discrete points within a specified grid. An analysis is conducted in stages representative of the sequenced, progressive stages of an engineering project. For each phase in the construction process, calculations are performed to provide an equilibrium condition from which modeled soil, rock, ground water, and structure behaviours are analyzed. The results from each phase form the initial conditions for the following phase.

The analysis for each phase is performed in a series of steps until global convergence is reached. A brief summary of the steps based on the elastic stiffness matrix is provided in Table 3.1, as described in Brinkgreve et al. (2016).

Of particular importance for this discussion are steps *8e*, *8f*, and *8g*. These three steps represent the incremental stress and strain changes and the plasticity check at each point in the continuum for each iteration. They are the only three aspects that a user defined soil model may interact with when developing constitutive models for Plaxis.

Prescribed inputs and outputs are required for the developed constitutive model to run in the Plaxis environment. Table 3.2 provides the inputs and outputs used in the swelling constitutive model.

### 3.2.2.2 Numerical procedure of the swelling constitutive model

This section provides the procedure for the calculation of swelling stresses and strains. The calculations are conducted in the Cartesian (x,y, and z) space. The stresses and strains are calculated at each node, and a yield function check is then performed (steps *8e*, *8f*, and *8g* in Table 3.1). Table 3.3 provides the inputs required by the model user to conduct the analysis.

Calculations begin in Cartesian (x,y, and z) space in the host program. The process is described in Figure 3.1, with details provided below.

First, the material stiffness matrix,  $\bar{D}^e$ , is established using the provided elastic properties of rock, i.e.:

$$\bar{D}^e = \begin{bmatrix} \frac{2G(1-\nu)}{(1-2\nu)} & \frac{2G\nu}{(1-2\nu)} & \frac{2G\nu}{(1-2\nu)} & 0 & 0 & 0 \\ \frac{2G\nu}{(1-2\nu)} & \frac{2G(1-\nu)}{(1-2\nu)} & \frac{2G\nu}{(1-2\nu)} & 0 & 0 & 0 \\ \frac{2G\nu}{(1-2\nu)} & \frac{2G\nu}{(1-2\nu)} & \frac{2G(1-\nu)}{(1-2\nu)} & 0 & 0 & 0 \\ 0 & 0 & 0 & G & 0 & 0 \\ 0 & 0 & 0 & 0 & G & 0 \\ 0 & 0 & 0 & 0 & 0 & G \end{bmatrix} \quad [3.4]$$

Table 3.1. Finite element calculation process in host program.

Step	Action	Description
1		Read input data
2	$\bar{K} = \int \bar{B}^T \bar{\sigma}_c^{i-1} dV$	Form stiffness matrix
3	$i = i + 1$	New step
4	$\bar{f}_{ex}^i = \bar{f}_{ex}^{i-1} + \Delta \bar{f}_{ex}$	Form new load vector
5	$\bar{f}_{in} = \int \bar{B}^T \bar{\sigma}_c^{i-1} dV$	Form reaction vector
6	$\Delta \bar{f} = \bar{f}_{ex}^i - \bar{f}_{in}$	Calculate unbalance
7	$\Delta \bar{v} = 0$	Reset displacement increment
8a	$j = j + 1$	New iteration
8b	$\delta \bar{v} = \bar{K}^{-1} \Delta \bar{f}$	Solve displacements
8c	$\Delta \bar{v}^j = \Delta \bar{v}^{j-1} + \delta \bar{v}$	Update displacement increments
8d	$\Delta \bar{\epsilon} = \bar{B} \Delta \bar{v}; \delta \bar{\epsilon} = \bar{B} \delta \bar{v}$	Calculate strain increments
8e	$\bar{\sigma}^{tr} = \bar{\sigma}_c^{i-1} + \bar{D}^e \Delta \bar{\epsilon}$	Calculate stresses: Elastic
8f	$\bar{\sigma}^{eq} = \bar{\sigma}_c^{i,j-1} + \bar{D}^e \delta \bar{\epsilon}$	Equilibrium
8g	$\bar{\sigma}_c^{i,j} = \bar{\sigma}^{tr} - \frac{\langle f(\bar{\sigma}^{tr}) \rangle}{d} \bar{D}^e \frac{\delta g}{\delta \bar{\sigma}}$	Constitutive
8h	$\bar{f}_{in} = \int \bar{B}^T \bar{\sigma}_c^{i,j} dV$	Form reaction vector
8i	$\Delta \bar{f} = \bar{f}_{ex}^i - \bar{f}_{in}$	Calculate unbalance
8j	$e = \frac{ \Delta \bar{f} }{ \bar{f}_{ex}^i }$	Calculate error
8k	If $e > e_{tolerated}$ – new iteration (step 8a)	Accuracy check
9	$\bar{v}^i = \bar{v}^{i-1} + \Delta \bar{v}$	Update displacements
10		Write output data
11		If not finished, new step

Table 3.2. List of input and output variables provided by the host program.

Variable	Input/output	Description
$T_0$	Input	Time at start of step
$\Delta t$	Input	Time increment
Props	Input	List with model parameters
$\bar{\sigma}_c^{i,j-1}$	Input	Stresses at start of step
$\delta \bar{\epsilon}$	Input	Strain increment
$\bar{\sigma}_c^{i,j}$	Output	Resulting stresses

Table 3.3. Swelling constitutive model input parameters.

Input variable	Description
$G$	Shear modulus [kPa]
$\nu$	Poisson's ratio
$C$	Cohesion [kPa]
$\phi$	Friction angle [degrees]
$\psi$	Dilation angle [degrees]
$\sigma_{tension}$	Tensile strength [kPa]
$\dot{\epsilon}_{fh}$	Horizontal free swell potential [strain/log cycle of time]
$\sigma_{th}$	Horizontal threshold stress [kPa]
$\sigma_{sh}$	Horizontal suppression stress [kPa]
$\dot{\epsilon}_{fv}$	Vertical free swell potential [strain/log cycle of time]
$\sigma_{tv}$	Vertical threshold stress [kPa]
$\sigma_{sv}$	Vertical suppression stress [kPa]
PPR	Pseudo-Poisson's ratio

The stresses at the beginning of the step are then calculated as per step  $\delta e$ , i.e.

$$\Delta \bar{\sigma}^{i,j} = \bar{D}^e \delta \bar{\epsilon} \quad [3.5]$$

The consideration of the time dependant swelling behaviour is initiated through the constitutive model calculations. This is accomplished by evaluating the stresses due to swelling,  $\bar{\sigma}_{swell}$ , for the equilibrium step ( $\delta f$ ). The stresses at the beginning of the phase ( $\bar{\sigma}_c^{i,j-1}$ ) are converted from Cartesian co-ordinates to principal stress coordinates ( $\bar{\sigma}_p^{i,j-1}$ ) and the orientations of the three principal stresses ( $\bar{\mu}_1$ ,  $\bar{\mu}_2$ , and  $\bar{\mu}_3$ ) are established.

The 3x3 swelling property matrices are generated using the material parameters , i.e.,

$$\dot{\bar{\epsilon}}_{fc} = \begin{bmatrix} \dot{\epsilon}_{fh} & & \\ & \dot{\epsilon}_{fv} & \\ & & \dot{\epsilon}_{fh} \end{bmatrix} \quad \bar{\sigma}_{tc} = \begin{bmatrix} \sigma_{th} & & \\ & \sigma_{tv} & \\ & & \sigma_{th} \end{bmatrix} \quad \bar{\sigma}_{sc} = \begin{bmatrix} \sigma_{sh} & & \\ & \sigma_{sv} & \\ & & \sigma_{sh} \end{bmatrix} \quad [3.6]$$

The swelling property matrices are then transformed into the principal stress space via:

$$\bar{x}_p = \bar{R}^T \times \bar{x}_c \times \bar{R} \quad [3.7]$$

Where  $\bar{x}_p$  and  $\bar{x}_c$  are the free swell, threshold stress, and suppression stress matrices in the principal and Cartesian coordinate systems, respectively, and  $\bar{R}$  is the transformation matrix given by:

$$\bar{R} = \begin{bmatrix} \bar{\mu}_1(1) & \bar{\mu}_2(1) & \bar{\mu}_3(1) \\ \bar{\mu}_1(2) & \bar{\mu}_2(2) & \bar{\mu}_3(2) \\ \bar{\mu}_1(3) & \bar{\mu}_2(3) & \bar{\mu}_3(3) \end{bmatrix} \quad [3.8]$$

For each principal stress, the swelling potential is calculated using the relationships provided in Equation 3.1, where the applied stress values,  $\sigma_m$ , are the principal stresses  $\bar{\sigma}_p^{i,j-1}$ . The free swell potential, threshold stress, and suppression stress are provided by  $\bar{e}_{fp}(m,m)$ ,  $\bar{\sigma}_{hp}(m,m)$ , and  $\bar{\sigma}_{np}(m,m)$ , respectively, where  $m = 1, 2, \text{ or } 3$ .

The effects of PPR are then accounted for as per Equation 3.3, and the swell potential matrix is populated by:

$$\dot{\bar{\epsilon}}_{pot} = r_{max} \times \dot{\bar{\epsilon}}_p \quad [3.9]$$

The swelling strains in the principal stress directions are then calculated via:

$$\bar{\bar{\epsilon}}_{p,tdd} = \log\left(\frac{t_0 + \Delta t}{\Delta t}\right) \times \dot{\bar{\epsilon}}_{pot} \quad [3.10]$$

These strains are then rotated back to Cartesian space with the inverse of rotation calculation provided in Equation 3.9, and  $\bar{\bar{\epsilon}}_{c,tdd}$  is derived.

The stresses are calculated in the Cartesian space using the material stiffness matrix, i.e.:

$$\bar{\bar{\sigma}}_{c,tdd} = \bar{\bar{\epsilon}}_{p,tdd} \times \bar{\bar{D}}^e \quad [3.11]$$

The stresses due to swelling are listed in vector form,  $\bar{\bar{\sigma}}_{c,tdd}$ . This value is then added to the initial stress and the Step incremental stress so that Step  $\delta f$  becomes:

$$\bar{\sigma}^{eq} = \bar{\sigma}_c^{i,j-1} + \bar{\bar{D}}^e \delta \bar{\epsilon} + \bar{\bar{\sigma}}_{c,tdd} \quad [3.12]$$

The calculated stresses are then examined against the yield criteria (Step  $\delta g$ ), considering the Mohr-Coulomb yield function. If the yield criteria is reached, the stresses are then limited and associated flow strains are calculated.

Finally, if the resulting stresses are within acceptable tolerance as described in Equation 3.13, the Phase ends and the next Phase time step begins. If the stresses do not result in acceptable tolerance, then another Step is run.

$$e = \frac{|\Delta \bar{f}|}{|\bar{f}_{ex}^i|} \quad [3.13]$$

It should be noted that even though the constitutive is incorporated into Plaxis 2D version, it has been developed assuming a fully three-dimensional problem. As such, the constitutive model could be easily incorporated into a three-dimensional host program.

One of the important input parameters to the analysis is the size of time step,  $\Delta t$ . A sensitivity study described later in this Chapter demonstrates that the size of time step controls the

magnitude of calculated swelling. If the selected time step is too large, the stress conditions may not be accurate and the magnitude of swelling will be incorrectly assessed, whereas the time and cost for the computational effort increase substantially if the selected time step is too small.

In PLAXIS, the size of time step is calculated as a function of element size, coefficient of permeability, and elastic modulus. In practical analysis cases,  $\Delta t$  could be considered small enough as long as the initial time step is properly chosen. The value of the initial time step is selected as part of the ‘Numerical control parameters’ in Plaxis, as shown in Figure 3.2, labeled First Time Step. The First Time Step value must be chosen carefully. Very small values (automatic value is  $1 \times 10^{-9}$  days) may result in model instability and large values do not properly capture the swelling behaviour. Various analyses conducted for modeling swell test samples and case studies indicate that acceptable range of First Time Step is between 0.05 and 1.0 days. It is suggested to conduct a limited sensitivity analysis to establish the size of first time step when comparing the model results to test or monitoring results.

All subroutines written by the author have been included in Appendix 1.

### 3.3 Model verification

This section presents verification tests that are conducted to ensure that the constitutive model can accurately predict the swelling behaviour. In each case, an axisymmetric model with dimensions of 50 mm high and 25 mm in radius is considered. The model considers the line of symmetry at the left side boundary. The bottom boundary is fixed vertically but free horizontally, and the top and right boundaries are free in all directions. Figure 3.3 displays the mesh and boundary conditions. The sensitivity analysis considered the following parameters:

1. Mesh density,
2. First Time Step,
3. Ratio of vertical to horizontal free swell potentials,
4. Horizontal and vertical applied stress, and
5. PPR.

Table 3.4 presents the base line parameters used in the sensitivity analysis. These base line values are then varied depending on the examined parameter or ratio of parameters.

Table 3.4. Baseline parameters for verification testing.

Parameter	Value
Unit weight [kN/m <sup>3</sup> ]	26.0
Elastic modulus [kPa]	14000
Poisson's ratio	0.20
Cohesion [kPa]	1000
Friction angle [°]	35
Horizontal and vertical free swell potential [strain/log cycle of time]	$3.0 \times 10^{-3}$
Horizontal and vertical threshold stress [kPa]	10
Horizontal and vertical suppression stress [kPa]	1000
PPR	0.0
Number of elements in mesh	196
First Time Step [days]	0.8

Mesh density is known to impact numerical modeling results. In order to investigate the impact of both mesh density and area ratio (ratio between the area of the largest mesh to the area of the smallest mesh) on the constitutive model behaviour, a series of analyses is conducted with the following conditions: 2 elements, 196 elements, 1802 elements, and one analysis with an aspect ratio of approximately 4000. Results are provided in Figure 3.4. The vertical swelling strain is plotted on the log time scale, with the theoretical ideal swelling shown as dashed line and the results obtained from analyses are represented by symbols. The results shown in Figure 3.4 indicate that the performance of the constitutive model is independent of mesh size or area ratio. Given the importance of meshing in general numerical method practice, careful consideration should still be applied when generating the mesh.

The First Time Step is an input required by PLAXIS, but impacts the predictions of the constitutive model. Three analyses are performed considering the first time step to be 0.05, 0.8, or 1.0 and the obtained results are shown in Figure 3.5. Initial values were chosen between 0.1 and 1.0 due to the logarithmic calculations. Values less than 0.1 were considered but found



to increase the calculation time without providing additional accuracy. Values over 1.0 were considered, with results discussed below. The vertical swelling strain is presented over log time. The results indicate that the First Time Step is a critical input; it affects the magnitude of swelling strain but the swelling potentials remain unaffected. Thus, a change in First Time Step can result in a noticeable change in swelling strains calculated by the model. In this particular case, decreasing the First Time Step causes an increase in the calculated swelling strains. Additional analyses were conducted considering first time step of at 0.0001 days and 10 days. The lower value resulted in non-convergence of the model, and the large value resulted in unrealistic swelling. The results using a First Time Step of 10 days are shown in Figure 3.6. The Figure is displayed in linear time with results providing a linear increase in strain rather than logarithmic. The total magnitude is lower than the theoretical ideal. Of note, there were only three steps calculated between 10 days and 100 days, a strong indication of the choice in First Time Step resulting in undesirable and unrealistic conditions.

The effect of free swell potential parameter on the swelling behaviour is examined by varying the ratio between the swell potential in the horizontal and vertical directions. The ratios considered are 1, 3, 5, and 10. Figure 3.7 shows the results for five tests where the horizontal potential is kept at  $1.0 \times 10^{-3}$  strain/log cycle of time and the vertical potential is increased by a factor of 1, 3, 5, and 10. The figure shows the vertical and horizontal strains over 100 days in log time. The lines represent the perfect theoretical strains and the model predictions are represented by the symbols. A similar analysis was conducted by keeping the vertical swelling potential constant and increasing the horizontal free swell potential by the same ratios. The results were identical.

To examine the effect of applied stress on swelling strains, three analyses are analyzed with the following horizontal and vertical stresses: Test 1 – 100 kPa and 500 kPa; Test 2 – 700 kPa and 0 kPa; Test 3 – 1000 kPa and 10 kPa. Figure 3.8 presents the results obtained from the analysis along with the Hefny et al. confining stress-swell potential relationship, which is used in this analysis. Since the inputs are isotropic, this relationship is valid for both directions. For each test and in both horizontal and vertical directions, the swelling potential calculated from the model is plotted against the theoretical swelling potential. The figure shows that the model predictions agree well with the idealized values.

To analyze the effects of PPR on the model behaviour, a confining stress of 700 kPa was applied in the vertical direction. The PPR value was selected as 0.0, 0.5, or 1.0, and the corresponding strain in the horizontal direction is recorded. Figure 3.9 compares the horizontal strain in log time obtained from the analyses (symbols) and the theoretical strains (lines). As can be noted from Figure 3.9, there is an excellent agreement between the two sets.

The results obtained from the verification analyses demonstrate that the constitutive model can closely predict the swelling behaviour. Minor differences are observed between idealized and analyzed results are shown for the lower applied stress condition. However, the differences between modeled and idealized results are less than 5%, indicating acceptable performance.

### 3.4 Case study – Heart Lake Road

The tunnel at Heart Lake Road is a well-documented case study. Lo et al. (1978) provided a detailed description of the construction, field testing, and over twenty seven years of inspections. The tunnel was first inspected approximately 2 years after the TBM section was constructed, whereupon sever cracking was observed in the drill and blast section of the tunnel. A robust field and laboratory investigation was conducted to identify the cause of the cracking, while field observations continued. Field investigation included borehole logging, sample retrieval, in-situ horizontal stress measurements, and concrete coring. Laboratory testing include stress-strain uniaxial unconfined compression tests, free swell tests and semi-confined swell testing. The results of the field and laboratory testing are provided in Lo et al. (1979) and Yuen (1979). A summary of the observed cracking and tunnel performance over 27 years is provided in Table 2 in Lo and Micic (2010) and is shown below for reference. Continuing deterioration of the drill and blast and cut and cover (C&C in the table) section was observed with spring line cracking progressively extending into the TBM tunnel section

The tunnel was constructed in three sections: a 1500 m long Tunnel Boring Machined (TBM) section, a 183 m long drill and blast section, and a 232 m long cut and cover section. The TBM and cut and cover sections were constructed as planned without difficulties. The section constructed employing drill and blast technique experienced overbreak and stability issues. As reported in Lo et al. (1978), significant cracking and deterioration of the tunnel structure, especially at the spring line, began in the drill and blast section. The TBM section experienced

cracking 2.5 years after the lining was installed. After significant cracking along the tunnel spring line was observed, an investigation program was initiated. As part of this investigation, the in-situ stresses were measured, and the horizontal stress was found to be up to 5 MPa.

*Table 2. Summary of post construction performance (as observed by the first author)*

Date of Inspection	Time Elapsed After Completion of Permanent Lining		Chaining Inspected	Principal Observations
	D&B Section (Comp. July 1974)	TBM Section (Comp. April 1975)		
April, 1977	2 years, 9 months	2 years	136+50 (outfall) to 152+61	Cracking at springline for entire D&B section. No crack in TBM section
Sep., 1977	3 years, 2 months	2 years, 5 months	136+50 (outfall) to 152+61	Deterioration in section under Heart Lake Road. No crack in TBM section.
Oct., 1977	3 years, 3 months	2 years, 6 months	136+25 (MH X2) to 152+61 (outfall)	Cracking in TBM section first appeared between 135+00 to 138+40.
May, 1978	3 years, 10 months	3 years, 1 months	104+55 (bulkhead) to 152+61 (outfall)	Slight deterioration under Heart Lake Road. Cracking extended slightly. Continuous cracking extended upstream to 128+25.
March, 1983		~8 years		Extended 10 m upstream.
May, 1986		~11 years		Extended to 127+77.
Nov., 1999		24 years, 7 months	Inspected section below Tomken Road (formally Heart Leak Road)	Serious deterioration between MH X1 and C&C section. Continuous crown spalling and crack widening at springline.
May, 2001		~27 years		Continuous serious deterioration in section below Tomken Road. Cracking in C&C and TBM sections (progressed to 126+00).

\*Table recreated from Lo and Micic 2010, for ease of reference

The analysis reported herein considers the TBM section. The construction sequence, rock and structural parameters, and section geometry are those reported by Lo et al. (1978), Lo and Yuen (1981), Yuen (1979), and Hawlader et al. (2005) and are summarized in Table 3.5. The test results reported by Yuen (1979) for vertical swelling have been summarized in Figure 3.10.

The excavation and construction sequence followed those described in Lo et al. (1978) and Lo and Yuen (1981). The TBM section was excavated over approximately four months, with excavation progressing upstream. Construction of the final 0.3 m thick, 35 MPa concrete liner began at the upstream end of the tunnel one week after the end of excavation and continued for approximately 140 days.

Three sections have been analyzed considering the stress and installation conditions provided in Table 3.6. Figure 3.11 presents the model mesh used for the analysis of the tunnel section. The model is 75 m deep and 200 m wide and comprises 2950 elements. The vertical boundaries

are fixed in the horizontal direction and free in the vertical direction. The lower boundary is fixed in all directions.

Table 3.5 Input parameters for the Heart Lake Road analysis.

Parameter	Units	Value
Excavated tunnel radius	[m]	1.675
Lining thickness	[m]	0.3
$f'_c$	[MPa]	35
Elastic modulus of concrete, $E_{concrete}$	[MPa]	28,000
Poisson's ratio of concrete		0.25
Time of lining installation	[days]	60-140
Elastic modulus of rock, $E_{rock}$	[MPa]	12,400
Poisson's ratio of rock, $\nu_{rock}$		0.15
Cohesion, $c$	[MPa]	2.0
Friction angle, $\phi$	[°]	39
Horizontal free swell potential, $\dot{\epsilon}_{h,free}$	[strain/log cycle of time]	$1 \times 10^{-3}$
Horizontal threshold stress, $\sigma_{h,t}$	[MPa]	$1.0 \times 10^{-3}$
Horizontal suppression stress, $\sigma_{h,s}$	[MPa]	650
Vertical free swell potential, $\dot{\epsilon}_{v,free}$	[strain/log cycle of time]	$6.1 \times 10^{-3}$
Vertical threshold stress, $\sigma_{v,t}$	[MPa]	$1.0 \times 10^{-3}$
Vertical suppression stress, $\sigma_{v,s}$	[MPa]	1.60
Initial horizontal stress	[MPa]	1.5, 3, or 4
First Time Step	[days]	0.8

Horizontal in-situ stresses are generated using the methodologies outlined in Lardner (2011). The model is first initialized via gravity loading using an upper layer of rock with a high unit weight ( $1600 \text{ kN/m}^3$  for Chainage 136+20) and Poisson's ratio of 0.49 and the main rock mass with a low unit weight ( $9 \text{ kN/m}^3$ ) and the same Poisson's ratio. Next, the soil and rock layers

for the initial conditions are activated. The result is a horizontal stress independent of vertical stress, which is desired in rock conditions. Figure 3.12 provides an example of the initial horizontal stresses, showing a near-uniform 4 MPa in the un-weathered Georgian Bay Formation at Chainage 136+20.

Once the liner is installed, the analysis is conducted for an additional 1, 2, 5, and 10 year periods. Figure 3.13 shows the horizontal deformations around the tunnel for the analysis considering an in-situ stress of 4 MPa after 10 years. The figure shows the extent of swelling rock influence, with horizontal deformations due to swelling over 2 mm extending approximately 24 m away from the tunnel.

Figure 3.14 shows the deformed tunnel shape after 10 years at Chainage 136+20. The results for the other horizontal stress conditions show similar behaviour. The deformed tunnel shape is roughly oval, with greater inward deformations at the springline. Over 10 years of swelling, the maximum tunnel convergence at the springline, which is the reduction in distance between opposite points along the tunnel circumference, is estimated to be approximately 20 mm, 16 mm, and 8 mm, for Chainages 136+20, 125+00, and 120+00 respectively.

The calculated axial and bending stresses after 10 years are presented in Figure 3.15. Axial stresses under the low horizontal stress condition (Chainage 120+00) shows only compression, while the higher stress conditions resulted in tension roughly between the tunnel shoulder (45° up from the springline) and knee (45° down from the springline). Maximum moments occur at the crown and invert and minimum at the springline. Tangential stresses at the springline over a ten year period are shown in Figure 3.16. It is noted from Figure 3.16 that Chainages 136+20 would experience tension equal to tangential stresses at approximately 2.5 years, which matches the observed cracking. At Chainage 125+00, the calculated time until tension cracks at the springline is approximately 4.5 years, rather than 3.9 years as observed. Differences between the calculated and observed behaviour could be due to initial stress conditions or swelling parameters. Similarly, swell testing was conducted for samples retrieved between Chainage 136+20 and 143+00. Thus, the parameters may change over the nearly 330 m between Chainage 136+20 and 125+00.. At Chainage 120+00, the analysis indicates that no tension cracks are expected to occur, which is consistent with the results described in Table 2 of Lo and Micic (2010), provided on Page 48.

Table 3.6. Section details.

Chainage	Time until liner installed [days]	Horizontal in-situ stress [MPa]	Time until cracking observed [years]
136+20	140	4.0	2.5
125+00	90	3.0	3.9
120+00	60	1.5	No cracking after 11 years.

Horizontal in-situ stress measurements were performed as part of the investigation at Heart Lake Tunnel, at Chainage 136+20 two years after the liner was constructed. Figure 3.17 compares the test results presented in Lo et al. (1979) with the results obtained from the numerical analysis in the current study. The abscissa is the normalized radial distance from the rock-structure interface relative to the radius (R) of the excavated tunnel. The ordinate axis shows the radial stress normalized by the in-situ horizontal stress, which was taken as 4 MPa for Chainage 136+20. Several milestone dates are shown in Figure 3.17; i) immediately after construction of the tunnel lining ( $t_0$ ); ii) 2 years after liner installation, which is when the in-situ measurements were taken; iii) 10 years after liner installation; and iv) 100 years after liner installation. Model results show acceptable agreement with the measured stresses. Results from the model show small change between the results of 2, 10, and 100 years. At the interface, the radial stress becomes less compressive as time increases.

The results discussed above demonstrate collectively that the developed constitutive model could predict the time dependent deformations of the Heart Lake Tunnel. This confirms the validity of the developed model as a design tool. In addition, it can be used for design of mitigating solutions should the the calculated response indicates unacceptable levels of deformation or stresses in the tunnel liner.

Additionally, results from the model verification (Section 3.3) show reasonable agreement with theoretical behaviour. Given the positive results, the constitutive model will be used to further investigate swelling rock behaviour for a circular tunnel in different rock formations (Zone 1

Water Main Chapter) and for rectangular shafts (Billy Bishop Pedestrian Tunnel Chapter). The constitutive model will also be used to explore the effects of swelling mitigation materials, such as low density cellular grout and extruded polystyrene foam, on the impact of swelling strains on buried structures.

### 3.5 Summary and conclusions

Time-dependent deformation of shaly rock in southern Ontario is a well-known issue. Design methods for predicting the magnitude of swelling strains and stresses began with closed-form solutions provided by Lo and Yuen (1981) and later by Hefny and Lo (1996). Although these closed form solutions provide adequate “back of the envelope” calculations, the values for swelling-induced stresses and strains are conservative. Numerical methods for estimating the swelling behaviour of rock have been developed for a variety of swelling constitutive models. Models have been developed for swelling rocks with varying complexity. Many of the models, based on international experience and on rock in southern Ontario, follow the Lo and Hefny (1996) model, which considers the confining stress-swelling potential relationship. Of these models, few currently capture the full behaviour of swelling rock in southern Ontario, including the swelling anisotropy and accounting for the “pseudo-Poisson’s ratio.”

The constitutive model described in this chapter was developed to provide a practicing engineers a way to estimate the effects of the swelling phenomena on the rock mass and buried structures. The model is based on the anisotropic, time, and stress dependent behaviour that has been researched over the last several decades (Lo et al. 1978, Lee and Lo 1993, Hefny et al. 1996) and includes the effects of the “pseudo-Poisson’s ratio.” The model uses inputs provided by a swell testing program that is considered the industry standard in southern Ontario and has been developed at the Geotechnical Research Centre at The University of Western Ontario. A conservative approach has been adopted for the implementation of the PPR. This approach allows the engineer to analyze a project’s sensitivity to the effect but preventing the model from providing overly conservative results. The model was found to be sensitive to the First Time Step, an important input parameter in the host program, but outside of the model created for this research. The impact of the First Time Step must be explored by the engineer during analysis in order for the most appropriate value to be chosen and for the engineer to comprehend the influence on results.

The model provides acceptable results when compared to swell tests, including the free swell test, semi-confined swell test and null swell test in both the vertical and horizontal directions. Swelling potentials and strains are calculated to a high degree of accuracy. The constitutive model successfully recaptured the performance of the Heart Lake Tunnel, providing acceptable results to observed behaviour such as springline cracking due to tangential stresses, and horizontal stress distribution in the rock two years after tunnel structure installation.

The model developed for this research represents an improved method for the design of excavations and structures in swelling rock. Any rock mass that experiences swelling that can be described by the stress-swell potential relationship (Lo and Hefny 1996) can be modeled with the use of this code, allowing an engineer to estimate the stresses and strains imparted by the swelling rock mass onto the buried structure.

This constitutive model purposefully dissociates from other models based on inputs, calculations, and intents. This paragraph will discuss the constitutive model developed for this research and the models described in Section 2.4. The Lo and Hefny (1996) model was chosen as the base model for the ability to capture the behaviour of swelling rocks in southern Ontario, where there is a known issue and market for this model, and the behaviour of any swelling material able to be derived by the three swelling tests described in Section 2.3. This separates the model from others such as the Anagnostou and Kramer and Moore models. Model inputs have been specifically limited to the six swelling test inputs and the “pseudo-Poisson’s ratio” for ease of use. Models such as Wittke involve multiple inputs beyond the basic swelling, some of which cannot be derived from swelling tests. Anagnostou requires multiple non-standard laboratory tests as well as expensive in-situ testing for deriving inputs. All swelling inputs were kept as anisotropic to properly capture the swelling behaviours, which differs from the Hawlader and Lee models. The calculations for this model have been specifically chosen to address the author’s perceived issues with other models. The Wittke model calculations have two key differences from other models. The first is that the swelling potential at a particular time step is a function of the swelling strains up to that point and the total swelling strain. The second is that the swelling strains are reduced by the elasto-plastic volumetric strains, representing the reduction in swelling that is assumed as the rock mass hydraulic-conductivity reduces as the volume increases. The volumetric strain inputs are empirical and



are predominantly used to control the rate of swelling over time but do not affect the ultimate swelling strain. However, the potential swelling strain may be greatly affected during time-periods of interest in engineering applications. If a structure is placed in swelling rock shortly after excavation, the magnitude of strains that affect the structure are greatly dependent on the swelling rate. The constitutive model created for this research simplifies the calculations by considering the swelling potential at the calculated time step and does not consider the effect of reduced hydraulic-conductivity on the swelling potential, which is very poorly understood especially at a rock mass and project scale. The rotation calculations used by Hawlader et al. and Carvahlo using Equation 2.4 are based on two-dimensional rotation only. The matrix calculations eliminate the need to determine which stresses are acting in-plane. In addition, the matrix calculations provided in Equation 3.7 for the swelling potentials will sometimes yield non-zero values in the shear positions ( $\vec{e}_{pot}(m,n)$ ,  $m \neq n$ ). Although these values are very small, in practice they lead to a more stable calculation at small confining stresses. When internal stresses in the continuum do not provide a distinct principal stress direction throughout the continuum, the vector calculations result in abnormal shear stresses, likely due to the accumulated rounding errors not captured by Equation 2.4. The matrix calculations eliminate much of this issue.

### 3.6 Acknowledgments

The author would like to acknowledge the help and mentorship offered by Dr El Ansary of the Department of Civil and Environmental Engineering at The University of Western Ontario and Dr J. Carvahlo of Golder Associates.

### 3.7 Figures

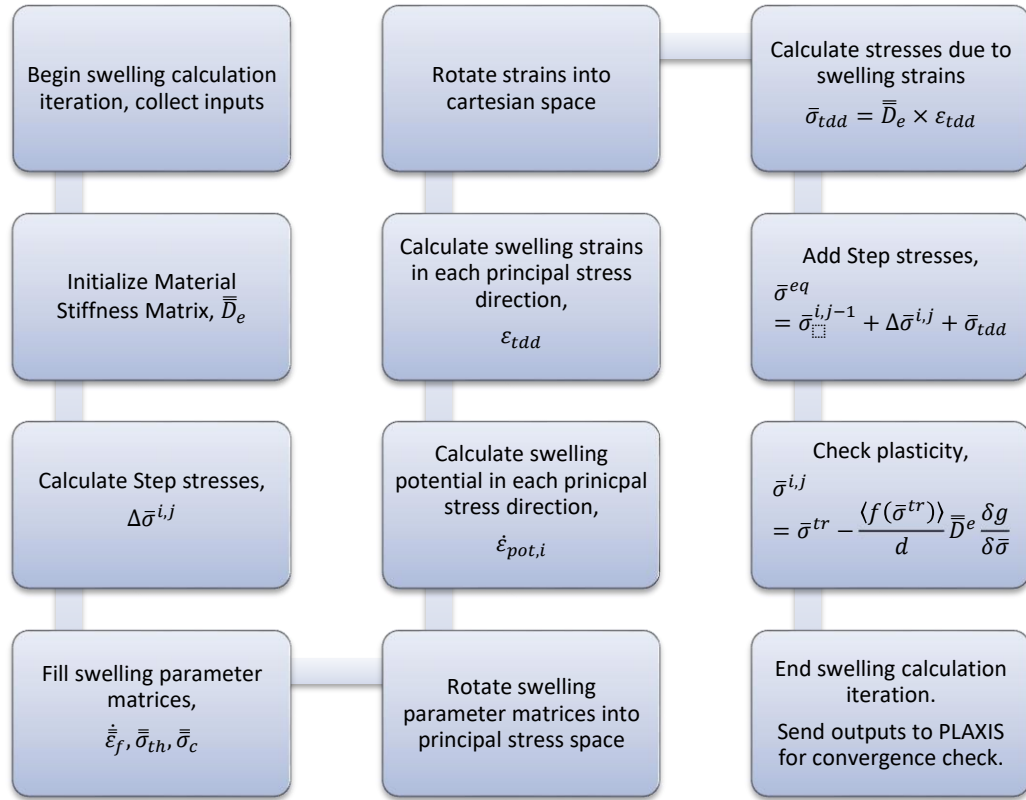


Figure 3.1. Flow chart of swelling rock constitutive model.

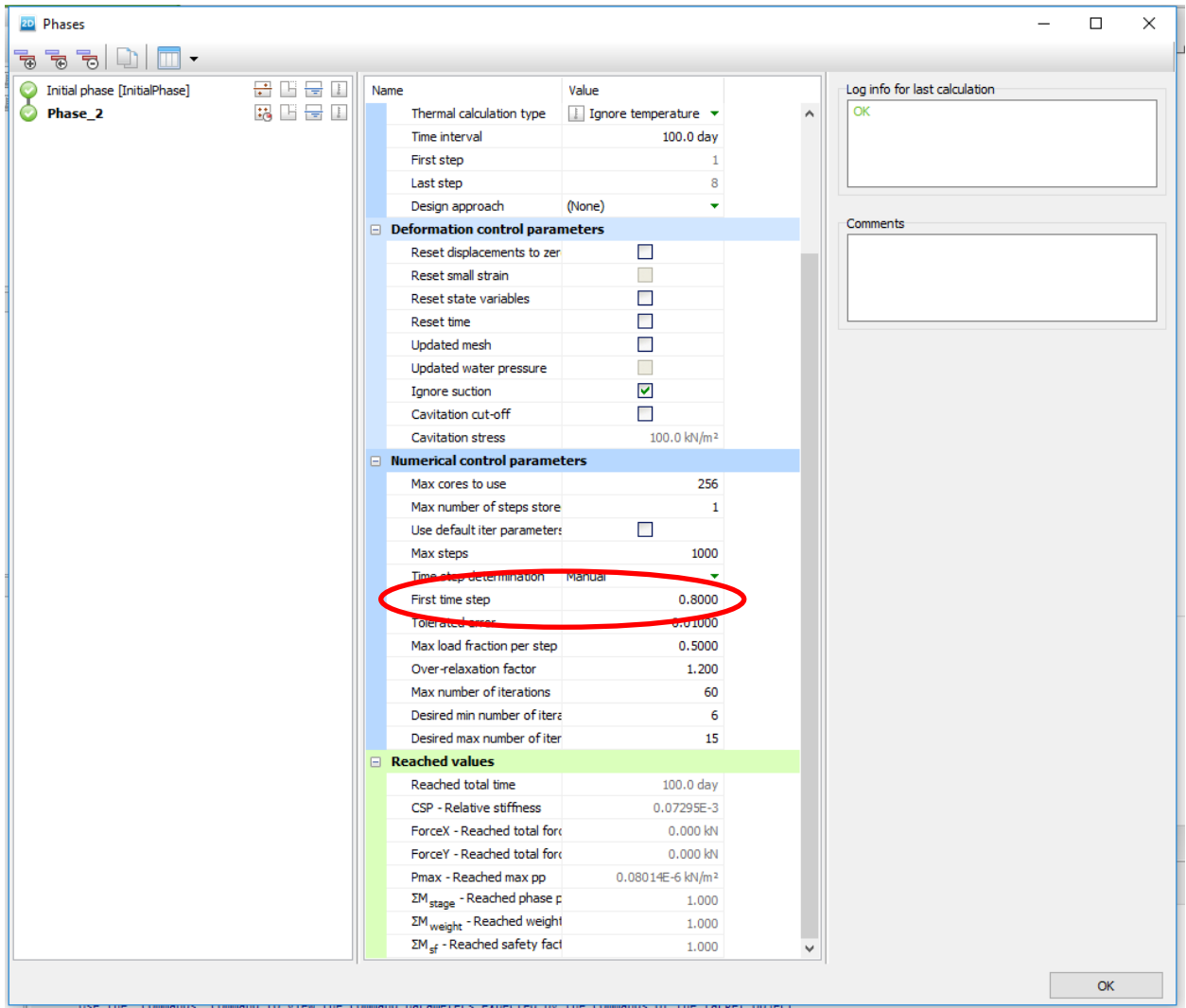


Figure 3.2. First Time Step input.

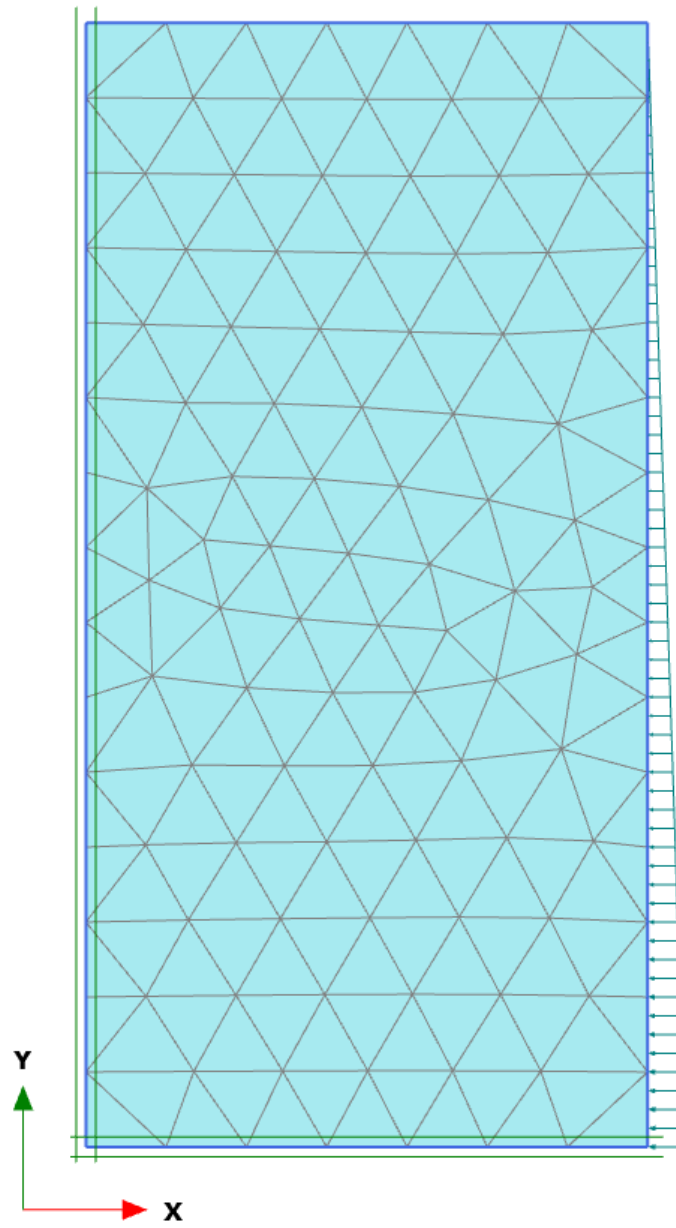


Figure 3.3 Typical mesh and boundary conditions for model verification.

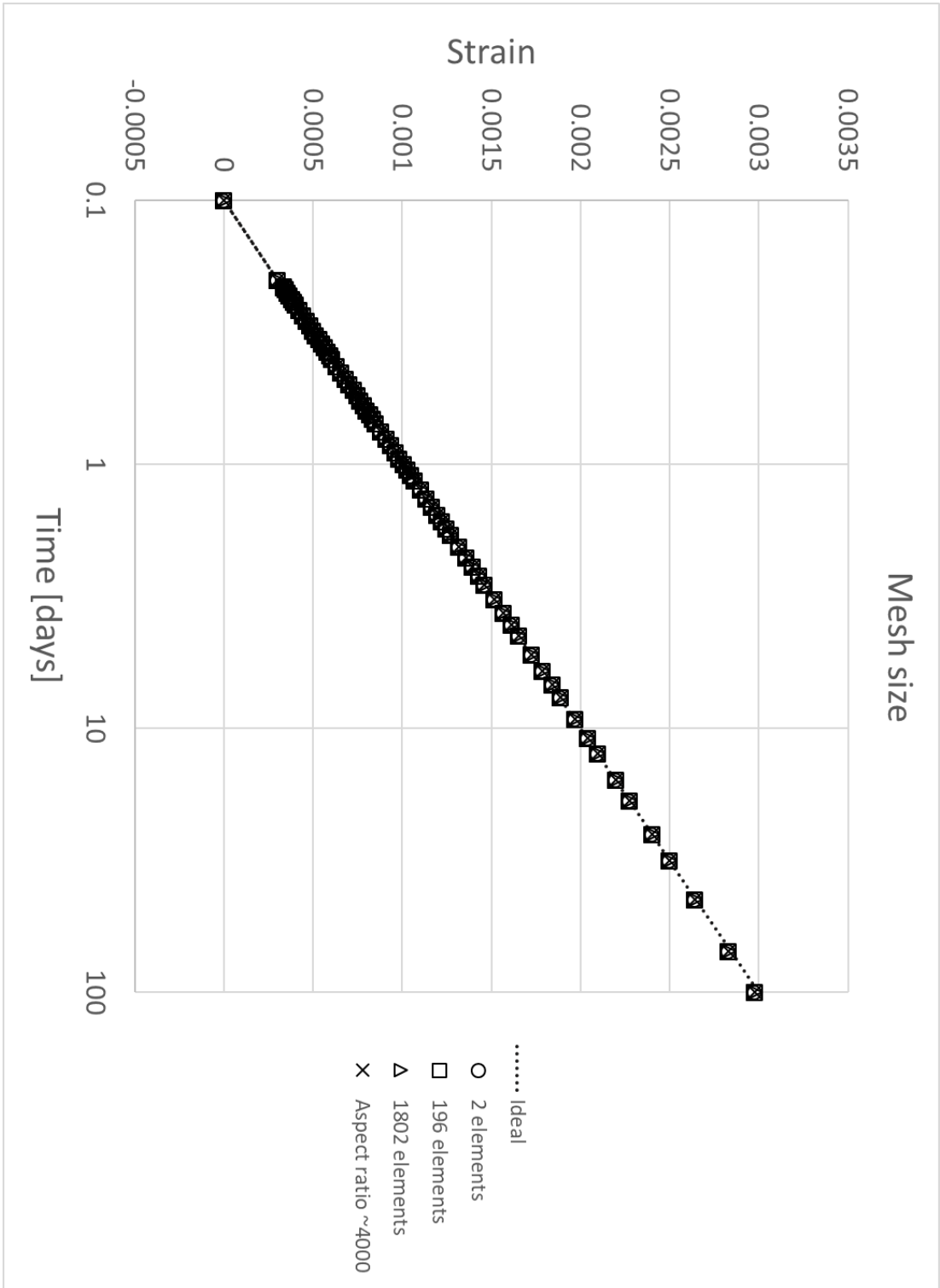


Figure 3.4. Effect of meshing on constitutive model behaviour.

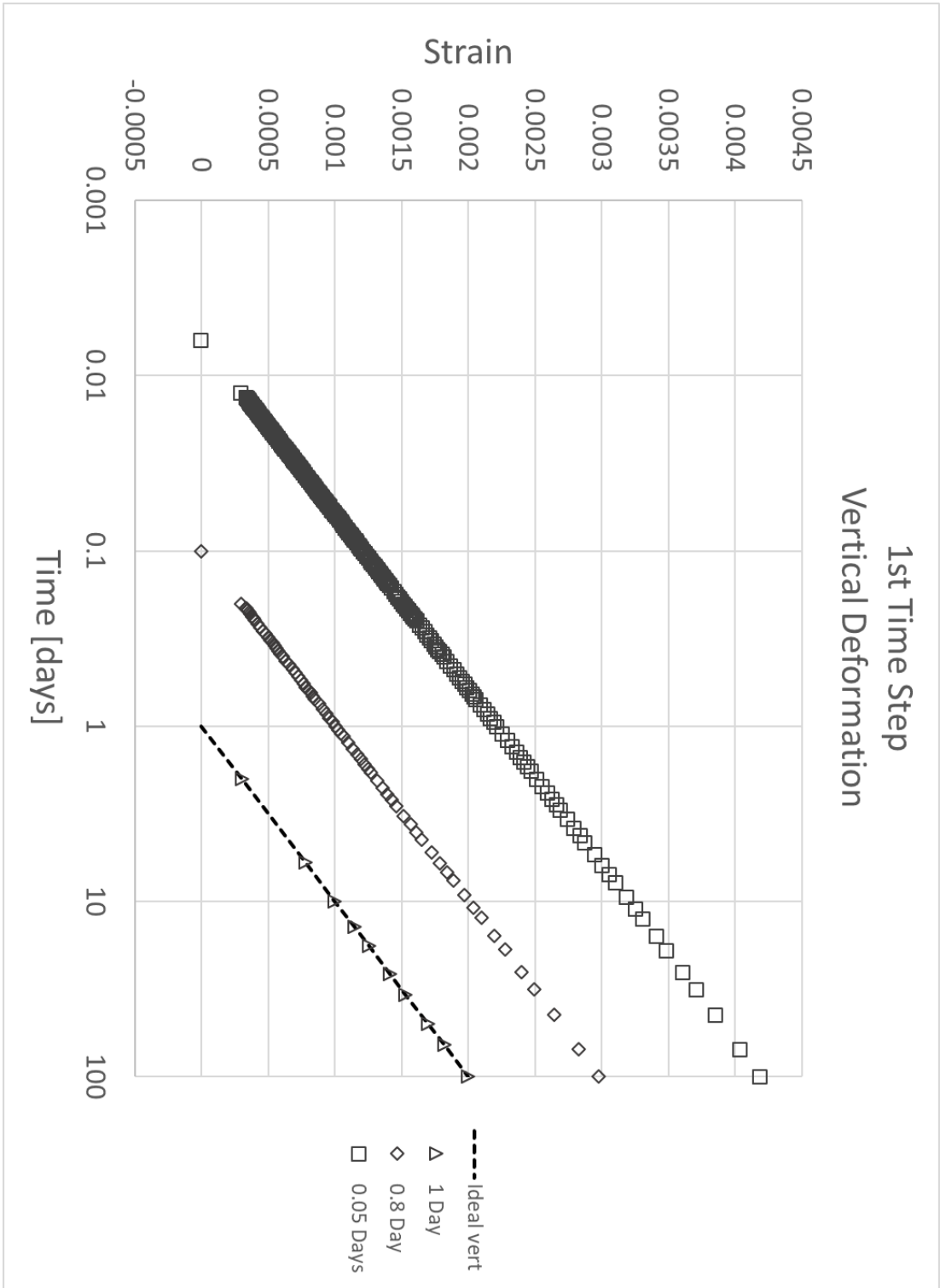


Figure 3.5. Effect of First Time Step input on the behaviour of the constitutive model.

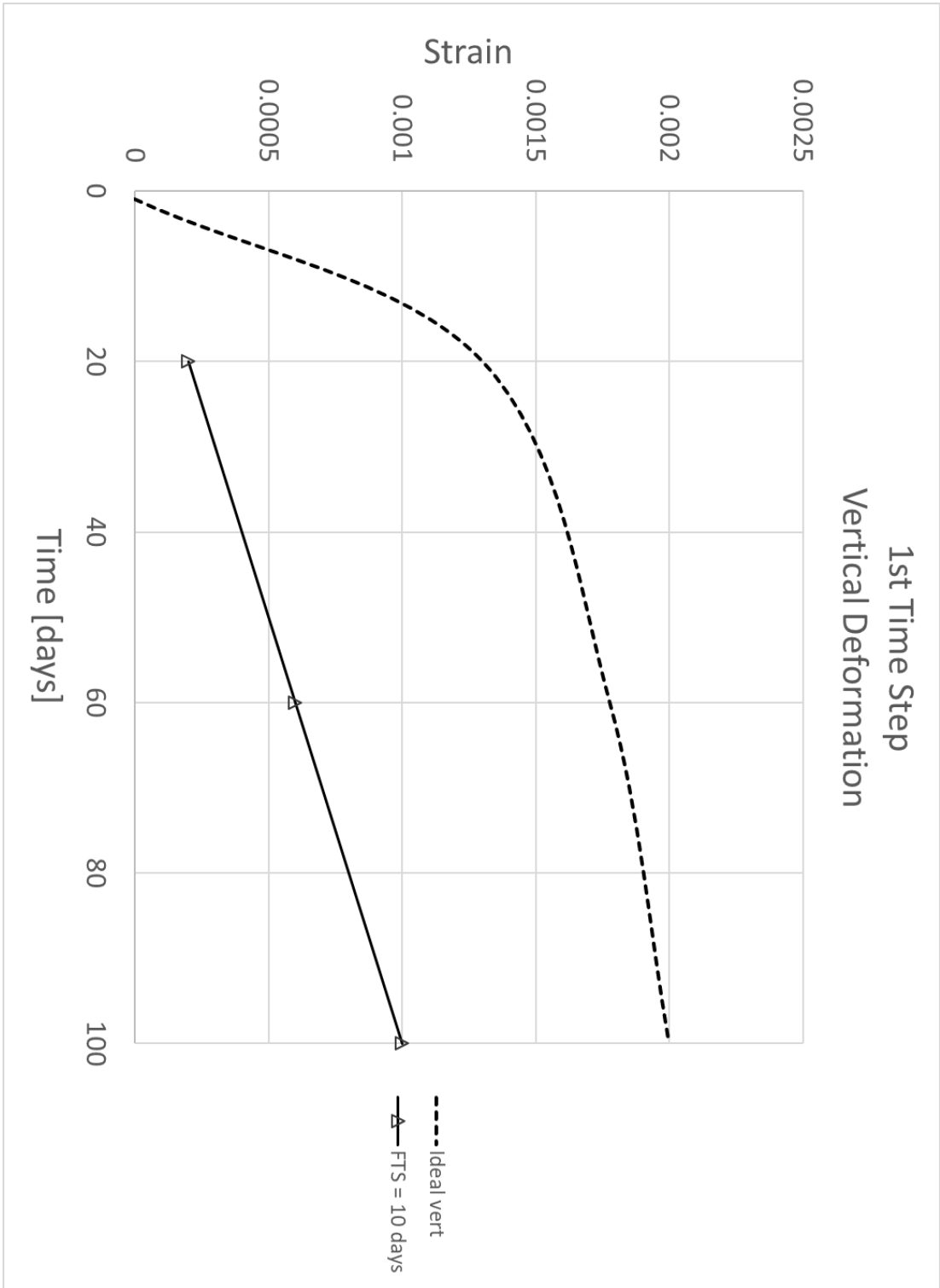


Figure 3.6. Swelling results using a First Time Step value of 10 days.

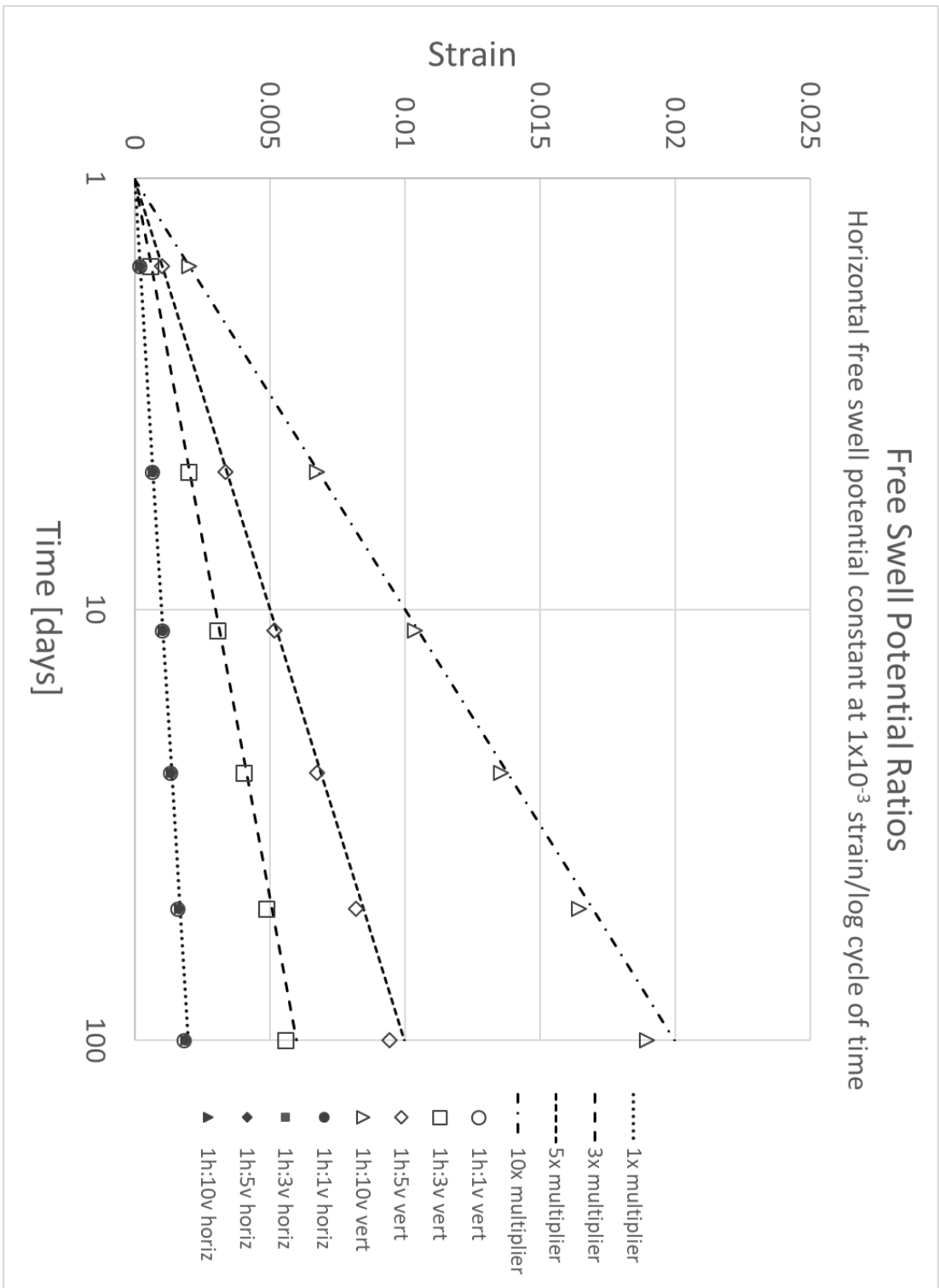


Figure 3.7. Verification of free swell potentials, with constant  $\epsilon_{fh}$ .



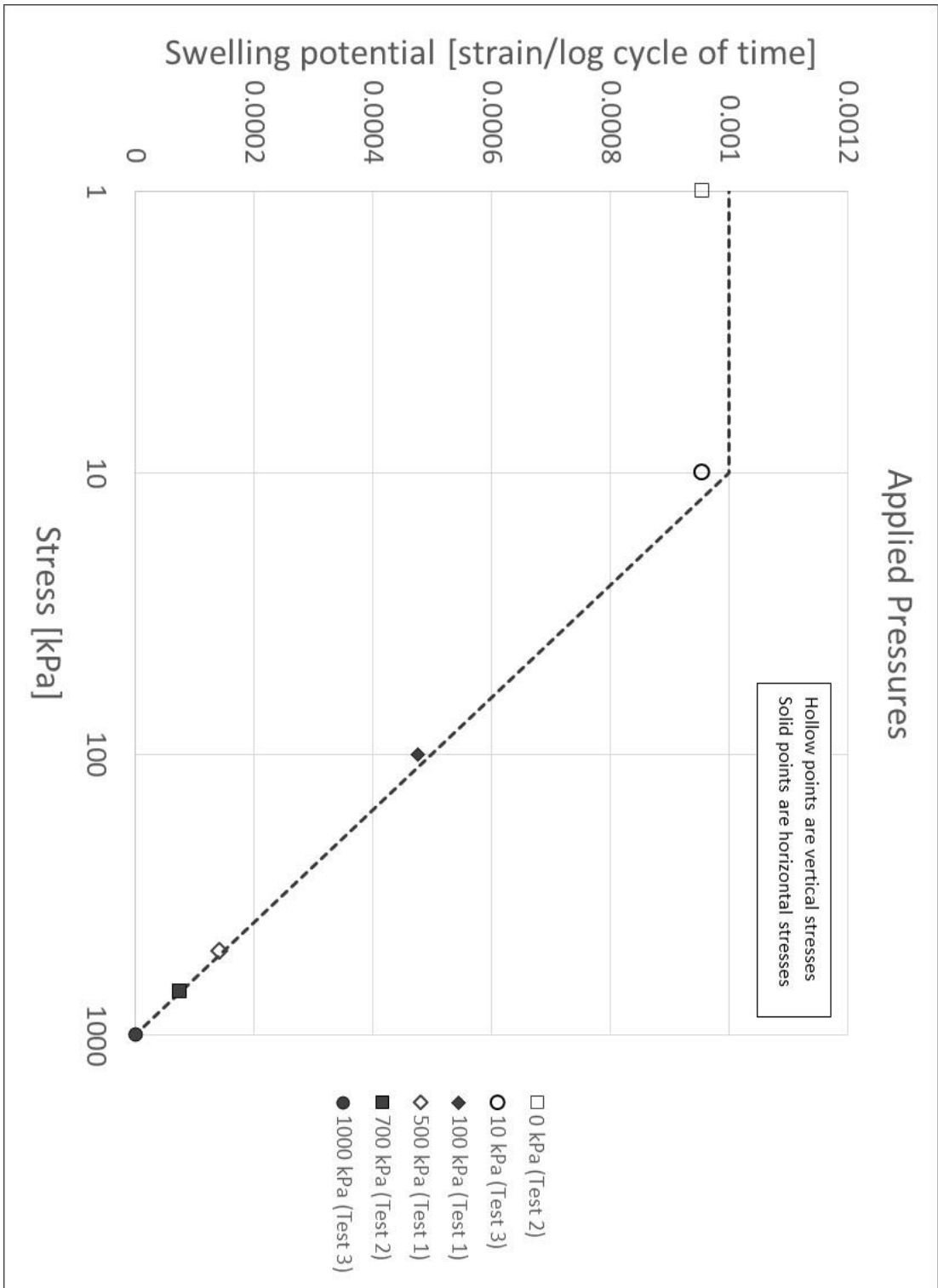


Figure 3.8. Effects of applied stress on swelling potential selected by model.

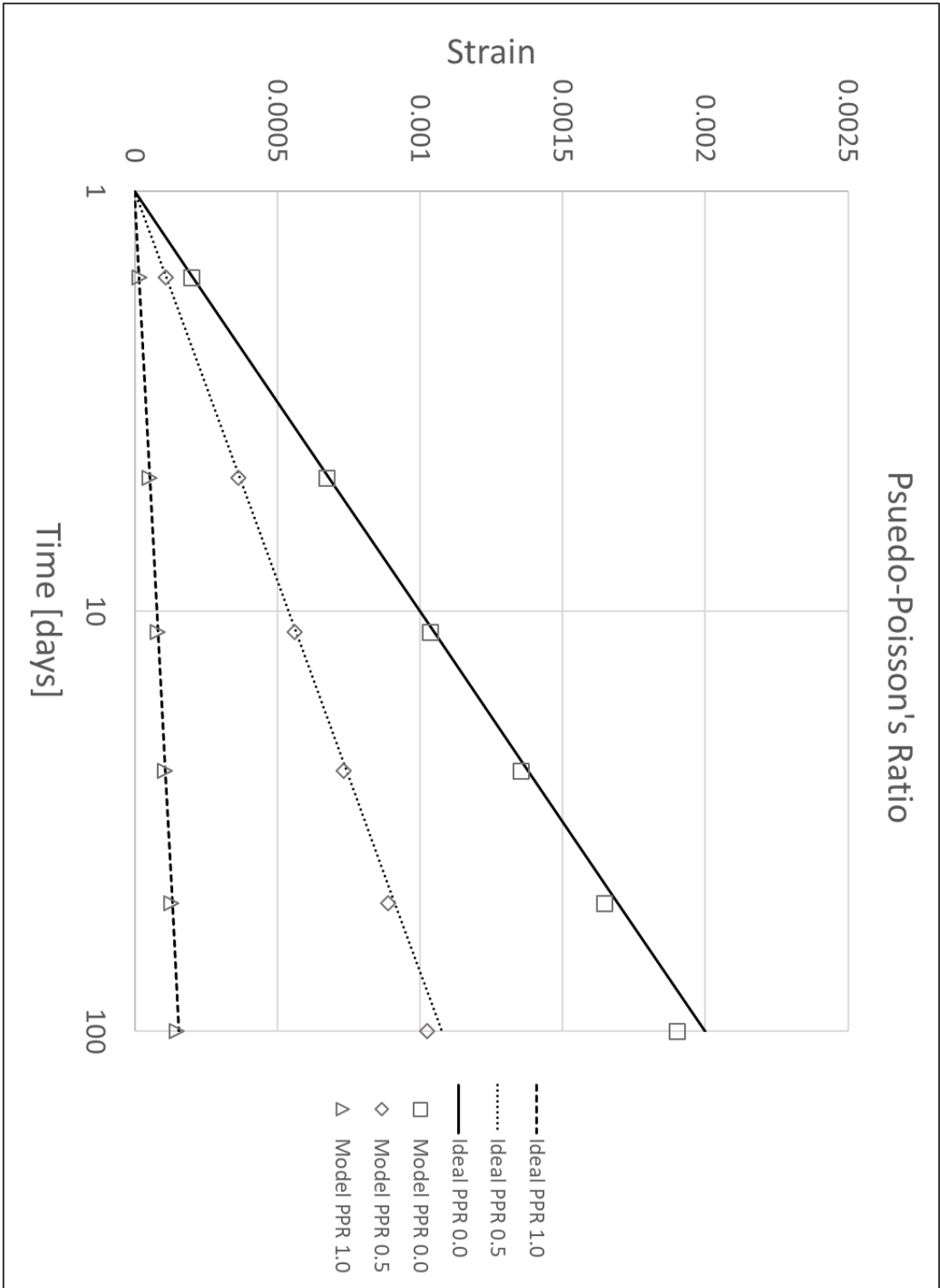


Figure 3.9. Model verification of PPR values.

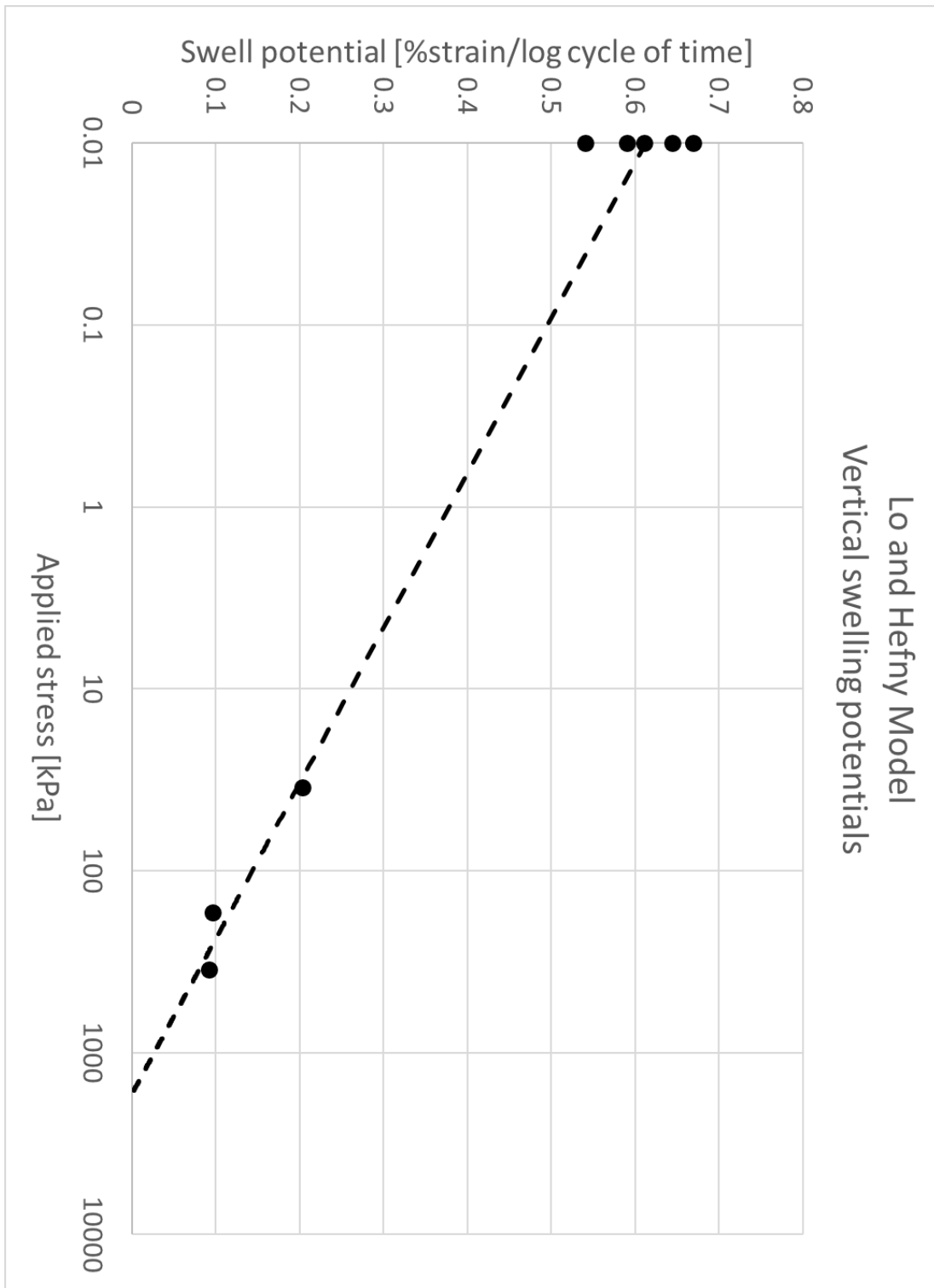


Figure 3.10. Vertical swell potential Lo and Hefny model derived from Yuen (1979).

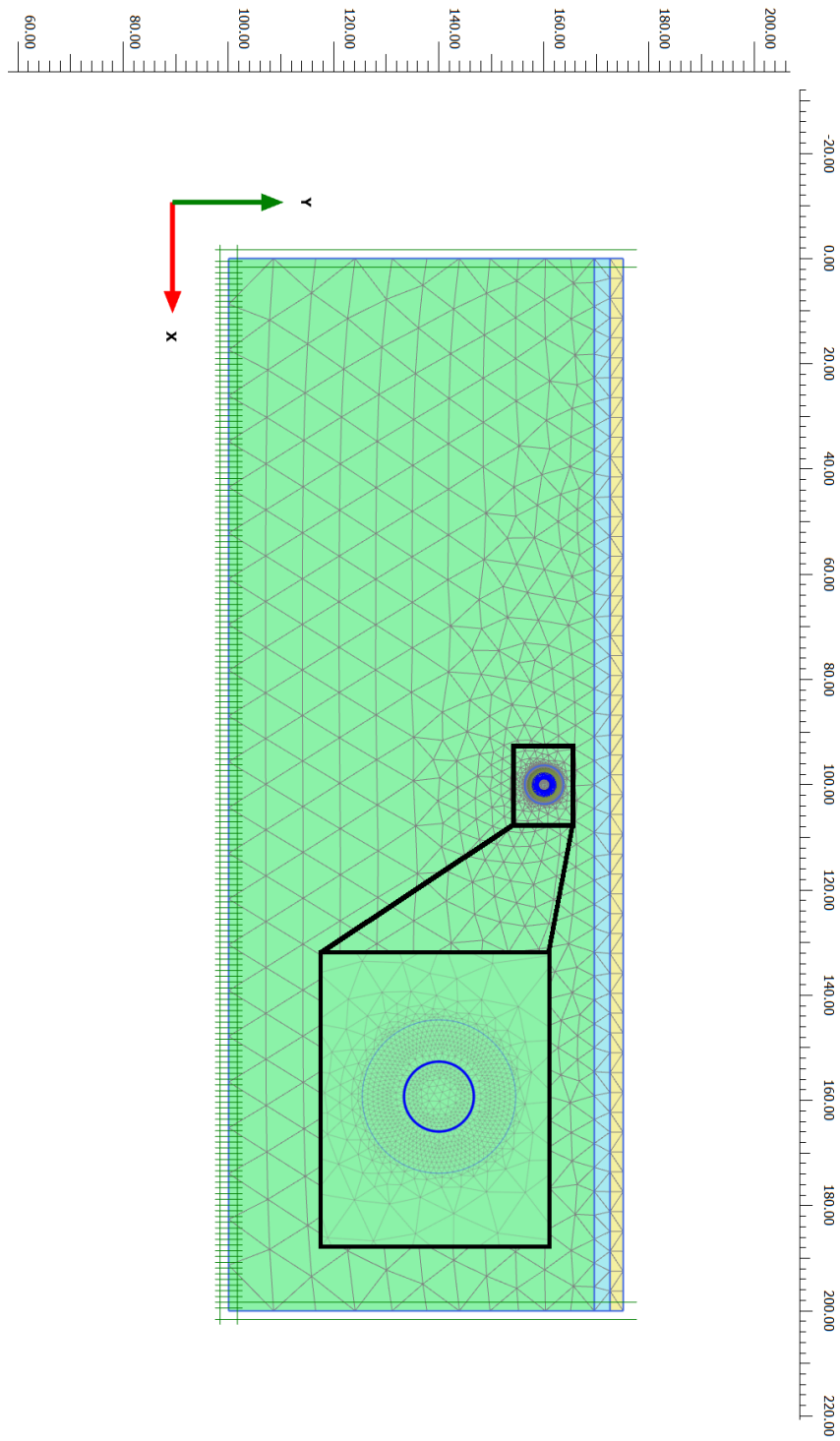


Figure 3.11. Heart Lake Tunnel mesh and boundary conditions.

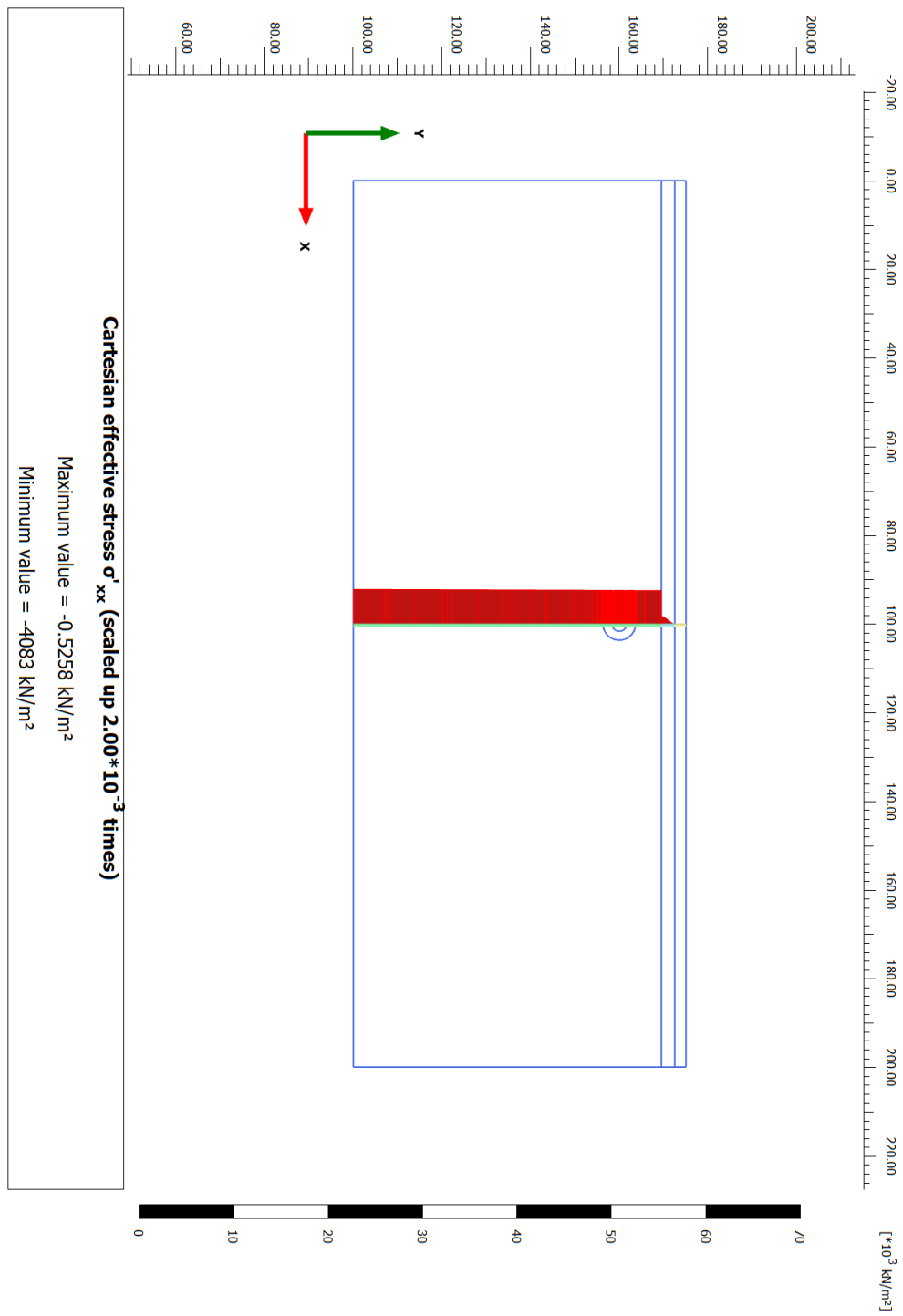


Figure 3.12. Initial uniform horizontal stress of 4 MPa in Georgian Bay Formation.

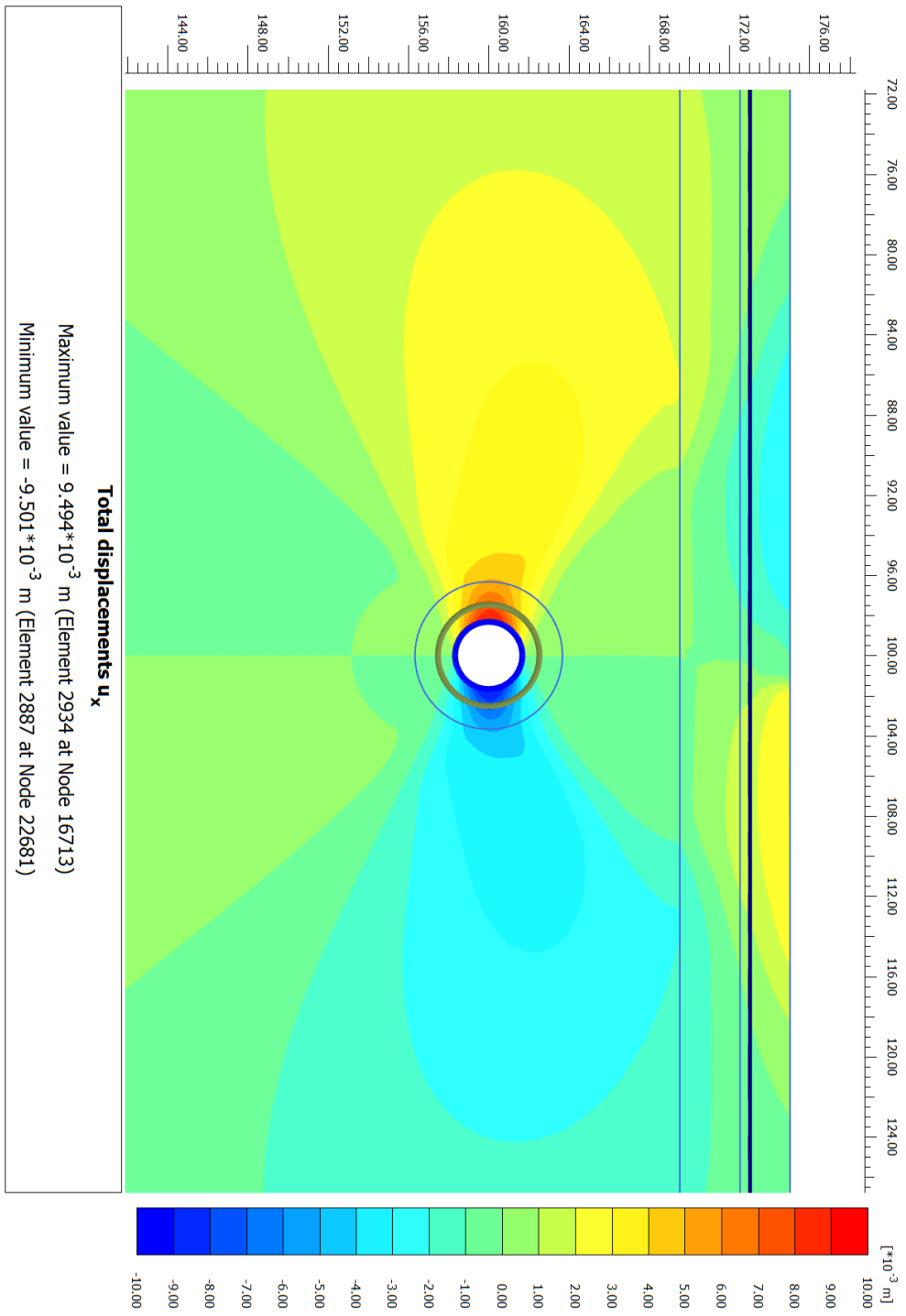


Figure 3.13. Horizontal deformations due to swelling after 10 years at Chainage 136+20.

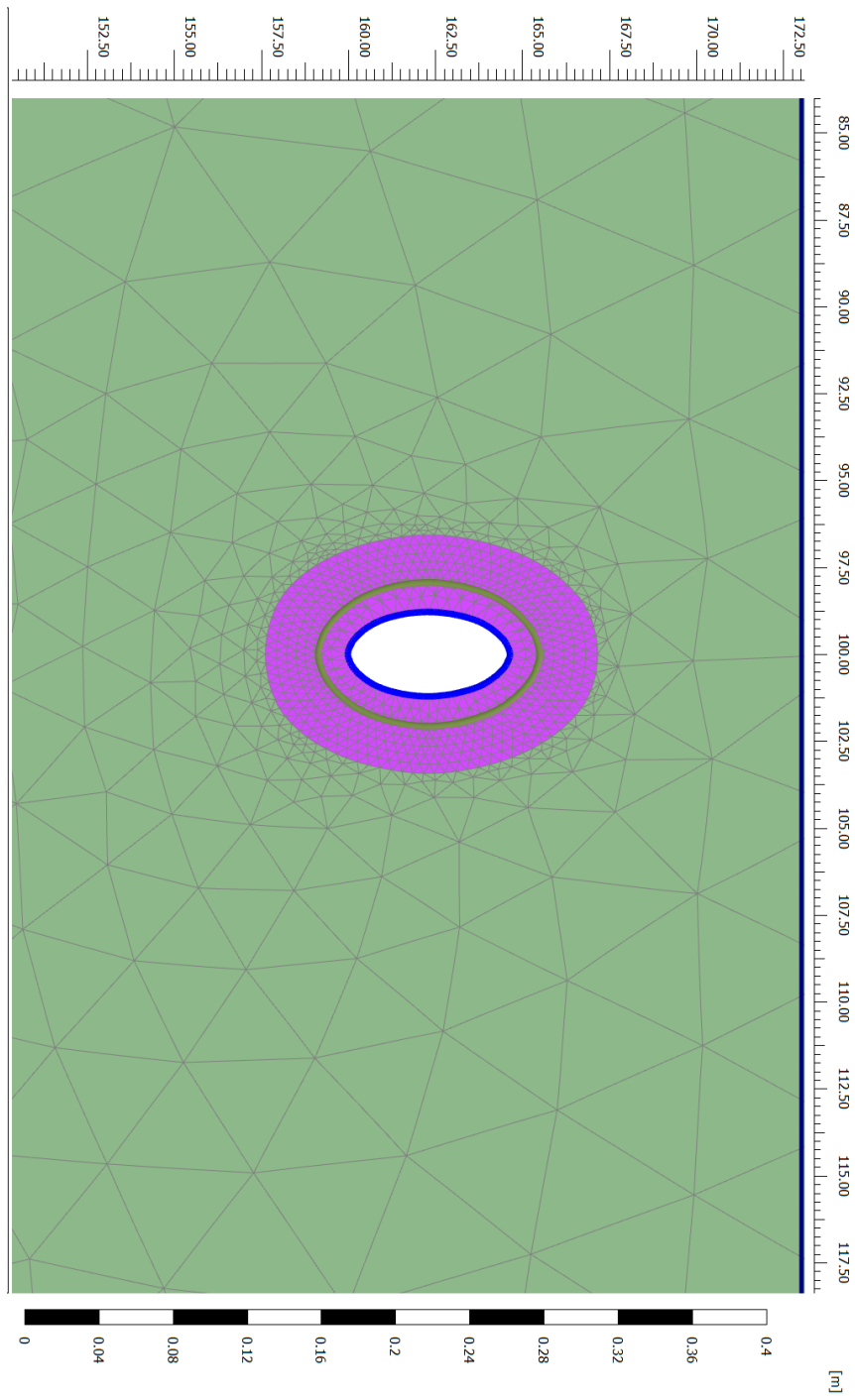
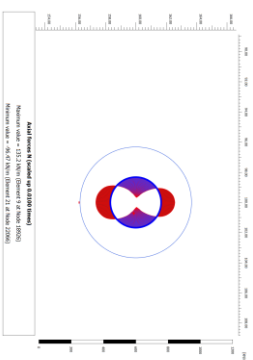
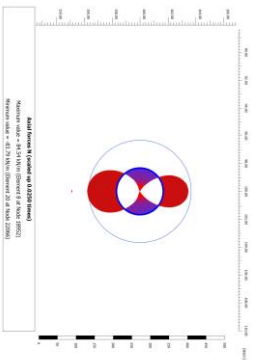
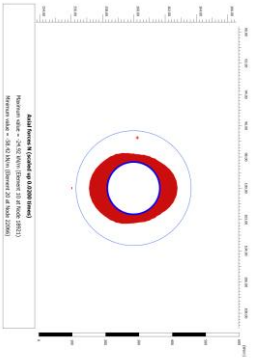


Figure 3.14. Deformed tunnel after 10 years at Chainage 136+20.

Chainage 120+00,  $\sigma_h = 1.5 \text{ MPa}$       Chainage 125+00,  $\sigma_h = 3 \text{ MPa}$       Chainage 136+00,  $\sigma_h = 4 \text{ MPa}$

Axial forces  
[kN/m]



Bending moments  
[kNm/m]

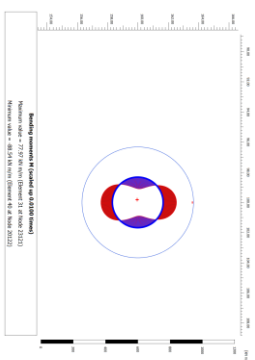
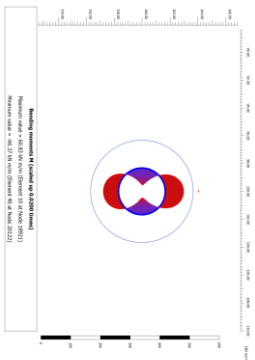
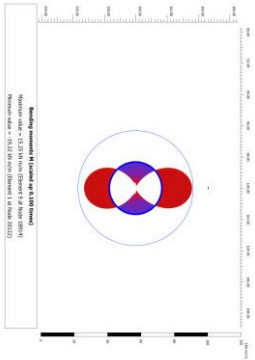


Figure 3.15. Axial and bending forces after 10 years.



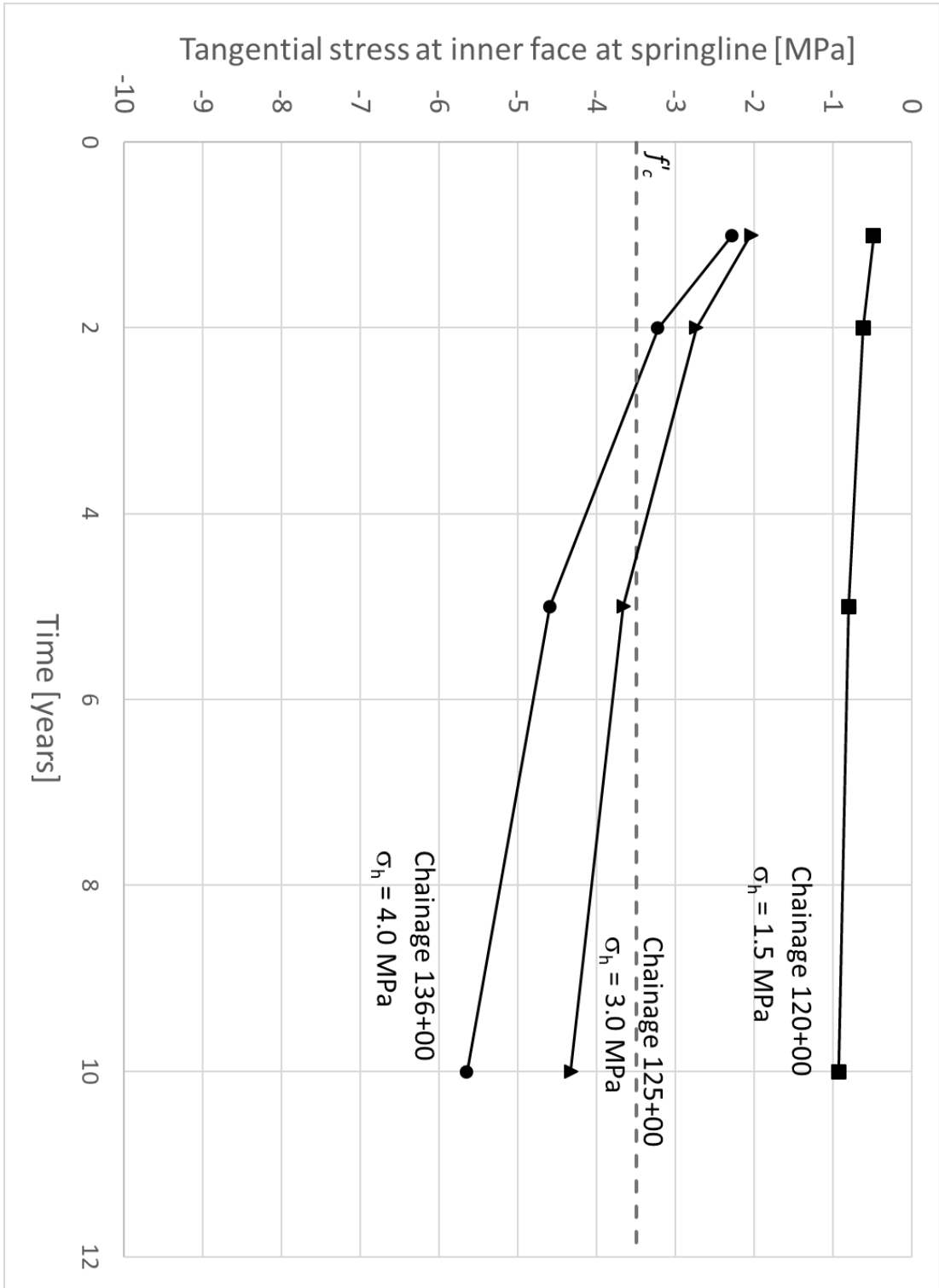


Figure 3.16. Tangential stress at springline over 10 years.

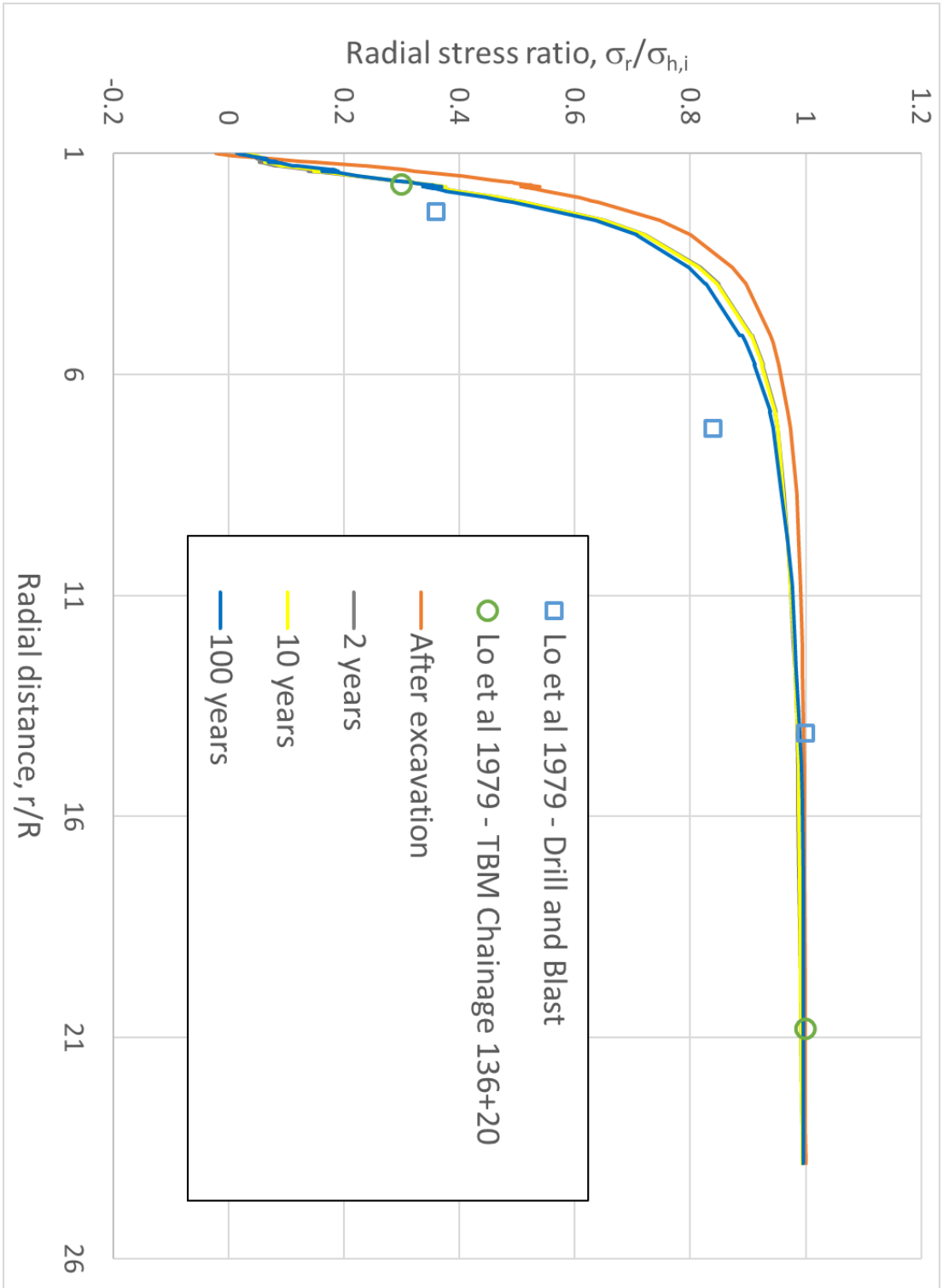


Figure 3.17. Variation of radial stress with distance from interface over time.

## Chapter 4

### 4 Investigation of swell mitigating material

#### 4.1 Introduction

Long-term swell creep has the potential to increase stresses and consequently cause damage to buried Infrastructure constructed in swelling rock years, and possibly decades, after installation (Lee and Lo, 1976; Lo et al., 1979; Carvalho, 2015). This may result in costly repairs or replacement of the damaged structure. The current design practice for tunnels in swelling rock involves identifying the swelling properties of the rock and predicting the time-dependent swell behaviour and stresses imparted on the proposed structure. The swelling deformations generally vary logarithmically with time; therefore, it is often advisable to provide a waiting period between 90 and 100 days between excavation and installation of the buried structure to allow a significant portion of the rock movement to occur unimpeded (Lo and Yuen 1981, Carvalho 2015). However, this delay can be quite costly and is impractical for some projects. Alternatively, the design approach may involve placing a compressible material between the rock and the structure to mitigate the negative effects of swelling. For example, Lo et al. (1987) described the application of a mix of preformed foam planks and spray-on polyurethane foam in the design of a tunnel and Carvalho (2015) reported using low strength (2 MPa) grout. Generally, application of spray-on foams can be problematic, whereas grouts can be effectively formed to the desired shape or injected into an annulus.

Although employing a compressible material has been in use for more than 30 years, the development and characterization of materials suitable for this purpose is lacking. Nehdi et al. (2002) first identified cellular grout as a potential material to mitigate impacts of swelling rock. Zhao et al. (2015) proposed using a cellular grout to absorb dynamic impacts in tunnels. On the other hand, Chen et al. (2015) evaluated the mechanical properties of EPS foam board.

Materials for this research were chosen after consultation with excavation, foundation, and tunnel contractors. EPS foams were chosen for their ease of installation, access to supply, and known material behaviour. Cellular grout was chosen based on constructability (the ability to form preferred shapes and fill voids) and ability to select strength properties based on design requirements. Spray-on polyurethane foams were discussed but were considered undesirable

by the contractors due to constructability issues. The most common complaint was the difficulty securing the foams to overhead surfaces. Poured polyurethane foams were also initially considered. The poured polyurethane foams have many of the same advantages of cellular grout; they can be formed to a desired shape and the strength properties can be controlled via mix design. Initial testing at the desired strengths (1 MPa) resulted in strengths less than 10% of design. No further testing was conducted.

#### 4.1.1 Purpose of this research

This chapter explores EPS foam and cellular grout as potential compressible materials for mitigating the effects of swelling rock on buried infrastructure. The purpose of this chapter is to investigate the behaviour of the two materials under monotonic, low strain rates mimicking the swell behaviour. As discussed in Section 2.6.1, the effect of low strain rates on EPS foam yield strength, elastic modulus, and post yield behaviour has not been researched in previous studies. Cellular grout with a void ratio of 75 % is poorly understood, as the majority of studies concentrate on void ratios of 35 % or less. The effects of confinement on the behaviour will be studied.

Testing was conducted on both materials in order to evaluate their mechanical properties and determine their engineering parameters required for design purposes. Consequently, recommendations are made for testing and specifications in contractual works.

## 4.2 Experimental program

### 4.2.1 EPS foam

The current study examines the effect of strain rate on the mechanical properties of EPS foam to determine its properties for use in tunnel applications in swelling rock. Two EPS foam densities were considered: EPS22 with density of 21.6 kg/m<sup>3</sup>; and EPS39 with density of 38.4 kg/m<sup>3</sup>. The compressive loading was applied with strain rates ranging from 0.02% /min to 10% /min. All samples had approximately the same dimensions of 100x100x25 mm. The test samples were placed in an MTS hydraulic compression machine, and were subjected to strain rate-controlled loading. Strains and stresses were recorded using a Sciometric Series 7000 data recorder to an accuracy of ±1%.

A total of 8 uniaxial compression tests were conducted, four on EPS22 and four on EPS38, each with a different strain rate. Samples were placed between steel loading plates slightly larger than the sample size to ensure uniform loading. Each test was conducted with a constant strain rate, and the load and deformation were recorded until strain reached approximately 70%.

Monotonic loading was applied at very low strain rate to simulate the strain rate associated with the slow-rate irreversible rock deformations during the swelling process. Table 4.1 summarizes the elastic modulus, yield strength and post-peak behaviour of the foams.

Table 4.1. Results of compression tests on EPS foams.

Sample	Strain rate	Elastic modulus	Yield strength	Post-yield modulus
	%/min	[MPa]	[kPa]	[kPa]
EPS22 – 1	10	3.3	80.2	248
EPS22 – 2	1	3.5	77.8	247
EPS22 – 3	0.1	3.1	64.3	82
EPS22 – 4	0.02	3.5	67.6	107
EPS39 – 1	10	6.7	158	364
EPS39 – 2	1	8.3	165	385
EPS39 – 3	0.1	4.2	235	445
EPS39 – 4	0.04	4.6	173	296

Figure 4.1 and Figure 4.2 present the results of the uniaxial compressive loading conducted at different strain rates up to a maximum strain of more than 60% for EPS22 and EPS39, respectively. For the purpose of comparison, the stress-strain behaviour for the foams following the ASTM recommended strain-rate (10%/min) are also shown in Figure 4.1 and Figure 4.2 as applied stress at specific total values of 1, 5, and 10 % strain. . In all cases, the general behaviour was similar. The material behaved elastically until the yield strength. In all cases, the general behaviour was similar The post-yield behaviour resulted in a linear stress-

strain behaviour at a much lower value than the elastic modulus. At some point after approximately 35%, the rate of stress increase with strain begins to increase exponentially, representing stress hardening behaviour.

In the zone of elastic behaviour (typically strain less than 10%), the effect of strain rate is less pronounced. For EPS 22, the elastic modulus between the strain rates varied between 3.1 and 3.5 MPa. For EPS 39, the two high strain rates, 1 and 10% strain/min, the elastic modulus was 8.3 and 6.7 MPa, respectively. For the two low strain rates, 0.1 and 0.04% strain/min, the elastic modulus was 4.2 and 4.6 MPa. The limited results show some difference in EPS 39 when the strain rate is lower than 1 MPa. Strain rate appears to have little effect on elastic modulus.

The effect of strain rate on yield strength is less pronounced. For EPS 22, the yield strength varied between 80.2 kPa for a strain rate of 10% strain/min to 67.6 kPa for a strain rate of 0.02% strain/min. For EPS 39, the yield strength typically varied between 158 and 173 kPa, with the exception of the test at 0.1% strain/min which had a yield strength of 235 kPa. For both types of EPS foam, no clear relationship between the strain rate and yield strength was observed.

Figure 4.3 presents the variation of the post-yield deformation modulus (defined as the change in stress over the linear portion of the post-yield strain) with the strain rate. Figure 4.3 shows a general trend of the post-yield deformation modulus increasing as the strain rate increases. This is particularly pronounced for the EPS22 foam. Comparing the deformation modulus with the elastic modulus, it is noted that for EPS39 foam, deformation modulus decreased by approximately 20% as the strain rate decreased from 1% to 0.02% while, deformation modulus of EPS22 foam decreased by approximately 57%. This difference in behaviour may be attributed to the difference in density, where the lower density material experiences significant loss of structure post yield.

Strain hardening is defined as the condition when the post-peak deformation modulus begins to increase. For the EPS foam samples tested in the current study, strain hardening appears to occur at strains greater than 35%.

Given that swelling rock experiences monotonic slow-rate deformations (with strain rate typically between 0.3 and 0.005% per log cycle), the design parameters of EPS should be established from compressive load tests with strain rate matching the maximum strain rate measured from rock sample swell testing. In addition, the observed behaviour justifies the design of compressible materials in swelling rock applications considering reduced yield strength and a suitable deformation modulus for the plastic zone up to approximately 35% strain.

#### 4.2.2 Cellular Grout

The load tests conducted herein aim to identify the engineering properties of cellular grout required for its incorporation in the design of tunnels constructed in swelling rock. Three series of tests were conducted to determine the grout mechanical properties including: four uniaxial compression tests as per ASTM C495/C495M-12, three uniaxial compression tests at reduced strain rates, and five CID (ASTM D7181-11) triaxial tests.

#### 4.2.3 Sample preparation

The grout samples were provided by Elastizell Canada Inc. and were mixed and set in their Michigan laboratory. The requested properties were a porosity of 75% and a uniaxial compressive strength (UCS) of 1.0 MPa. The foaming agent used is a blend of protein-stabilized surfactants, with a mix ratio of water to foaming agent of 40:1. The foam is created using a specifically designed nozzle with pressurized air. The grout was a mix of cement and water. The cement : water : foaming agent ratio was 9.1:5.4:1.0. The cement and water were mixed for approximately 5 minutes, after which foaming agent was added and mixed for an additional 2 minutes. The samples were then cured for 8 days to provide strength prior to shipping. The samples were then protected with bubble wrap and shipped to The University of Western Ontario and were received by the researchers 23 days after mixing. The samples were then cured for a short period prior to being stored for safety purposes.

Samples used for uniaxial compression tests were capped with hydrostone after curing according to ASTM C617/C617M-12.

## 4.2.4 Unconfined compression strength tests

### 4.2.4.1 ASTM test set

The first series of unconfined compression tests followed the ASTM C495/C495M-12 Standard Test Method for Compressive Strength of Lightweight Insulating Concrete. Four samples were tested and their density at the time of testing varied were between 417 to 458 kg/m<sup>3</sup>.

An MTS compression machine equipped with a 2000 kN load cell with an accuracy of  $\pm 0.25$  kN, and was connected to a data logger to collect the test data. The loading was applied at a rate of 14.5 kN/sec to ensure the sample failure occurs within 50 to 80 seconds, as per the Standard requirements. The samples were loaded until collapse occurred. Figure 4.4 presents the stress-strain behaviour of the cellular grout samples obtained from the unconfined compressive load tests. It is noted from Figure 4.4 that the peak strength of the test samples varied between 770 and 1013 kPa. It is also noted from the test results presented that the samples exhibited ductile failure, and displayed post-peak behaviour with a constant rate of reduction in strength with strain increase. By inspecting the tests samples, it was observed the failure mode involved crushing at the loading plate followed by a combination of shear and splitting failure within the sample body. Figure 4.5 shows a typical sample set-up for testing (a) and the failure modes post-test (b).

### 4.2.4.2 Variable strain test set

Unconfined compression tests were conducted on six additional samples. The sample density varied between 397 and 443 kg/m<sup>3</sup>. The three pairs of tests at strain rates of 0.17, 0.035, and 0.007 % strain/min. Figure 4.6 presents the stress-strain behaviour of the samples tested at 0.17 % strain/min, while Figure 4.7 and Figure 4.8 present the results for 0.035 and 0.007 % strain/min respectively. Test number UCST-CG-08 experienced abnormal behaviour during initial loading, and the results are shown, but are not considered in the analyses. The behaviour is indicative of a seating issue during test set-up. It can be observed from the figures that the peak strength varied between 610 and 1020 kPa, with an average of 730 kN. This is approximately 30% less than the peak strength for the samples tested after 30 days but at a faster load rate. However, the post-peak behaviour was similar to that observed from the



ASTM standard testing. Elastic moduli and ultimate strength are shown in Figure 4.9. Test results indicate that there is little effect on unconfined compression strength (UCS) due to strain rate, but a noticeable trend of increasing  $E_{50}$  with decreasing strain rate. .

#### 4.2.5 Cellular grout triaxial tests

A series of triaxial tests were conducted on cellular grout samples with approximate dimensions of 50 mm diameter and 100 mm length, with an average unit weight of 4.3 kN/m<sup>3</sup>. Three sets of tests were conducted in an attempt to understand the effects of saturation, backpressure, and stress history. The intended use of the cellular grout is to be placed between buried structures and swelling rock, where it will provide mitigation of swelling strains. It was originally anticipated that the grout would be saturated under triaxial loading conditions in the field.

##### 4.2.5.1 Triaxial set No. 1

Five Consolidated Drained (CD) triaxial tests were conducted, with the initial purpose of identifying the strength and strain properties of a saturated cellular grout sample under triaxial load conditions. Each sample was removed from the protective wrap and casing, and the ends were leveled using rough sandpaper. The pre-test radius was measured at the top, middle, and bottom of samples by averaging two diameter readings. The length was determined by averaging three measurements at 120° apart. Each sample was prepared so that the difference between the smallest and largest length reading was less than 0.5 mm. The samples were weighed and the pre-testing density was calculated. Each sample was then dried for 24 hours and then weighed again for the dry density. The samples were then submerged in water for 24 hours prior to starting the test. Due to the voids along the surface of the sample, each was prepared with a double sleeve. The testing apparatus for the first round of tests was the Wykeham Farrance machine. In general, the backpressure and cell pressure were increased until approximately 175 kPa and 210 kPa respectively, where the pressures were held until a constant volume was reached. The backpressure was then reduced to approximately 50 kPa and the cell pressure was brought to the desired testing pressure. The change in volume during consolidation was recorded, and each sample reached consolidation/constant volume within approximately 20 minutes. Each sample was tested with constant axial strain of approximately

0.04%/minute. After testing, samples were then removed from the apparatus and photographed. Given the porosity of the samples, large water loss occurred during sample removal, preventing the measurement of wet and dry weights at the end of the test. Figure 4.10 shows a typical pre-test sample, test set-up and sample post-test.

#### 4.2.5.2 Triaxial set No. 1 results

The testing details for each Set #1 sample are provided in Table 4.2. Figure 4.11 shows the deviatoric stress results up to a 10% strain. Figure 4.12 shows the change in volume. Figure 4.13 shows the effective stress Mohr Circle results for the average stresses between 8 and 10% of strain.

Table 4.2. Triaxial Set #1 test results.

Test #	$\rho_{\text{test}}$ [kg/m <sup>3</sup> ]	$\rho_{\text{dry}}$ [kg/m <sup>3</sup> ]	Axial pressure [kPa]	Cell pressure [kPa]	Back pressure [kPa]	$\sigma'_1$ [kPa]	$\sigma'_3$ [kPa]
1	431	N/A	487	149	56	582	94
2	414	372	422	249	58	614	191
3	404	365	309	351	53	607	298
4	396	358	268	451	53	666	398
5	423	390	382	554	55	881	499

Results from the testing do not indicate the typical response of increasing strength with increasing confinement. Figure 4.11 indicates that Tests #2 to #5 reached a peak strength, followed by a sudden loss of strength, with a gradual increase to a residual strength. Once yield occurs, the deviatoric stress generally increases up to a residual strength, with some variation as the strain increases. Test #1 experienced an elastic response until yield, with a gentle increase in deviatoric stress with additional strain and not sudden strength loss. The behaviour indicates that collapse of the cellular grout matrix at yield is not a uniform behaviour between all samples. The random size and distribution of the void spaces potentially explains these post-peak behaviours. In all cases, the deviatoric stress does not appear to be influenced by strain or confinement.

The Mohr's circles of effective residual strength (Figure 4.13) show a general decrease in strength with confining pressure, which is not expected, and does not provide any useful engineering strength parameters. The failure mode on each sample appears to be crushing or void collapse along a near horizontal plane. Figure 4.14 highlights the crushed zone. The crushed zone was composed of granular material. No sample displayed typical shear failure modes.

The results from Set #1 indicated possible issues with the testing methodology. Two concerns were the level of saturation and the effect of drying the sample prior to testing. To address these concerns a new test methodology was adopted.

#### 4.2.5.3 Triaxial set No. 2

For the second set of triaxial tests a new methodology was adopted, with the goal of adhering to ASTM 7181-11 as practically as possible knowing the samples were cellular grout and not cohesive soil.

Each sample was removed from the protective wrap and casing, and the ends were leveled using rough sandpaper. The pre-test radius was measured at the top, middle, and bottom of samples by averaging two diameter readings. The length was determined by averaging three measurements at 120° apart. Each sample was prepared so that the difference between the smallest and largest length reading was less than 0.5 mm. The sample was weighed and the pre-testing density was calculated. Unlike the first set, the samples were not pre-dried. The samples were then submerged in water for 24 hours prior to starting the test. Due to the voids along the surface of the sample, each was prepared with a double sleeve. The testing apparatus for the second round of tests was the GDS systems machine. To reach a high level of saturation (B value greater than 80%), the cell pressure and backpressure were raised in steps no greater than 35 kPa, while the difference between the cell and backpressure was never more than 35 kPa. Backpressures of 900 kPa were required to reach high B values. The cell and backpressure were then reduced allow for testing, once again ensuring that the difference between them did not exceed 35 kPa. The B-value was checked at the test backpressure, and then the cell pressure was increased to the desired testing pressure while the backpressure remained constant. Each sample was consolidated for approximately 20 minutes. The samples

was then loaded at a rate of approximately 0.01 %/minute until 10% axial strain had occurred. Samples were then removed from the apparatus and photographed.

#### 4.2.5.4 Triaxial set No. 2 results

The results for Set #2 are summarized in Table 4.3. Figure 4.15 and Figure 4.16 show the deviatoric stresses and volume change up to 10% strain, respectively. Figure 4.17 shows the effective stress Mohr Circles averaged over 8 to 10%.

Table 4.3. Triaxial Set #2 test results.

Test #	$\rho_{\text{test}}$ [kg/m <sup>3</sup> ]	B-value at test	Axial pressure [kPa]	Cell pressure [kPa]	Back pressure [kPa]	$\sigma'_1$ [kPa]	$\sigma'_3$ [kPa]
6	392	0.89	441	891	787	545	104
7	407	0.74	261	905	598	568	308
8	401	0.88	159	900	398	662	502
9	390	0.83	373	701	498	576	203

During each test, the B-values were checked with a backpressure of 900 kPa, with each value greater than 90%. The B-values at the test backpressure were measured over a period of 10 minutes, with the value at 2 minutes as per the ASTM (ASTM 7181) being presented. Over the wait period, the backpressure continued to rise, with all values exceeding 90% by the end of 10 minutes.

Results shown in Figure 4.15 indicate similar results from Set #1. Tests #6 and #7 show a peak strength with a sudden loss, followed by a gradual increase to a residual strength. Test #9 shows a near linear increase in strength until yield and a near constant residual strength. Test #8 does not show typical behaviour. The effective confining stress ( $\sigma'_3$ ) for this test was 500 kPa, which is 50% of the ideal unconfined compressive strength. During the cell pressure increase leading up to the test pressure, the sample visibly crushed along the top surface, as shown in Figure 4.18. Similar to Set #1, the deviatoric stresses general increased post-yield up to a residual strength, which varied with strain.

The effective stress Mohr Circles shown in Figure 4.17 show a similar behaviour to those in Set #1. In general, the maximum shear stress decreases with confining pressure. In addition, the Mohr Circles in Set #2 tend to be smaller than the Set #1 results for the same confining stress.

Results from the second set of triaxial tests did not address some of the questions raised from the first set. The issue of decreasing strength with confining stress remains, implying that the saturation level and strain rate have little to no effect on behaviour. In order to reach high saturation levels, unrealistically high backpressures were required. A backpressure of 900 kPa represents over 90 m of head in a water table, which is significantly higher than most project applications. Given the issues with the backpressures and saturation, a third set of triaxial tests were conducted.

#### 4.2.5.5 Triaxial set No. 3

The third set of triaxial tests used the GDS apparatus and test methodology similar to the second set. Given the issues with high backpressure for saturation that Set #2 experienced, this test set limited the backpressure to 100 kPa. In general, the methodology used for Set #3 was the same as per Set #2. The major difference was that the backpressure and cell pressure were raised by increments of 25 kPa to a maximum backpressure of 100 kPa, where a B-value measurement was taken. The cell pressure was then increased to the testing pressure.

#### 4.2.5.6 Triaxial set No. 3 results

The results for Set #3 are summarized in Table 4.3. Figure 4.19 and Figure 4.20 show the deviatoric stresses and volume change up to 10% strain, respectively. Figure 4.21 shows the effective stress Mohr Circles averaged over 8 to 10%.

Table 4.4. Triaxial Set #3 test results.

Test #	$\rho_{\text{test}}$ [kg/m <sup>3</sup> ]	B-value at test	Axial pressure [kPa]	Cell pressure [kPa]	Back pressure [kPa]	$\sigma'_1$ [kPa]	$\sigma'_3$ [kPa]
10	416	0.05	379	201	97	477	101
11	400	0.04	262	301	97	466	204

As per the other listed results, the stresses are averaged from readings taken between 8 and 10 % strain. The B-values for both tests were 0.05 or less, indicating very low saturation. Results shown in Figure 4.19 indicate elastic and post-yield behaviour similar to the previous tests. Neither the yield point nor the residual strength appear to be dependent on the confining stress. The results of the Mohr Circles (Figure 4.21) for this set are similar to set #2, and indicate smaller maximum shear stresses per confining stress from set #1. Given the results of the first two tests in this set, further tests were abandoned.

#### 4.2.5.7 CD triaxial test summary and conclusions

Results of the CD triaxial tests conducted on the 1 MPa, 75% void content cellular grout indicated unexpected behaviour. Test methodologies considering the effects of drying, saturation, and backpressure were varied in an attempt to determine the conditions affecting the behaviour. In all cases, the yield and residual strength of the material did not indicate the typical trend of increasing magnitudes with increasing confining stress.

The Mohr Circle plots indicate a reduction in maximum shear stress with increasing confining pressure. This implies a mechanical reaction to either pre-loading or straining causing a change in the physical properties. One possibility is that high backpressures are creating micro-cracks within the cellular grout. The voids within the grout are partially connected, with those unconnected having thin grout walls. High back pressures will break these grout walls around unconnected pores causing a reduction in strength. Figure 4.22 shows the maximum shear stress compared to the maximum backpressure experienced during saturation and consolidation phases. In Set #2, each sample was brought to approximately 900 kPa backpressure prior to bringing them to the test pressure. In test Set #3, the maximum backpressure was limited to 100 kPa, which was assumed to limit the possible damage. In both test sets, the same reduction in shear strength was observed, implying that the possible micro-cracking may have affected the results, but another phenomena is required to describe the observed behaviour.

### 4.3 Summary and discussion

Design considerations for structures in swelling rock are fairly unique. Potential strains from the rock are monotonic and typically occur over the span of months to years. Once initiated,

the rock mass strains are economically impractical to stop and necessitate proper engineering solutions in order to protect the built structure. This research study has explored two potential swelling strain mitigation materials: EPS foams and cellular grout. Past research into these materials has not considered the effects of slow strain rate on the material behaviour.

When compared to the minimal values for stress and strain at 5 % and 10 % provided in ASTM D6817, the reduced strain rate appears to have minimal impact on elastic modulus and yield strength for EPS 39. For EPS 22, the elastic modulus appears deviate minimally from the ASTM standard, while the yield strength is reduced by approximately 17 %. This indicates that material behaviour under low strain rates may be affected by EPS density. When looking at post-yield behaviour, the reduction in strain rate resulted in a noticeable reduction in post-peak elastic modulus. Generally, the lower the strain rate the lower the modulus with the material behaviour approaching linear-elastic perfectly plastic.

Future research into using EPS foams for this application includes testing the material under confined conditions using a triaxial cell to determine effect on the yield and elastic modulus. Long-term creep tests including measuring the load imparted on the bearing side will identify how the material reacts to the rock stress imparted on the EPS and how the stress is transferred to the structure. With the observed reduction in strength in the lighter EPS foam under low strain rates, additional testing of foam densities is recommended.

Cellular grout has a good potential for the mitigation of swelling strains. The crushable behaviour indicates that it can prevent significant amounts of stress from the swelling rock reaching the structure. Unlike the EPS foams, the post-peak behaviour under uniaxial loading indicated stress-softening behaviour. Triaxial test results show a material behaviour similar to loose sands, with no peak strength.

Uniaxial test results indicate that the low strain rates result in a reduction in the elastic modulus, but have negligible affect on the strength. This study looked at the effects of confinement and saturation of a grout with 75 % void ratio with a low strain rate. Triaxial results are difficult to interpret. The Mohr Circle plots do not follow conventional behaviour as the maximum shear strength decreases with increasing confining pressure. Test results indicate that the

cellular grout is behaving as a three-phase material, with the solid, liquid, and gas/air phases presenting difficult to interpret results.

Observation from visual inspection of the samples shows that not all of the voids were connected, and that void size varied. As the backpressure or pore pressure increases, the non-connected voids would have experienced high pressures along their cell walls. This would likely lead to micro-cracking, which would decrease the strength of the sample. This effect would have to be balanced with the cell pressure – pore pressure behaviour that typically results in higher strength at higher confinement. Additional work need to be done to understand this behaviour.

Ameer et al. (2015) observed that unifying the void size increased the average strength and decreased the variation in strength per batch. That study considered void ratios up to 36%, much lower than this study. Since the void ratio, void size, and void connectivity of the tested cellular grout are likely contributors to the observed behaviours, additional work is required to further understand their influence. Studying various mixes with controlled void size, variation in void sizes, and interconnectivity of the voids and the resulting behaviour under confined conditions is recommended. An effort should be made to see how well a mix can be made to maintain the requested void characteristics through a sample. Methods outlined in Ameer et al. (2015) provide a starting point in such works. Given the sudden loss of strength after yeild, a study looking at the void wall collapse during loading would provide insight into the mechanical behaviour of the grout. This would involve terminating a series of tests at the yield point and at select stresses past the yield and using non-destructive methods to identify the void wall integrity at the yield location. Although tension is an unlikely scenario in underground excavations, the tensile behaviour of high porosity grout should also be explored.

Consideration for engineering QA/QC is required as the goal is to provide a practical and constructable material for the mitigation of swelling rock.

The high backpressures (900 kPa +) required for saturation of 80% or more observed in triaxial set #2 are unrealistic considering practical engineering. This would be equivalent of a tunnel under 90 m of groundwater pressure, which is greater than most non-mining applications.



Future work should look at the behaviour in a semi-saturated state, with long term soaking with appropriate backpressure.

The observed decrease in shear strength with increasing confining stress presents an engineering problem: what strength parameters can be used for design? If the expected design confining stress can be isolated to a narrow window, representative tests can be run to identify the resulting strength. For complex stress paths, advanced models will have to be developed.

#### 4.3.1 Design recommendations

Several design recommendations and considerations can be discussed based on the testing results and material behaviour. Typical design using EPS foam as a protective material is to limit the strain to 10 % or less in order to contain the behaviour within the linear-elastic zone. This is advantageous for applications involving swelling clay soils as multiple swelling/receding cycles can be expected over the lifetime of the structure. With the monotonic behaviour of swelling rock it may be advantageous to limit the material to 35 % strain or less. By exceeding the yield point but limiting deformations to prevent strain-hardening, the design can achieve saving by applying a thinner EPS layer. This would save material and excavation costs. Since EPS is pre-cast into boards the material is best suited for flat walled excavations such as rectangular shafts.

Cellular grout has significant design potential and is a preferred material amongst consulted contractors. The abilities to form a desired shape, fill voids, and control the material behaviour via mix composition were stated as major contributors in material selection. Design recommendations include conducting a suit of triaxial tests under a series of backpressures representing the expected range of porewater pressures to derive the material properties. Uniaxial tests should be conducted according ASTM C495/C495M-12 (at 28 day strength) to verify mix design. Additional UCS tests should be conducted at a low strain (0.1 strain/min or less). The curing time effect on strength and elastic modulus should also be considered when using cellular grout. Installation of the grout will always occur while the rock swells, and the grout will undergo stresses and strains prior to fully curing.

The bouyancy of both EPS foams and cellular should be considered. Both materials are lighter than water and buried structures can safely be assumed to be submerged during at least part

of their life span. Any potential loads from the bouyant materials should be a design consideration.

Design staging should also be considered when using these materials. The material must be balanced between providing mitigation from swelling rock but withstand all expected loads throughout the construction and life span.

## 4.4 Figures

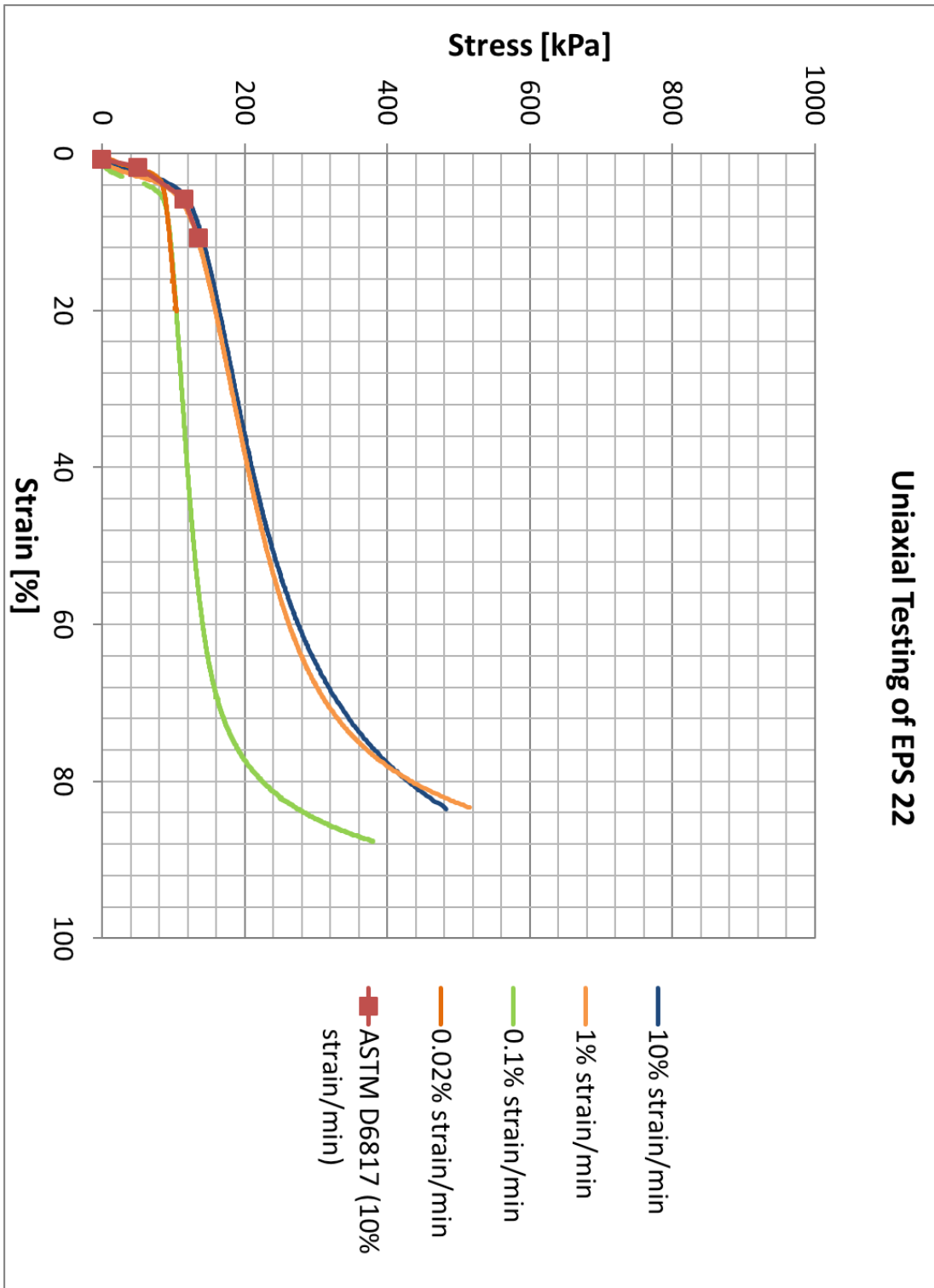


Figure 4.1. Results of uniaxial compression tests with variable strain rate on EPS22 geofoam.

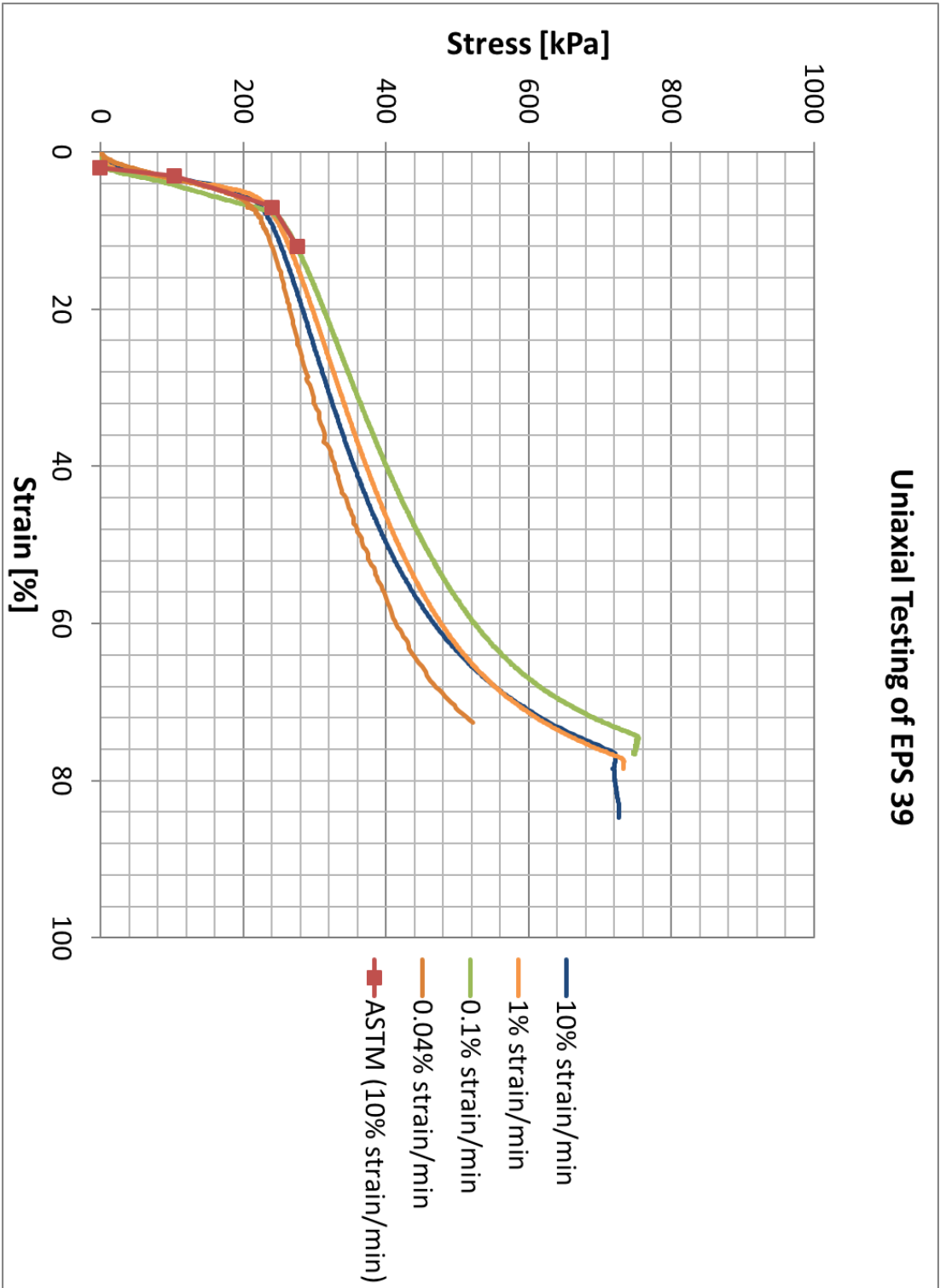


Figure 4.2. Results of uniaxial compression tests with variable strain rate on EPS39 geofoam.

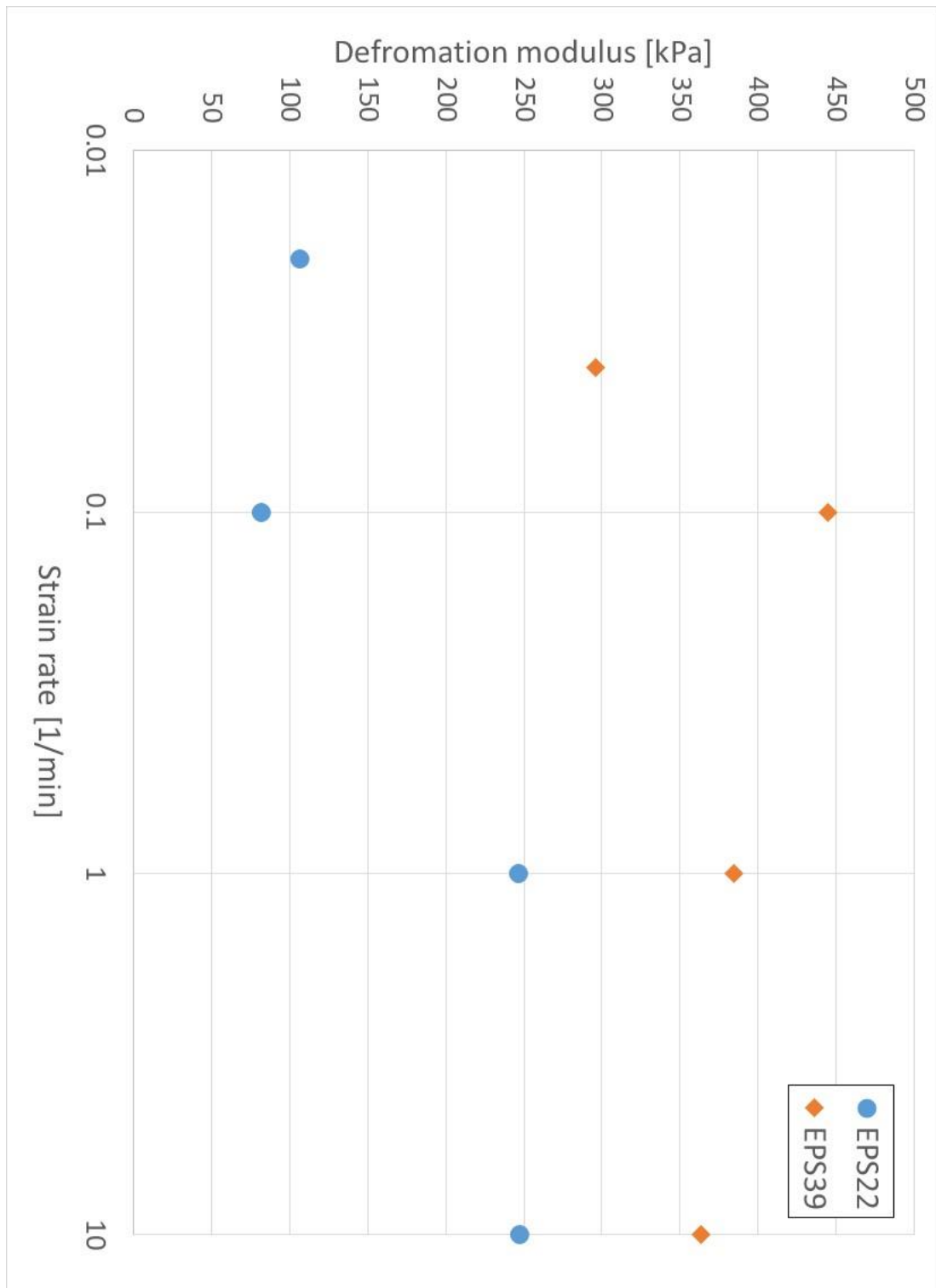


Figure 4.3. Deformation modulus based on strain rate in post-elastic zone.

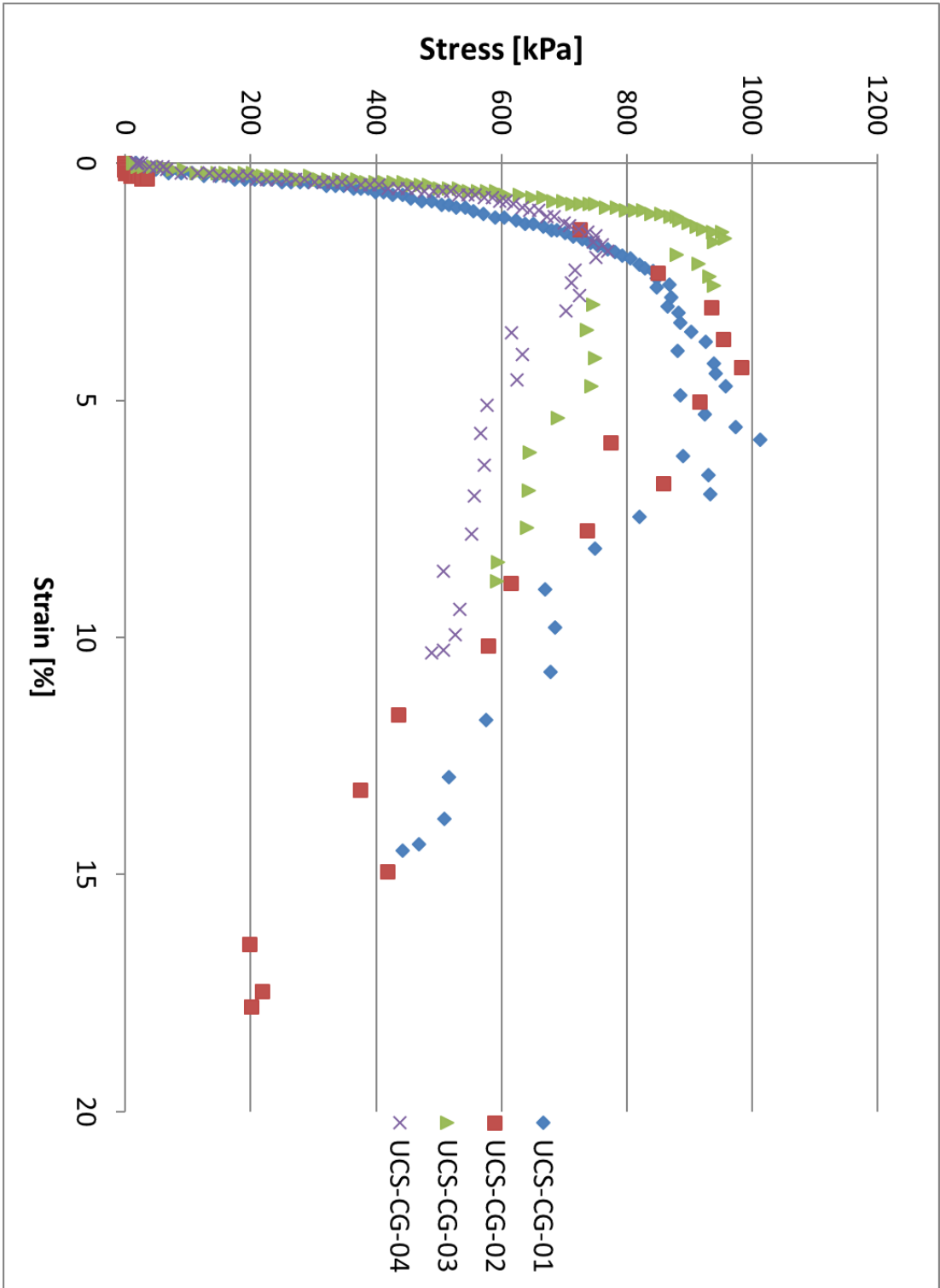


Figure 4.4. Results of ASTM UCS tests on cellular grout.



(a)



(b)

Figure 4.5. Typical pre (a) and post failure (b) UCS test results.

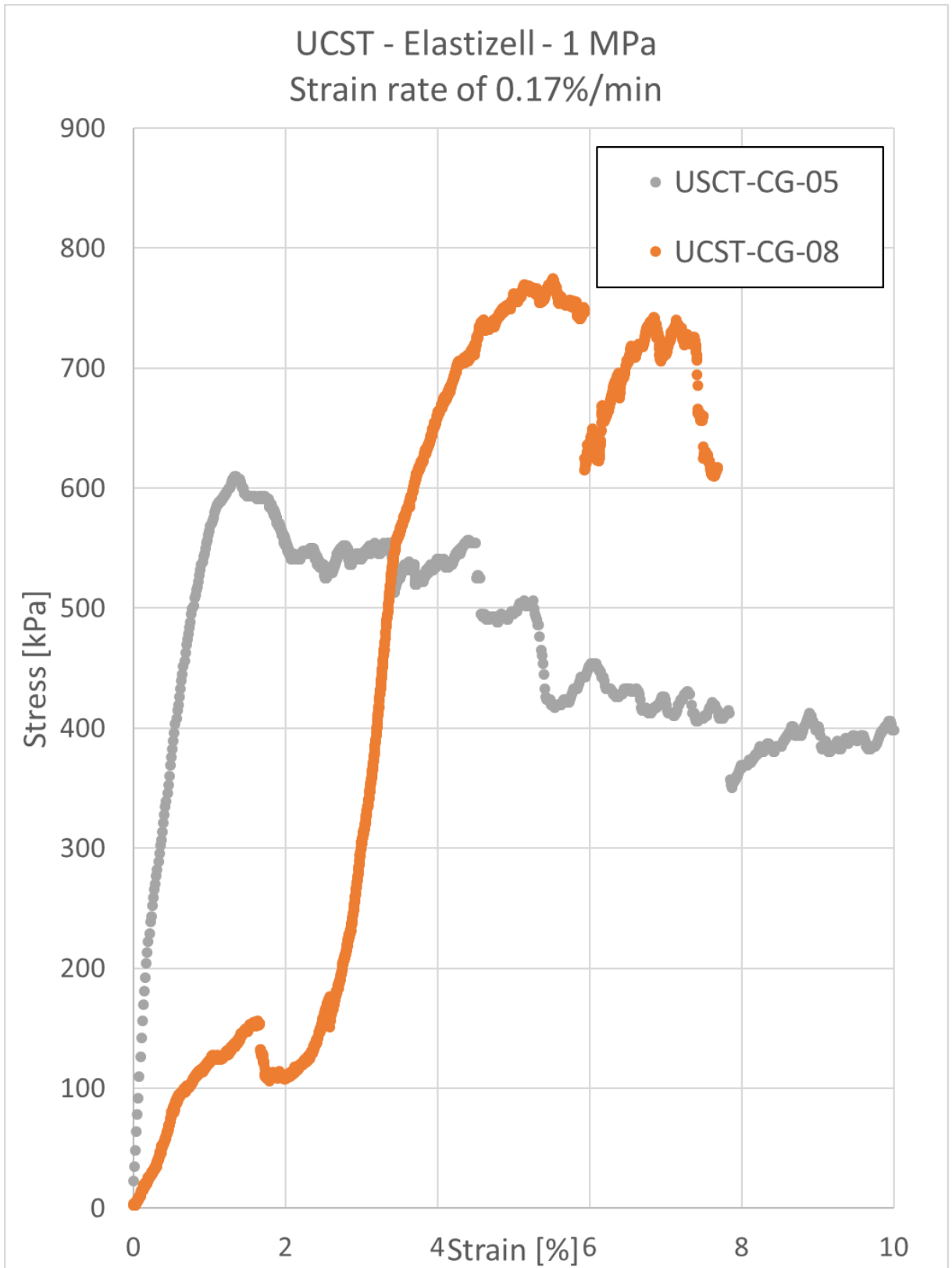


Figure 4.6. UCS test results for strain rate of 0.17 %/min.



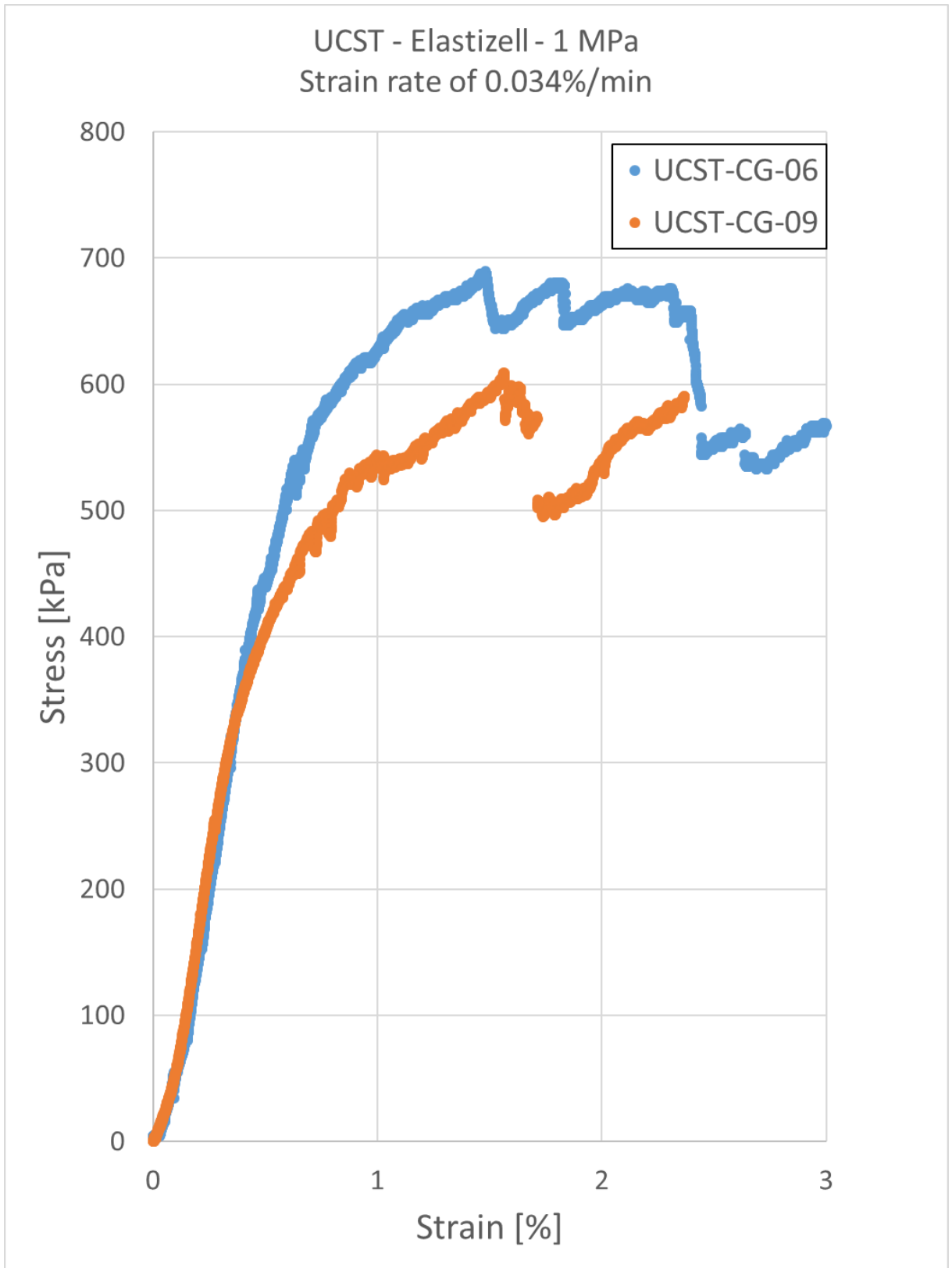


Figure 4.7. UCS test results for strain of 0.034 %/min.

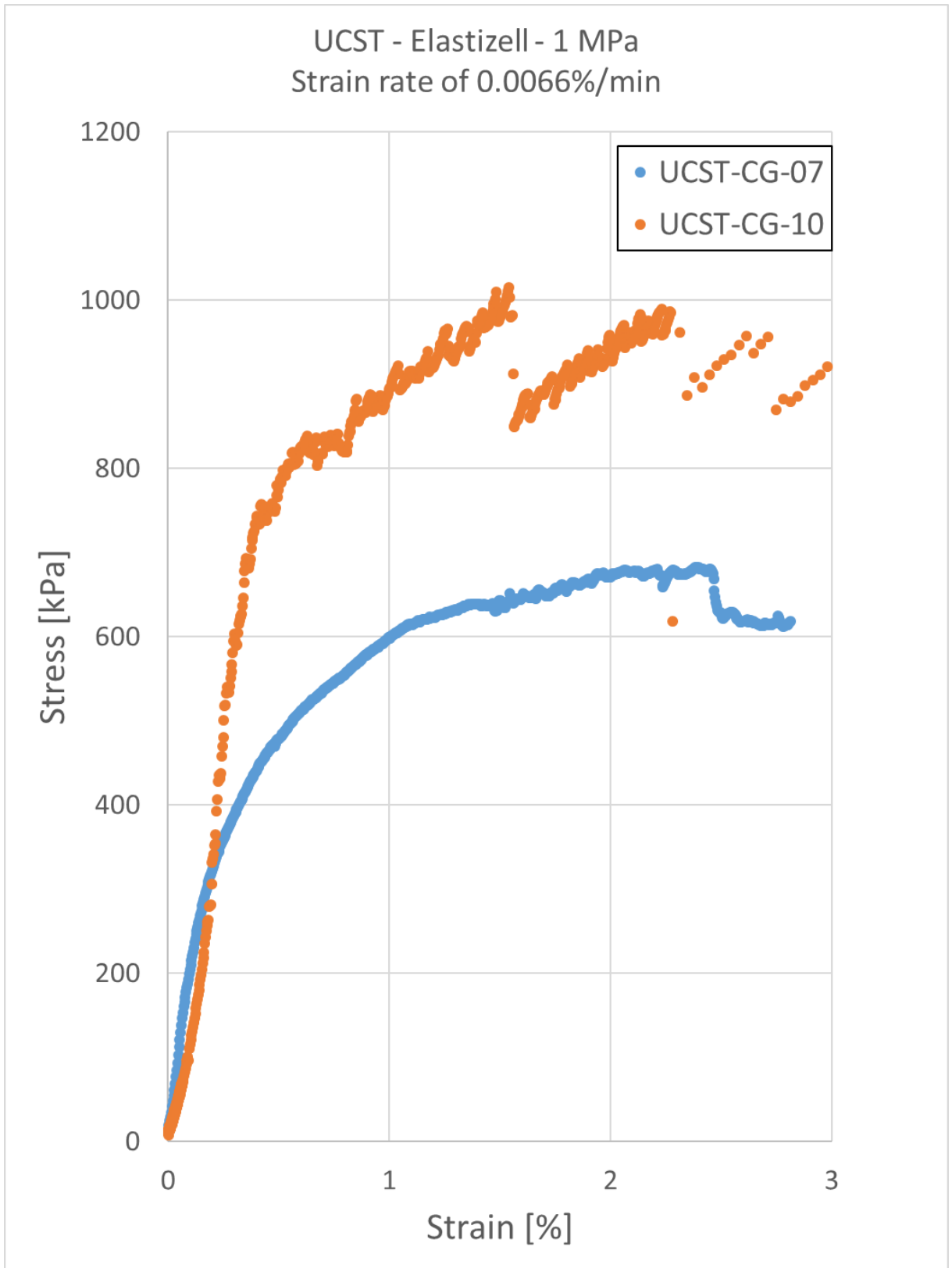


Figure 4.8. UCS test results for strain rate of 0.007 %/min.

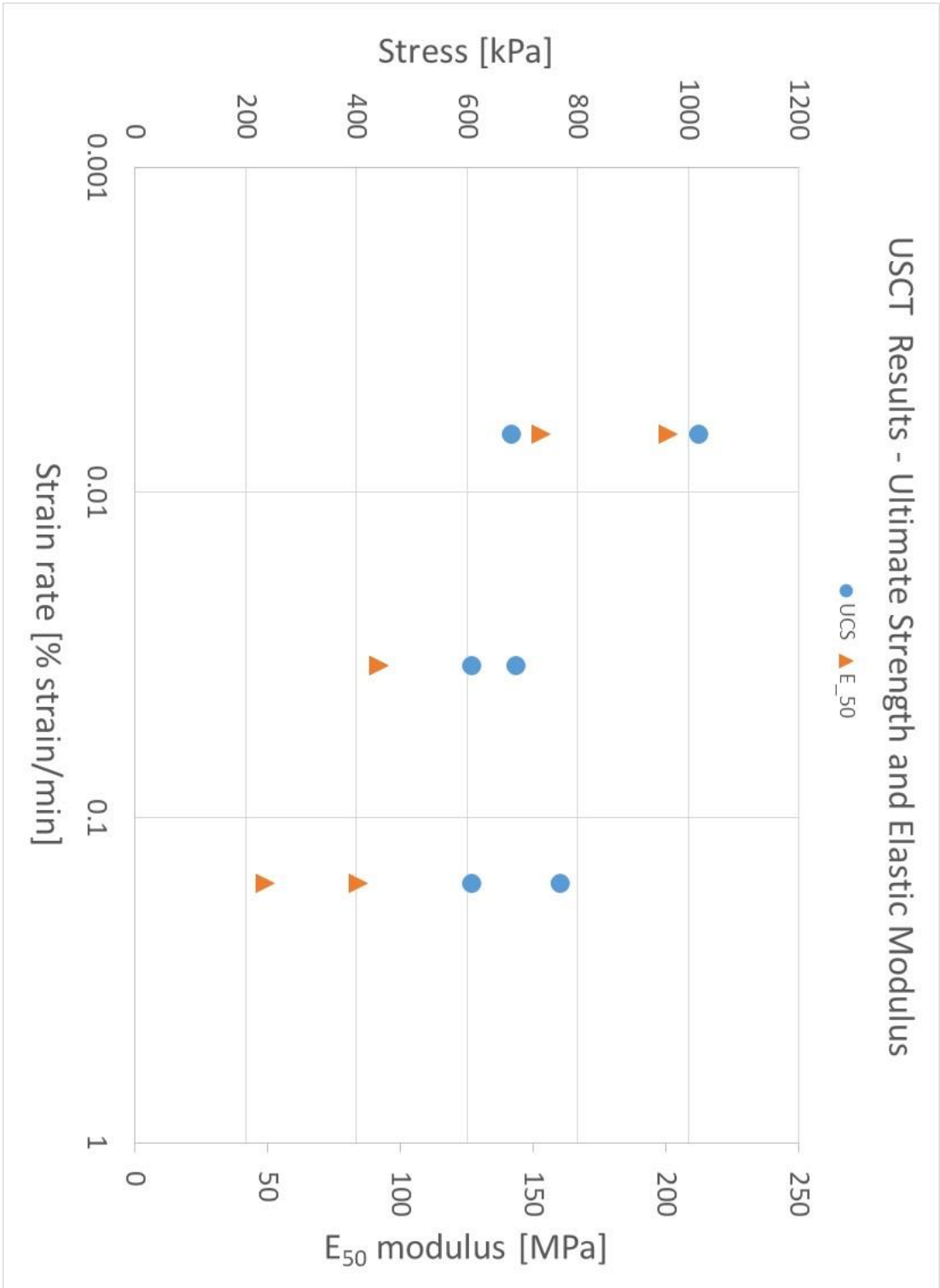


Figure 4.9. Ultimate strength and E<sub>50</sub> modulus from variable strain rate UCS tests.



(a)



(b)



(c)

Figure 4.10. Typical triaxial samples (a), test set-up (b), and post-test results (c).

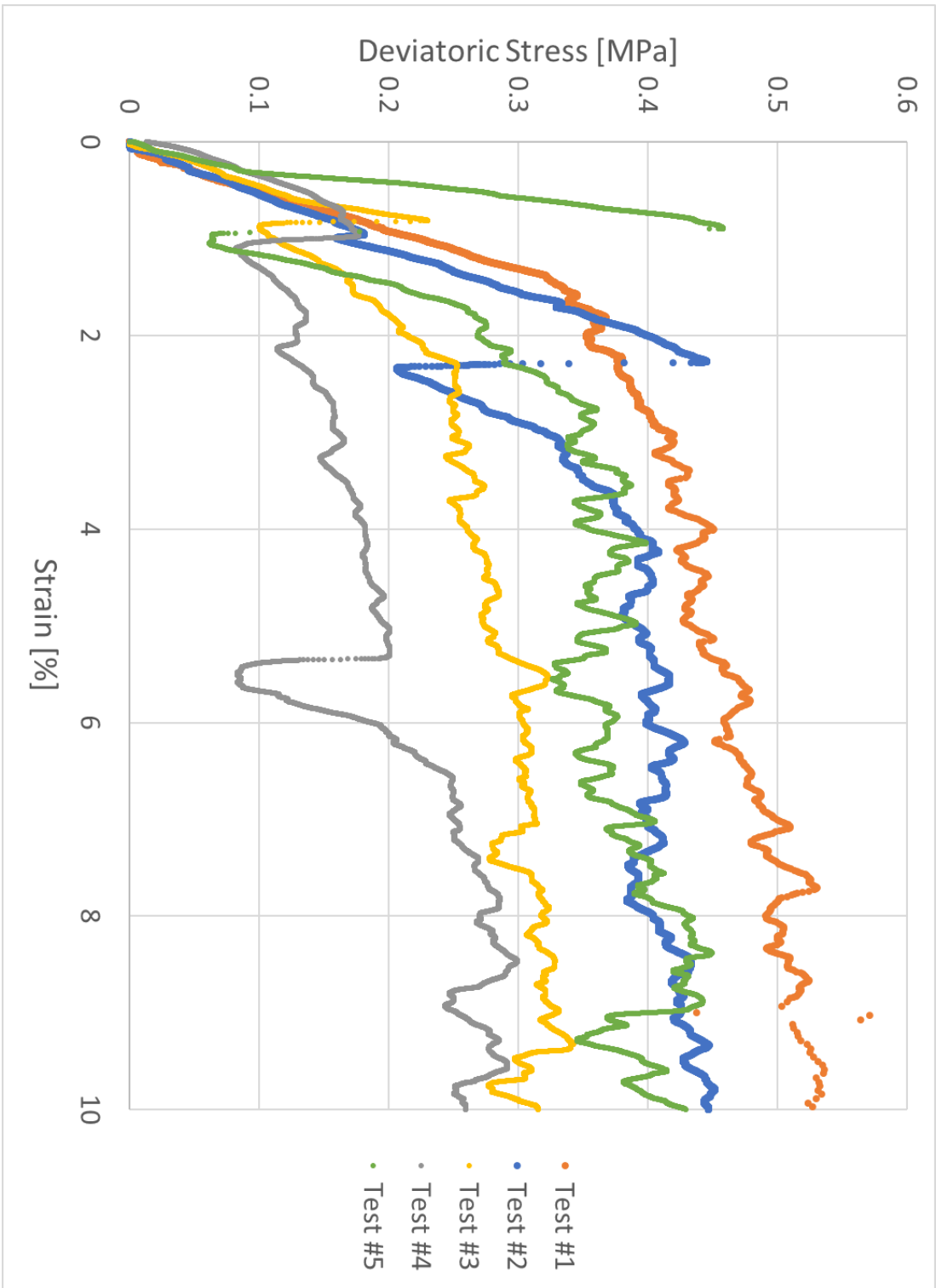


Figure 4.11. Deviatoric stresses for Set #1.

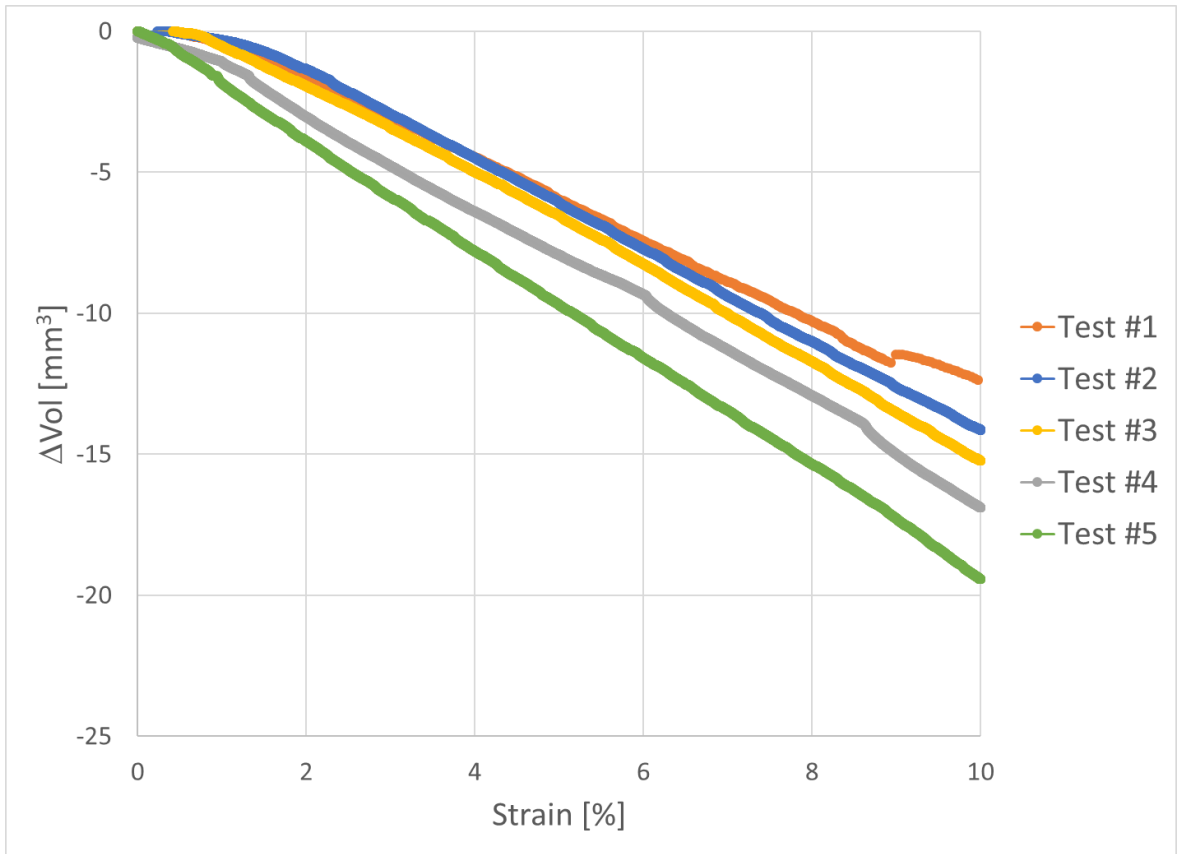


Figure 4.12. Volume change during shearing in Set #1.

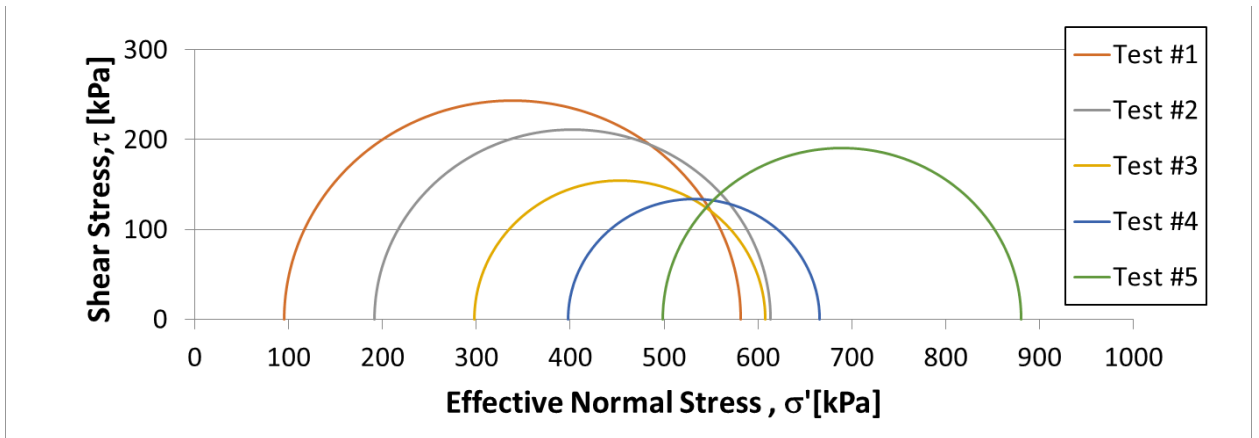


Figure 4.13. Mohr's circles for residual strength in Set #1.

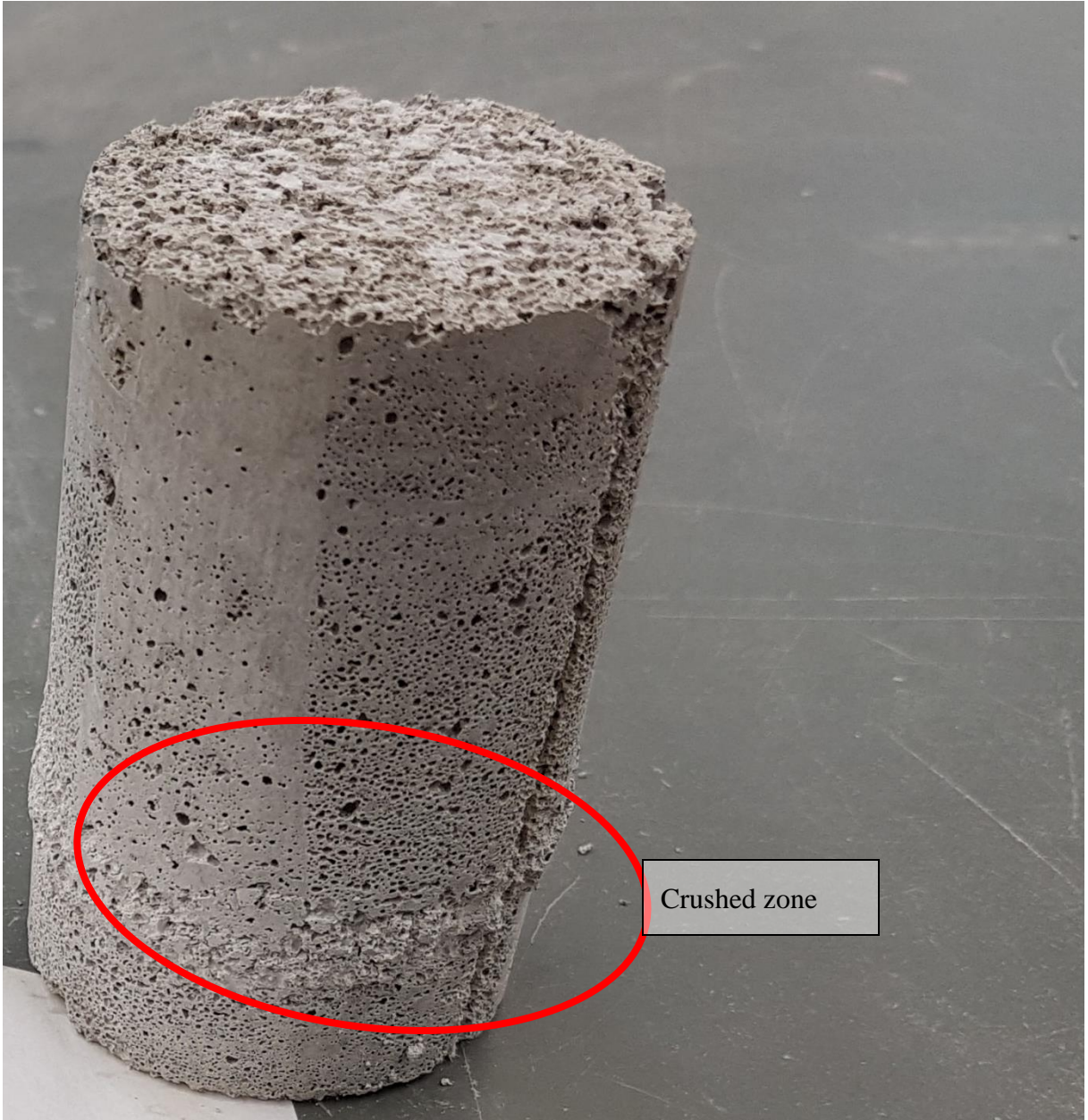


Figure 4.14. Post-test sample showing crushed zone.

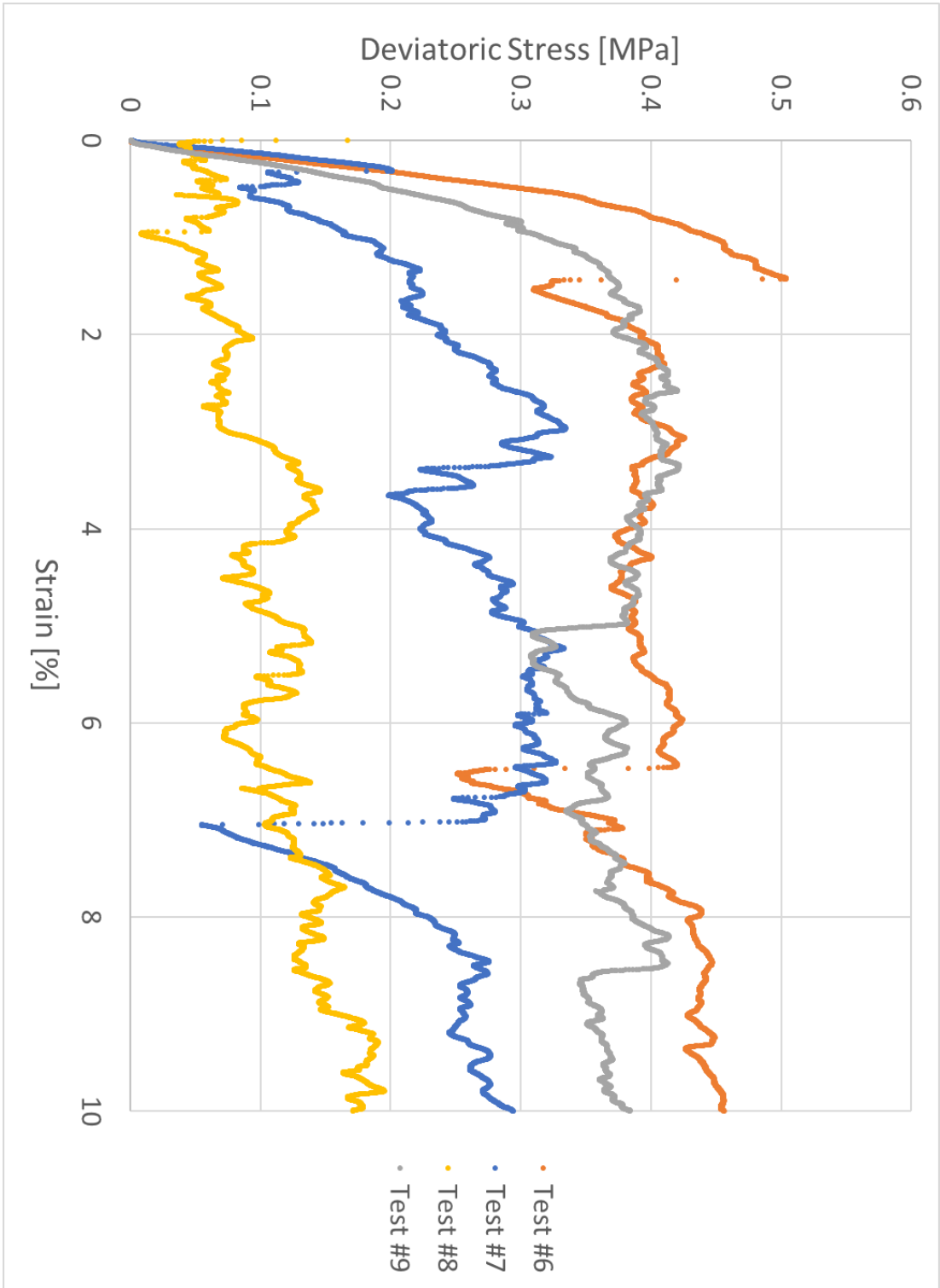


Figure 4.15. Deviatoric stresses for Set #2.



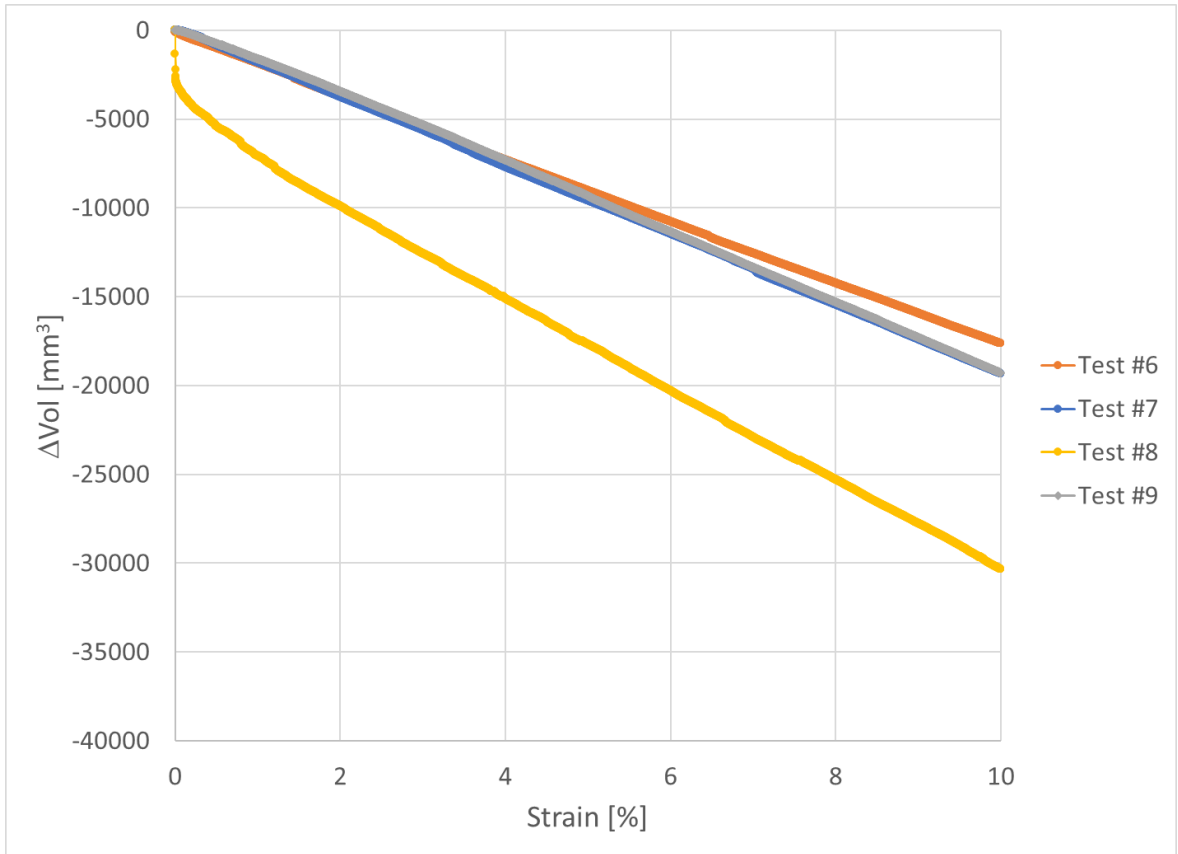


Figure 4.16. Volume change during shearing in Set #2.

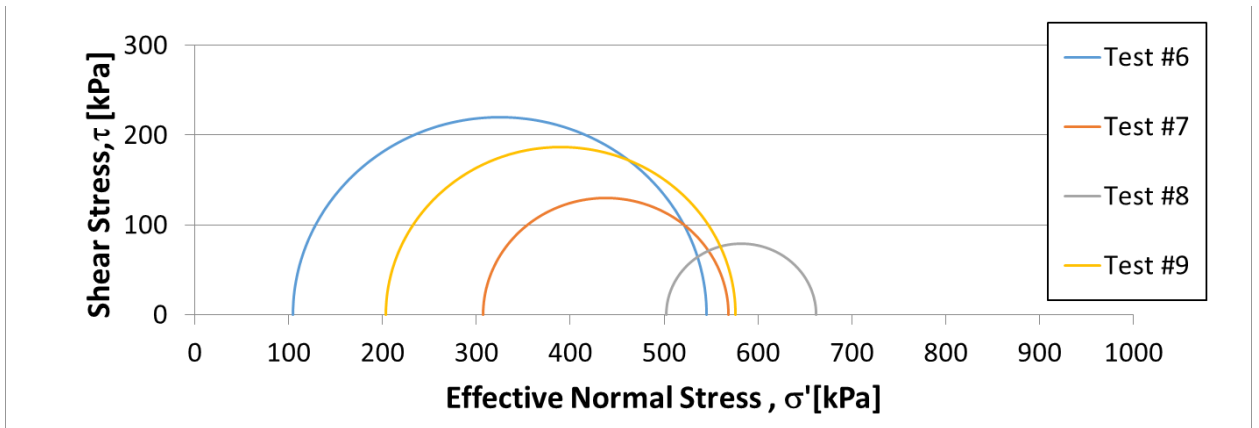


Figure 4.17. Mohr's circles for residual strength in Set #2.

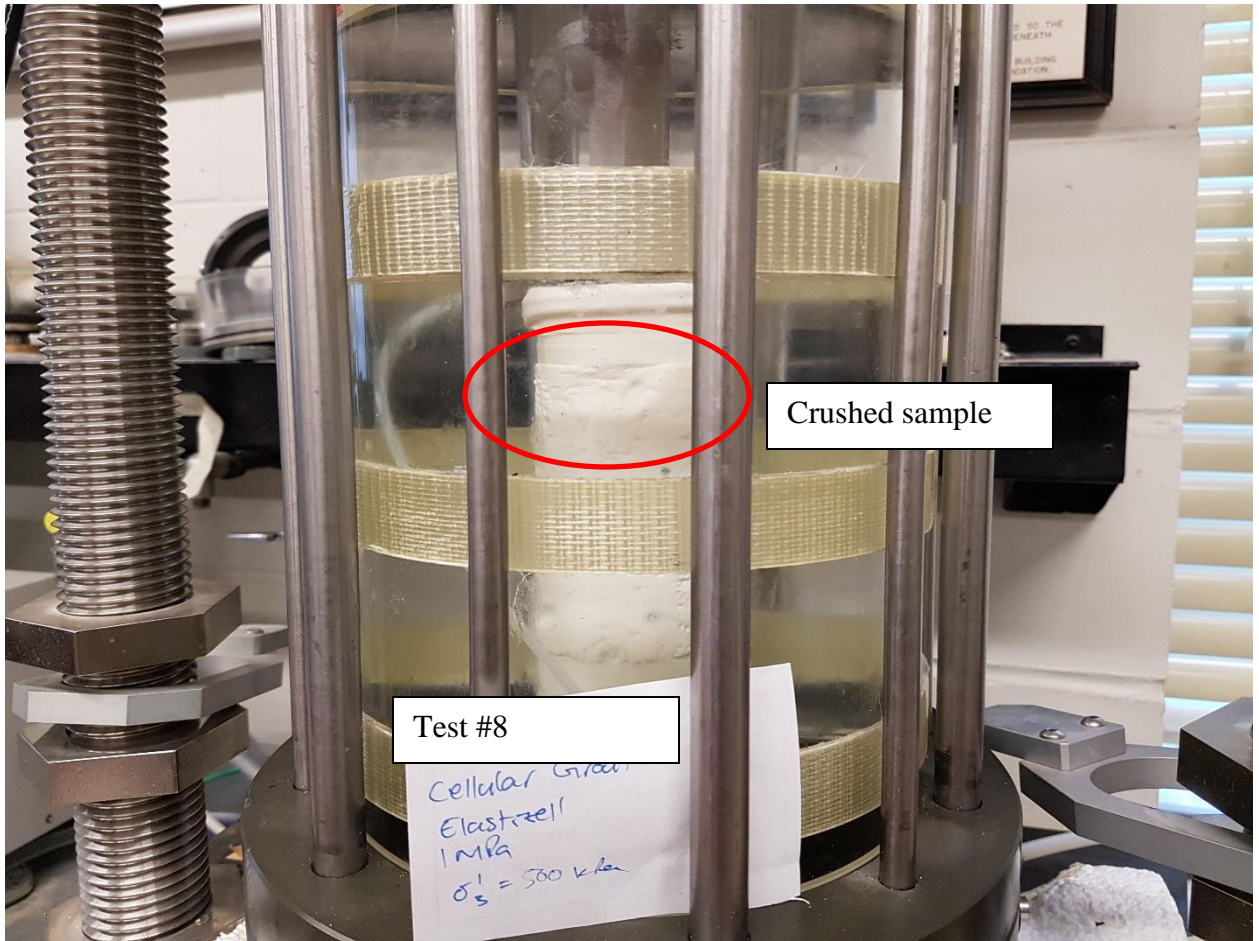


Figure 4.18. Test #8 with a crushed portion of cylinder due to cell pressure of 500 kPa.

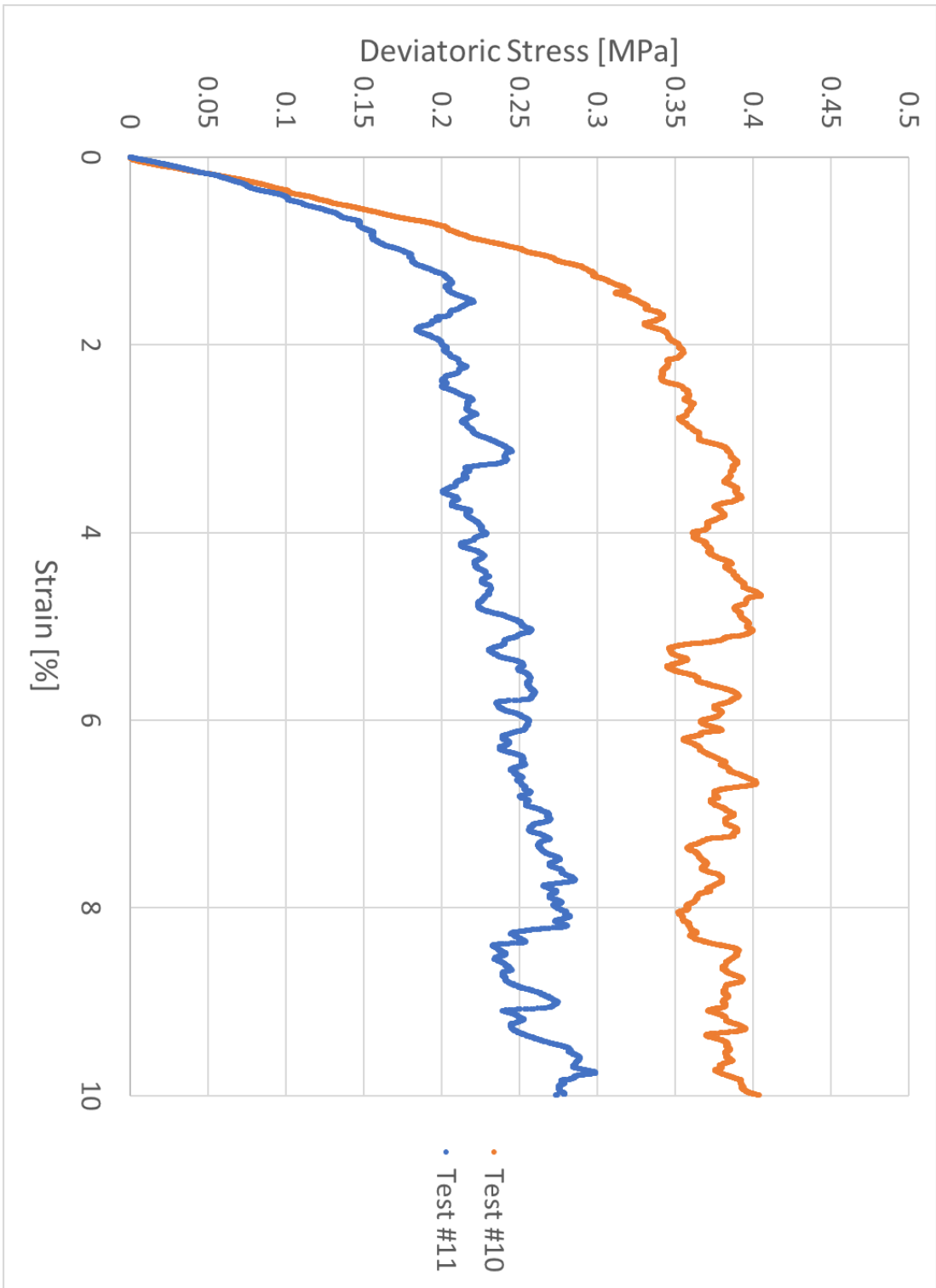


Figure 4.19. Deviatoric stresses for test set #3.

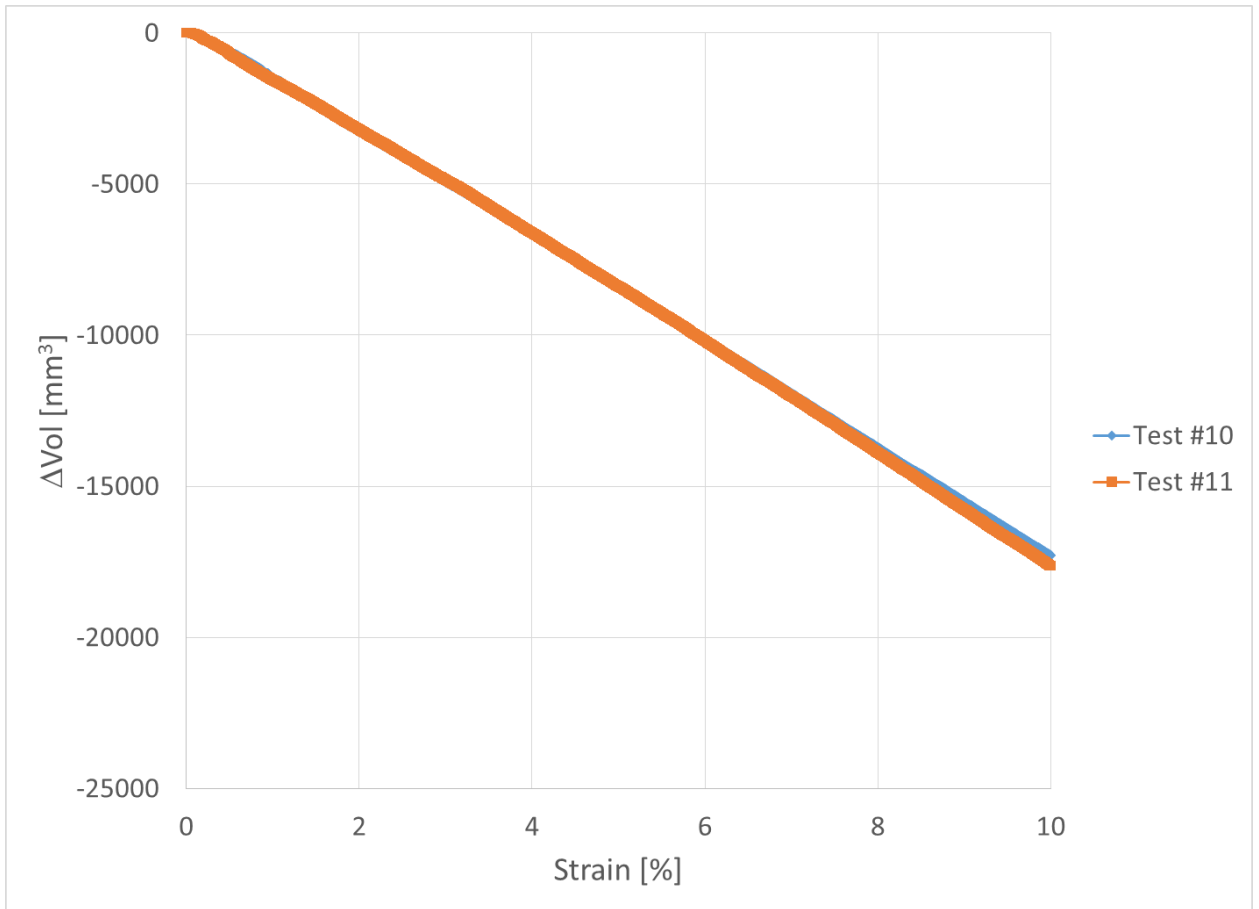


Figure 4.20. Volume change during shearing in test set #3.

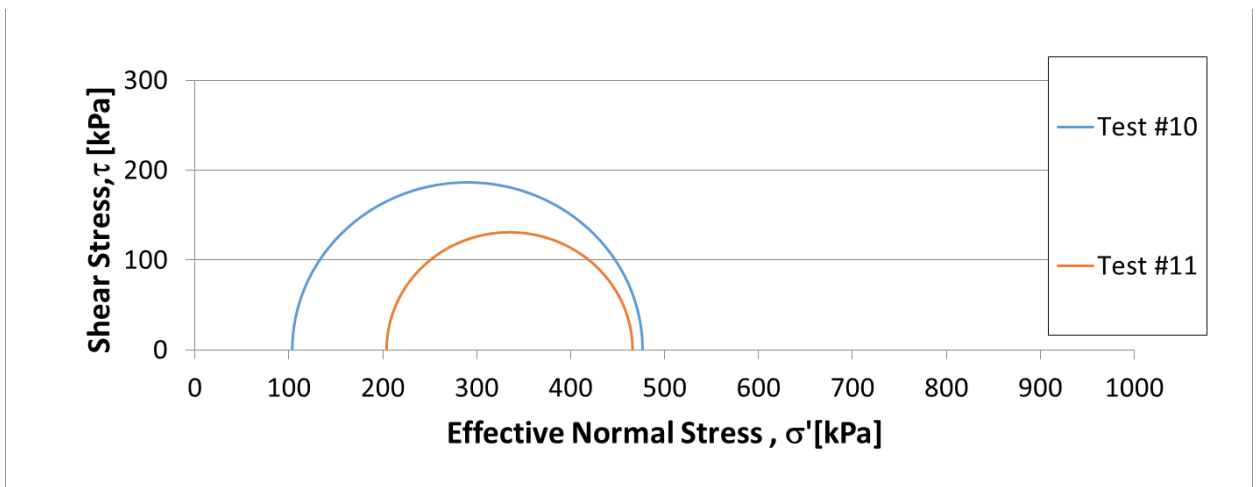


Figure 4.21. Effective stress Mohr Circles for test set #3.

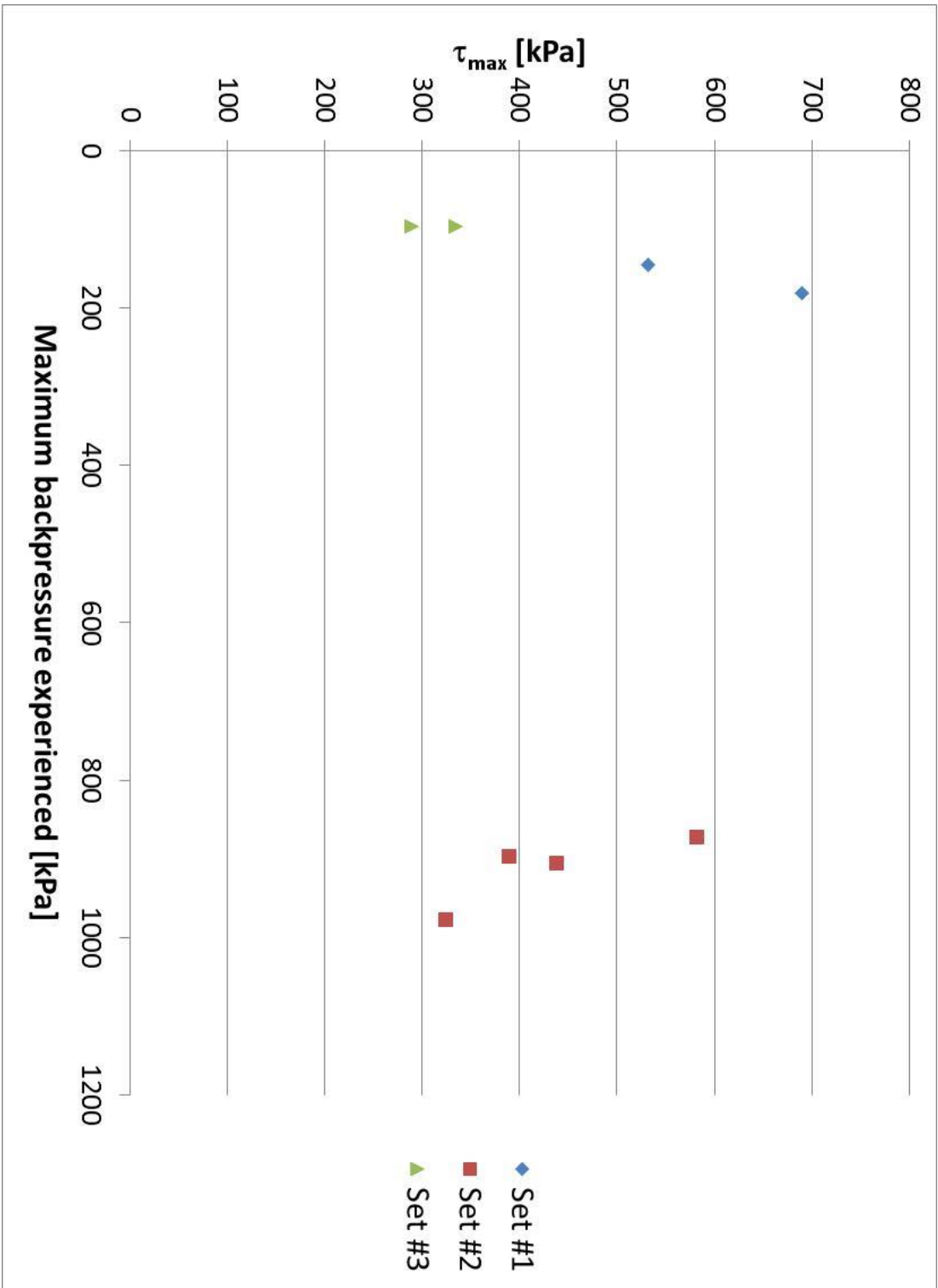


Figure 4.22. Maximum shear stresses per backpressure.

## Chapter 5

### 5 Case study of circular excavations in swelling rock – Zone 1 Water Main Project

#### 5.1 Introduction

The Zone 1 Water Main (Z1WM) project in Burlington, Ontario comprises a series of tunnels and pumping stations that connects the Burlington Water Purification Plant to the Kitchen Reservoir and Pumping Station as shown in Figure 5.1. The project comprised a tunnel 6.3 km long and four vertical shafts. The entry shaft for the tunnelling works, located close to Highway 403, was approximately 13 m in diameter and 42 m deep and was supported by ribs and lagging into the rock. Excavation of the shaft began in August 2015 and reached final depth at the end of October of the same year. The rock face was protected with shotcrete and mesh. The tunnel was excavated with a 2.6 m diameter main-beam Tunnel Boring Machine (TBM) in the Queenston Shale, with 15 to 60 m of cover predominantly in rock. The tunnel rock was supported by a McNally Support System, which comprised a series of wood slats at the crown that are pulled from the TBM shield during advancement and secured to the tunnel roof utilizing straps and bolts. Figure 5.2 shows the slats and straps installed in the tunnel. Excavation of the tunnel north of the main shaft, where the tunnel monitoring section was located, began in July 2016 and the permanent tunnel structure was finished in May 2017. The anticipated completion of the project is April 2019.

Vancheri and Braczek (2014) identified the swelling rock as a potential risk to the tunnel and vertical shaft structures. The proposed solution was to encase the steel pipes of the tunnel and the shaft in cellular grout with a 28 day compressive strength of 2 MPa. This cellular grout has the capacity to resist the hydrostatic forces and is expected to limit the potential time-dependent strains and stresses acting on the steel liner. The tunnel will be analyzed to estimate the effects of swelling rock on the tunnel structure, including the mitigation from the 2 MPa grout. Therefore the main objectives of this paper are to evaluate the short term and long term behaviours of the tunnel and vertical shaft, and to characterize the effectiveness of cellular grout in mitigating the rock swelling effects.

The horizontal in-situ stresses were not measured at this site. Yuen et al. (1992) investigated the horizontal stresses in the Queenston shale for the tunnel project using hydro-fracturing and overcoring techniques, and reported horizontal stresses ranging between 9 and 23 MPa. The location of their tests were in Niagara Falls, where the Queenston Formation is located at significant depth (200m) rather than near ground surface. Grunicke et al. (2013) and Parras et al. (2015) identified the elevated horizontal stresses in the Queenston shale as the leading cause of the observed damage to the Niagara Tunnel Project.

As part of this study, a comprehensive site investigation was conducted involving field and laboratory investigations of the rock mass at the entry shaft, installation and reading of three inclinometers around the shaft, and monitoring of a tunnel section 50 m north of the shaft with two borehole extensometers installed at the spring line and a series of tape extensometer points located around the circumference of the tunnel. Figure 5.3 shows the shaft and inclinometers layout.

Figure 5.4 shows the shaft section. Figure 5.5 shows the monitoring instrumentation along the tunnel section.

Results from the monitoring program and laboratory tests will be used to perform an analysis to evaluate the time dependent behaviour of the shaft and tunnel. The analysis of the shaft data will be used to estimate the horizontal in-situ stress. Previous measurements in the Queenston shale in Niagara Falls, at depths of up to 200 m, indicate that the horizontal stress ranges between 9 and 23 MPa (Yuen et al 1992). The site of the current study is located at the bottom of the Niagara Escarpment, where the Queenston shale is at the ground surface. Therefore, in-situ stresses are expected to be different from those reported by Yuen et al (1992).

## 5.2 Geotechnical investigation

The project site is located in the Queenston Formation, an Ordovician period sedimentary unit that is a part of the Appalachian basin (Armstrong and Carter 2006). The unit is predominantly composed of soft red shale, with thin lenticular layers of harder siltstone and limestone. The formation is well known for its swelling characteristics (Lee and Lo 1993, Hefny et al. 1996, Al-Maamori et al. 2016).

### 5.2.1 Line Drilling and rock core logging

Ground surface at the site was at approximate Elevation 114 m. The soil deposit at the entrance shaft is less than 3 m thick and is composed of fill and reddish brown Halton Till. The standard penetration test (SPT) blow count, N, ranged between 7 to 30 in the Fill and 10 to 100+ in the till.

One borehole was advanced as part of the project geotechnical investigation and three more boreholes were advanced and logged by the author as part of the inclinometer installation to investigate the swelling behaviour of the Queenston shale. Borehole logs conducted by the author are presented in Appendix B. Weathered rock was encountered between 2.2 and 5 m from the surface in the initial investigation, with unweathered bedrock encountered at approximate Elevation of 108 m. The results of the geotechnical investigation indicated that the average Rock Quality Designation (RQD) of the Weathered and Sound rock was 57 and 85 %, respectively.

Three HQ size boreholes (96.1 mm ID and 63.5 OD) were drilled along the circumference of the entry shaft (at a distance of 1.2 m away from the shaft edge) approximately 120 degrees apart. Boreholes extended approximately 10 m below the bottom of the shaft. At the time of inclinometer installation, the upper 5 m of soil and rock were excavated and replaced with lean concrete for the beginning of the shaft excavation. Rock was encountered below Elevation 101 m and missed the upper weathered zone. Rock cores were extracted and the following details were recorded for the cores during the coring process: total core recovery, solid core recovery, fracture frequency, fracture orientation, fracture type (if applicable), fracture roughness, fracture weathering, infill, and RQD.

Observed RQD ranged between 22 and 100 %, with an average of 91%. The variation of RQD with depth is shown in Figure 5.6. The majority of discontinuities were bedding planes, with clean, rough surfaces. Some sub-vertical joints were also encountered, along with the occasional thin clay infill layer. Grey limestone layers were encountered and ranged in thickness between 10 mm and 100 mm.

At approximate Elevation 65 m, below the base of the shaft, each borehole encountered the conformable gradational contact with the Georgian Bay Formation. The grey Georgian Bay



formation composed the remaining portion of the boreholes (approximately 5 m) and was composed of grey shale with a significant number of limestone layers.

## 5.2.2 Laboratory testing conducted for this study

Samples were taken from the inclinometer boreholes at various depths and were prepared for transportation to the geotechnical laboratories at the University of Western Ontario. The samples photographed dry, then wetted and photographed again. If still wet, the sample were dried with a rag, wrapped in plastic wrap, and then firmly wrapped in electrical tape. Each sample was then wrapped in bubble-wrap before being placed in a 100 mm diameter PVC pipe. Pieces of soft lumber were placed on the ends of the sample and compressed using a clamp. The samples that were not immediately prepared for testing were encased in wax at the laboratory. The laboratory tests included UCS and elastic modulus tests and a suit of swell tests composed of six Free Swell tests, three horizontal Semi-Confined Swell tests, two vertical Semi-Confined Swell tests, one horizontal Null Swell tests, and three vertical Null Swell tests.

### 5.2.2.1 Uniaxial compressive strength tests

Several UCS and elastic modulus tests were conducted, but only one vertical test provided acceptable results. Multiple attempts at re-coring horizontal samples were made; however, the samples broke along the bedding planes.

The samples were tested according to ASTM D7012 Standard Test Method for Compressive Strength and Elastic Moduli of Intact Rock Core Specimens under Varying States of Stress and Temperatures. Core samples were unwrapped in the lab and photographed. The desired test section was identified and marked. The sample was then cut using a diamond saw to ensure smooth, even, parallel faces, with a minimum length to diameter ratio of 2:1. After cutting, samples were immediately measured and weighted in order to determine its density. A piece of the core adjacent to the sample was collected in order to perform a moisture content test. Four 10 mm strain gauges were attached to the samples; two vertical gauges and two horizontal gauges were used in order to evaluate elastic modulus and Poisson's Ratio. The tests were conducted using the MTS hydraulic compression machine. Strains and stresses were recorded using a Sciometric Series 7000 data recorder with an accuracy of  $\pm 1$  %. The tests were

conducted utilizing a strain rate of 0.05 mm/min in order to reach failure within the time specified by the standard.

The results obtained from the UCS test are shown in Figure 5.7. These results indicate that the  $E_{50}$  modulus is 14000 MPa, the UCS is 23 MPa, and the average Poisson's Ratio was 0.17. The test set up and the specimen after failure are shown in Figure 5.8. As shown, the failure modes appear to be a mix of axial and shear failures.

#### 5.2.2.2 Swell tests

The swell tests conducted as part of this study included: six Free Swell Tests (FST), three horizontal Semi-Confined Swell Tests (SCST), two vertical SCST, three vertical Null Swell Tests (NST), and one horizontal NST. As per the UCS tests, many horizontal tests were attempted and were damaged during re-coring. Descriptions and details of each test are provided below.

For each test sample, the core samples were unwrapped and the desired section was identified and marked. Samples for FST and vertical SCST and NST were re-wrapped with plastic wrap and electrical tape and then cut to the desired length using a diamond saw. Samples for horizontal SCST and NST were cored using an BQ (36.4 mm ID) diamond tip bit. Portions of the core adjacent to the test samples were collected to perform ancillary tests for moisture content, salinity, and calcity content.

Test samples were taken from core retrieved between Elevations 85 and 71.5 m. Samples taken at 85 m depth were chosen as representative of the unweathered rock in the midpoint of the shaft depth. Lower samples were chosen between approximately two times the diameter of the tunnel above and below the tunnel springline as representative of the rock mass affecting the tunnel behaviour.

Free swell test results are shown in Figure 5.9, which include the recorded horizontal and vertical swelling potentials. Results indicate the vertical free swelling potential ranges between 0.43 and 0.63% strain/log cycle of time, with an average value of 0.50% strain/log cycle of time. In the horizontal direction, the free swell potentials ranged between 0.17 and 0.36% strain/log cycle of time, with an average value of 0.24. Figure 5.10 shows the horizontal and

vertical semi-confined swell test results. Figure 5.11 summarizes the NST results. In general, the swelling potentials are within known ranges of 0.03 to 0.34% strain/log cycle of time and 0.14 to 0.54 %strain/log cycle of time in the horizontal and vertical directions, respectively. (Lee and Lo 1976, Hefny et al. 1996, Al-Maamori et al 2014), which indicates the results were not affected by the high calcite content of the test samples. Al-Maamori (2016) conducted a series of tests in the Queenston shale in the Milton area and found similar results with results showing high calcite content (up to 37%) with average vertical and horizontal free swell potentials of 0.19 and 0.156% strain/log cycle of time, respectively.

The results of the swell tests are summarised in Table 5.1. Ancillary tests were conducted for each of the swell tests. Moisture content ranged between 1.4 to 3.6 %. Salinity ranged between 129 and 261 g/L and calcite content ranged between 9.3 and 26.9 %. Moisture content and salinity values are within typical ranges, but the calcite content is consistently high across all boreholes and depths.

The results of the swell tests are used to create a site specific Lo and Hefny swelling model. An idealized version is shown in Figure 5.12. The model identifies the swelling potential's relationship to applied stress. The swelling potential of a rock can be classified into one of three conditions: as free swelling, where the applied stress is under the threshold pressure ( $\sigma_{th}$ ) and the maximum swelling occurs; semi-confined, where the applied stress is between the threshold and critical pressures ( $\sigma_c$ ) and the swelling is reduced from the free swell conditions; or full suppressed, where the applied stress is above the critical pressure and swelling does not occur. The results of swell tests are compiled in Figure 5.13 along with the Lo and Hefny (1996) swelling model. The results show that the free swell potentials are on average 0.50 and 0.24% strain per log cycle of time in the vertical and horizontal directions, respectively. Based on the best-fit line from the Lo and Hefny (1996) models shown in Figure 5.13, the critical pressures are estimated to be 2.4 MPa in the vertical direction and 1.0 MPa in the horizontal direction. In the horizontal direction, the swelling envelope was developed by applying a logarithmic trend line using the least-squares method using the data from the SCST and NST results. The average value of the FST was used as the free swell potential. The threshold stress was taken as the intersection between the above mentioned trend line and the free swell

potential value and was found to be 0.05 MPa. The anisotropic swelling behaviour is typical of shales in southern Ontario (Al-Maamori et al. 2014).

Table 5.1. Swell test summary at Zone 1 Water Main.

Sample	Borehole	Sample Elev. [m]	Applied Pressure [MPa]	Vertical swell potential [% strain/ log cycle of time]	Horizontal swell potential [% strain/ log cycle of time]
FST1	2	77.5	0	*	0.36
FTS2	2	77.6	0	0.57	0.20
FTS3	3	77.4	0	0.43	0.24
FST4	1	71.5	0	0.63	0.17
FST5	2	85.0	0	0.44	0.21
FST6	1	71.4	0	0.45	0.27
SCSTV1	2	82.0	0.068	0.08	--
SCSTV2	3	77.4	0.346	0.28	--
SCSTH1	4	85.0	0.052	--	0.33
SCSTH2	3	77.5	0.086	--	0.19
SCSTH3	4	84.9	0.124	--	0.15
NSTV1	1	71.5	3.21	0	--
NSTV2	1	82.1	0.738	0	--
NSTV3	3	77.4	2.43	0	--
NSTH1	4	84.8	1.250	--	0

\*Sample broke in vertical direction

### 5.2.3 Additional laboratory and in-situ testing

The geotechnical investigation for the project involved laboratory and in-situ testing. Laboratory tests on the Queenston shale included uniaxial compression strength tests and swelling tests conducted outside of the University of Western Ontario.

Uniaxial compression strength (UCS) test results conducted for the investigation showed that the shale UCS was 19.4 MPa. The average elastic modulus for the Queenston Formation provided was 4900 MPa, and Poisson's Ratio was 0.24. The geotechnical report of the project

did not state whether the samples were tested in the vertical or horizontal direction. The average bulk density from 97 samples was 25.9 kN/m<sup>3</sup>. It should be noted that the elastic modulus from the testing program at Western were higher than the average provided in the geotechnical report, while the UCS value is well within the typical values.

The geotechnical report for the project also included the results of the Free Swell Tests (FSTs) and Semi-confined Swell Tests (SCSTs) conducted on rock samples; however, the test details were not provided in the report. The results presented in the report indicated negative strain on both horizontal FST and some SCST tests as well as irregular, large variations in day-to-day strains. Due to the lack of test details and the irregular results renders the results unreliable.

The geotechnical investigation included an in-situ dilatometer testing at a borehole located approximately 865 m away from the entry shaft. A Probex borehole rock dilatometer was used to measure the rock mass elastic modulus. The probe operates via a radially expandable stiff plastic membrane with a factory resolution of 0.25%. Six tests were conducted in an NQ size (75.7 mm OD diameter) borehole from Elevations 92 m to 82.3 m. The rock elastic modulus values ranged between 1400 and 6000 MPa with an average of 4500 MPa. The results are lower than the laboratory results, which is to be expected as rock mass elastic modulus is reduced due to discontinuities and fractures that are not present in intact laboratory samples.

Hydraulic conductivity of the rock mass was measured via packer tests at 35 different 3 m long intervals over seven boreholes. The measured hydraulic conductivity ranged between  $1 \times 10^{-2}$  to  $7 \times 10^{-4}$  m/s.

### 5.3 Monitoring program

A monitoring program was enacted at the main shaft and in the tunnel at Chainage 310+015. The shaft monitoring program involved three inclinometers installed to a minimum depth of 52.0 m, a minimum of 10 m below the shaft base. The tunnel monitoring section was located 50 m north of the main shaft and comprised two 9 m long borehole extensometers and a series of tape extensometers.

### 5.3.1 Shaft monitoring

The shaft monitoring consisted of three inclinometers, spaced at 120 degrees apart along the circumference of the shaft as shown in Figure 5.3, with depths shown in section in

Figure 5.4. Inclinometer 1 was installed to a depth of 52 m, Inclinometer 3 was installed to a depth of 52.5 m, and Inclinometer 4 was installed to a depth of 52 m. Inclinometer 2 was damaged during active excavation and was replaced with Inclinometer 4. Prior to inclinometer installation, approximately 5 m of the upper soil and rock was removed and replaced with lean concrete at the shaft location for construction purposes.

Inclinometers 1 and 3 were initialized in August 2015, when the excavation was approximately 4.5 m below the ground surface. Inclinometer 4 was initialized in October 2015, when the excavation was 33 m below the ground surface. Readings were taken throughout active excavation of the shaft and for the next 7 months.

Inclinometer readings were recorded employing a DIS-500 digital inclinometer system by RocTest Telemac, with a system accuracy of  $\pm 2$  mm per 25 m of depth. The readings were acquired in pairs, with the inclinometer run in the “positive” direction and then the “negative” direction, with their average represented the full reading, provided that the difference is less than 2mm. The reading quality was assessed using the Checksum method. In this method, the sum of the “positive” and “negative” readings is calculated from the raw data. This sum should ideally be zero; however, biases and errors can accrue from variations in casing grooves, reading practices, and instrument maintenance. Higher Checksum values indicate lower quality total magnitude readings, and a higher standard deviation of Checksum values indicates lower quality relative magnitude readings.

The value of Checksum varies based on the inclinometer manufacturer, as the provided data will be a function of the inclinometer output. Table 5.2 provides the average Checksum values for the readings obtained as part of this study and their standard deviations. The Checksum values are large, indicating poor total magnitudes. However, the standard deviations are small, approximately 3% of the averages in general, indicating acceptable differential readings. Therefore, the inclinometer readings are deemed acceptable as the deformation relative to the initial readings is used in the analysis.

Select results from the three inclinometers are provided and discussed herein. Figure 5.14 displays the variation of deformation along the shaft depth at project milestones: first reading after initialization, shaft half-excavated, excavation reaches final elevation, and last reading. Figure 5.15 shows a selection of readings to indicate the variability in monitoring results. In general, succedent readings rarely differed by more than  $\pm 1$  mm, with some readings registering as negative, or out-of-site. As can be noted from both figures, the observed deformations are minimal with the majority of recorded deformations are less than 3 mm. It should be noted that the expected accuracy over a 52 m deep inclinometer would be  $\pm 4$  mm. Inclinometers 1 and 3 indicate inwards movement, while Inclinometer 4 shows very little deformation, likely due to the delayed installation.

Figure 5.16 displays the variation of deformations at certain elevations with time with the excavation progress. Readings show general into-site deformations during active excavation. Clearly identifiable deformations halt shortly after the end of active excavation in Inclinometers 1 and 4. In inclinometer 3, deformations of approximately 1 mm occur over a 50 day period after active excavation.

All three inclinometers show deformation along a plane at approximate Elevation 68 m, which correlates to the observed horizon between the Queenston and Georgian Bay Shales observed in the boreholes.

Table 5.2. Checksum averages and Standard Deviations of inclinometer readings.

Date	Borehole 1		Borehole 3		Borehole 4	
	Average	StdDev	Average	StdDev	Average	StdDev
2015-08-18	-270.9	6.7	-278.7	8.3		
2015-08-26	-281.9	7.1	-282.4	8.5		
2015-09-01	-265.2	7.1	-263.1	8.8		
2015-09-09	-254.6	7.5	-264.1	7.8		
2015-09-09			-269.2	8.0		
2015-09-17	-268.2	8.3	-273.7	7.3		
2015-09-23	-281.0	9.3	-288.2	12.2		
2015-10-06	-297.7	7.5	-301.0	8.8		
2015-10-16	-306.8	9.2	-304.3	8.2		
2015-10-18					-314.4	8.4
2015-10-22	-301.6	9.7	-291.0	10.1	-306.0	11.7
2015-10-30	-305.4	9.6	-312.3	8.2	-313.3	7.2

2015-11-04	-297.2	8.1	-296.4	9.3	-297.4	11.5
2015-11-11	-303.1	5.7	-307.3	7.1	-310.1	6.5
2015-11-18	-296.6	7.7	-295.9	7.3	-299.1	8.3
2015-11-26	-282.0	6.8	-291.2	7.1	-293.6	6.6
2015-12-02	-277.6	14.9	-282.9	8.4	-287.0	9.4
2015-12-11	-286.9	6.5	-292.6	13.4	-291.3	6.8
2015-12-16	-294.3	7.2	-300.7	7.3	-302.5	6.1
2016-01-07	-300.5	7.3	-305.0	7.7	-305.8	6.5
2016-01-28	-285.4	8.1	-297.8	8.3	-291.8	7.1
2016-02-12	-309.8	8.5	-305.0	7.7	-315.8	10.1
2016-02-29	-276.0	7.6	-287.8	8.1	-283.5	6.1
2016-03-21	-320.2	10.0	-321.1	8.4	-308.0	11.6
2016-04-11	-301.4	7.9	-307.1	9.3	-300.3	7.6
2016-05-03	-313.6	8.1	-312.4	9.4	-321.5	6.8

### 5.3.2 Tunnel monitoring

A monitoring section was installed in the tunnel approximately 50 m north of the main shaft, outside of the excavation influence. The monitoring section is shown in Figure 5.5 and consisted of two sub-horizontal extensometers installed at the springline and a tape extensometer layout. Each extensometer was 9 m long, with nodes at 1 m, 2 m, 4 m, 6 m, and 9 m depth. The extensometers were rod-type borehole extensometers with hydraulic anchor heads, vibrating wire transducers, and with an accuracy of  $\pm 0.1$  % full scale (Geokon). The digital tape extensometer had an accuracy of  $\pm 0.1$  mm (Roctest). Installation of the tunnel monitoring occurred when the TBM was approximately 50 m beyond the extensometer point, indicating that the elastic response to excavation would not be captured by the monitoring data. Readings were recorded regularly over a period of approximately 4 months, after which the cables leading to the data recorder were damaged and data from that point forward was corrupted.

Figure 5.17 shows the east extensometer readings and Figure 5.18 shows the west extensometer readings. Readings from the east extensometer show negligible deformations and the west extensometer shows less than 1 mm of deformation at the face over the 4 month period. Readings from the east wall extensometer at the 4 m node were abnormal and have not been included.



Tape extensometer readings are shown in Figure 5.19. The spring line readings demonstrate approximately 1 mm of convergence, while the vertical deformation shows negligible extension.

## 5.4 Interpretation and analysis of shaft monitoring

Shaft deformations observed from the inclinometer readings can be analyzed to estimate the horizontal in-situ stresses. The low magnitude of deformations makes precise calculations of the stresses difficult. Stresses can be estimated considering a circular opening in an elastic continuum using the following equations (Obert and Duval 1967, Timoshenko and Goodier 1970):

$$u = \frac{1+\nu}{E} \left\{ P_0 \frac{R_2^2}{r} + 4(1-\nu)Q_0 \frac{R_2^4}{r^3} \cos 2\theta \right\} \quad [5.1]$$

Where:

$\nu$  = Poisson's Ratio of the rock mass;

$E$  = Elastic modulus of the rock mass;

$r$  = Radius of the circular excavation;

$R_2$  = Radius of the desired deformation point;

$\Theta$  = Angle from horizontal line to desired deformation point;

And:

$$P_0 = \frac{\sigma_1 + \sigma_3}{2} \quad [5.2]$$

$$Q_0 = \frac{\sigma_1 - \sigma_3}{2} \quad [5.3]$$

The rock mass modulus was estimated based on the intact modulus and the fracture frequency (average of 0.4 fractures per 300 mm in the unweathered rock) as per Lo and Hefny (2001).

The resulting rock mass modulus of 9000 GPa and a Poisson's Ratio of 0.17 from the UCS test results are used to estimate the in-situ stress based on the observed shaft deformations. Figure 5.20 shows the results assuming a uniform horizontal in-situ stress of 4 MPa. In Figure 5.20, the shaft outline is represented by the solid black circle and radius of the inclinometer array is represented by the dashed line. The small circle markers show the calculated elastic deformation of the rock mass from the inclinometer array radius (7.5 m). Inclinometer 1 and Inclinometer 3 deformations from Elevation 95 m are shown with the large circle markers and are labeled. All deformations have been scaled by 1000. Inclinometer 4 is not shown, since it was initialized after missing a significant portion of the deformations due to excavation.

Deformations from the shaft monitoring were minimal, with the differential between initialization and final readings being less than the possible error. Time dependent deformations are minimal in the observed movements. Inclinometers 1 and 4 show negligible to no movement, while Inclinometer 3 shows approximately 1.0 to 1.5 mm of potential swelling. With the limited results, numerical analysis would not provide significant insight.

The estimated horizontal stress is 4 MPa, which is close to the horizontal stress of 5 MPa discussed in Vancheri and Braczek (2014). The result is within the expected range of horizontal stress. The likely isotropic magnitude also offers an explanation for the lack of time-dependent deformation. A circular opening in an elevated, isotropic stress state would not result in a reduction in stress – one of the key components of initiating swelling (Lee and Lo 1993). Shotcrete was constructed on the excavation face for support and to prevent weathering. This protective cover would also have prevented water from readily entering the rock mass, further reducing the possibility of swelling.

## 5.5 Analysis of tunnel monitoring

### 5.5.1 Swelling rock constitutive model

A swelling rock constitutive model for the time-dependent rock behaviour was developed as part of this study and has been used in the analysis of the monitoring results. The constitutive model, discussed in detail in Chapter 3, was created to calculate the swelling strains and stresses in a rock mass based on the Lo and Hefny (1996) swelling model. It considers the

logarithmic behaviour and stress dependency of the swelling potential as described in Lo and Lee (1993), and Lo and Hefny (1996) as discussed earlier in this chapter.

The constitutive model was implemented in a commercially available finite element software (PLAXIS 2016). The main inputs of the constitutive model are evaluated from the free swell tests, semi-confined swell tests, and null swell tests. Six main inputs are required for the model, including: the free swell potential, the threshold stress at which stress dependency of the swell potential begins, and the critical stress at which no swelling occurs, for both the horizontal and vertical direction. A seventh parameter is required to simulate the pseudo-Poisson's ratio (Lee and Lo, 1993; and Hawlader et al. 2005). The "pseudo-Poisson's ratio" (PPR) effect describes the suppression of swelling potential that occurs in one direction due to a greater suppression in the orthogonal direction.

The constitutive model evaluates the swelling potential at each calculation point based on the principal stresses. The swelling potentials are derived from the principal stress condition. If the stress is less than the threshold pressure, the swelling potential is taken as the free swell value. If the stress is greater than the critical pressure then the swelling potential is zero. In between these values, the free swell potential is reduced as per the Lo and Hefny (1996) model.

The value of PPR is difficult to measure, and the observed ratios of transferred suppression obtained from different tests are not consistent. The developed model allows for the practicing engineer to explore the effects of a range of PPR values between 0 and 1. A value of 0 means the effects of PPR are not considered in the analysis. A value of 1 results in each swelling potential being reduced by the greatest amount experienced amongst the three principal directions. Details of this effect are described in Section 3.2.1.

Varying this input parameter in the analysis allows performing sensitivity analyses to explore the effects of the PPR on rock swell and the resulting stresses and strains on the buried structure.

The base assumption for the swelling behaviour, and hence the constitutive model, is the presence of fresh water within the rock mass. This model assumes that the rock is fully

saturated in order for swelling to occur. In general, this assumption would result in conservative estimations of swelling.

The constitutive model calculates the swelling strains and stresses at each time step per node. At the beginning of each time step, the initial stresses and strains are used to determine the swelling potentials in the principal stress directions. The swelling strains are calculated within the logarithmic time step and applied to the node. The development of plastic strains is examined and the stress convergence at the node is checked. The analysis proceeds to the next step if the convergence criterion is met using the equation below:

$$Global\ error = \frac{\sum \|Out\ of\ balance\ forces\|}{\sum \|Active\ loads\| + CSP \cdot \|Inactive\ loads\|} \quad (PLAXIS\ 2016) \quad [5.4]$$

Where CSP is the current value of the stiffness parameter, which is a function of the strain, stress, and elastic material matrix. *Global error* is typically set to 0.01.

If the stresses do not meet the convergence criteria, the stress results are used as the input stresses for the next iteration.

To verify the performance of the constitutive model, a series of analyses was conducted to model swelling behaviour measured in the free swell tests, semi-confined swell tests and null swell tests. An axisymmetric model was established with sample dimensions in the swelling tests, i.e., 63 mm in height and 31 mm in radius. The swelling rock parameters used in these finite element models for the verification process are provided in Table 5.3. Each analysis simulated 100 days of swelling, similar to the test requirements.

Table 5.3. Swelling parameters used in finite element analysis.

Direction	Free swell potential	Threshold pressure	Critical pressure
	% strain/log cycle of time	[MPa]	[MPa]
Horizontal	0.28	0.05	1.0
Vertical	0.5	0.001	2.4

The confining stress in the vertical direction was varied to cover the range used in the tests, i.e., 0 kPa, 200 kPa, 750 kPa, 1500 kPa, and 2400 kPa. Similarly, the confining stress in the horizontal direction was varied, i.e., 0 kPa, 50 kPa, 600 kPa, and 1000 kPa. In all cases the PPR was 0.0.

The free swell results are shown in the vertical and horizontal direction in Figure 5.21. The results from the free swell tests are plotted in semi-log space, with the solid line displaying the results of the finite element analysis employing the constitutive model. The results are plotted in semi-log space in order to compare swelling potentials from testing with the model results, which cannot be done effectively when plotted in linear time. The swelling potential of any result is considered as the slope of the straight line in semi-log space between 10 and 100 days.

The free swell potential modeled was 0.28 % strain per log cycle of time in the horizontal direction, and 0.5 in the vertical direction. These values were chosen as the best fit for the Lo and Hefny (1996) model and not necessarily the average of the test values. As shown in the Figure, the model results provide adequate results when comparing to the slope of the lines between 10 and 100 days.

Figure 5.22 shows the results from a series of analyses considering different confining stresses. The swelling potentials adopted in the constitutive model for each condition align with the theoretical Lo and Hefny swelling model. In general, the swelling constitutive model accurately portrays the time-dependent deformations based on the swelling parameters input into the finite element analysis.

### 5.5.2 Tunnel analysis

The time-dependent behaviour of the tunnel was analyzed employing the verified finite element model to evaluate the effects of swelling on its stresses and deformations. The main objective of the analysis was to evaluate the effectiveness of employing the 2 MPa grout for mitigating the stresses from time-dependent rock swelling and the developed stresses in the steel liner compared to using a 35 MPa concrete

The tunnel excavation was simulated in the finite element model in phases representing: the initial state of stress (geostatic stresses), excavation, construction, and post-construction

phases. In each phase, the unbalanced forces are analyzed until the convergence criterion was satisfied. The stresses and strains at the end of the step would be used as the initial conditions for the subsequent step.

The mechanical properties of the soil and rock are obtained from the field and laboratory tests. Soil and rock materials were modeled with a linear-elastic perfectly plastic constitutive model with the Mohr-Coulomb yield criterion. Soil parameters were obtained from correlations with SPT blow counts and soil type. Rock parameters were based on the laboratory results of intact samples conducted for this research (Section 5.2.2.1) and for the project design (Section 5.2.3) and empirical relationships with the fracture frequency and RQD. The mechanical properties of soil and rock used in the analysis are provided in Final liner installation and grouting occurred approximately 300 days after excavation. The analysis considered swelling in two stages, the first over the 300 days with no tunnel structure, and the second over a 75 year period with the steel liner and fill material. The fill material between the tunnel lining and the rock was modeled as either 35 MPa concrete or 2 MPa grout. The effect of PPR was also considered.

Table 5.4. The un-weathered rock mass elastic modulus was adjusted from the laboratory results based on the averaged fracture frequency using the relationship provided in Lo and Hefny (2001). Based on the RQD results completed for the project construction and for this research, the upper 5 m of rock was considered weathered.

The swelling rock constitutive model discussed in Chapter 3 was used to calculate the stresses and strains due to the rock swelling. The measured vertical critical pressure of 2.4 MPa from the null swell tests is significantly higher than the in-situ vertical stress. A result of this inconsistency is that using the test value of the critical pressure results in unrealistic vertical swelling deformations. The model begins with the in-situ pressures under the critical stress and the model begins to swell upwards immediately, which does not happen in reality. As per Lee and Lo (1993), an initial reduction in stress is a requirement for initiating swelling.

A practical solution to this problem is to use the in-situ vertical stress as the critical stress in the swelling model, as described by Carvahlo (2015). This solution prevents large vertical

swelling deformations from occurring, and limits the vertical swelling to areas where stress decreases, as per the Lee and Lo (1993) requirement.

Final liner installation and grouting occurred approximately 300 days after excavation. The analysis considered swelling in two stages, the first over the 300 days with no tunnel structure, and the second over a 75 year period with the steel liner and fill material. The fill material between the tunnel lining and the rock was modeled as either 35 MPa concrete or 2 MPa grout. The effect of PPR was also considered.

Table 5.4. Soil and rock parameters.

Parameter	Soil	Weathered rock	Un-weathered rock
Unit weight [kN/m <sup>3</sup> ]	19.0	24.0	26.0
Elastic modulus [MPa]	100	4500	9000
Poisson's ratio	0.3	0.17	0.17
Cohesion [kPa]	1.0	700	1400
Friction angle [°]	28	31	31

The rock and tunnel deformations were compared to the monitoring results. Convergence comparisons are provided in Table 5.5. The provided deformations from the finite element analysis only consider the deformations over the first 120 days, as measured by the tape and borehole extensometers. The results obtained from the finite element analyses demonstrate that the effect of the pseudo-Poisson's ratio should be considered in the analysis in order to realistically simulate the tunnel deformations. When PPR effects are considered in the analysis, the calculated deformations follow the observed tunnel deformations.

Spring line convergence over 75 years is shown in Figure 5.23 for the dual conditions of PPR 0 or 1 or using 2 MPa grout or 35 MPa concrete. The results obtained from the analyses indicate minimal deformations using a PPR of 1. The calculated time-dependent deformations

over the period between 300 days and 75 years are 3.1 mm convergence using 2 MPa grout and 2.8 mm using 35 MPa concrete. The finite element analyses conducted assuming PPR = 1 demonstrated negligible deformations over the period between 300 days and 75 years.



Table 5.5 Spring line convergence over 120 days from excavation.

	Measured	PPR = 0.0	PPR = 1.0
Spring line convergence [mm]	0.8	9.4	1.4

Table 5.6 shows the maximum and minimum bending moments experienced by the steel liner after 75 years. In all cases, the calculated bending moment is less than the permissible 32 kNm bending moment.

Table 5.6. Bending moments in steel liner after 75 years.

Analysis case	Bending moment [kNm]	
	Maximum	Minimum
PPR = 0 + Grout	0.37	-0.30
PPR = 0 + Concrete	0.12	-0.12
PPR = 1 + Grout	0.24	-0.23
PPR = 0 + Concrete	0.0058	0.0004

## 5.6 Summary and conclusions

The Zone 1 Water Main tunnel, constructed in the Queenston shale formation, was subject to loading due to the relief of elevated horizontal in-situ stress and time-dependent deformations. The structural design of the tunnel incorporated a thin-walled steel liner encased in a minimum of 300 mm thick 2 MPa cellular grout.

Monitoring of the mainland shaft consisted of three inclinometers at 120° apart; each toed a minimum of 10 m below the bottom of excavation. The results indicated less than 3 mm of inward deformation of the rock mass due to relaxation of the in-situ stress. Analysis of the results assuming a circular opening in a linear-elastic continuum in an isotropic horizontal

stress field indicates that the in-situ horizontal stress is approximately 4 MPa, which is close to the value of 5 MPa reported by Vancheri and Braczek (2014).

The swelling behaviour of the Queenston shale at the main shaft was measured in a series of tests conducted at the Geotechnical Research Centre, which identified the input parameters for the Lo and Hefny swelling model. The mechanical properties of the soil and rock were established from the geotechnical investigation preceding the construction and additional UCS tests conducted for this research.

The swelling behaviour of the Queenston shale was calculated using a constitutive model that was developed by incorporating the Lo and Hefny swelling model. The constitutive model performance was verified by comparing its predictions with the observed test data and excellent agreement was observed.

A tunnel section was analyzed using the developed finite element model established employing the finite element program Plaxis, which incorporated the swelling rock constitutive model. The finite element model was employed to investigate the effect of the pseudo-Poisson's ratio and the effect of using the 2 MPa grout on the steel liner. The results obtained from the analysis indicate the following:

1. The calculated stresses and deformations of the steel liner for both cellular grout and concrete fill cases are within acceptable limits.
2. The comparison between the numerical model predictions and the measured tunnel deformations obtained from the monitoring program over a 120 day period indicates that using  $PPR = 1$  results in realistic predictions of tunnel spring line convergences, and correspondingly negligible rock mass deformations over 75 years.
3. Employing  $PPR = 0$  in the analysis, the rock mass deformations, liner bending moments, and liner rotations were greater for the 2 MPa grout than the 35 MPa

concrete. These results contradict the expected behaviour when using low strength grout.

4. The analysis results also imply that the less stiff and weaker 2 MPa grout prevents the build up of suppression pressure in the swelling rock. Thus, the effect of reducing the swelling potential (using 35 MPa concrete) would outweighs the stress mitigation (using 2 MPa grout).
5. The elevated in-situ stress of 4 MPa is significantly higher than the horizontal suppression pressure of 1 MPa. The circular excavation of the tunnel with minimal damage to the rock mass prevents excessive loss of stress. This allows for the stresses to remain high, providing a natural suppression pressure to reduce the swelling potential around the opening.
6. The measured response from the monitoring program through the tape and borehole extensometers indicate that the rock mass deformations over 120 days due to time-dependent deformation is less than 2 mm. Results from the tape extensometer readings show that the maximum convergence due to swelling occurred after approximately 40 days, which is less than the recommended 90 to 100 days in typical tunnelling projects.

Grout properties

## 5.7 Acknowledgements

The authors would like to acknowledge the gracious support from the project team, including the Region of Halton, R.V. Anderson Associates Ltd., and C&M McNally Tunnel Contractors.



## 5.8 Figures



Figure 5.1. Zone 1 water main tunnel location in Burlington and Oakville, Ontario.



Figure 5.2. Excavated tunnel showing the McNally support system.

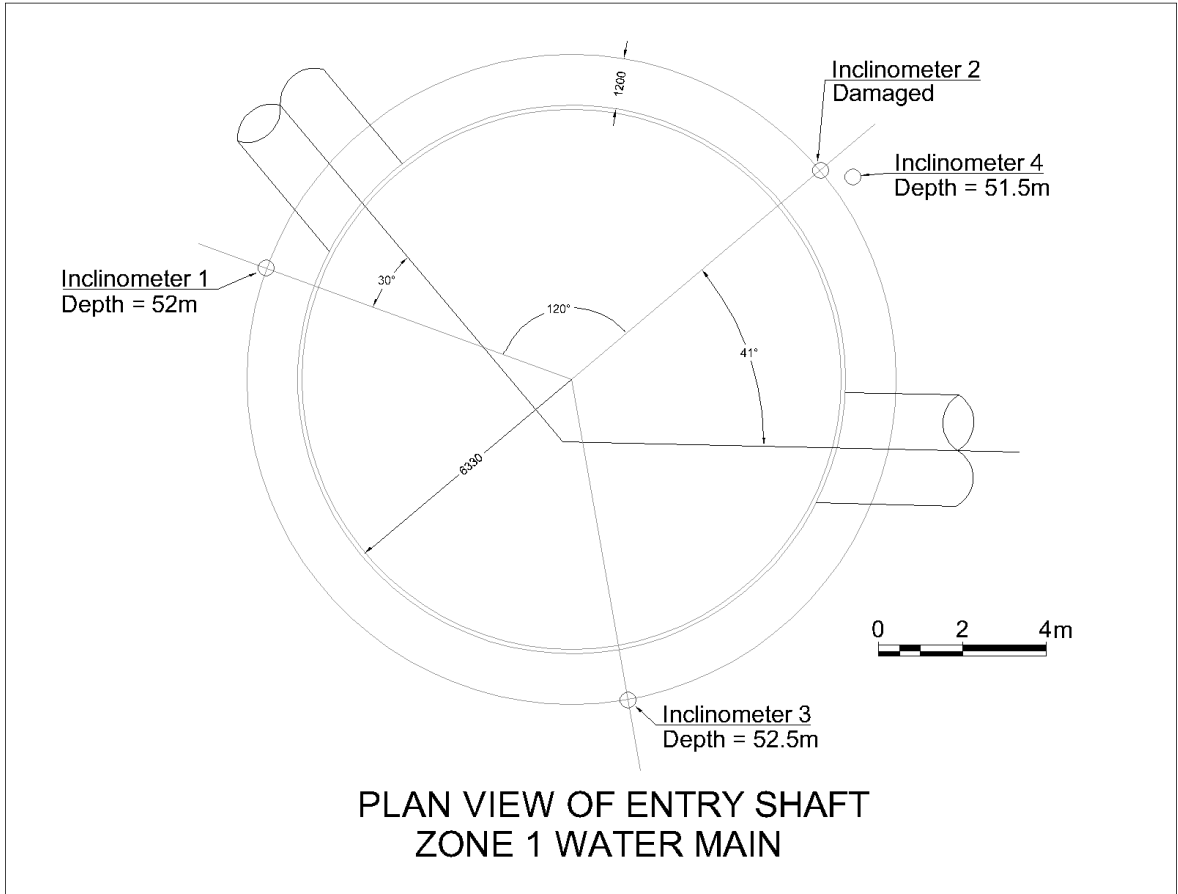


Figure 5.3. Plan view of shaft and inclinometer location (dimensions are in mm).

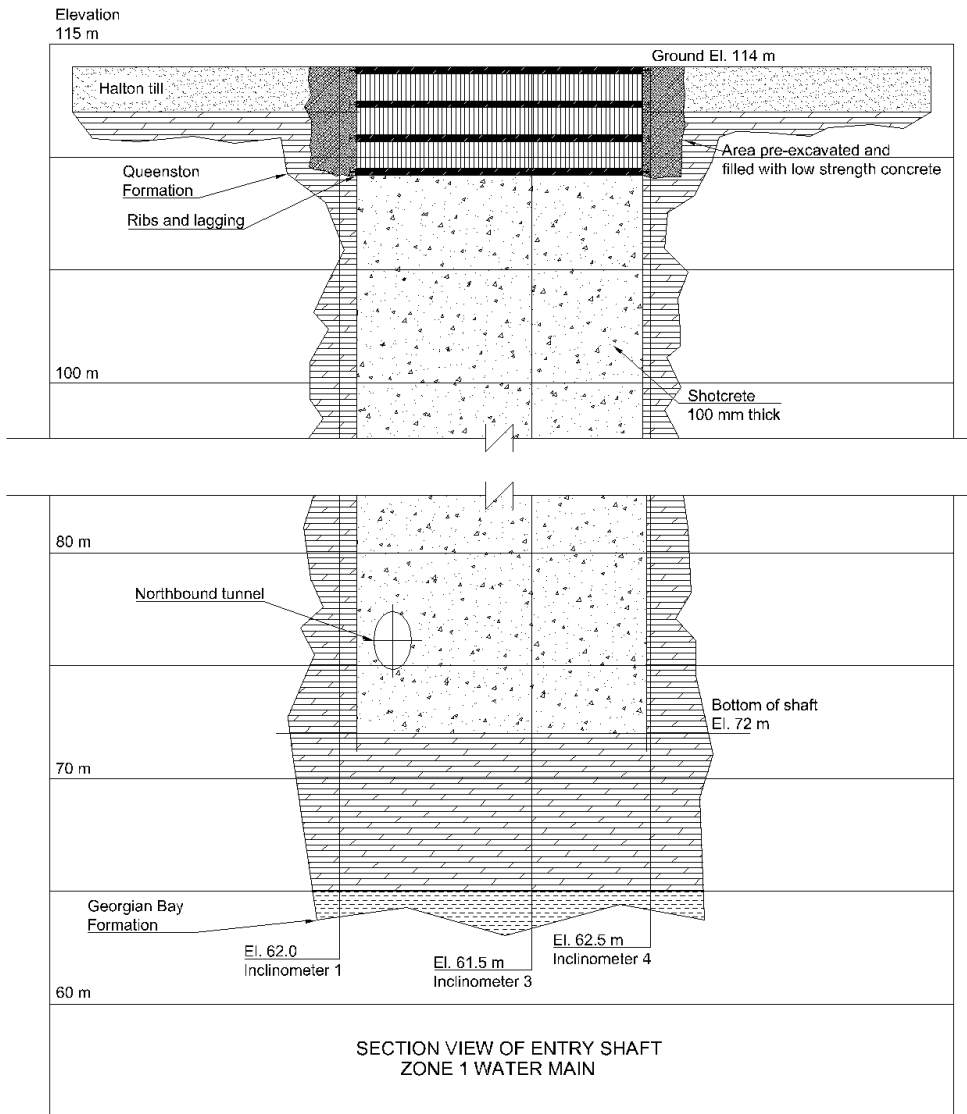


Figure 5.4. Entry shaft section.



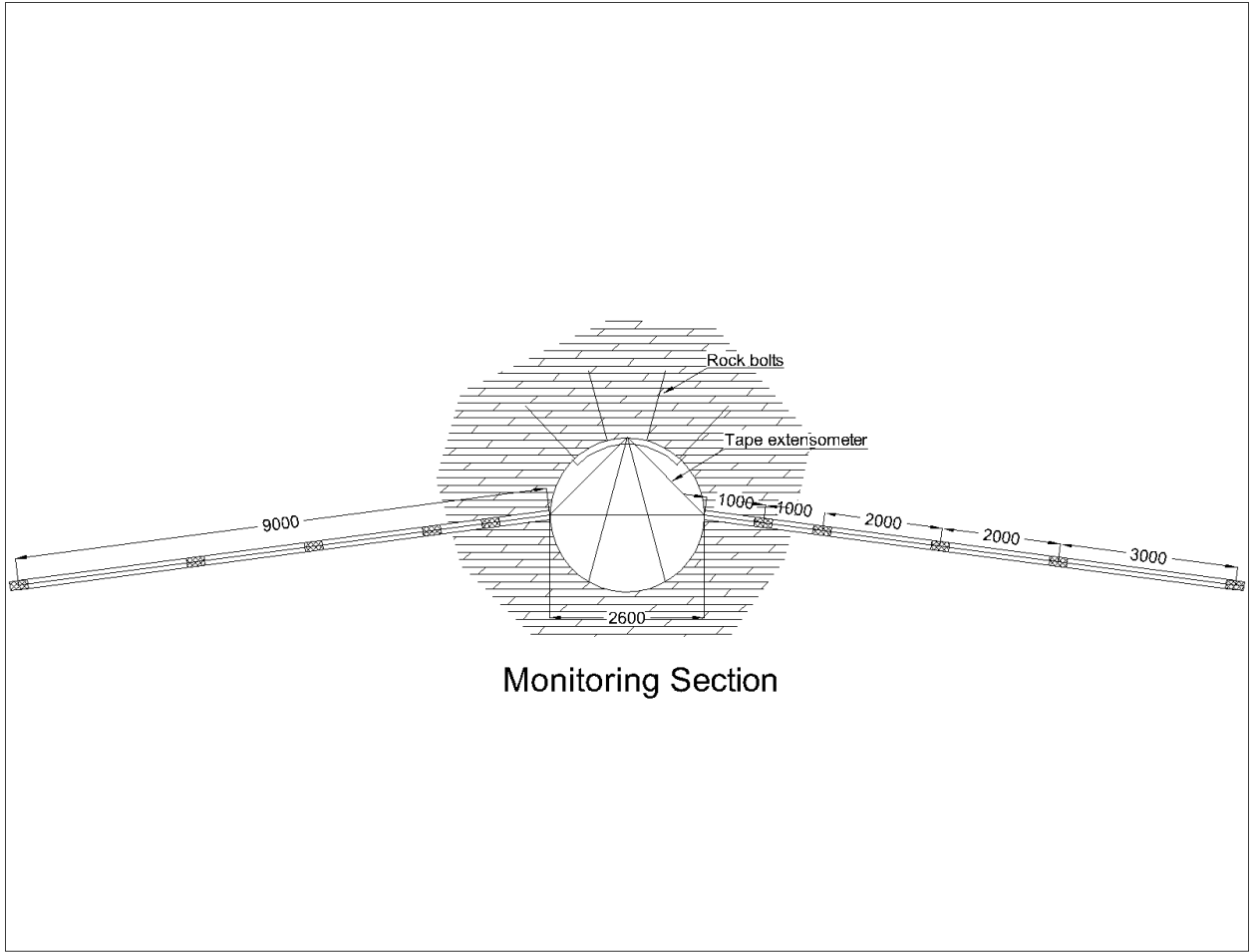


Figure 5.5. Monitoring section in tunnel showing borehole and tape extensometer layout (Dimensions are in mm).

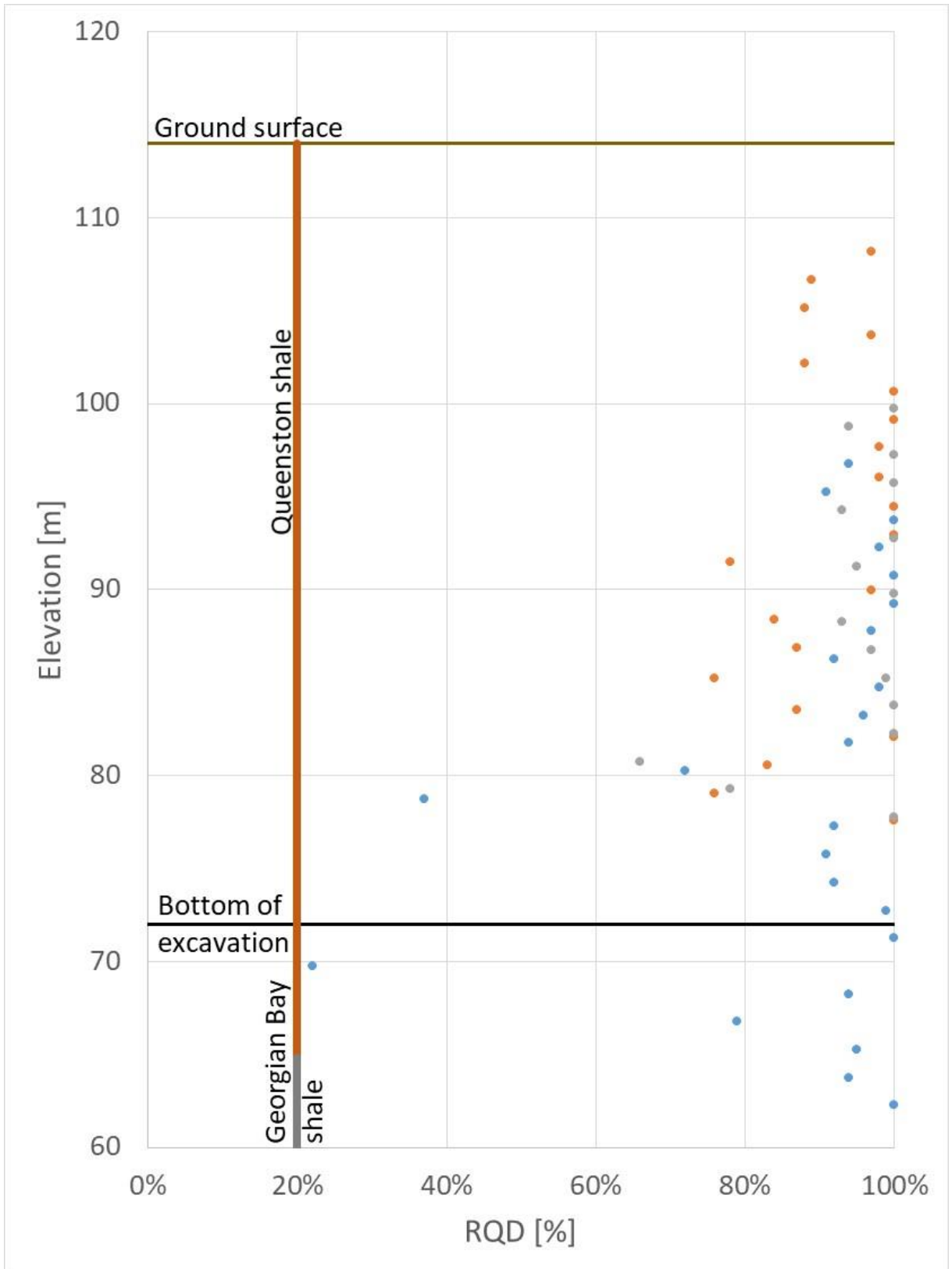


Figure 5.6. RQD with depth from borehole inclinometer drilling.

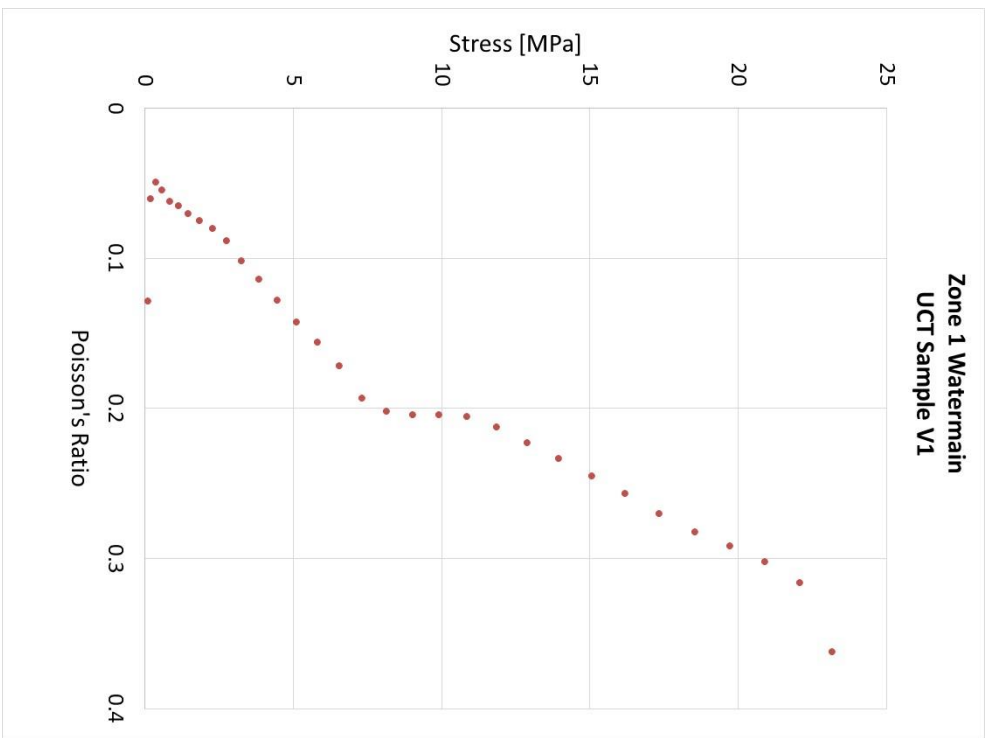
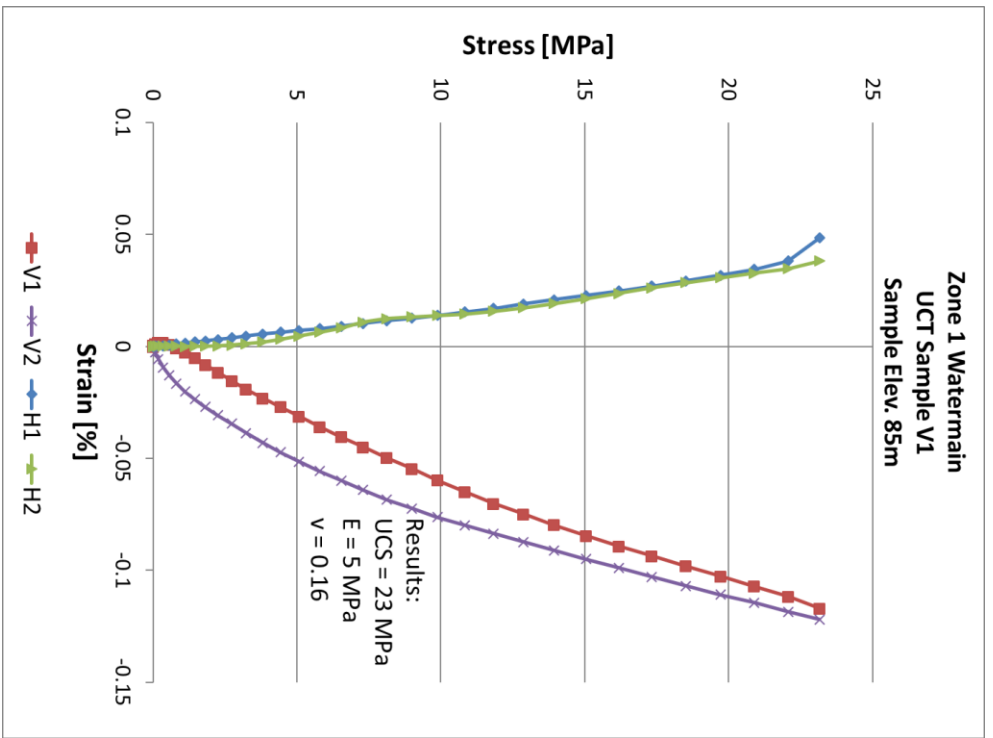


Figure 5.7. UCS test results for Queenston shale.



(a)



(b)

Figure 5.8. UCS test pre (a) and post (b) failure.

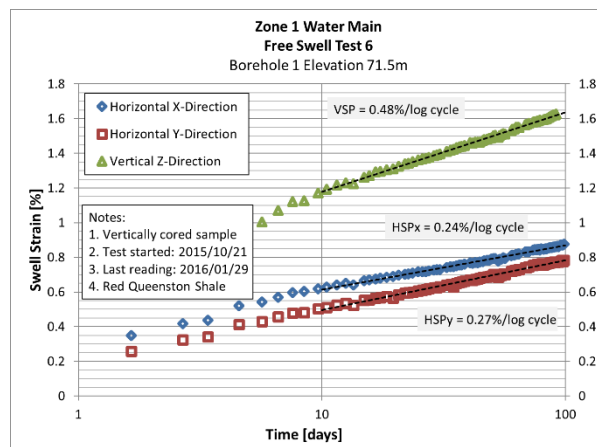
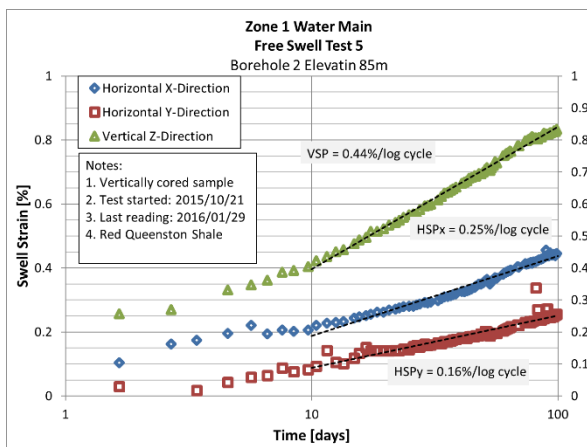
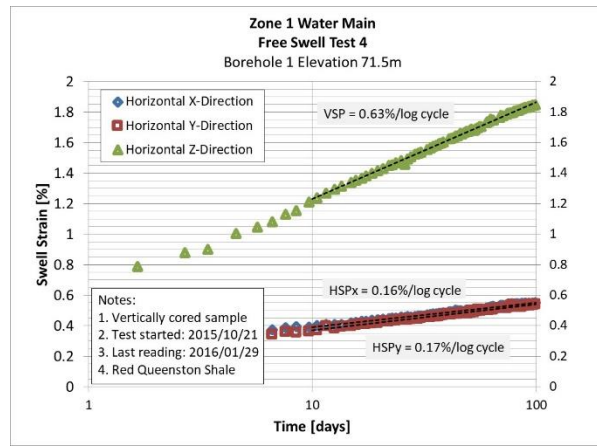
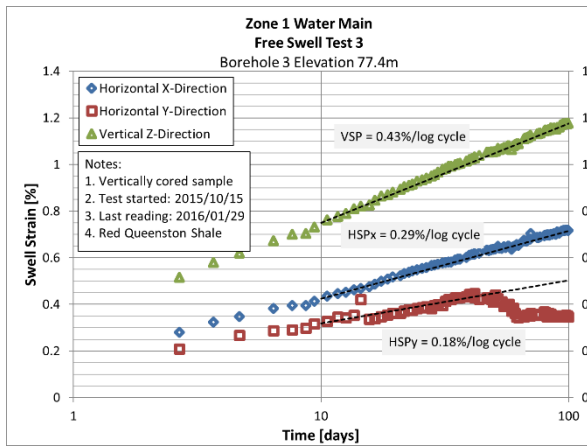
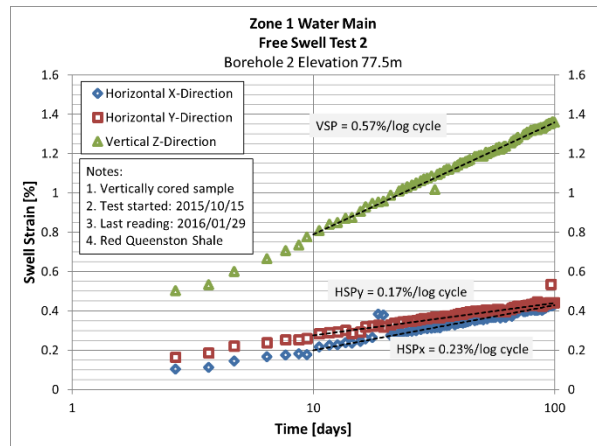
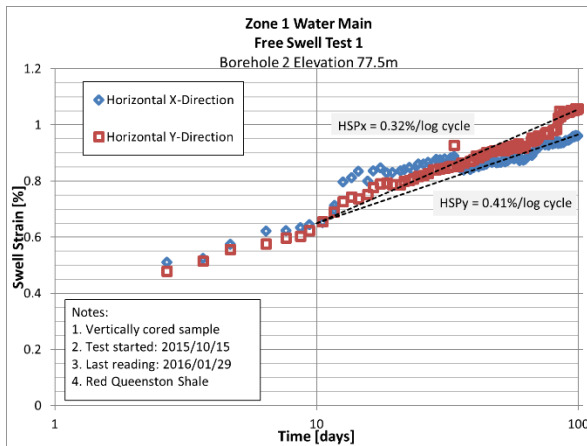


Figure 5.9. Free swell test results at Zone 1 Water Main

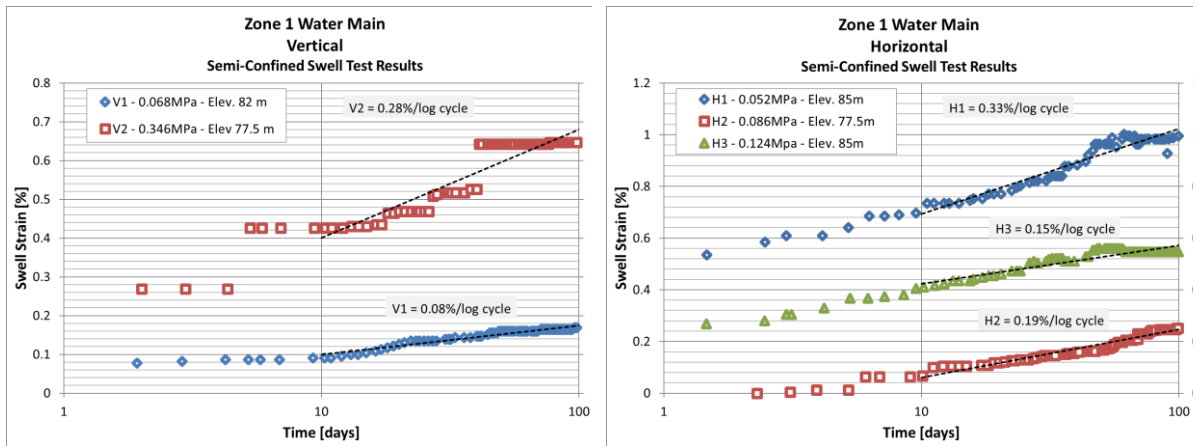


Figure 5.10. Semi-confined swell test results.

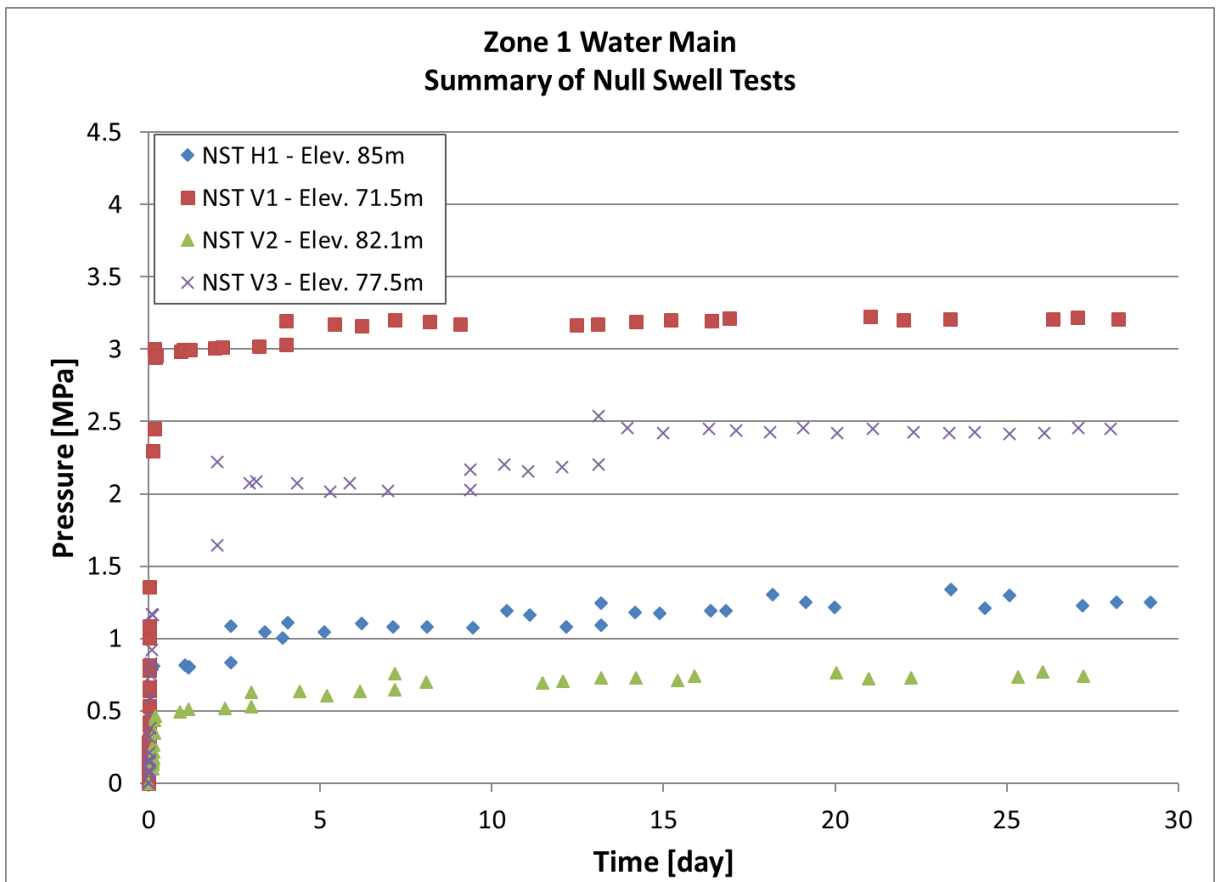


Figure 5.11. Summary of null swell tests.

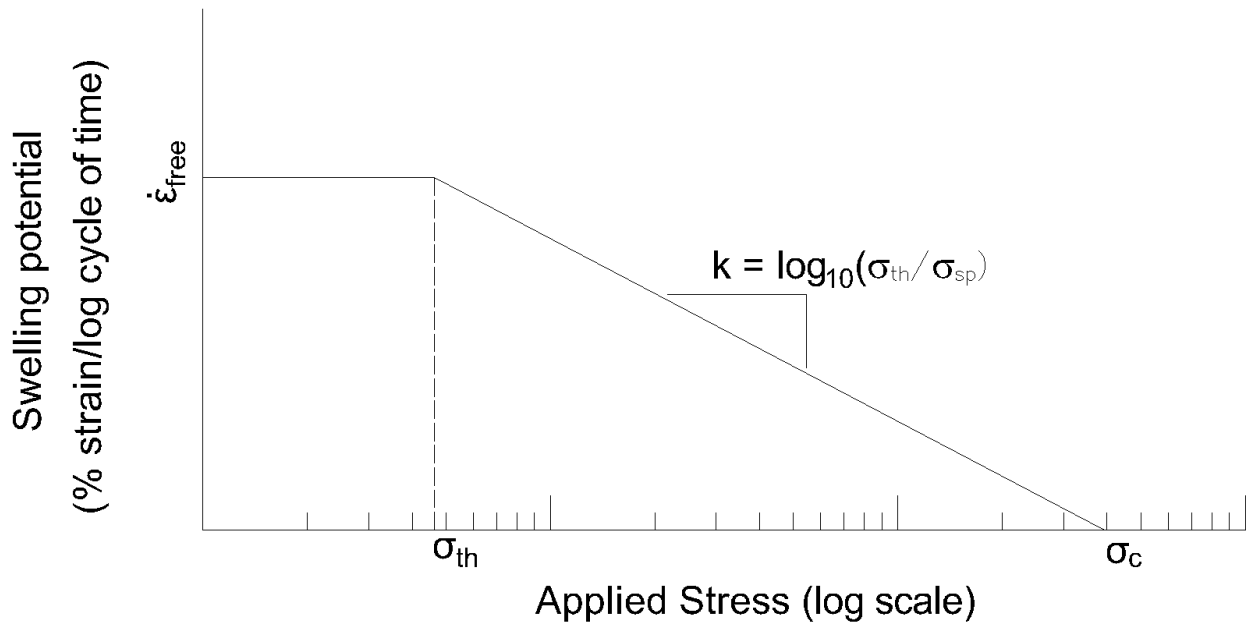


Figure 5.12. Lo and Hefny (1996) swelling model.

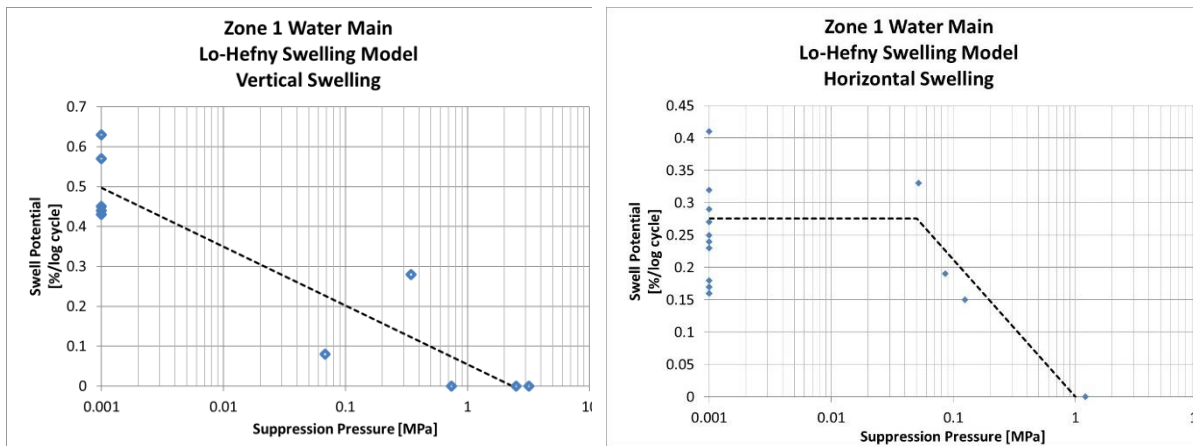
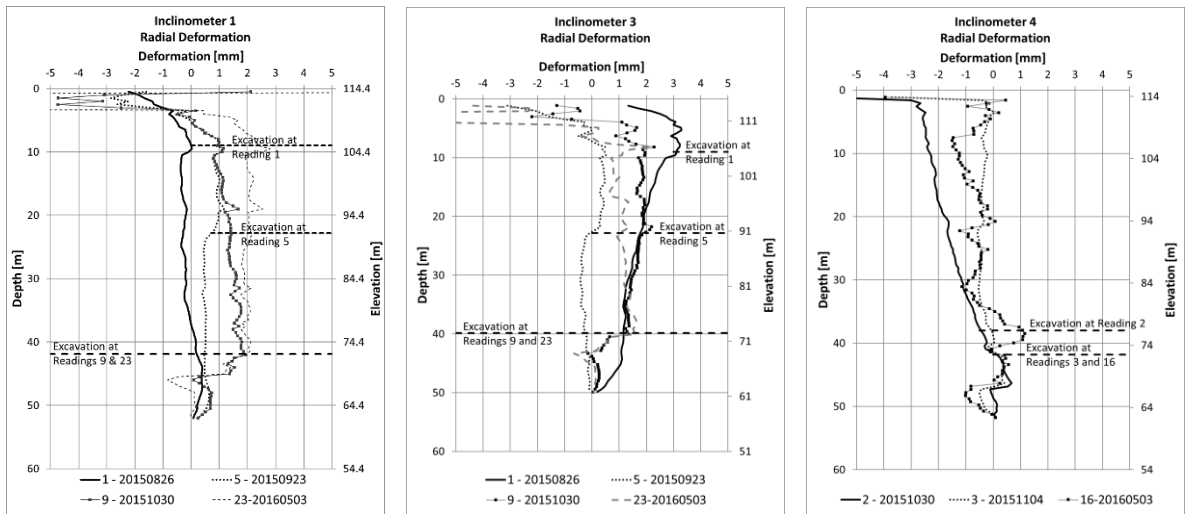
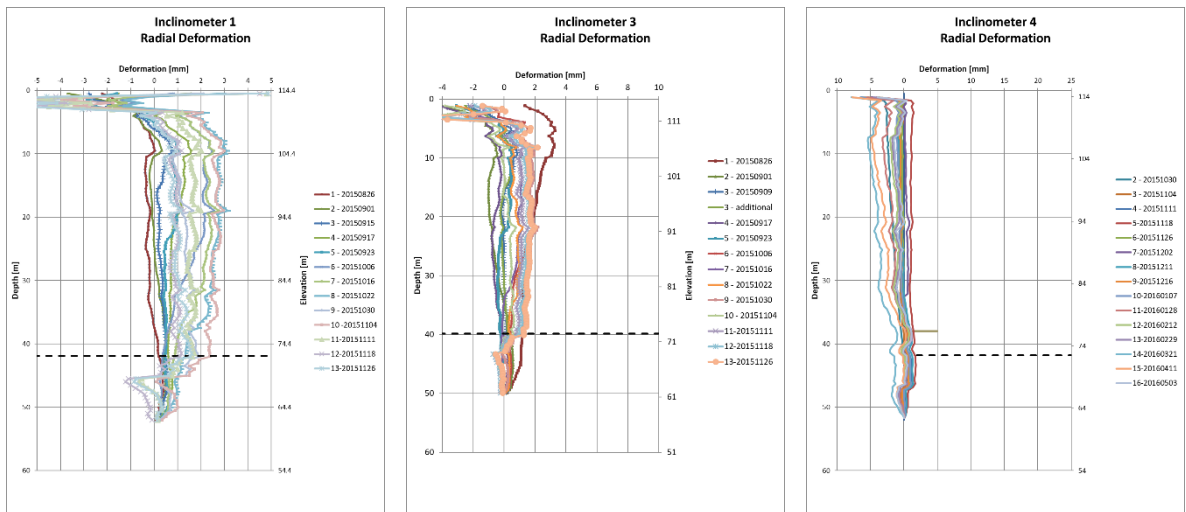


Figure 5.13. Lo-Hefny swelling characteristics for vertical and horizontal swell potentials.



\*positive deformations are into site.

Figure 5.14. Select inclinometer results from the main shaft.



\*positive deformations are into site.

Figure 5.15. All inclinometer results from the main shaft.



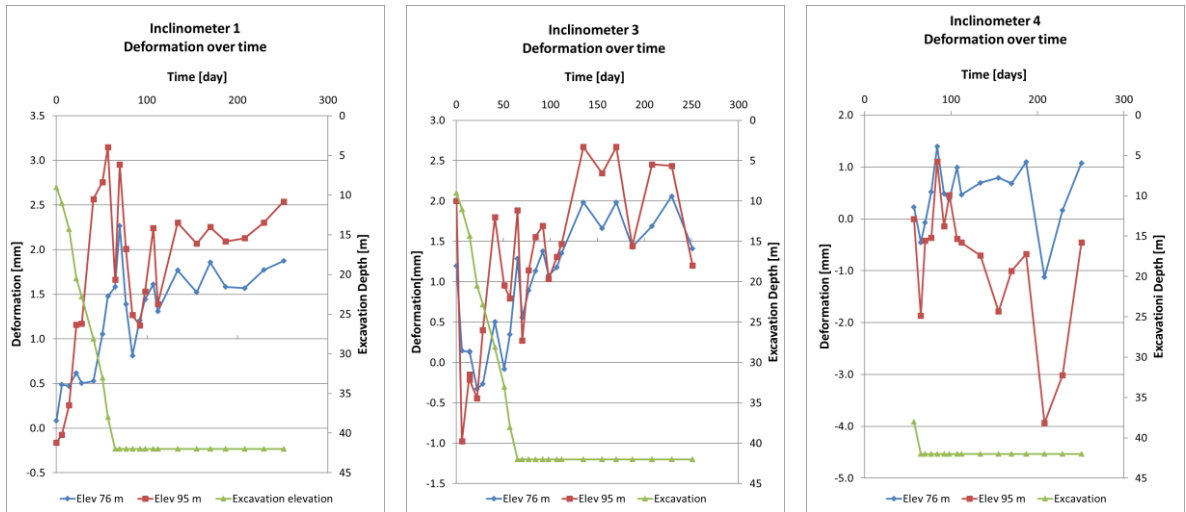


Figure 5.16. Deformation over time at main shaft at two Elevations.

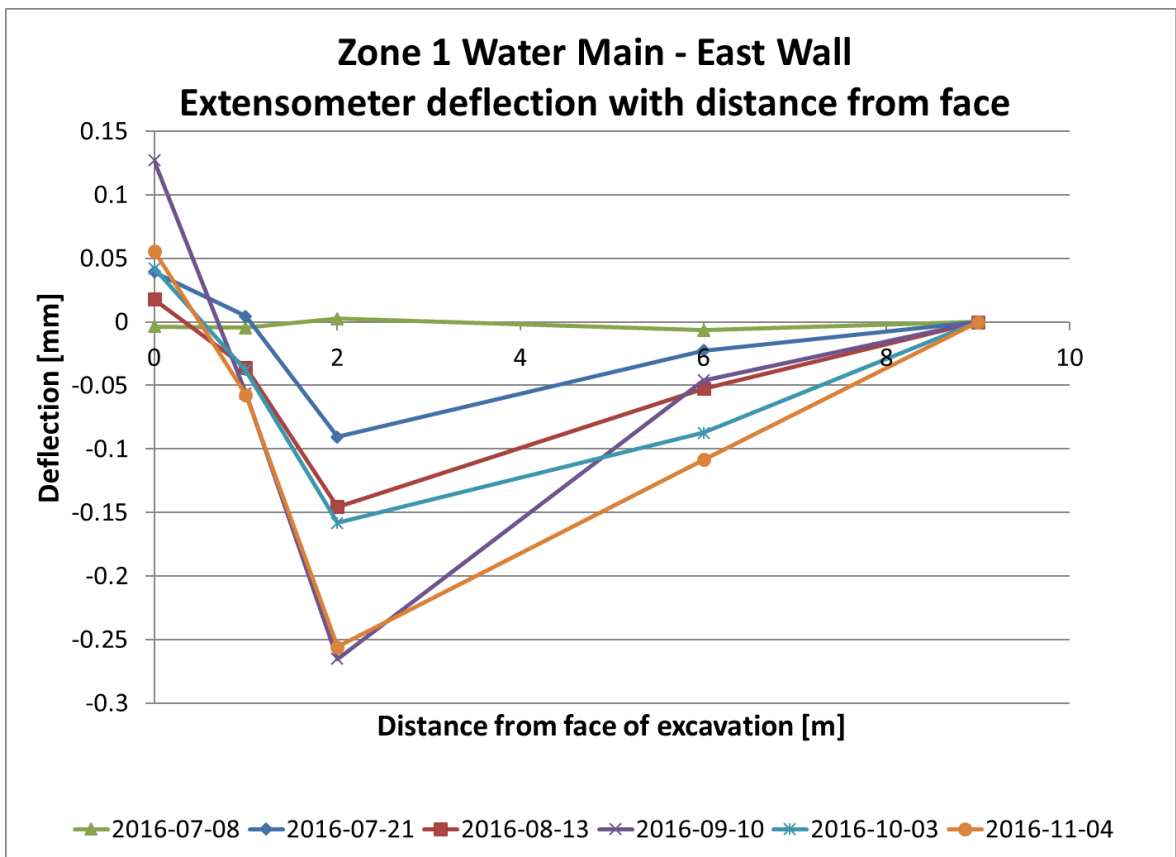


Figure 5.17. Select readings from East extensometer.

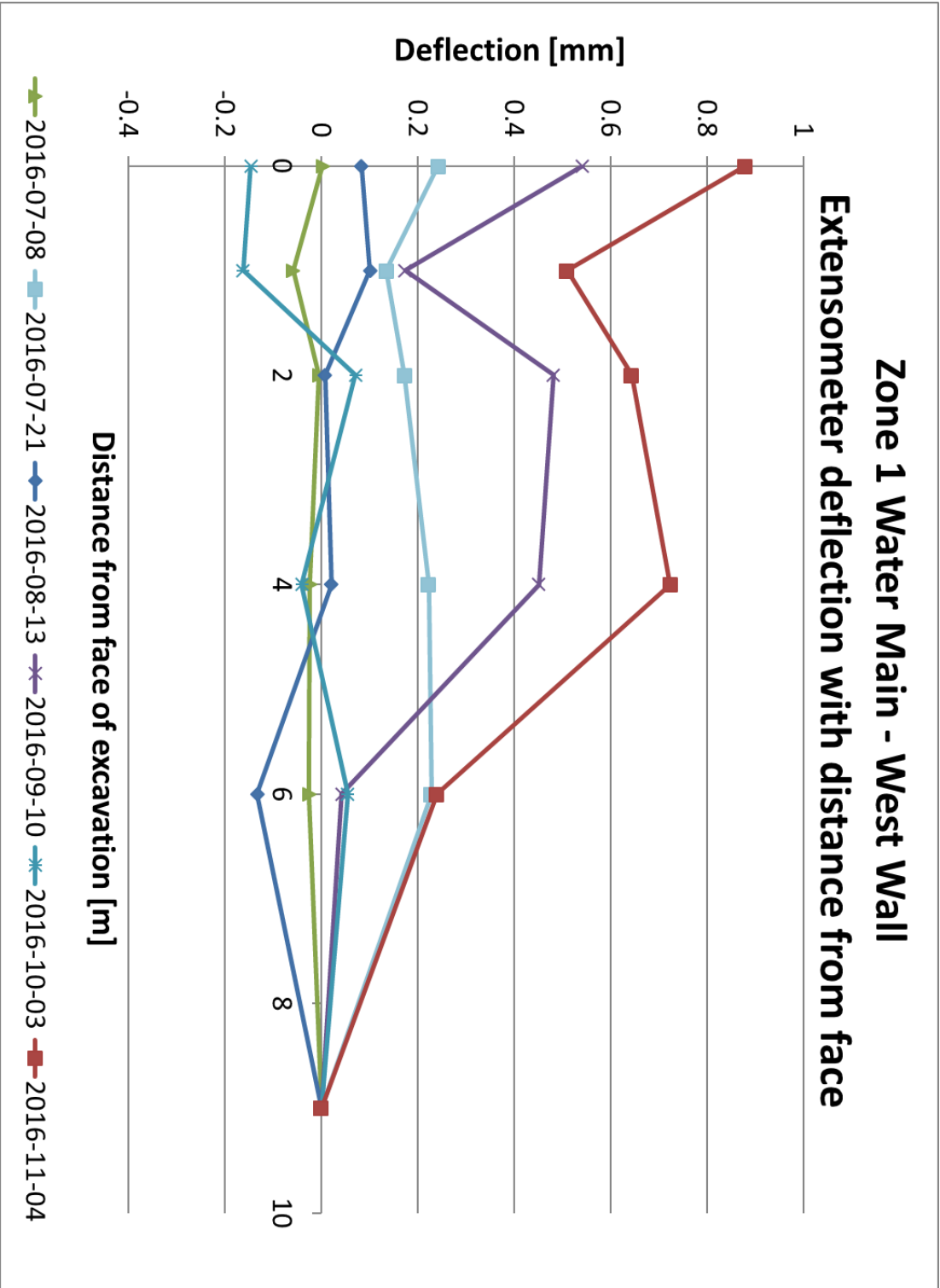


Figure 5.18. Select readings from West borehole extensometer.

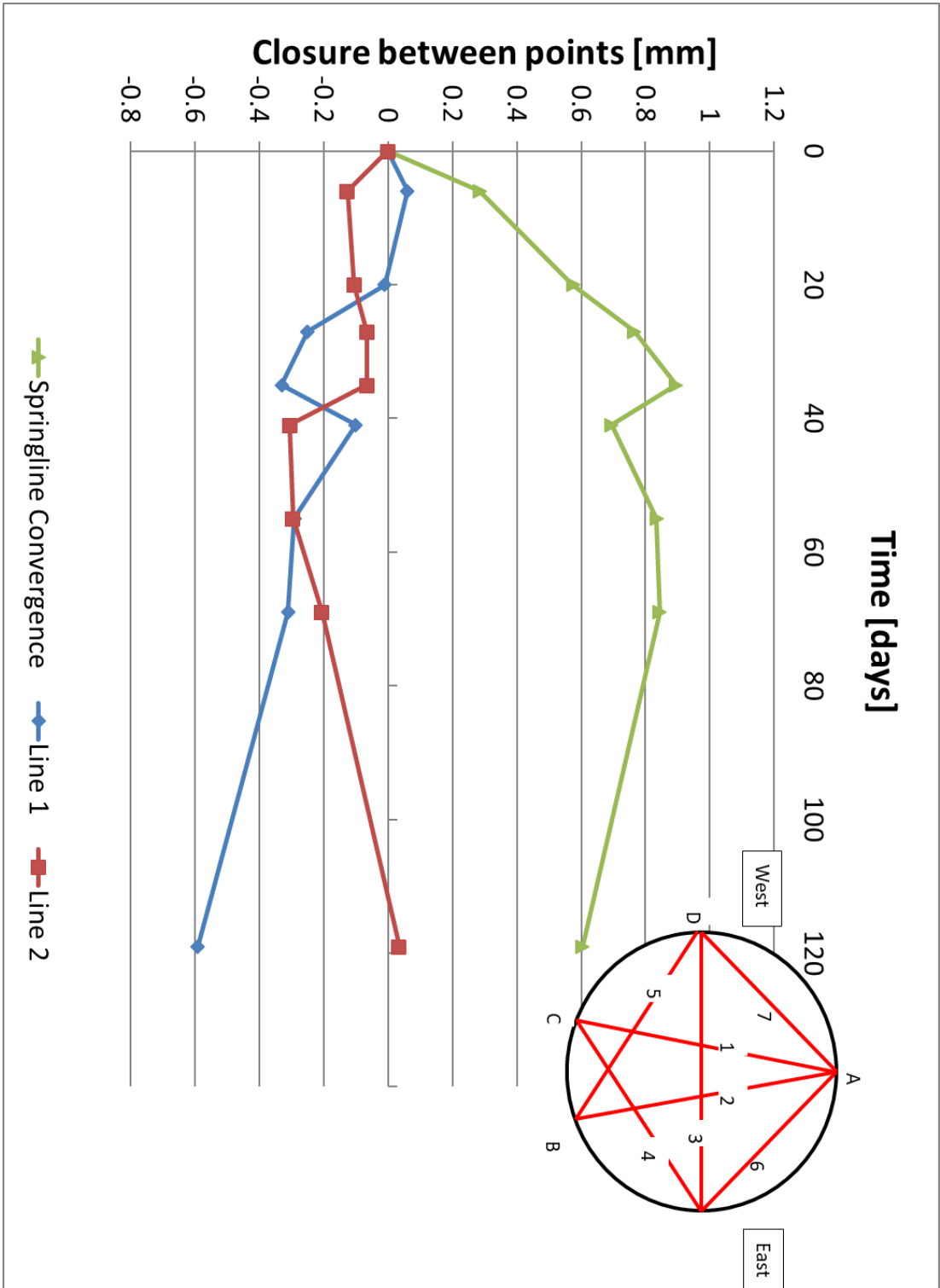


Figure 5.19. Tape extensometer readings.

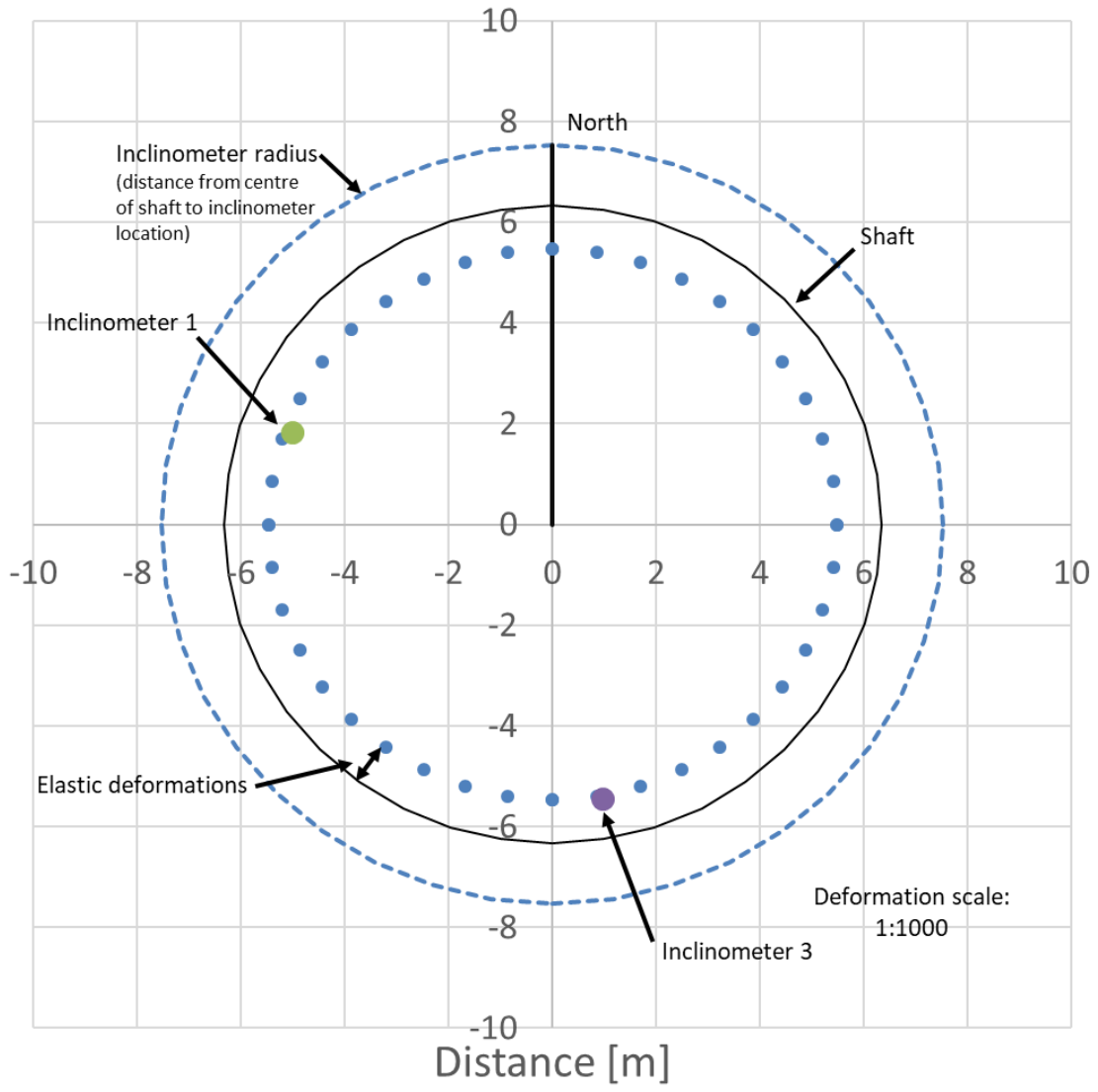
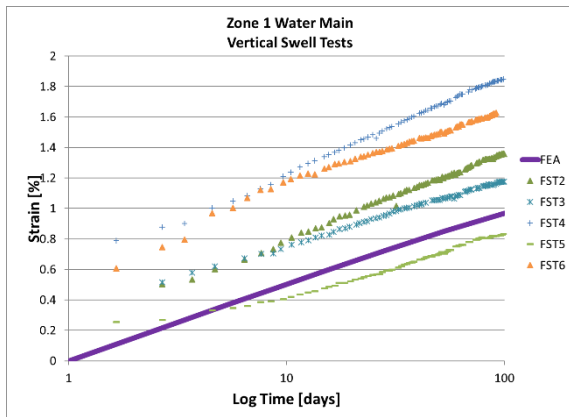
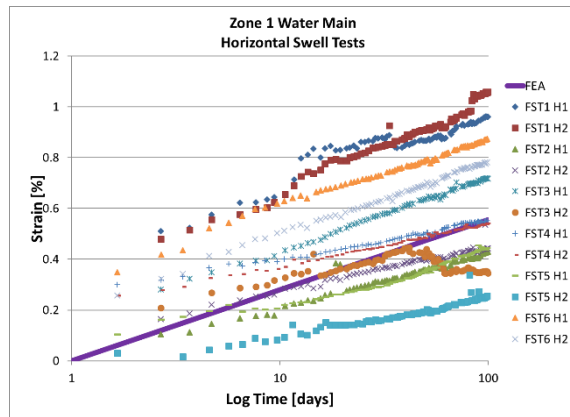


Figure 5.20. Shaft analysis comparing calculated and observed deformations.

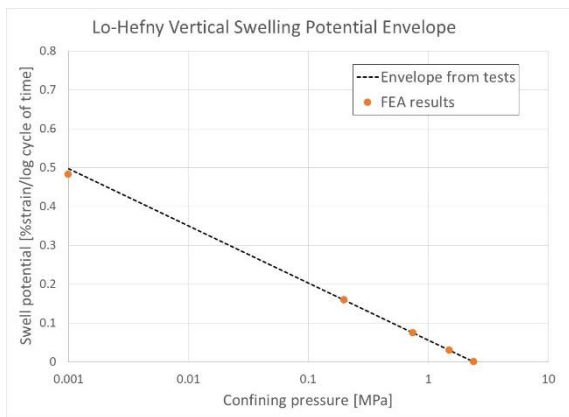


(a)

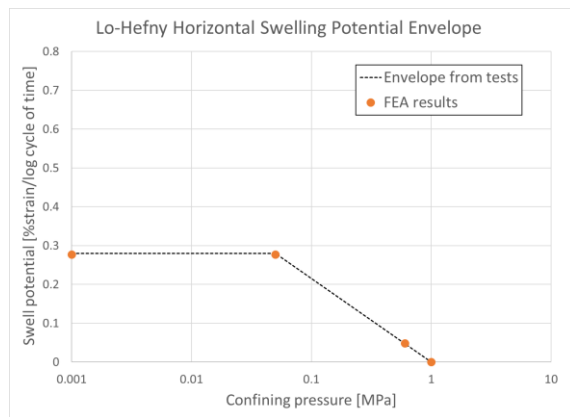


(b)

Figure 5.21. Comparison of swelling constitutive model with free swell test results



(a)



(b)

Figure 5.22. Constitutive model results at varying confining stresses.

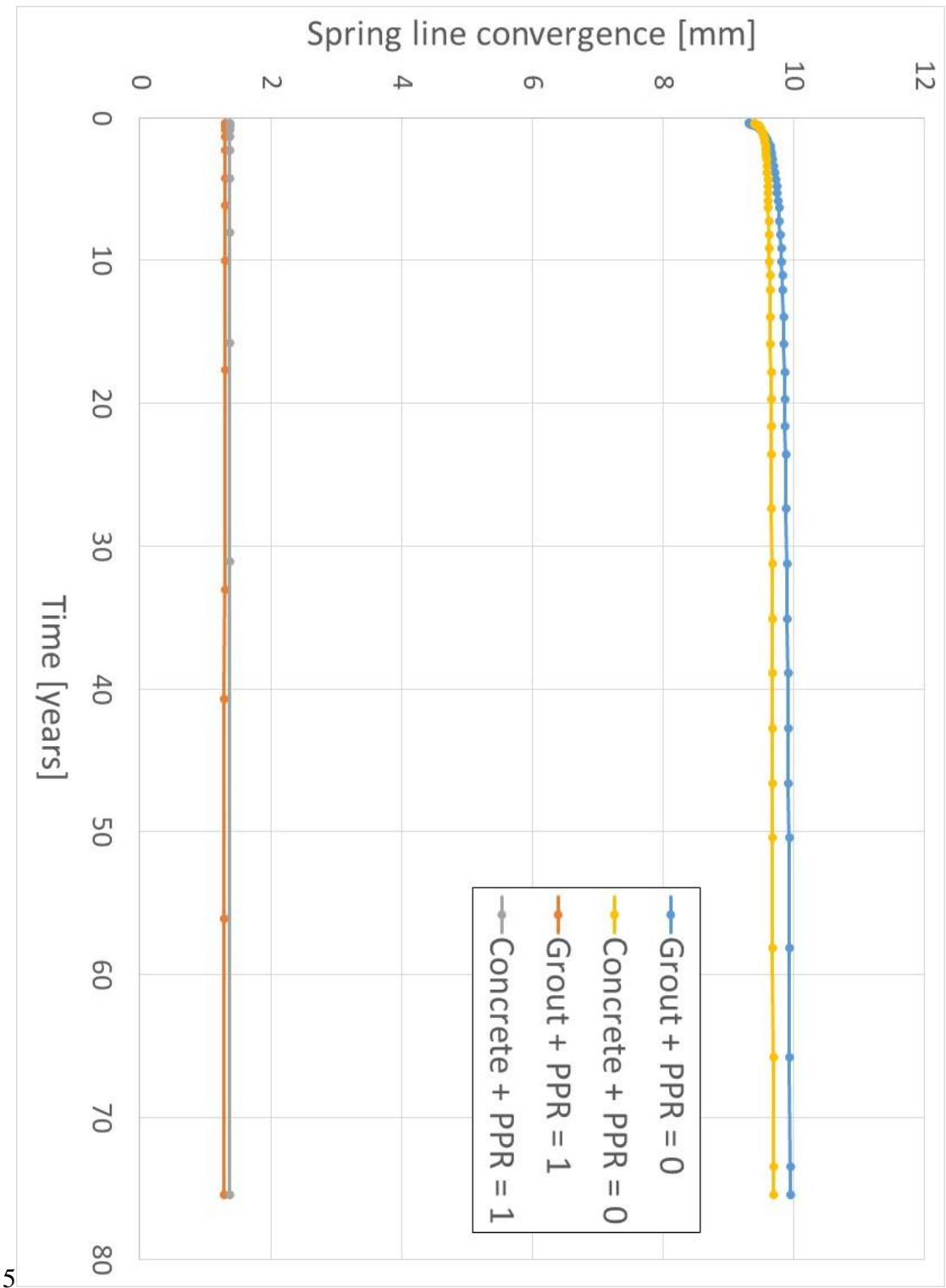


Figure 5.23. Springline convergence over 75 years.

## Chapter 6

### 6 Case study of rectangular shaft in swelling rock – Billy Bishop Pedestrian Tunnel Project

#### 6.1 Construction history

The Billy Bishop Pedestrian Tunnel (BBPT) project, shown in Figure 6.1 is located at Lower Bathurst Street, and connects the mainland to the Toronto Island airport. The tunnel, shown in Figure 6.2., is approximately 10 m across at the spring line and 7.5 m high. The mainland shaft, shown in Figure 6.3., was 35 m deep, with a footprint of 33 m by 14 m, and houses a bank of elevators with the structure shown in Figure 6.4.. The shaft was located approximately 4 m from the western channel of Toronto Harbour and less than 10 m from the ferry terminal, which remained in operation throughout the tunnel construction. The exit shaft contains a series of escalators from a depth of 30 m, and attached to the existing terminal.

The main shaft excavation occurred between June 2012 and May 2014, with long breaks between active excavation for support construction and tunnelling. The shaft was composed of secant caissons through the soils and toed into the rock a minimum of 3 m. Upper supports were composed of continuous whaler and struts, with lower supports composed of pre-stressed anchors near the bottom of each pile. Short rock bolts and mesh were also installed on the north and south walls to prevent loose rock from falling. Excavation occurred with a large hydraulic hammer mounted on an excavator, and progressed at high rate. No precautions for limiting the damage to the rock mass were taken. The joints and bedding in the upper portion of the shaft were frequent and had a high persistence. Given the proximity to the lake the discontinuities, especially on the south wall, contained significant amounts of water and a high flow was experienced throughout the life of the excavation.

Tunnel work started with the excavation and construction of the roof support arch, composed of 7 interlocking 1.9 m tunnels that were excavated using a pair of tunnel boring machines (TBM) and filled with concrete. The tunnel excavation occurred in 4 stages, as shown in Figure 6.2. The first stage was the excavation of two drift tunnels, the second was the centre portion of the tunnel, the third stage was the sidewalls, and the fourth was the excavation of the tunnel base to design elevation. The drifts were excavated with the same TBM's that were used for

the roof support arch and allowed for increased excavation rate of the main tunnel excavation (stage 2) using a large diesel hammer on an excavator. Sidewall excavation (stage 3) was conducted with a rotary head with carbide teeth that greatly reduced the damage to the rock mass and provided a relatively smooth surface. Site visit observations by the author during tunnel excavation noted that the rock mass was generally intact, with few visible joints, bedding planes or other discontinuities. Observed joints tended to have a strike perpendicular to the tunnel axis. Water flow through the joints was negligible.

The design decision for the shafts and tunnel was to seal the structure against water with a continuous PVC membrane against the rock face. In practice, significant water ingress through the membrane was experienced.

## 6.2 Purpose of chapter

This chapter presents a case study of the Billy Bishop Pedestrian Tunnel project, located in Georgian Bay shale in Toronto, Ontario, Canada. The mainland shaft excavation is analyzed with two goals. First, a calibration analysis of the elasto-plastic rock mass parameters, swelling rock parameters, and horizontal in-situ stress is conducted with the results compared to observed deformations. Second, the results of the calibration analysis are used to predict the long term effects of swelling on the mainland shaft structure and the effect of Extruded Polystyrene (EPS) foam in mitigating the swelling rock impact. The analyses are conducted using a swelling rock constitutive model developed for this thesis.

## 6.3 Geotechnical investigation

The BBPT project was constructed within the Georgian Bay Formation, which is composed predominantly of a soft grey shale, with lenses of harder siltstone and limestone. Previous work in the Georgian Bay Formation include the excavation for the Scotia Plaza (Trow and Lo 1989), the John Street Tunnel (Lo et al. 1987), and more recently the Coxwell Bypass Tunnel (Atlwegg et al. 2017). In-situ stress measurements were conducted at Scotia Plaza in downtown Toronto, and the Coxwell Bypass Tunnel which runs northward from the lakeshore roughly following the Don River. Results from Scotia Plaza indicate horizontal stresses between 2.0 and 5.2 MPa, with the principal maximum horizontal stress in the direction of approximately N58°E. Results from the Coxwell tunnel indicated horizontal stresses ranging



between 0.5 and 12 MPa. Near the lakeshore, the major horizontal stress ranged between 1.1 and 8.3 MPa, and the minor stress between 0.5 and 5.4 MPa, with the major principal stress direction is between N79°E to S64°E.

The site is located in the reclaimed land portion of the Toronto Lakefront. The soil is composed of hydraulically placed sandy silt fill overlaying a thin layer of native soft sand. Borehole logs at the mainland shaft indicated very poor conditions in the upper 1 m of rock (RQD <50%), fair quality for another 12 m in the rock (average RQD of 71%), with good to excellent quality rock for the remainder of the shaft (RQD between 85% and 100%).

The investigation included rock profiling and laboratory testing. Laboratory tests included uniaxial compression strength (UCS) tests and swelling behaviour tests of the host Georgian Bay shale.

### 6.3.1 Site and laboratory work conducted outside of this study

A geotechnical site inspection involving two boreholes, one at each shaft, was conducted by the Project Team. The boreholes were used for logging, inspection, sample retrieval, and in-situ stress testing. This section summarizes the findings.

A series of packer tests were conducted by the Project Team in the rock mass in 3 m intervals in an attempt to estimate the secondary or “mass” hydraulic conductivity. Many of the tests resulted in “no-take”, indicating an intact rock. Hydraulic conductivity ranged between  $1.4 \times 10^{-7}$  to  $1.3 \times 10^{-8}$  m/s where readings were successful.

Lab testing reported by Micic et al. (2016) indicated uniaxial compression strengths ranging between 18.3 to 19.4 MPa vertically and 9.3 to 16.9 MPa horizontally. The average vertical elastic modulus was 2000 MPa and the horizontal modulus was 9800 MPa.

Swelling tests were conducted on samples extracted from the borehole investigation. In total, eight Free Swell Tests (FST), six vertical Semi-Confined Swell Tests (SCST), 6 horizontal SCST, 1 vertical Null Swell Test (NST), and 2 horizontal NST were conducted.

Results from the tests were used to estimate the free swell potentials and critical stresses using the Lo and Hefny model (1996). Table 6.1 shows the average values obtained from the testing in the horizontal and vertical directions.

Table 6.1. Lo and Hefny swelling model parameters for the BBPT (Micic et al 2016)

Direction	Free swell potential	Critical stress
	% strain/log cycle	MPa
Horizontal	0.27	0.64
Vertical	0.90	1.2

Figure 6.5 shows the Lo and Hefny (1996) swelling model in the horizontal (a) and vertical (b) directions, composed of the test results. In the horizontal direction, both Null Swell Tests provided a result of 0.64 MPa. The vertical test results provide a sufficient trend line, with an average free swell rate of 0.9 % strain/log cycle of time and a critical stress of 1.2 MPa.

### 6.3.2 Laboratory work conducted for this study

Two sets of block samples were retrieved from the site. Blocks Sample #1 was retrieved from elevation 46.5 m and Block Sample #2 from 43 m. Block samples were retrieved using an excavator to isolate the required zone of rock, with the sample removed from the rock using hand tools such as hammers and shovels. Block samples were then wrapped in plastic cling-wrap and two layers of duct tape. Samples were returned to the university and stored in a cool, dry area until sample preparation and testing.

Block Sample #1 was taken from the shaft wall during excavation of the undercut, shown in Figure 6.3., and was composed of siltstone. Significant issues with coring of Block Sample #1 led to cutting square section test samples using a band saw. The samples were cut to approximately 50x50x100 mm. Strain gauges were attached to the sides of the samples, with vertical and horizontal directions on opposite faces, as shown in Figure 6.6. Each sample was tested in the vertical direction, as all horizontal samples broke during preparation. Results are summarized in Table 6.2, and are shown in Figure 6.7 to Figure 6.10.

Table 6.2. Uniaxial compression test results on Georgian Bay siltstone

Test	Unit weight (kN/m <sup>3</sup> )	Moisture content (%)	E <sub>50</sub> (MPa)	Poisson's Ratio	UCS (MPa)
1	25.9	0.95	38000	0.14	70.2
2	25.8	1.07	35100	0.14	55.5
3	25.9	1.03	25900	0.14	44.2
4	25.	0.95	32800	0.28	37.2

Test results indicate an average elastic modulus of 33000 MPa and a strength of 37.2 to 70.2 MPa. The moisture content values ranged between 0.95 and 1.07 %, which is lower than expected, and may have influenced the strength values. The samples were from the excavation wall, exposing the rock for some time, and may account for the lower than expected moisture content.

Block Sample #2 was retrieved from the shaft base during excavation of the elevator pits. The samples were composed of Georgian Bay shale, and were tested for vertical and horizontal strength and strain properties. The block sample was retrieved, protected, and brought back to the University of Western Ontario where cylindrical samples were drilled. The samples were drilled horizontally from the rock block. Each sample had approximate diameter and height of 32 mm and 64 mm, respectively. Two samples were tested with vertical 10 mm strain gauges, and two were tested for strength only. The results are summarized in Table 6.3 and shown in Figure 6.11. and Figure 6.12.

Table 6.3. Uniaxial compression test results on horizontal Georgian Bay shale samples

Test	Unit weight (kN/m <sup>3</sup> )	Moisture content (%)	E <sub>50</sub> (MPa)	UCS (MPa)
5	25.4	3.8	6600	15.3
6	25.6	3.8	22400	14.4
7	25.4	3.9	8900*	12.3
8	25.6	3.9	14900*	15.3

\*E<sub>50</sub> values are from piston deformation, not strain gauges

Results from the testing indicate that shale has a horizontal elastic modulus ranged between 6600 and 22400 MPa and an average strength of 14.3 MPa. All values are within expected ranges. The average horizontal elastic modulus of 13200 MPa is higher than the values obtained from previous works, which only measured the modulus in one sample.

In general, test results indicate that the siltstone were harder, more competent layers. The shale material properties were well within the known values for the Georgian Bay formation.

## 6.4 Monitoring program

The monitoring program conducted at the BBPT main shaft and tunnel consisted of 4 inclinometers around the mainland shaft, precision survey targets at the top of each pile and at points of interest around the excavation, and two horizontal borehole extensometers in the tunnel. Figure 6.1 shows the location of the north wall inclinometers at the shaft and the extensometers within the tunnel.

### 6.4.1 Inclinometers

Three of the borehole inclinometers were drilled to depths of 37 to 40 m deep, which were deeper than the bottom of excavation in order to capture as much deformation as possible. The

forth was installed above the undercut on the south side and was meant to observe deformations of the shoring wall near the dock wall. The inclinometer installed on the west wall was to capture deformations that may affect the active ferry terminal, but was damaged during excavation. Inclinometers 8 and BH01 were installed in series behind the north wall, with Inclinometer 8 approximately 1 m behind the face of excavation and BH01 approximately 4 m from the face. All inclinometer were installed prior rock excavation. Readings were taken weekly during active excavation and bi-weekly during tunnelling and shaft build-out.

Figure 6.13 provides an example of deformation observed in Inclinometer BH01 and Inclinometer 8. Two sets of readings are provided in the Figure, one when the excavation reached Elevation 48 m (27 m deep), and at final excavation depth of 34.5 m (Elevation 42 m). Maximum observed deformations in the rock reached approximately 20 mm. As observed by the difference between the two readings, approximately half of the total movement occurs during the last few metres of excavation. Further, a significant amount of deformation between the two readings occurs from Elevation 55 m and below. There appears to be minimal lateral deformation occurring below the excavation elevation, implying a limited vertical zone of influence below the shaft.

Readings from Inclinometer BH01, located 4 m from the excavation face indicate that the zone of influence is well beyond the inclinometer. In general, Inclinometer BH01 recorded half of the deformations observed in Inclinometer 8.

Figure 6.14 shows the deformation over time at three different elevations derived from inclinometer data. The figure also shows the excavation stages, and clearly shows that deformations continued during times of no excavation, indicating time-dependent swelling. The maximum rock deformations recorded were 20 mm at Inclinometer 8 and 13 mm at Inclinometer BH01, both at approximate elevation 60 m.

#### 6.4.2 Precision survey monitoring

A precision survey monitoring program was conducted during active excavation and build-out of the main shaft. The points of interest for this study are the survey targets located near the top of each shoring pile. An example reading from the north wall of the mainland shaft (bottom of shaft Elevation of 42 m) is provided in Figure 6.15. The results from the pile targets were

used to supplement the inclinometer results. The top of inclinometer deformation should match the observed pile deformation, as both were initialized prior to any major excavation and was generally accurate for this project.

The other observation to be noted is the positive vertical deformation. The readings imply that the secant shoring wall experienced uplift. In general, the middle of the north wall experienced a maximum of approximately 5 mm of uplift during excavation and shaft construction.

### 6.4.3 Extensometers

The borehole extensometers were installed at the tunnel spring line (Elevation 49 m) approximately 20 m from the main shaft under supervision and direction by the author. Figure 6.2. shows the tunnel section including the extensometers. The west extensometer was 8 m long, with nodes at the tunnel face, and 1 m, 2 m, 5 m, and 8 m deep. The east extensometer was 12 m long, with nodes at the tunnel face, and 2 m, 5 m, 8 m, and 12 m deep. The nodes were vibrating wire transducers, secured through friction by an inflatable copper bladder. Automatic daily readings were recorded on a data logger. The author collected the data weekly during active excavation, and monthly during build-out. Extensometer installation occurred when the centre tunnel excavation (stage 2 as mentioned previously) had progressed to 60 m in from the shaft face, which was 40 m past the extensometer location. For installation purposes, approximately 10 m of the sidewall (stage 3) was excavated at the extensometer location. Given the amount of excavation that occurred prior to the instrument installation, a majority of the elastic response was missed.

Results from the East and West borehole extensometers are shown in Figure 6.16 and Figure 6.17., respectively. Both extensometers observed less than 1 mm of deformation in the rock mass. There are distinct deformations that correlate to additional excavation and elastic stress relieve such as the sidewalls (stage 3) and floor (stage 4). Some time dependent deformation is observed in the first 100 days. After installation of the concrete tunnel structure negligible deformations are recorded. There are several reasons for the low recorded deformations. First is that the elastic deformations from the main excavation had occurred by the time the extensometers were installed and initialized. This is a significant issue when interpreting tunnel deformation. The second issue is the lack of water in the tunnel. Even though the

humidity was high, and some water was used for the excavation and construction, the amount of water observed within the rock was minimal. It was not enough to cause permanent flow from the rock face, only dampening the rock in small locations. As discussed in Lee and Lo (1993), without access to fresh water rock will not swell. The excavation technique would have affected the rock mass parameters, and thus the observed deformations. Unlike the shaft, which was excavated as quickly as possible with a large hydraulic hammer, the tunnel walls were excavated using a rotary head. This type of excavation reduces the Excavation Damage Zone, preserving the rock mass strength and elastic characteristics, reducing the opening and formation of discontinuities, and preserving the in-situ hydraulic conductivity. All of these things reduce the potential for elasto-plastic and swelling deformation.

The tunnel swelling deformations were analyzed by Lee (2017), who developed a swelling constitutive model in a commercial finite difference program. The rock parameters used in the analysis were taken from testing described in Micic et al. (2016) and the geotechnical baseline report (GBR). Lee used a generalized back analysis of the shaft behaviour to justify the model inputs. The horizontal stress was 5.1 MPa in the East West direction and 4.7 MPa in the north south direction. The horizontal swell potential used was between 0.03 and 0.04 %/log cycle, and the Suppression Pressure (Critical Stress) was 3 MPa. The swell potentials used in the analysis were considerably lower than those reported by Micic et al. (2016) and shown in Table 6.1. The swelling constitutive model used considered only one suppression pressure for all directions, even though the swelling parameters are known to be anisotropic. The suppression pressure chosen for the model is similar to the higher values measured in the vertical direction, and more than three times the value of the horizontal suppression pressure, which would control the deformation observed in the shaft and tunnel. The in-situ stress is also higher than expected, with values within the range measured at the lakeshore for the major horizontal stress, but are high for the minor horizontal stress.

Model results adequately follow observed deformations. However, the measured swelling deformations were less than 1 mm. The small deformations could be due to the high horizontal stress suppressing the swelling or reduced swelling potentials. If the lack of fresh water prevented the swelling deformations from increasing to the potential maximum, then it implies that the in-situ stress would have to be lower than the assumed value in the numerical model.

## 6.5 Shaft modeling

A finite element analysis study of the recorded rock deformations during excavation and construction of the mainland shaft and the effect on the final structure is conducted as part of the current study. The analysis is conducted in two phases. The first is a calibration analysis of the rock mass properties and compares the results of the analysis to the observed inclinometer deformations. The second phase uses the results of the calibration analysis to predict the stresses within the final shaft structure adjacent to the rock mass.

The quality of the shaft monitoring data collected from two inclinometers in series with observed elasto-plastic and time-dependent deformation and detailed excavation and construction records provided the necessary information for building and verifying the numerical model.

### 6.5.1 Geotechnical parameters

The engineering parameters used in the analyses were based of the findings from the geotechnical investigation and laboratory work, complemented with engineering judgement and experience working with similar materials.

The soil located on site is predominantly composed of soft hydraulic sandy fill, with a thin layer of soft native Silty Sand just above the bedrock. No testing was conducted on the overburden soils, but the author has significant experience in the area and engineering with these soils. The analysis assumes that the fill and native soil are similar enough to be considered one unit, with low elastic modulus and effective friction angle.

The rock mass parameters were based on the results of the laboratory tests and borehole investigation. Horizontal deformations govern the major engineering concerns, so the results from the horizontal tests were used to estimate the rock mass properties. The average intact horizontal uniaxial compression tests were 14.3 MPa, and the average horizontal elastic modulus ( $E_{50}$ ) was 13200 MPa.

Measurements and observations (fracture frequency, total core recovery, rock quality designation) from the borehole investigation provided a clear indication that the rock above approximate Elevation 55 m was of lower quality, with an RQD between 60 and 95%, with an



average of 78%. The average RQD of the rock below Elevation 55 m is 96%. Figure 6.19 shows the RQD with depth for the BH01 at the mainland shaft location.

Using the UCS test results and the borehole information, the rock mass parameters were initially estimated using the Hoek-Brown Failure Criterion (Hoek and Brown 1980). Required inputs are the uniaxial compressive strength (UCS), intact elastic modulus ( $E_i$ ), Geological Strength Index (GSI), a rock type material constant ( $m_i$ ), and disturbance factor (D). The material constant for shales is six (6) (Hoek et al. 2005). The disturbance factor is based on the energy used during excavation of the rock and the potential damage taken by the rock mass during excavation. For heavy hydraulic hammers and scrapping, a disturbance factor of 0.5 was chosen. The GSI value is typically derived from Barton's (1989) Rock Mass Rating (RMR), with Hoek et al. (2005) recommending the following relationship:

$$GSI = RMR'_{89} - 5 \quad [\text{Eq. 6.1}]$$

The  $RMR'_{89}$  value is the rock mass rating using Bieniawski's (1989) updated methodology. The weathered and unweathered RMR were estimated to be 49 and 66, respectively. RMR values are established based on some subjective observations and are intrinsically variable to some extent.

The rock mass modulus is material parameter that will most effect the deformations. Observations from site indicated negligible yielding of the rock mass, since the only observed discontinuities were naturally occurring and no rubble zones developed. The rock mass modulus estimation is affected by the results of the intact modulus, the GSI, and the disturbance factor (D). For the purposes of this study, it is assumed that the rock mass modulus can vary up to  $\pm 40\%$ .

The in-situ horizontal stress is a significant input parameter. The magnitude of deformations due to excavation is driven by the in-situ stress. The swell potential at any point is determined by the confining stresses. If the in-situ stress is high, excavate results in larger elasto-plastic deformation and lower zone of swelling. Testing results near the lakeshore, as discussed in Section 1, indicated that the minor principal stresses could be as low as 0.5 MPa. The orientation of the cross section being analyzed is approximately N18°W which is in line with

the typical minimum stress (Lo 1989). For this study, the horizontal stress was assumed to be between 1.0 MPa and 3.0 MPa.

This study is predominantly concerned with the effects of long-term swelling on the mainland elevator shaft. The swelling parameters discussed in Section 6.3.1 will form the basis for much of the calibration analysis. Results from the vertical swell testing show a clear envelope of potentials. The horizontal results do not have the same pattern, but that is likely a result from the number of tests performed. This study will focus on the horizontal swelling more than the vertical as the main driver of TDD impact on the buried structure. Horizontal test results indicate a clear suppression pressure of 0.64 MPa, with free swell potentials ranging between 0.15 and 0.3 %/log cycle of time. These values will be used as the study envelope for the calibration analysis.

A known issue of modelling time-dependent behaviour is the vertical suppression pressure value is typically higher than the in-situ vertical stress (Lee 2017 and Carvalho 2015). Thus, if the suppression pressure value obtained from the laboratory swelling tests is used in the analysis, the numerical model will predict upward swelling, often by a significant amount, contrary to observed deformations in the field. The practical solution to this problem is to adjust the vertical suppression pressure to the in-situ stress state.

The first phase of the numerical analysis considers the variability in three of the major inputs: rock mass elastic modulus, in-situ horizontal stress, and horizontal swelling potential. Table 6.4. summarizes the variations used for the four inputs discussed.

Table 6.5 summarizes the strength and strain parameters used in the analyses. A linear-elastic perfectly plastic constitutive model was used in the analysis with a Mohr-Coulomb yield surface for the soil and rock units. The swelling parameters used in the analysis are provided in Table 6.1 in Section 6.3.1. For the analyses the vertical suppression pressure was adjusted to the in-situ pressure.

Table 6.4. Variable parameters used in calibration analysis.

Parameter		Minimal value	Middle of the range value	Maximum value
Elastic modulus [MPa]	Weathered rock	780	1300	1800
	Unweathered Rock	2300	3800	5300
Horizontal stress [MPa]		1	2	3
Horizontal free swell potential [strain/log cycle of time]		$1.5 \times 10^{-3}$	$2.5 \times 10^{-3}$	$3.0 \times 10^{-3}$

## 6.5.2 Model details and phases

The finite element program PLAXIS 2D (Brinkgreve 2016) was used to develop two-dimensional finite element model of the mainland shaft considering the geometry described in Section 6.1 and the geotechnical parameters described in Section 6.5.1.

The results from the phase 1 calibration analysis will be compared with the inclinometer and precision survey monitoring results discussed in Sections 6.4.1 and 6.4.2. Results showing an acceptable match to the observed behaviour will be used to estimate potential stresses on the final mainland shaft structure and the effect of EPS foam in mitigating swelling impact.

The model was 200 m wide and 70 m deep. The model contained 1387 elements, with a greater density within and around the excavation. Boundary conditions and mesh are shown in Figure 6.18. Triangular 15-noded finite elements were used to simulate the soil and rock in the

Table 6.5. Initial soil and rock parameters for finite element analysis.

Soil/Rock	Unit weight	Elastic modulus	Poisson's ratio	Effective cohesion	Effective friction angle
	[kN/m <sup>3</sup> ]	[MPa]		[kPa]	[degrees]
Soil	18	50	0.30	1.0	25
Weathered rock	24	780 – 1800	0.25	420	20
Unweathered rock	26	2300 – 5300	0.25	620	26

numerical model. The soil and rock behaviour were simulated using the linear-elastic perfectly-plastic Mohr-Coulomb model. Structural elements were modelled using linear-elastic theory and properties. The vertical boundary was placed at a distance of 100 m from the center of the shaft to minimize effect of boundaries on the calculated response. The bottom boundary was placed at a distance 34 m from the bottom of the shaft. The vertical boundaries were fixed horizontally and free in the vertical direction. The lower boundary was fixed in both horizontal and vertical directions.

The initial phases established the in-situ stresses in the soil and rock, and involved adding the Western Channel and dock wall. The excavation and shoring installation, including swelling steps, were modelled in 30 steps, with excavation limited to a maximum of 2.0 m in the rock. The structure build-out was modelled sequentially in 12 steps, roughly matching the construction sequence. In order to predict the long-term performance of the shaft, a 50 year period was modelled using the swelling rock constitutive model. The structural section is shown in Figure 6.4. The structure is composed of elevator lobbies at the top and bottom of

the shaft, with the portion between composed of compact fill around the structural elevator shaft.

The configuration of the structural elements used in the analysis was based on the actual design dimensions, and they are assumed to behave as linear-elastic materials. A 200 mm thick Extruded Polystyrene (EPS) 39 layer was installed between the rock and the lower elevator shaft. The EPS was treated as a linear-elastic material with properties derived from ASTM D6817 and testing done in Chapter 4.

The analysis predicted the stresses and strains within the zone of influence of the excavation, within the limitations of the assumed soil and rock conditions.

As the model adopts a two-dimensional plane strain behaviour, the inputs and outputs are in terms of units per metre of shoring wall. Structural information and external force inputs must be adjusted, based upon their respective spacing, to a unit thickness equivalent. Structural results must be scaled to the design spacing. For example, the caisson wall is modelled as a plate with combined structural capabilities of the continuous concrete secant caissons with the steel wide-flange king piles, which have a spacing of 2.25 m centre-to-centre. The structural properties of the caisson wall will have to be adjusted to account for the king pile spacing, and the resulting numerical model stresses acting on the king piles will have to be multiplied by their spacing.

### 6.5.3 Phase 2 – Long-term stresses on shaft structure

The results from the calibration analysis were used to conduct a long-term analysis on possible stresses and deformations on the shaft. The analysis was extended to include 12 phases in order to model the construction of the structure and a 50 year swelling period after the completion of construction. As can be noted from the structure cross-section shown in Figure 6.4., the lower portion is 1100 mm thick concrete, while the segment from the bottom floor to elevation 65.5 m is 800 mm thick. The remaining walls above Elevation 65.5 m is 500 mm thick. It is also noted Figure 6.4. that 200 mm thick EPS 39 foam boards were placed along the vertical sides of the structure from the shaft base up to Elevation 60.8 m,

The performance of the base portion of the structure, where the EPS is placed directly between the structure and excavation face, is of particular interest herein. This analysis will consider the 1100 mm thick wall at the base of the shaft structure on the north side, as indicated in Figure 6.4. This portion of the wall was chosen as there was only 200 mm of EPS foam between it and the rock and the north side of the structure would not be influenced by either the south wall undercut or the tunnel excavation.

Figure 6.23. shows the finite element details with the EPS foam and structural members adjacent to the rock at the bottom level of the shaft. The analysis assumed that the EPS was a linear elastic material, which is appropriate as long as the strain in the EPS material is less than 10%. The elastic modulus of EPS 39 is 7.7 MPa and was determined from the testing program discussed in Chapter 4 (Compressible/Crushable Materials). The concrete walls, roof, and supports were modeled with linear-elastic plate elements. The concrete elastic modulus was calculated according to CSA A23.3-04 section 8.6.2.3:

$$E_c = 4500\sqrt{f'_c} \quad [\text{Eq. 6.2}]$$

Where  $f'_c$  is 35 MPa. The structural units were modeled as plates. The shaft was supported by internal beams modelled as node-to-node anchors.

As discussed previously, the analysis considered three conditions of stress and strain for the prediction of rock swelling 50 years after construction, i.e.:

Case 1: Rock mass elastic modulus of 2300 MPa and horizontal stress of 1 MPa;

Case 2: Rock mass elastic modulus of 3800 MPa and horizontal stress of 2 MPa;

Case 3: Rock mass elastic modulus of 5300 MPa and horizontal stress of 3 MPa.

Considering the minimal effect of horizontal swelling potential, the average free swell rate and suppression pressure of 0.25 % strain/log cycle of time and 0.64 MPa, respectively, were used in all three analyses.

Strain in the EPS layer is shown in Figure 6.24 for the analysis using an elastic modulus of 3800 MPa and horizontal stress of 2 MPa, and indicates less than 10% strain along the span of the 1100 thick structural wall, justifying the linear-elastic assumption. Strains approach 10% at the connection between the structural base slab and the wall, which is a typical location of high stress. The other analyses show similar results, with strain under 10%.

Each analysis was run with and without using EPS 39 foam between the rock and the structure to evaluate the effect of EPS on mitigating the stresses imparted onto the structure from the swelling rock. Table 6.6 summarizes results of the runs, detailing the maximum and minimum bending moments. The Table includes the bending moments at the end of construction, after 50 years, and the change in stress due to swelling.

Table 6.6. Effect of EPS 39 on bending moments of foundation wall due to swelling rock.

Condition	EPS	Bending moment before swelling [kNm]		Bending moment after swelling [kNm]		Change in moment due to swelling [kNm]	
		Max	Min	Max	Min	Max	Min
E = 2300 MPa	Yes	773	-1260	1466	-2035	693.5	-775
$\sigma_h = 1$ MPa	No	213.5	-734	1419	-2001	1206	-1268
E = 3800 MPa	Yes	799	-1305	1513	-2137	714	-832
$\sigma_h = 2$ MPa	No	185	-741	1410	-2024	1225	-1309
E = 5300 MPa	Yes	816	-1348	1468	-2098	520.4	-668
$\sigma_h = 3$ MPa	No	160	-737	1408	-2025	1248.1	-1289

Results in Table 6.6 provide two significant observations. First, the total magnitude of stresses acting on the wall after 50 years is larger when the EPS 39 foam is present in all cases. When comparing the moments at the end of construction, the results from the numerical analysis provide much higher moments when the EPS is present. This would indicate that stresses during construction accumulate in the stiffer concrete structure rather than the softer EPS foam.

A second observation is the effect of EPS in reducing the swelling rock stress acting on the structure. In each case, the stress reduction due to swelling was between 39 and 58%. The numerical results indicate that the EPS is very effective at mitigating the effect of swelling on buried structures.

These results are explored in Figure 6.25, which show analysis results for Case 1. The figure shows the total normal stresses acting on the wall and the bending moments in a combination of four conditions: With and Without EPS foam, and Before Swelling and After Swelling. The Before Swelling case was taken as the moment construction of the shaft was finished. The After Swelling case provides forces and stresses after 50 years.

In Figure 6.25, the With EPS case show stresses gradually increasing with depth (compression in PLAXIS is negative), with a similar trend in the After Swelling case but with higher stresses, as expected. When no foam is present, the stress diagram shows obvious differences from the With EPS case. The Without EPS, Before Swelling case shows normal stress in tension at the top with minimal compressive stresses over the majority of the wall height, and negligible stresses at the bottom corner. After Swelling, the top and bottom corners of the wall show



large compressive stresses, with an increase from the Before Swelling in between the corners. The lack of EPS foam results in large stress concentrations at the foundation wall corners. Figure 6.26 is used to check deformations and shows the horizontal deformation at the face of excavation and of the foundation wall Before Swelling. In the case With EPS, the foundation wall top corner deformation (10 mm) is less than the deformation of the excavation face (21 mm), indicating that the EPS foam is under compression between the rock and structure. When the foundation wall is up against the rock, the deformations of the rock and structure at the top corner are 27 and 26 mm, respectively. The Without EPS case results in greater deformations at the top corner of the wall. The difference in deformations at the top corner between the With and Without EPS cases are a direct result of the presence of EPS foam as the loading and construction sequence is the same. The Without EPS, Before Swelling wall deformations, which are driven by the construction of the shaft, are pulling the top corner of the wall into the excavation. The geometry of the shaft structure, with the overhang at the top of the foundation wall, would result in inward rotations in a similar free standing structure. In the With EPS case, the lower horizontal deformations show that the EPS foams are preventing similar deformations. When looking at the relative deformations between the bottom and top corners of the foundation wall, the With EPS foams show a difference of 10 mm, while the Without EPS foams show a difference of 16 mm. Wall rotations Before Swelling are checked in Figure 6.27. The Without EPS condition results in a greater absolute magnitude of rotation at the top corner, as expected. The With EPS case shows  $0.03^\circ$  rotation at the top corner compared to  $0.04^\circ$  for the Without EPS case. The rotational behaviour of the Without EPS case also shows more rotation along the entire height of the foundation wall. Analysis results show that the EPS foams are put into compression during construction of the structure, allowing for a lower impact on the foundation wall due to construction. In the Without EPS case, the stiffer rock encourages higher rotation and greater deformations over the height of the foundation wall. This difference in behaviour results in calculated differences in applied normal stresses.

Effects of EPS foam can also be observed in Figure 6.25. In the case of With EPS, we can see that the bending moments approximately double between the end of construction and after 50 years. In the Without EPS case, the maximum bending moments increases from 213 kNm to 1495 kNm, an increase of approximately 700%. The negative bending moment decreases from -734 to -2001 kNm, an absolute magnitude increase of approximately 270%. As observed in

the Figure and detailed in Table 6.6, the EPS foams reduce the impact of swelling as the absolute magnitude of bending moment increase is far less for the With EPS case than the Without EPS case. When comparing the bending moments After swelling, there is minor difference between the With EPS case ( $|2035|$  kN) and Without EPS case ( $|2001|$  kN).

Figure 6.28 and Figure 6.29 show the normal forces acting on and bending moments in the foundation wall for Case 2 and Case 3, respectively. In general, the observed stresses and bending moments follow the same patterns as discussed in detail for Case 1. For both the Case 2 and Case 3 the applied normal forces on the foundation wall corners are significantly greater. For Case 1, the minimum applied stress was -1945 kPa. For Case 2 and Case three the force decreased to -8433 and -8520 kPa, respectively. This would indicate that the stiffer rock mass and higher horizontal in-situ stress results in greater concentration of forces at the structural corners.

## 6.6 Discussion and conclusions

Excavation of the Billy Bishop Pedestrian Tunnel was completed in 2015 and is currently serving as the main pedestrian link between the mainland and the island airport. Excavated in Georgian Bay shale, the mainland entry shaft was subjected to an elevated horizontal in-situ stress and time-dependent shale swelling, resulting in up to 25 mm of horizontal deformation.

Back analysis of the monitoring indicates that the horizontal stress was within 1 to 3 MPa. This value is typical for the minor horizontal stresses that have been measured in the Georgian Bay Shale. The orientation of the section analyzed align with the typical minimum principal stress.

Results from the back analysis indicate that elastic modulus and horizontal in-situ stress control the deformations during excavation, more so than the horizontal swelling potential. The calculated vertical deformation at the shoring wall was between 5 and 10 mm, which matches the observed deformations from survey monitoring. The predicted deformation over 50 years follows the expected logarithmic behaviour, with approximately 15 mm calculated from the finite element analyses using the time-dependent deformation constitutive model. Stresses

imparted on the structural walls of the shaft were within allowable limits. The 200 mm EPS 39 foam between the rock and structure acted as a buffer from the swelling effects. The foam remained within the elastic behaviour with strain under 10 %. The presence of EPS foam greatly reduces the effect of swelling on the adjacent structure, possibly as much as 58%. However, it does have the effect of adding more stress during the construction phases. This may be a site-specific effect but should be considered when designing swelling mitigation details.

Monitoring results during construction show significantly more swelling deformations in the shaft than in the tunnel. Shaft excavation occurred with high energy and damaging hydraulic hammering. Tunnel excavation included TBM based construction of a strong roof structure and gentle excavation of the last 300 mm of rock using a rototiller. These differences in excavation methodologies likely contributed to the differences in rock mass quality observed at the excavation face. Orientation likely played a significant role in the rock mass behaviour as well. The long axis of the shaft was oriented in the same direction as the strike of the major joint family in the Georgian Bay Formation, while the tunnel axis was perpendicular. Despite the relatively low cover for a tunnel of this size, the tunnel was still located in a region of rock with an RQD of 96% measured at the mainland shaft. The large horizontal deformations and observable swelling behaviour in the shaft is likely a result of the higher energy excavation, lower RQD values in the upper region, larger likely Excavation Damage Zone, the orientation of the long axis of excavation, and access to fresh water. The measured tunnel deformations were minimal. Although the elastic response to the main tunnel excavation was missed, the observed deformations after that were still under 1 mm, with negligible swelling behaviour observed.

It should be noted that the rock mass was of high quality and not subject to fresh water; Two conditions that would significantly limit swelling deformations. Since the tunnel and shaft were sealed against water, it would not be unexpected that the rock mass in the tunnel will become saturated in the long term, during the life of the structure. If so, additional swelling deformations may be initiated and would have to be controlled by the suppression pressures from the in-situ stress and the tunnel structure. Since the bending moments do not show the

same magnitude of absolute increase, the excess stress must be taken by the ceiling and floor structures.

### 6.6.1 Phase 1 – Model calibration and comparison with mainland shaft monitoring

A calibration analysis of the mainland shaft excavation was conducted, with results compared to the inclinometer readings taken throughout excavation and shoring construction. The elastic modulus, in-situ stress, and horizontal free swell potential were varied in the analyses in order to identify combinations that adequately match the observed inclinometer behaviour. Table 6.4. shows the values used in the calibration analysis. In total, twenty-seven analyses were conducted, with the parameters being either the maximum, middle of the range, or minimum values.

Results for each analysis are compared to three plots discussed in Section 6.4:

1. Inclinometer BH01 at end of excavation (Figure 6.20)
2. Inclinometer 8 at end of excavation (Figure 6.21)
3. Inclinometer 8 movement over time at Elevation 45 m (Figure 6.22)

Figure 6.20 compares the calculated results to the measurements from Inclinometer BH01 at the end of excavation, Figure 6.21 compares the calculated response to measurements from Inclinometer 8, and Figure 6.22 compares the calculated and measured deformation over time.

In the comparisons shown in Figures 6.20 and 6.21, the finite element analyses results have been zeroed at the bottom of inclinometer elevation to properly compare between readings and results. The inclinometer base is assumed to have zero deformation, while the numerical results show movement extending below the inclinometer bases.

The finite element results in Figure 6.22 have also to be adjusted. In order to properly compare the calculated results to the monitoring data, the deformation at the bottom of the inclinometers was subtracted from the target Elevations (45 m and 60 m) and then zeroed. Additional analyses were conducted considering higher horizontal stresses, but the results demonstrated that the rock mass would experience excessive yielding during set-up phases and excavation.

Results from the analyses indicate that at horizontal stress of 3 MPa, the resulting deformations for an elastic modulus of 3800 and 2300 MPa greatly overpredict the deformations observed in both inclinometers. Results from assuming horizontal stress of 1 MPa under predicted deformations with an elastic modulus of 3800 and 5300 MPa. Results using horizontal stress of 2 MPa are generally within the range of observed deformations, especially with an elastic modulus of 3800 MPa. In general, the effects from the varying horizontal free swell potential were negligible, with minimal difference in deformations.

It is interesting to note from Figure 6.22 that the inclinometer results at Elevation 60 m demonstrate a reduction in horizontal deformation between 560 and 580 days. The inclinometer readings are derived assuming the base does not move. However, the results of the finite element analysis show that the deformation at the base of the inclinometer is greater than the deformation at the midpoint of the excavation due to the excavation from Elevation 45 m down to 42 m. This observation from the finite element analysis results explains the measured deformation away from excavation; however, the FEA predicts the magnitude of the deformation reasonably well, but incorrectly evaluated the time for the observed deformation.

## **6.7 Acknowledgements:**

The author would like to acknowledge the support and aid from NSERC and the project team: Isherwood Associates, Technicore Underground Inc., and EXP Services Inc.

6.8 Figures

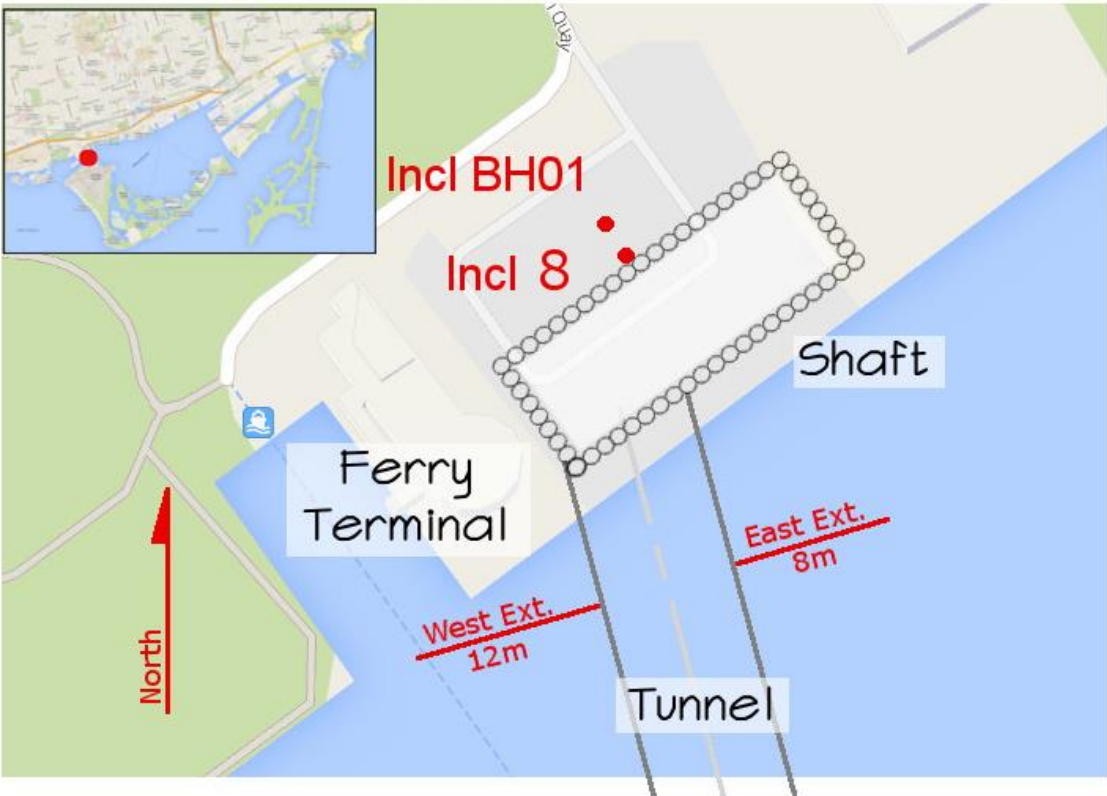


Figure 6.1. Billy Bishop Pedestrian Tunnel mainland shaft.

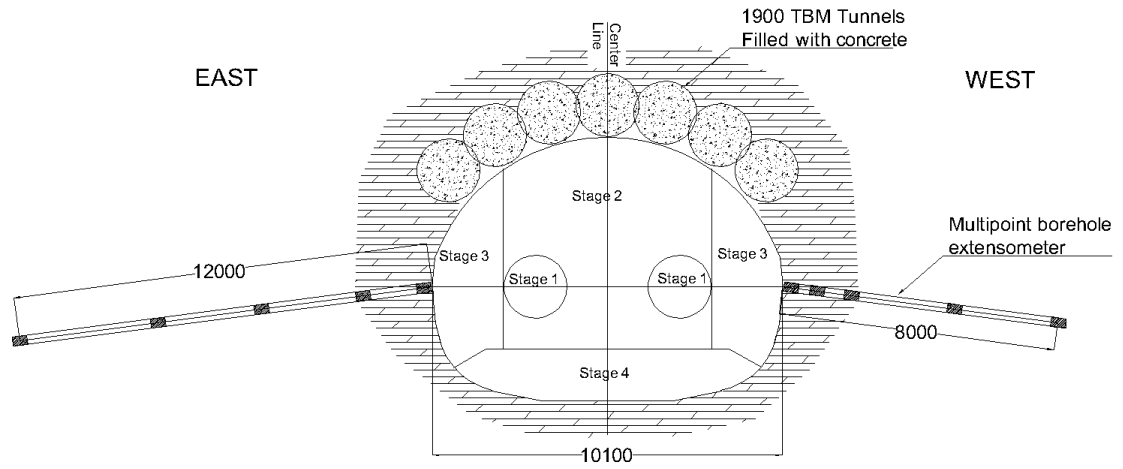


Figure 6.2. Billy Bishop Pedestrian Tunnel typical section (Dimensions in mm).

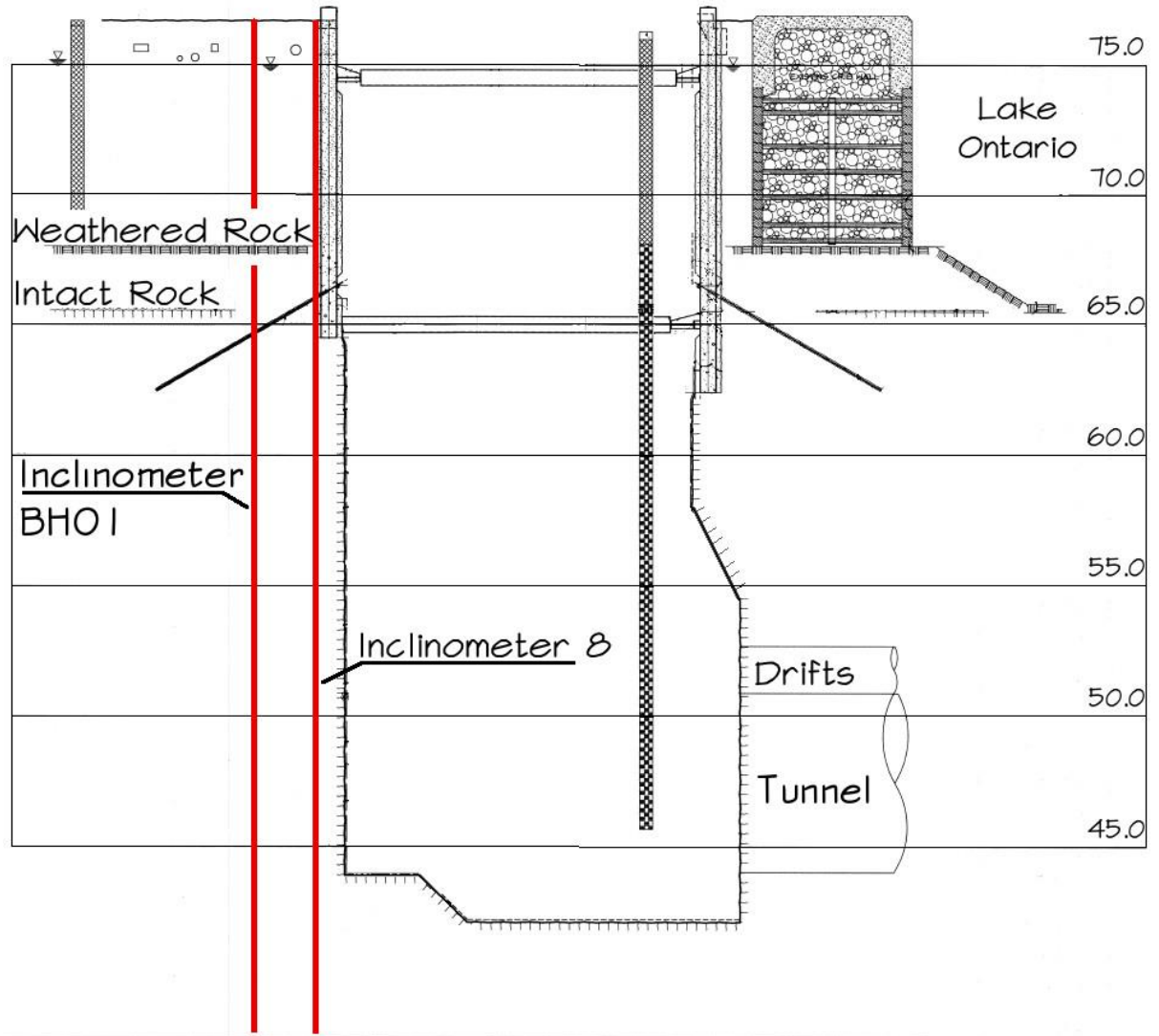


Figure 6.3. Billy Bishop Pedestrian Tunnel mainland shaft section (Elevations in m).



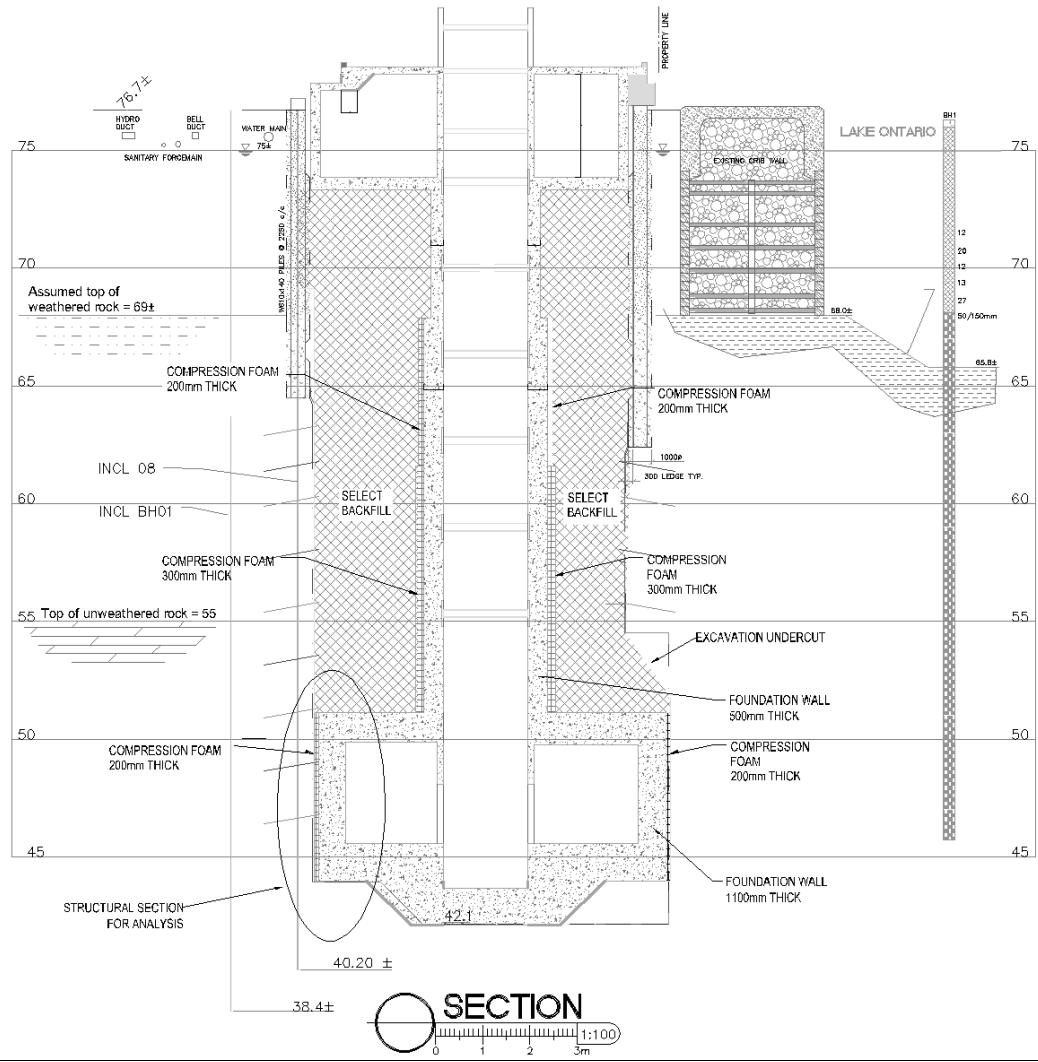


Figure 6.4. Shaft structure at section (Elevations in m).

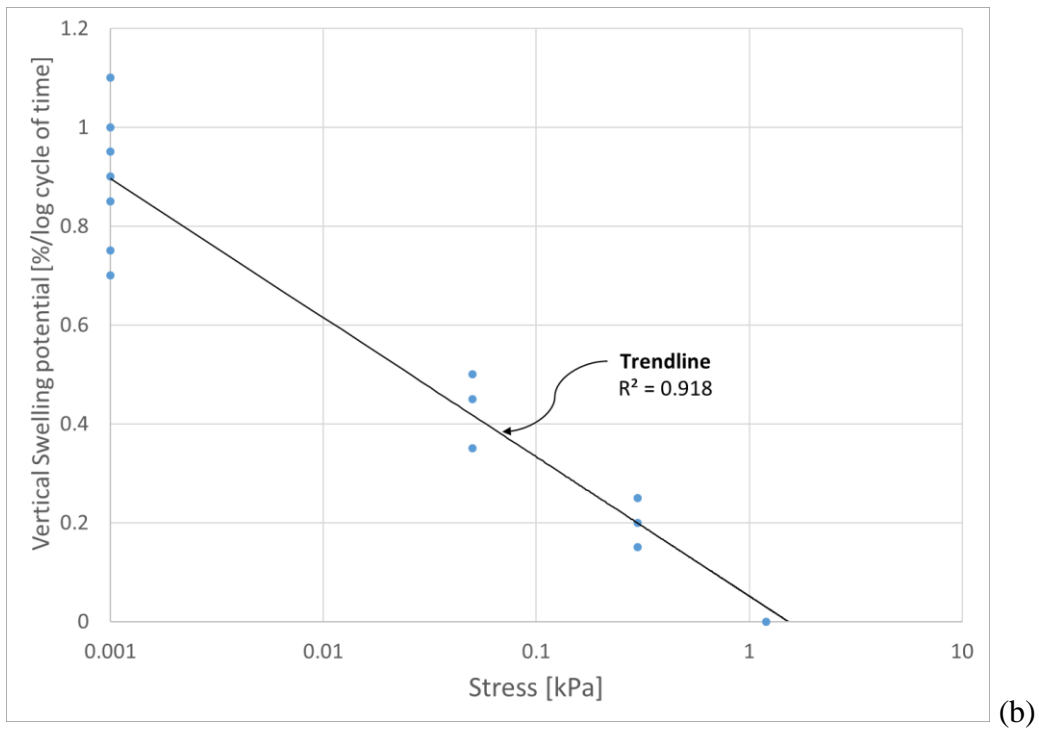
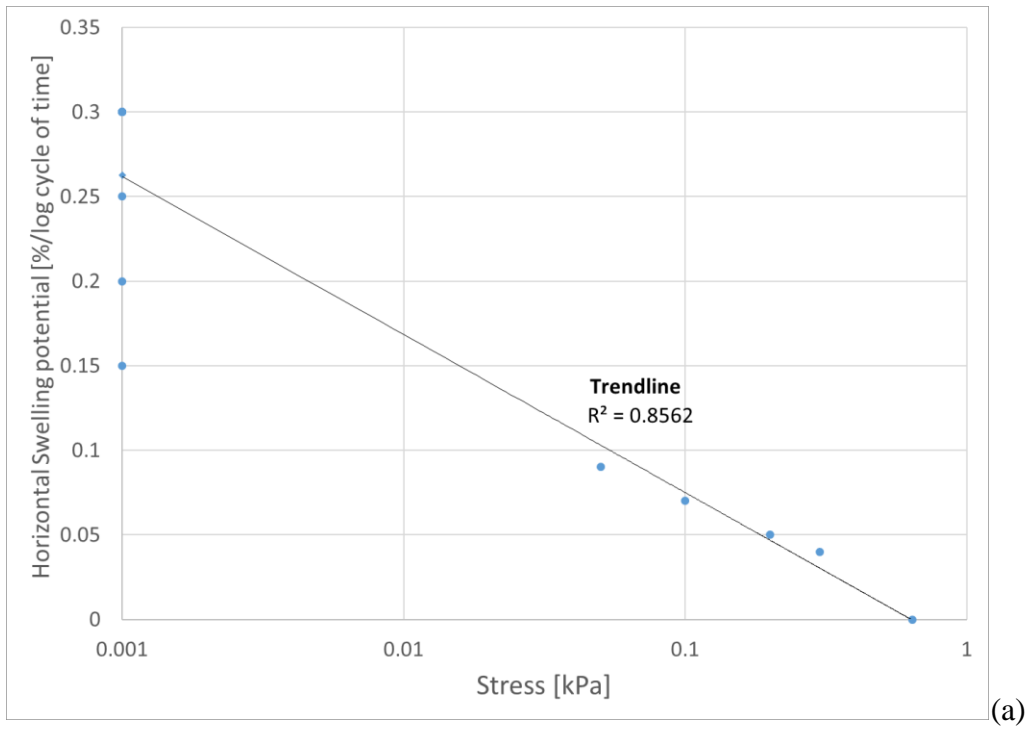


Figure 6.5. Measured horizontal (a) and vertical (b) swell potentials (Micic et al 2016).

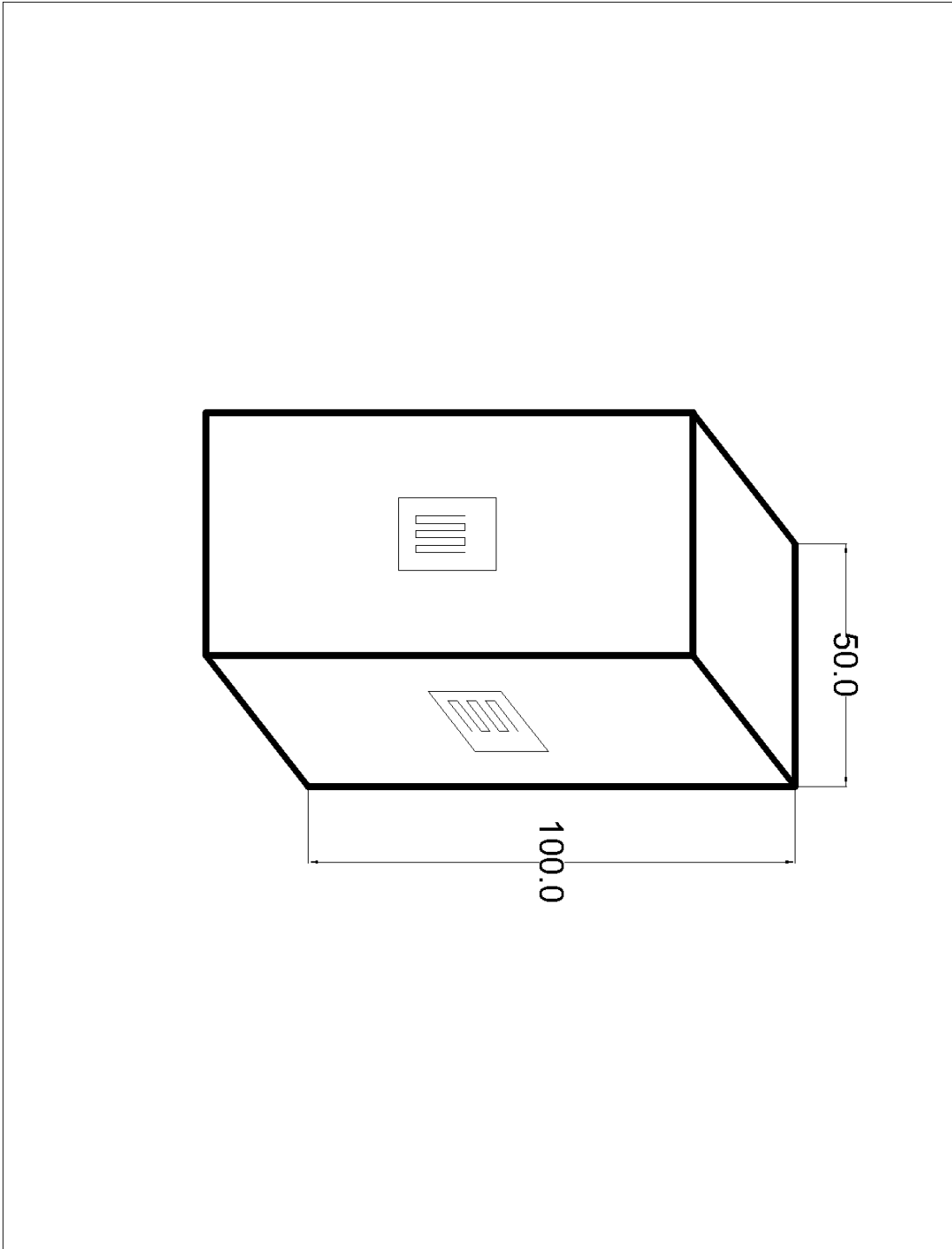


Figure 6.6. Square UCS test sample.

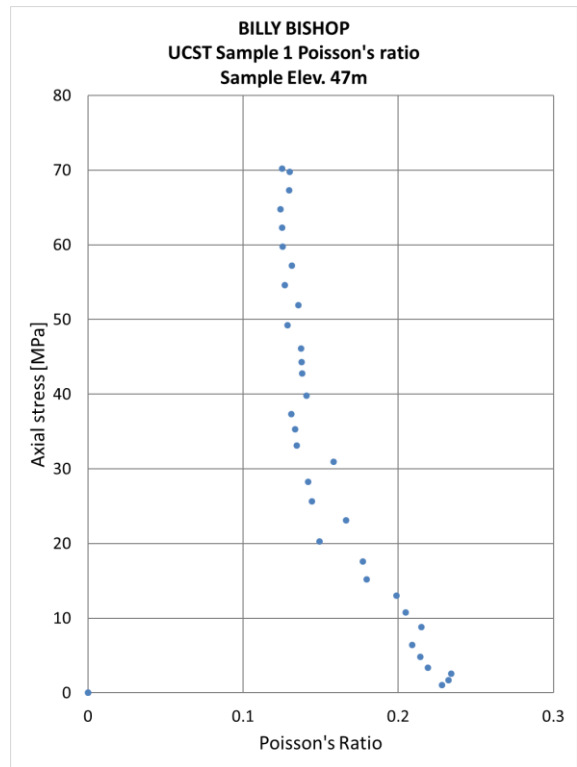
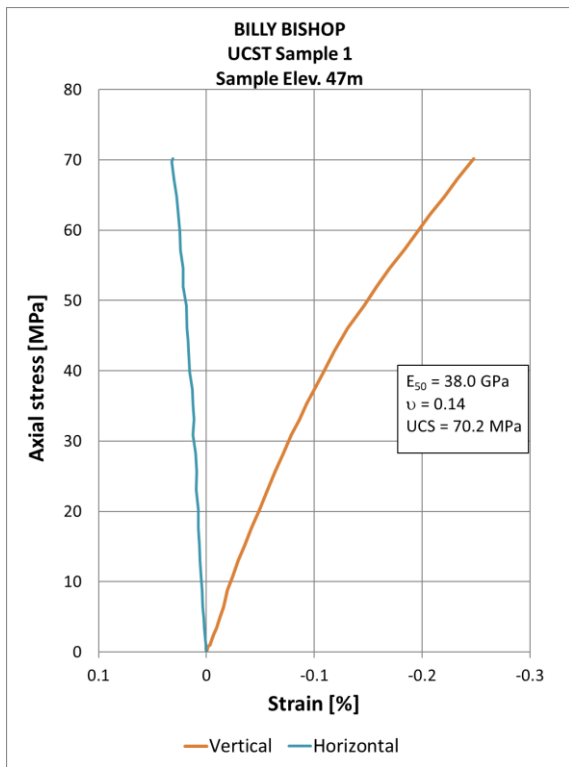


Figure 6.7. Results from USC test 1.

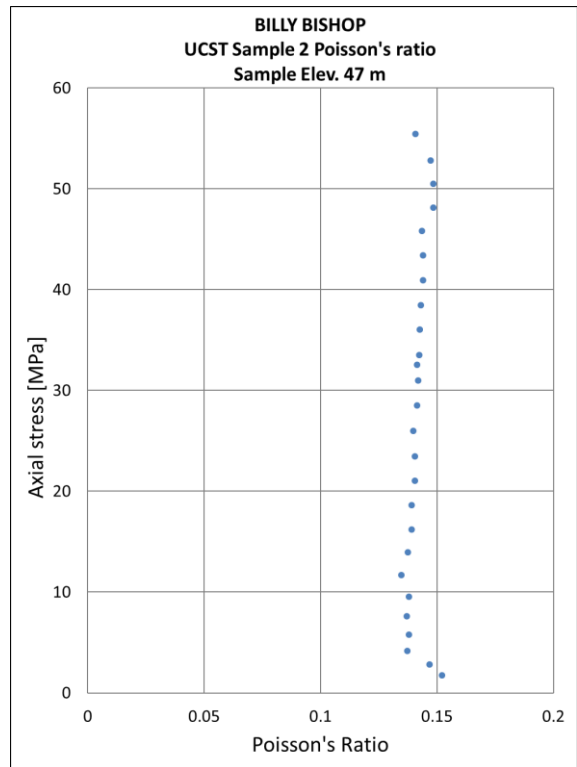
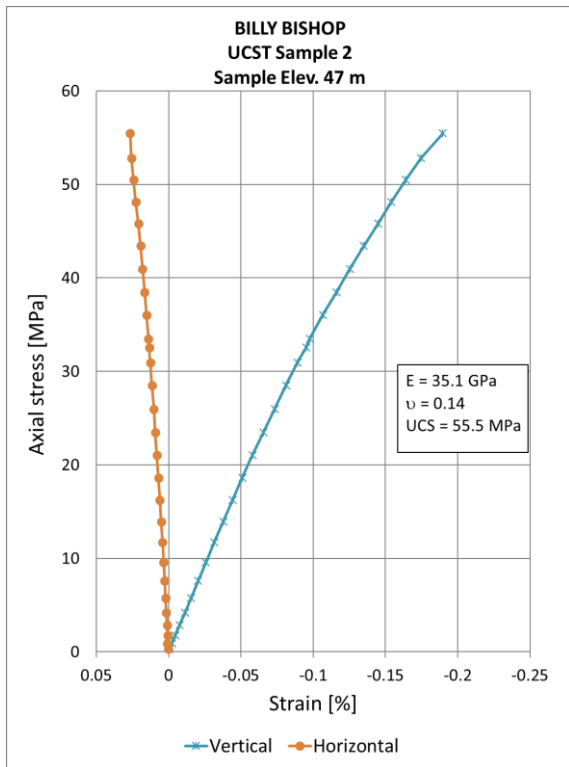


Figure 6.8. Results from USC test 2.

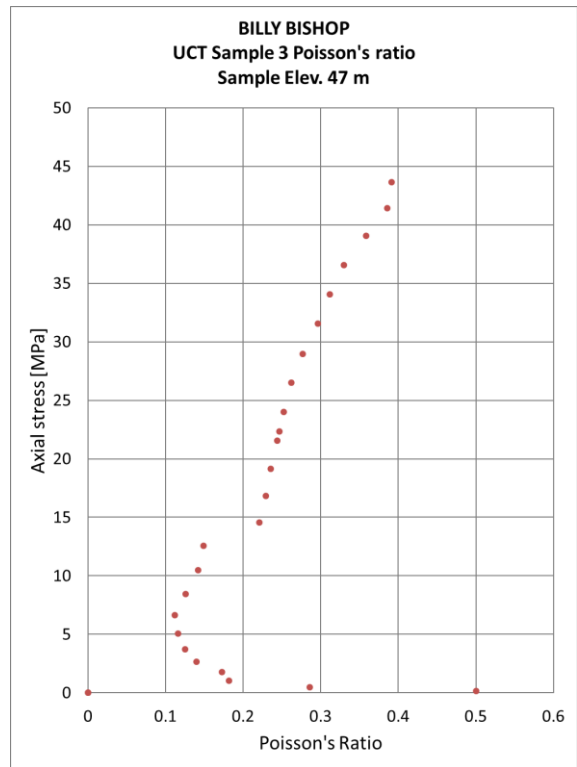
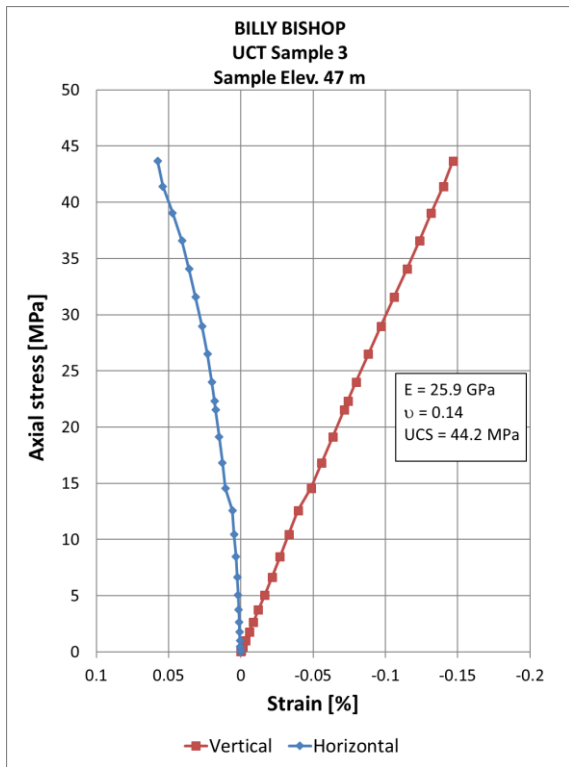


Figure 6.9. Results from USC test 3.

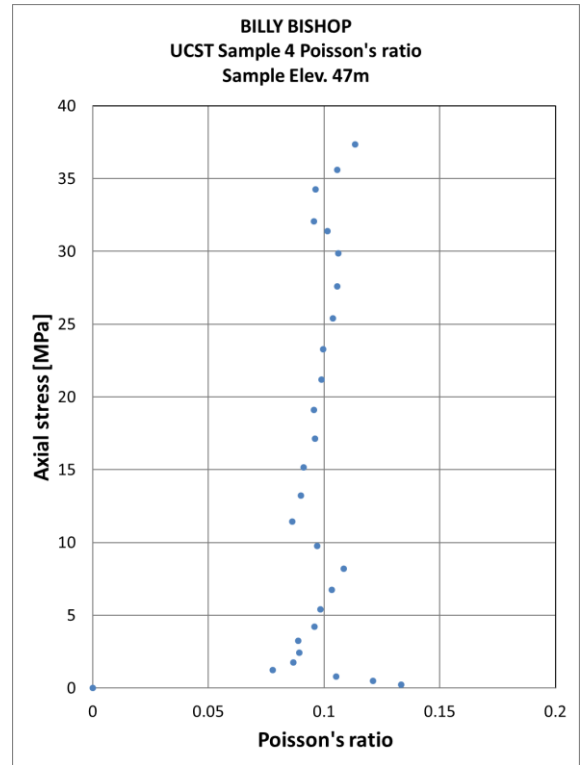
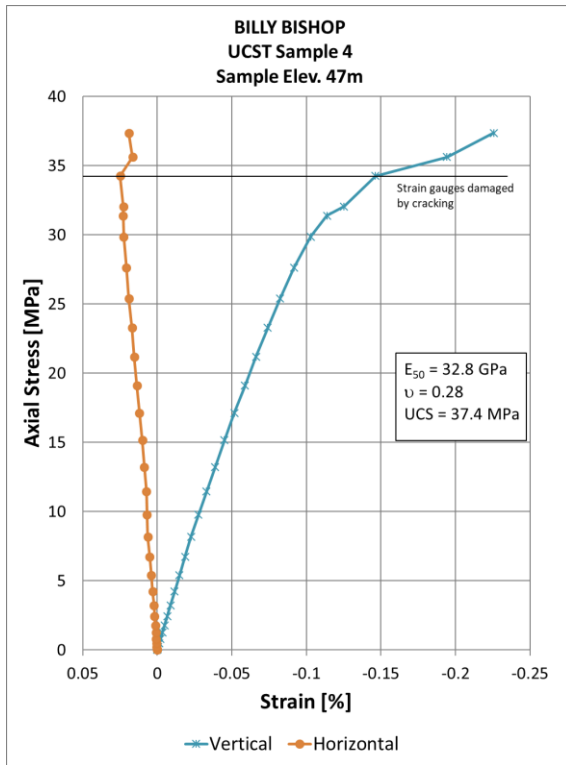


Figure 6.10. Results from USC test 4.

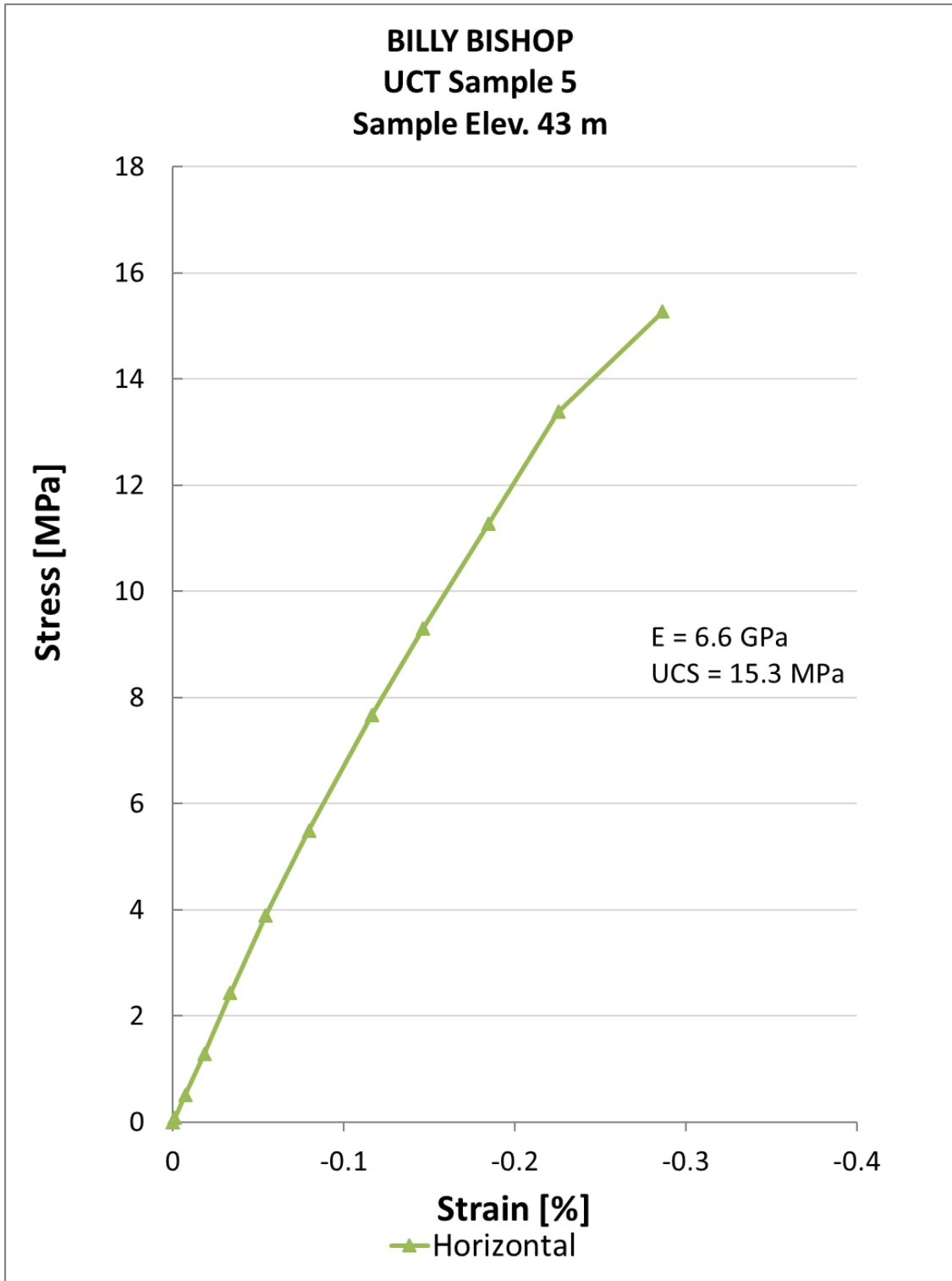


Figure 6.11. Horizontal UCST results from Sample 5.



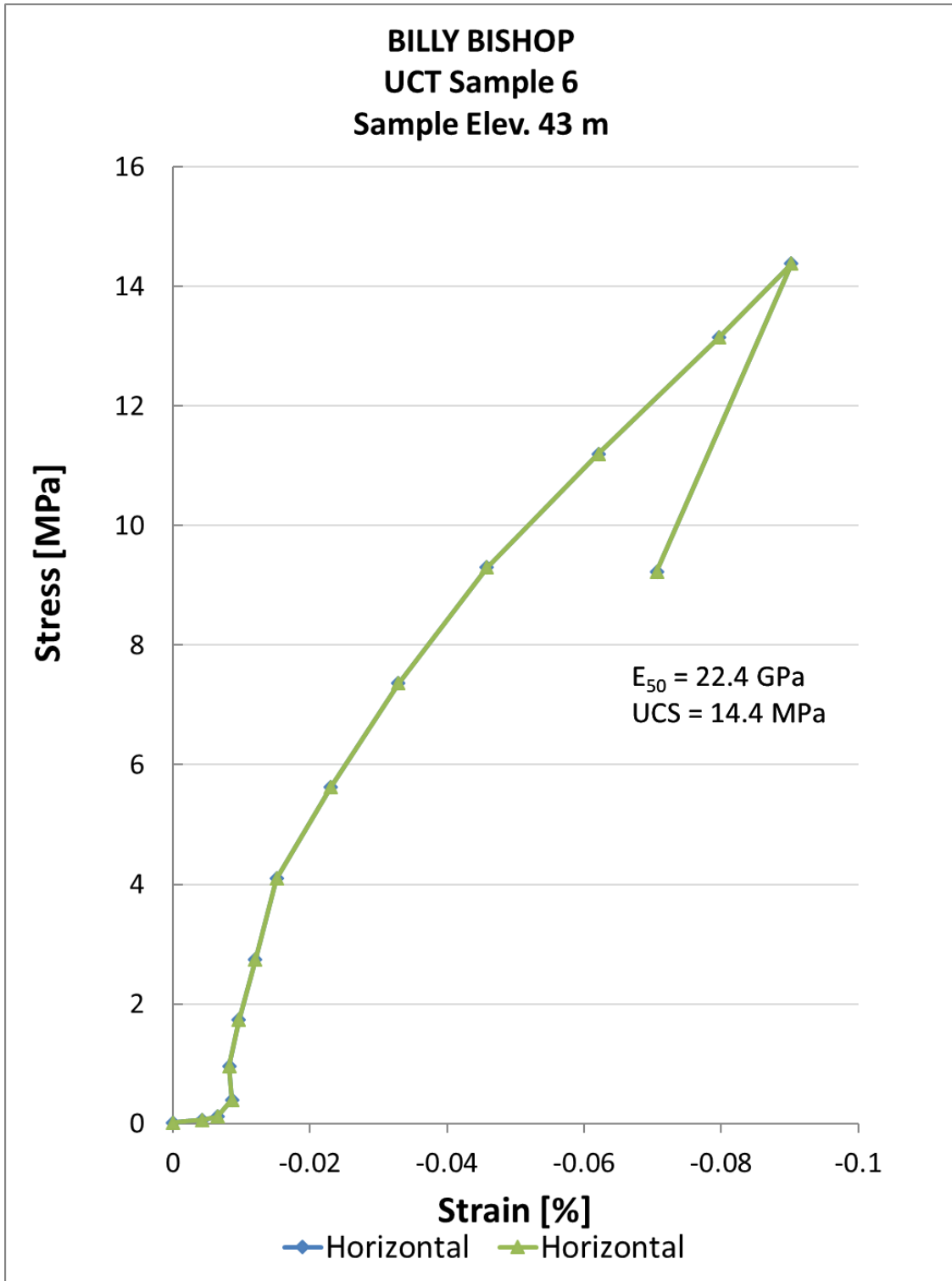


Figure 6.12. Horizontal UCST results from Sample 6.

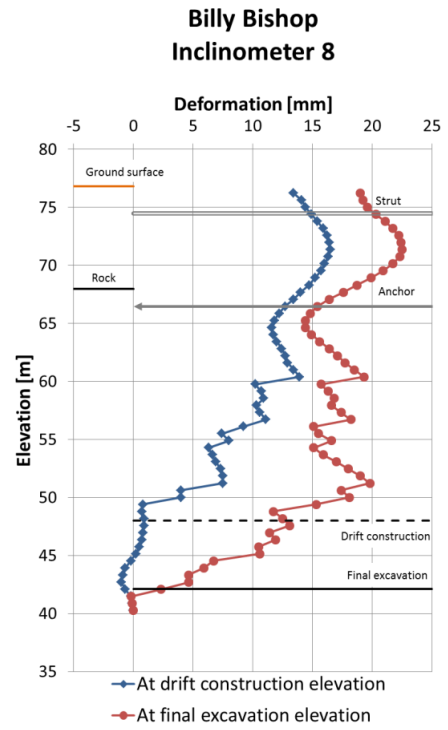
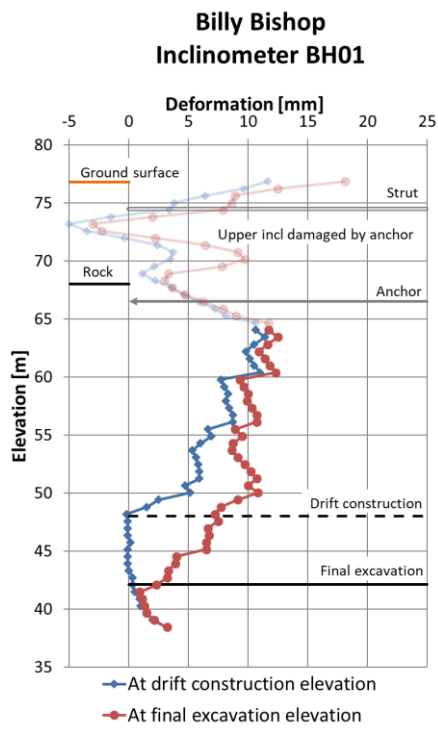


Figure 6.13. Inclinometer results from the north wall at BBPT.

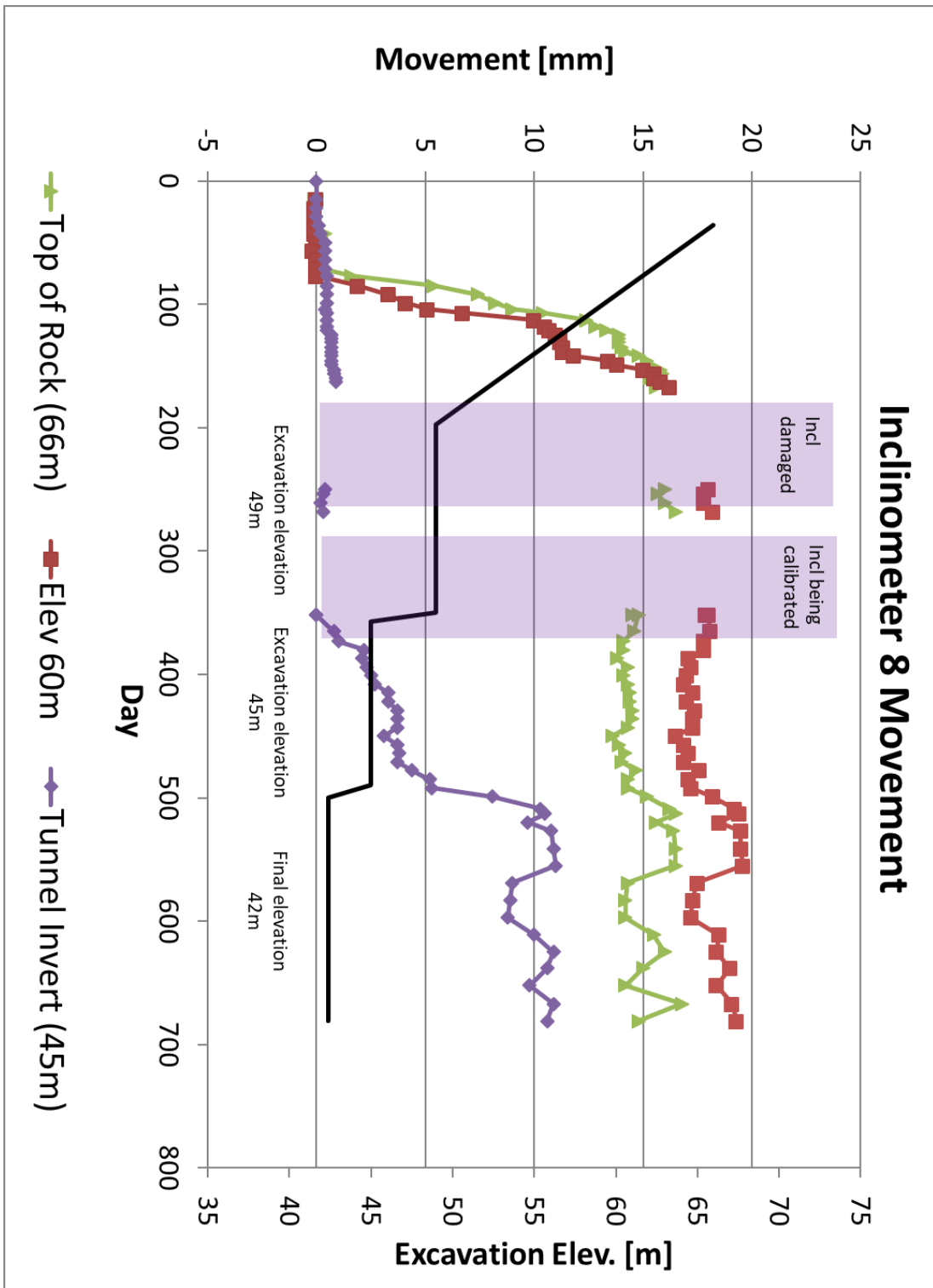


Figure 6.14. Deformation and excavation over time recorded by Inclinometer 8

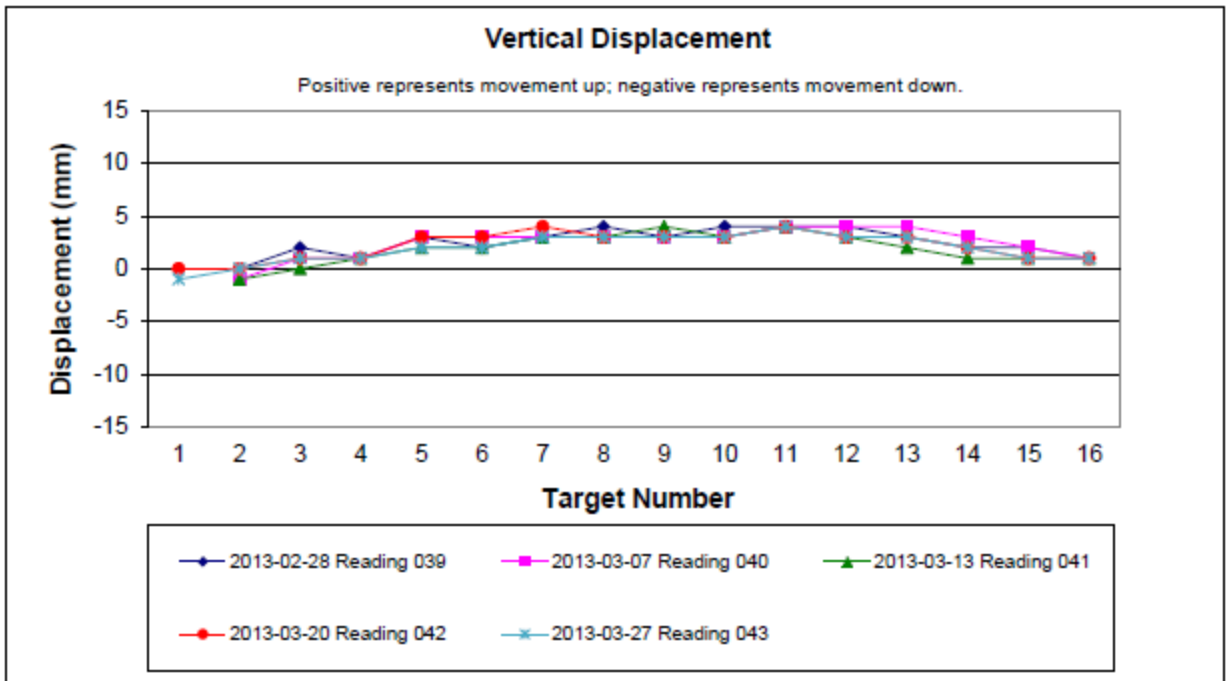
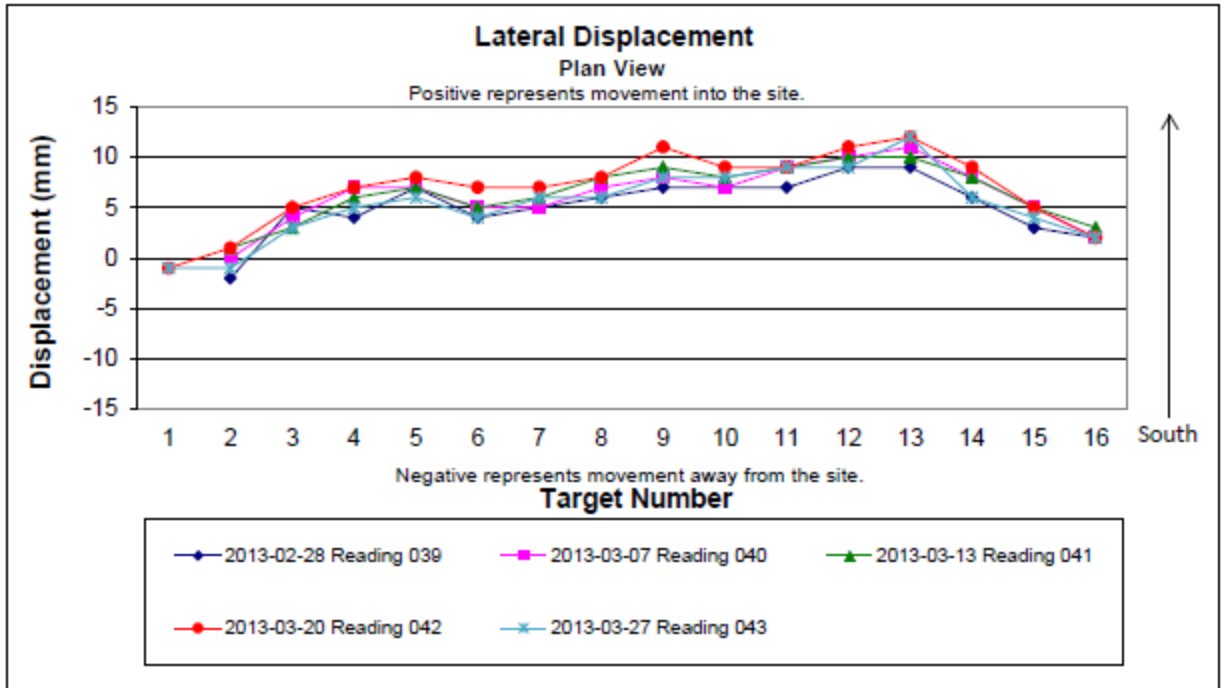


Figure 6.15. Example of pile survey results at north wall.

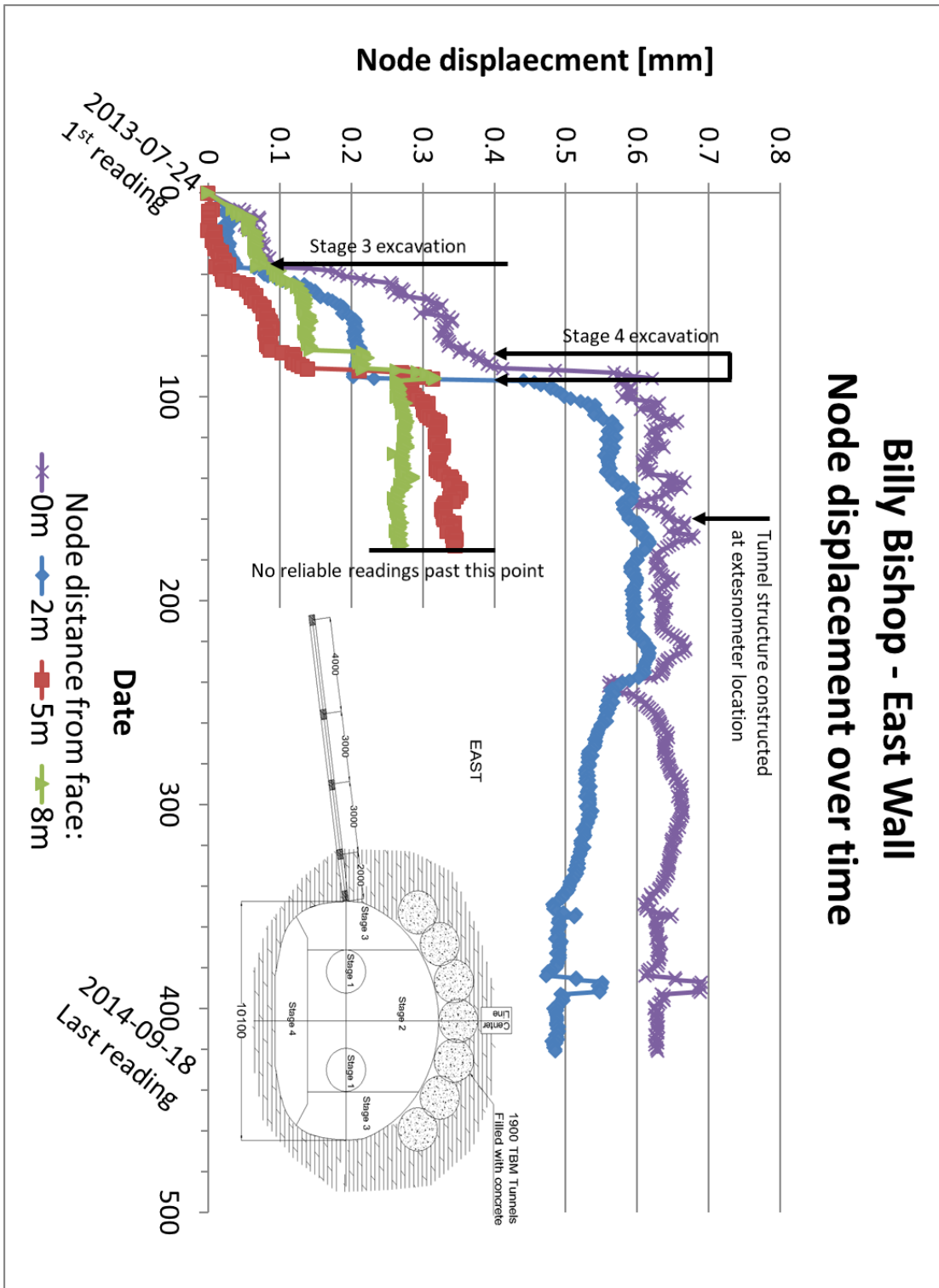


Figure 6.16. East wall extensometer readings.

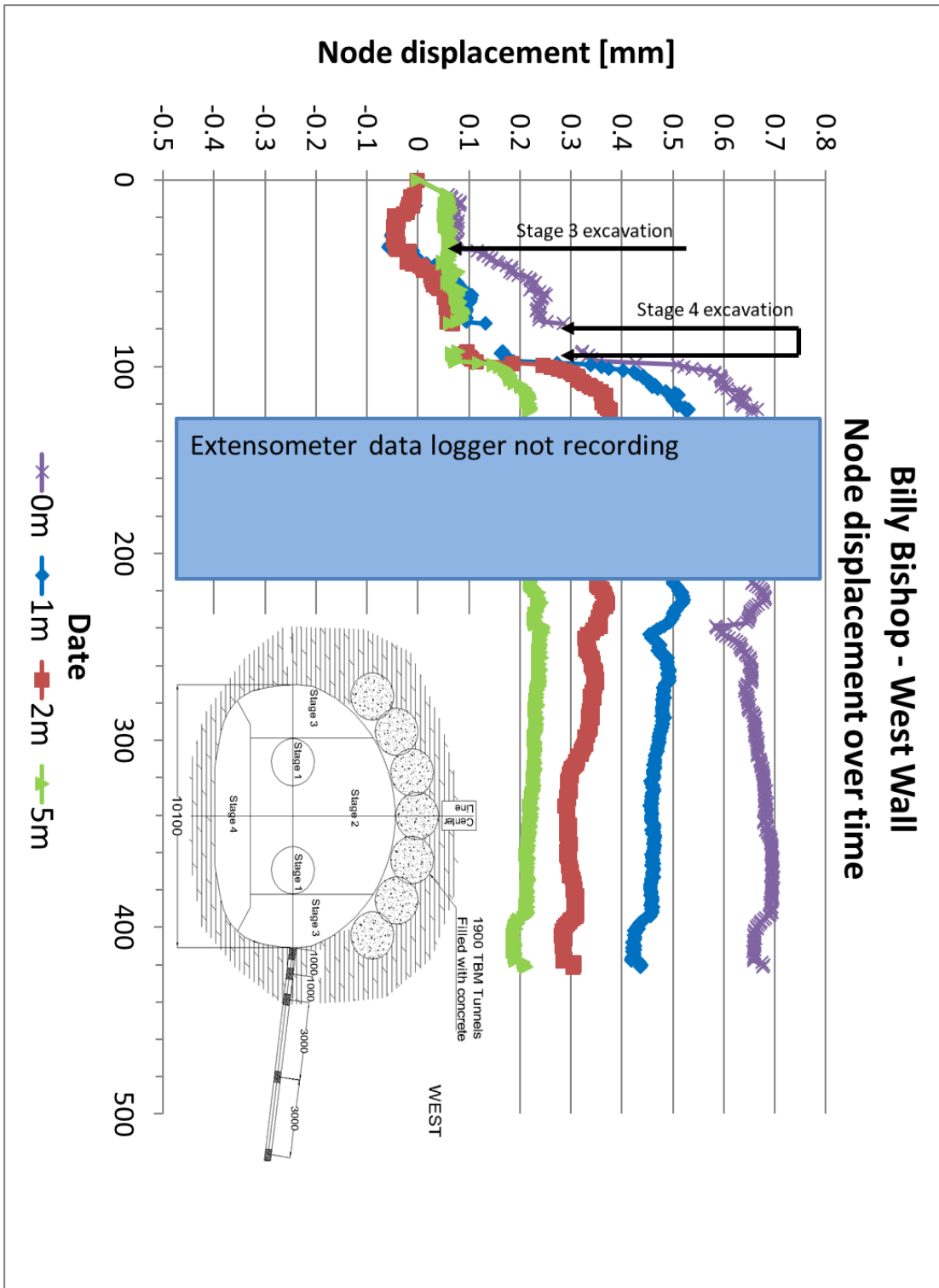


Figure 6.17. West wall extensometer readings.

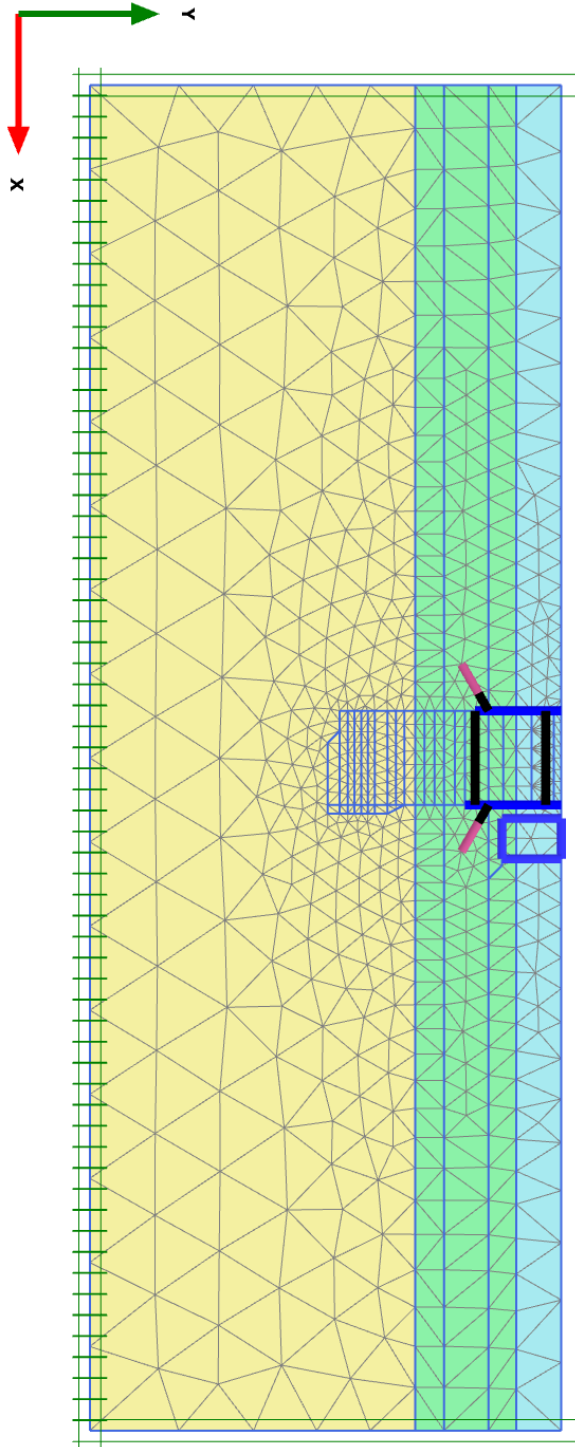


Figure 6.18. Numerical model connectivity plot showing mesh and boundary conditions.

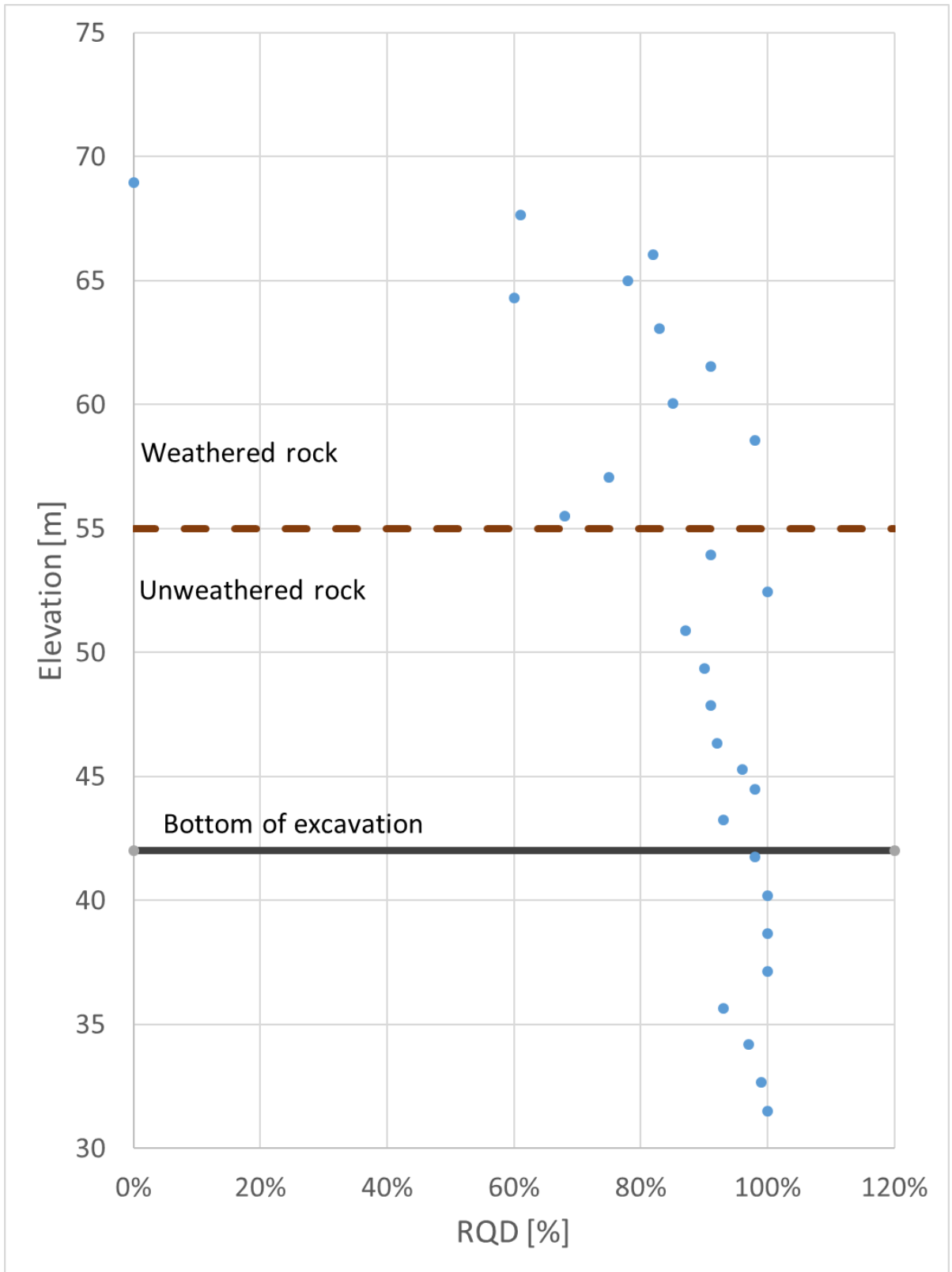


Figure 6.19. RQD with depth at the mainland shaft.



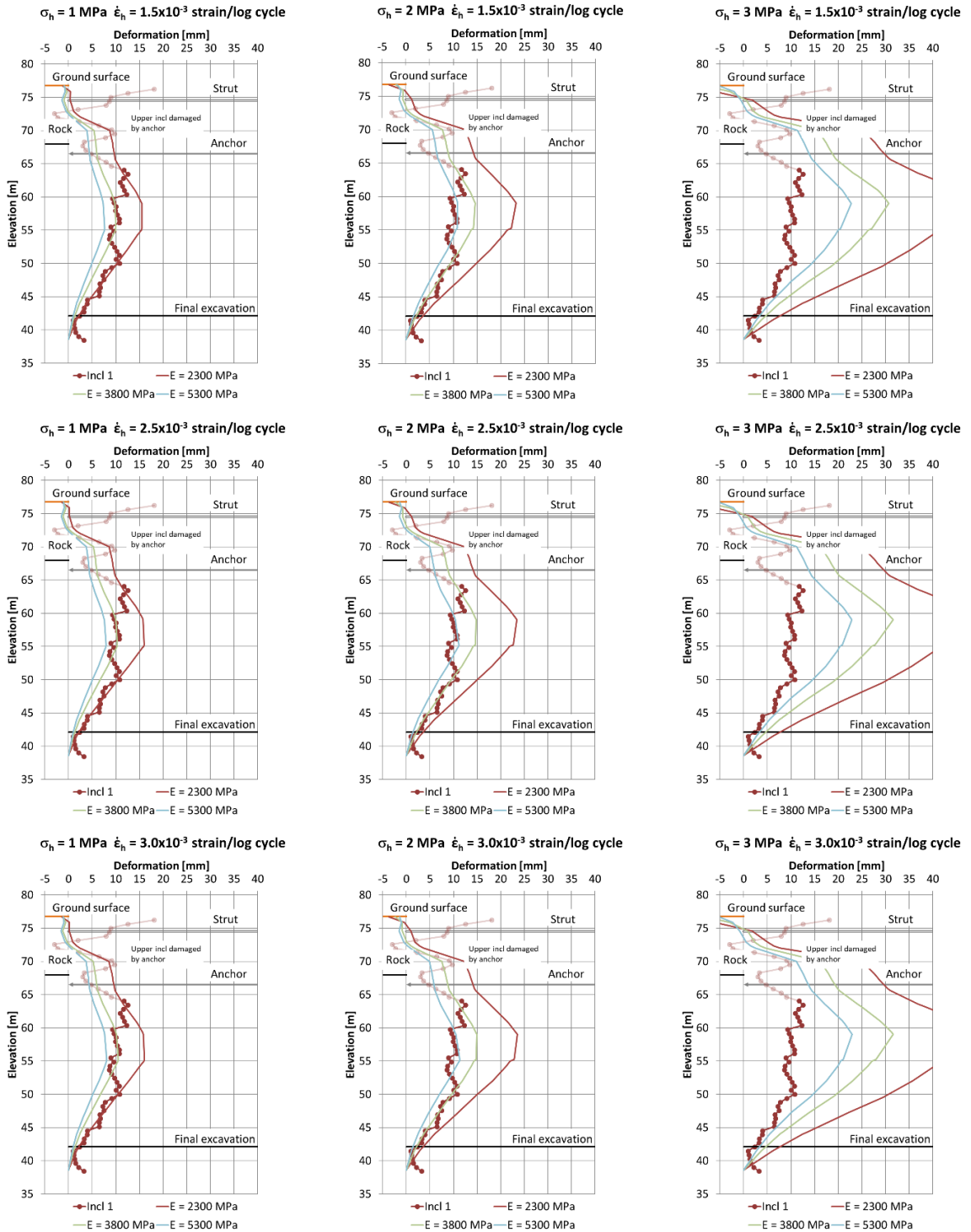


Figure 6.20. FE results compared to Inclinometer BH01 readings at the end of active excavations.

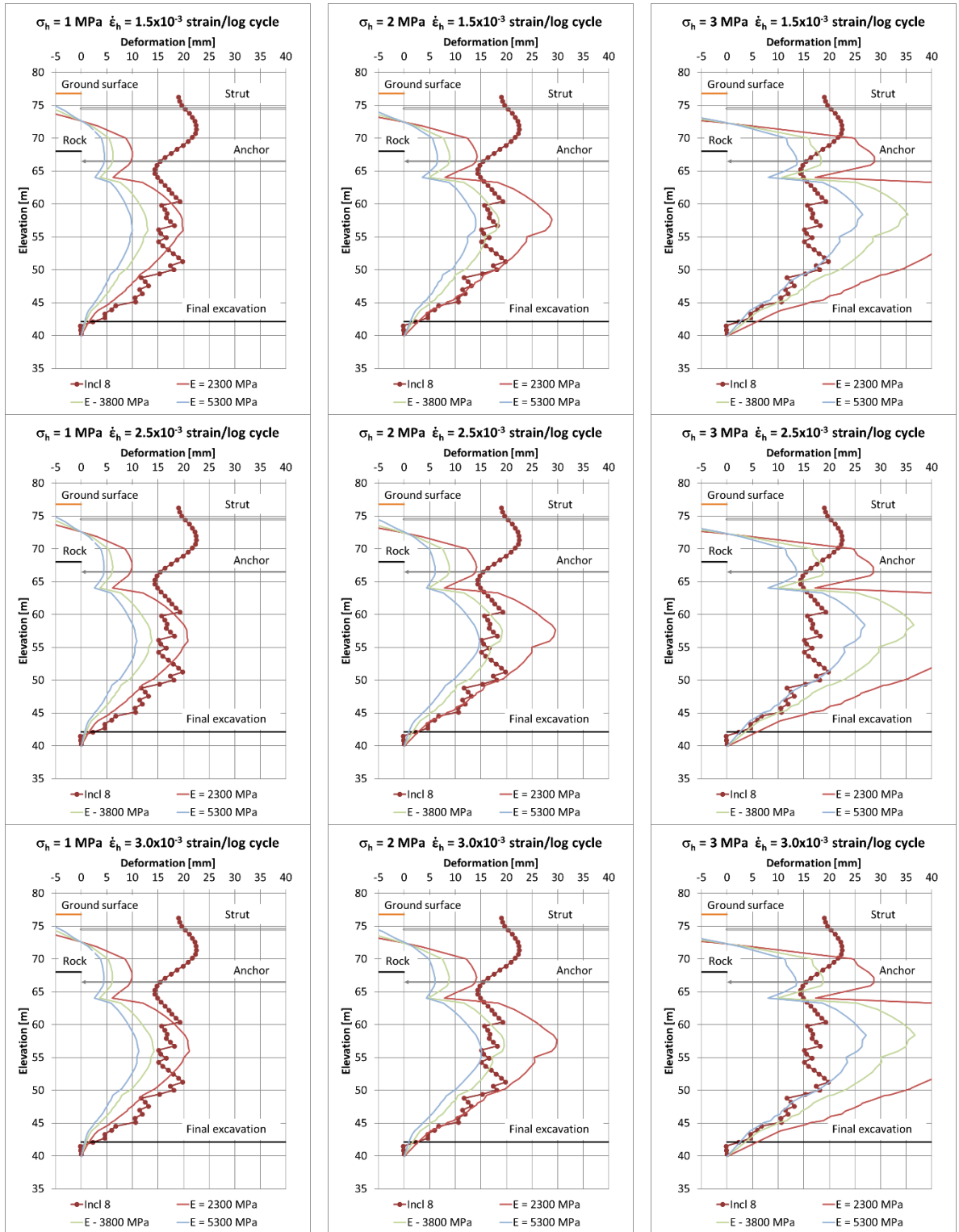


Figure 6.21. FE results compared to Inclinator 8 readings at end of active excavation.

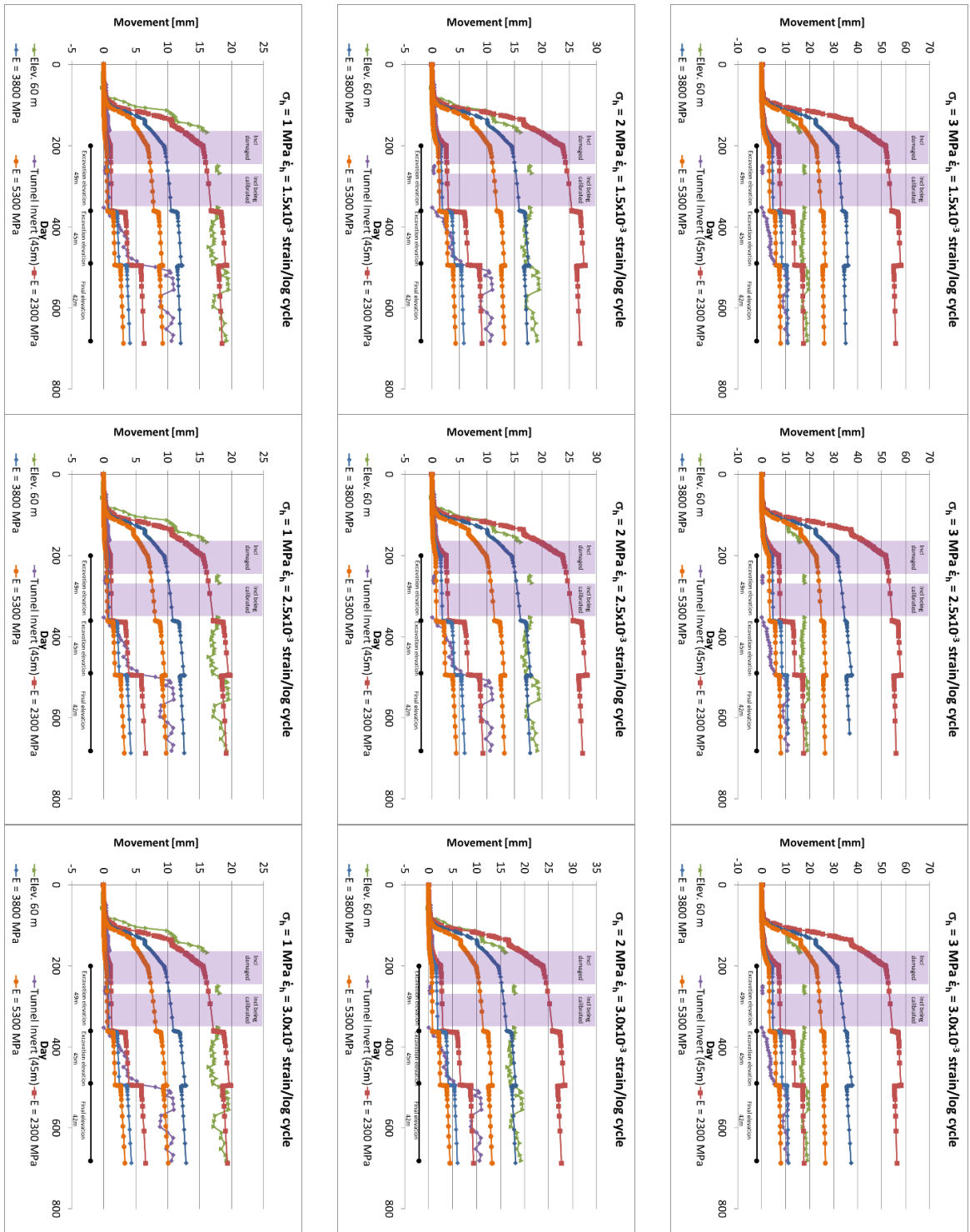


Figure 6.22. FE comparison to Inclinometer 8 movement over construction period.

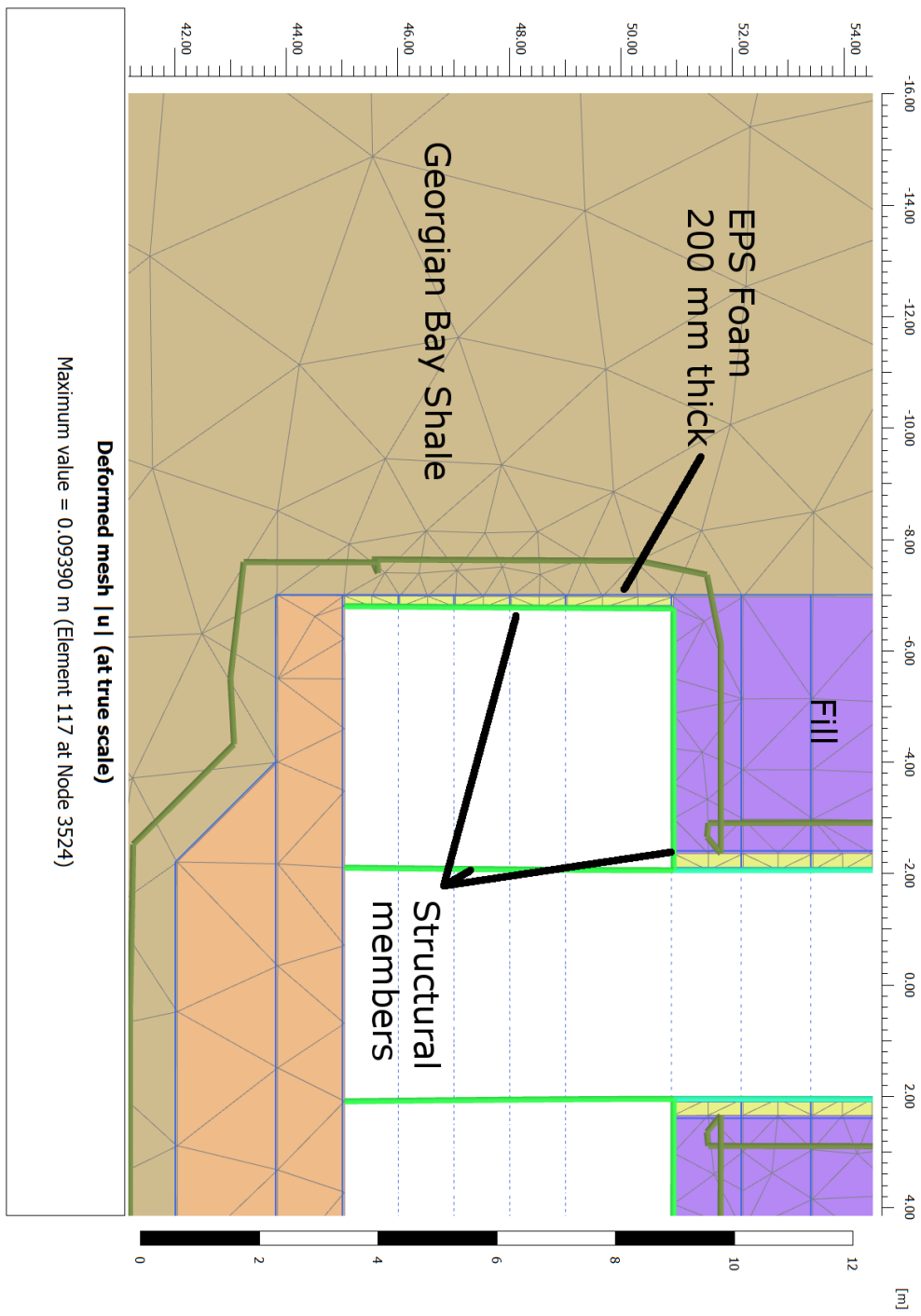


Figure 6.23. Detail of EPS foam in FEA.

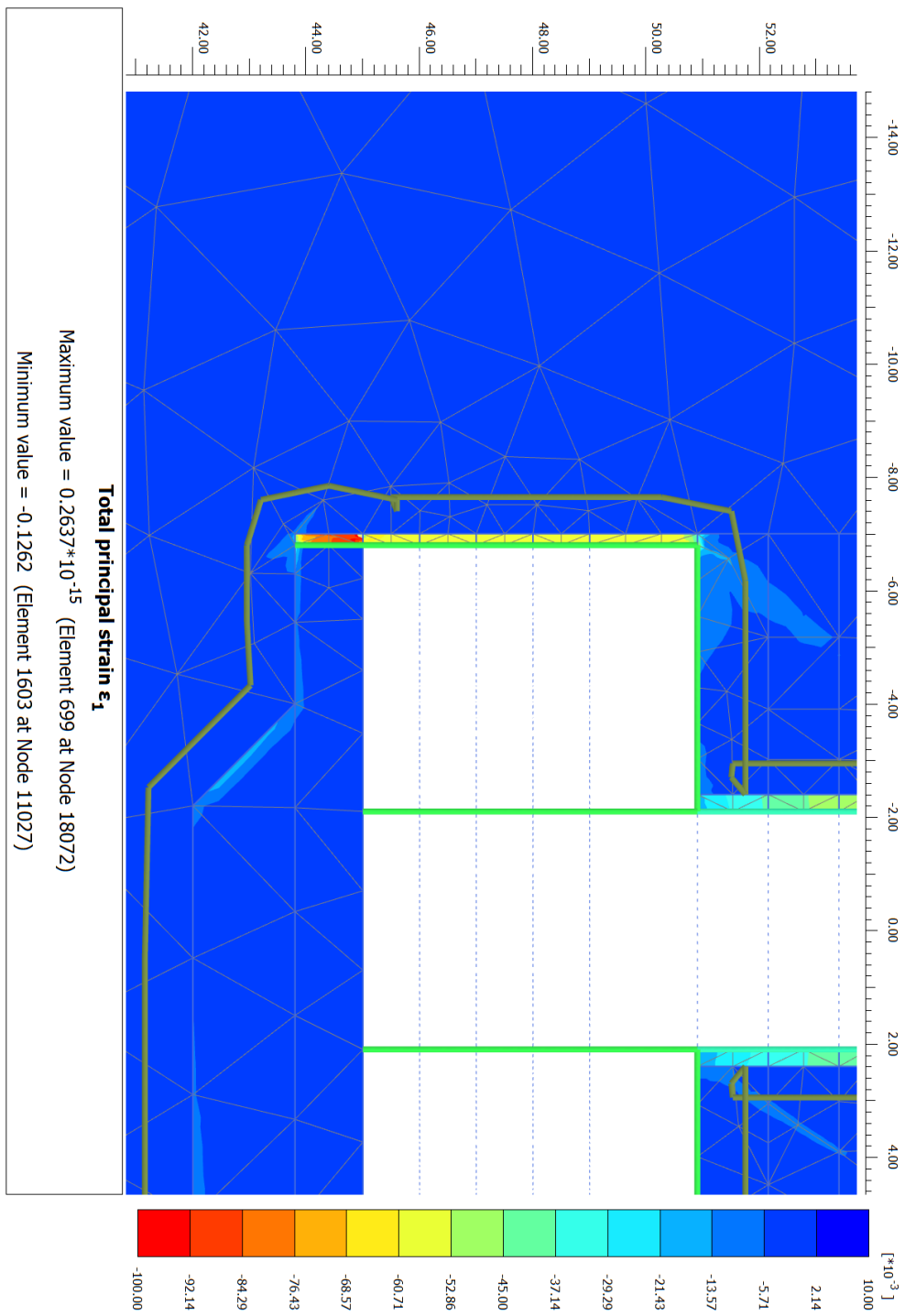


Figure 6.24. Principal strains in EPS 39 foam after 50 years of swelling.

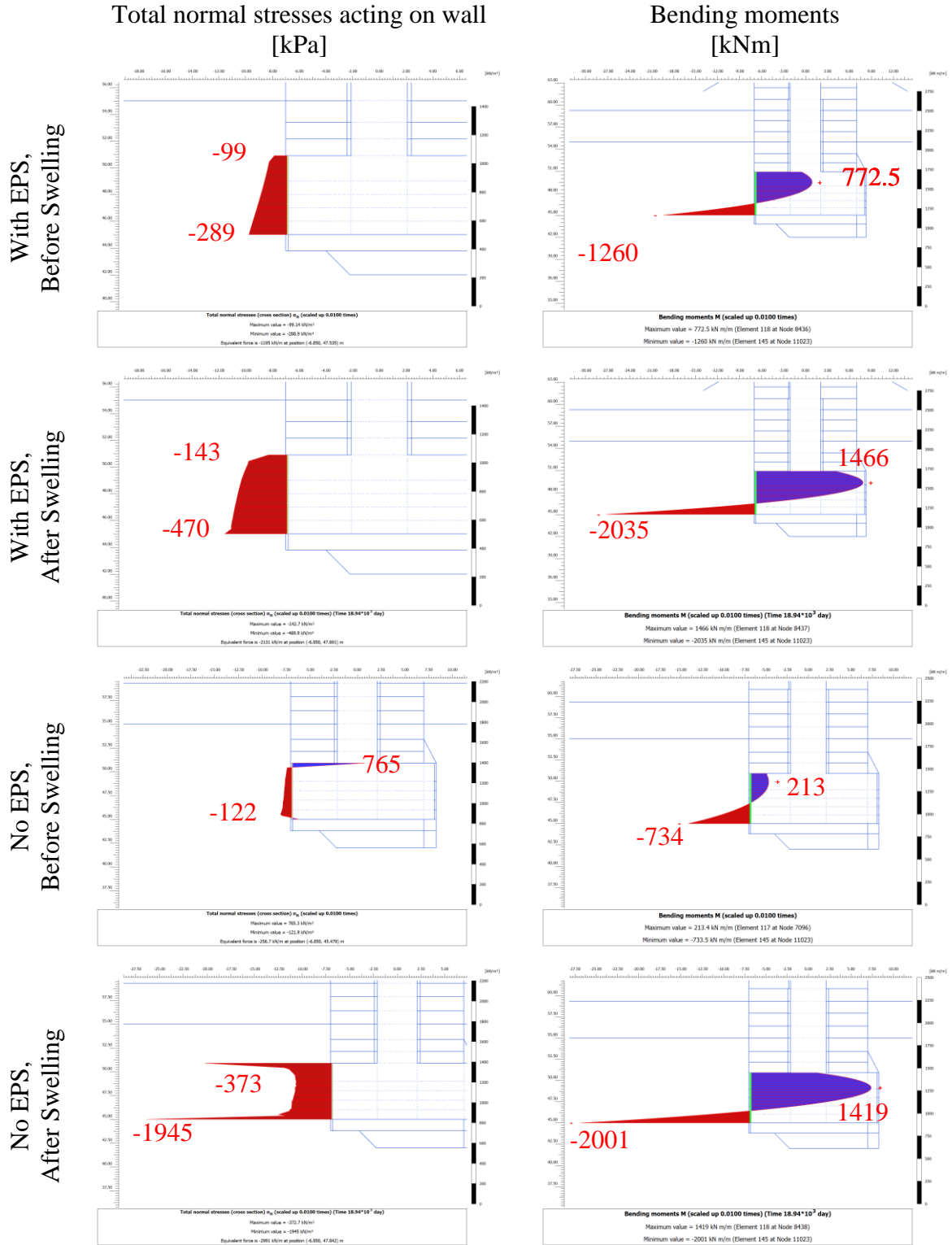


Figure 6.25. Normal stress and bending moments for Case 1.

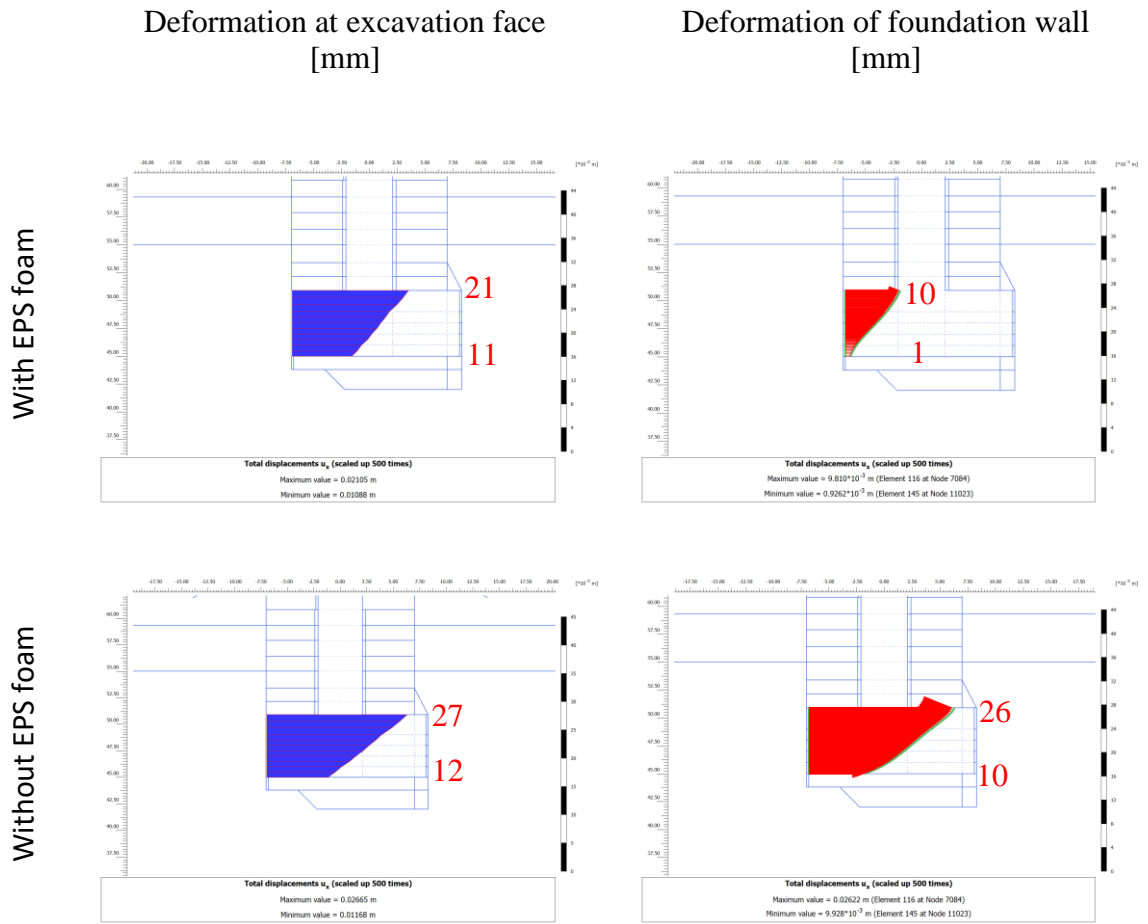


Figure 6.26. Horizontal deformations at end of shaft construction.

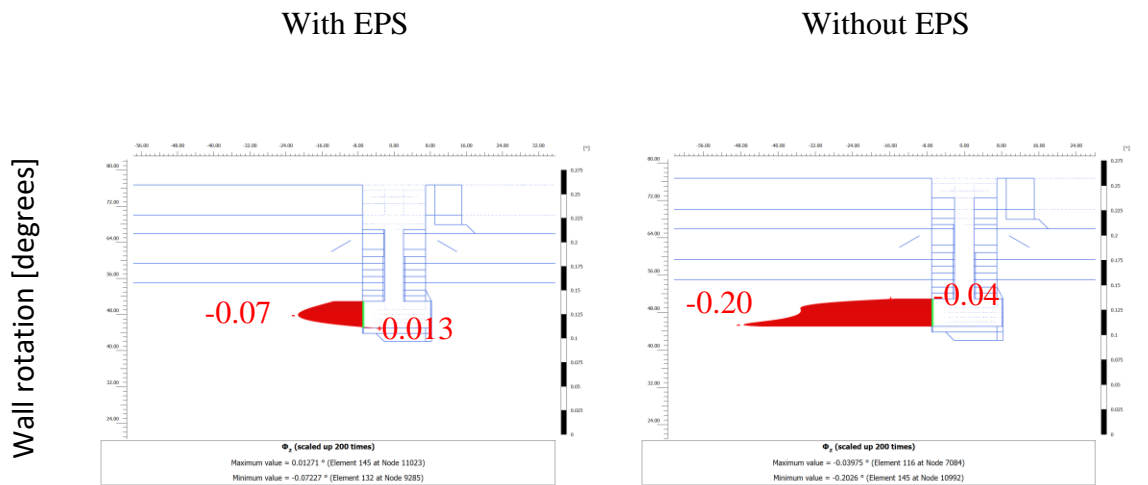


Figure 6.27. Foundation wall rotations at end of shaft construction.

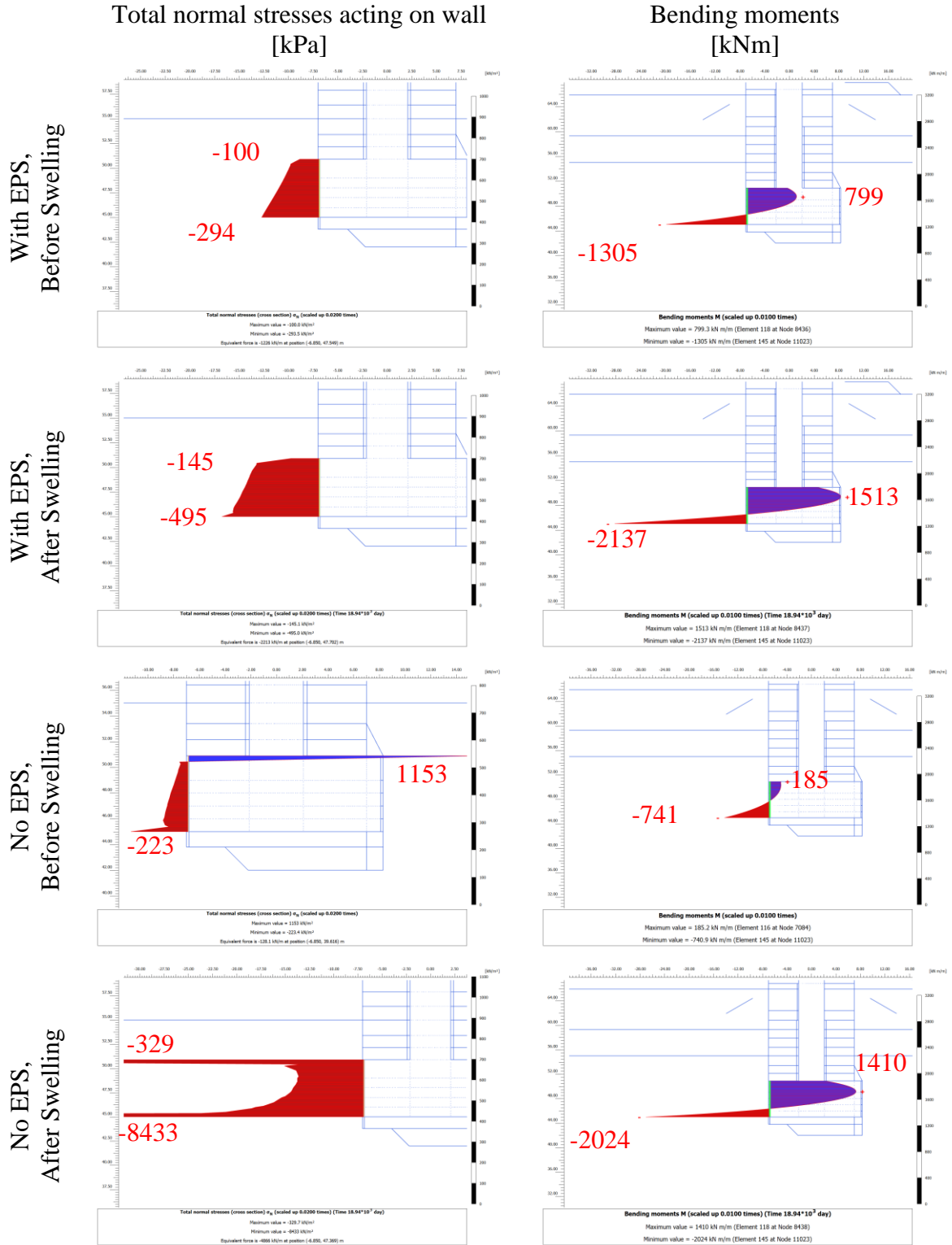


Figure 6.28. Normal stress and bending moments for Case 2.



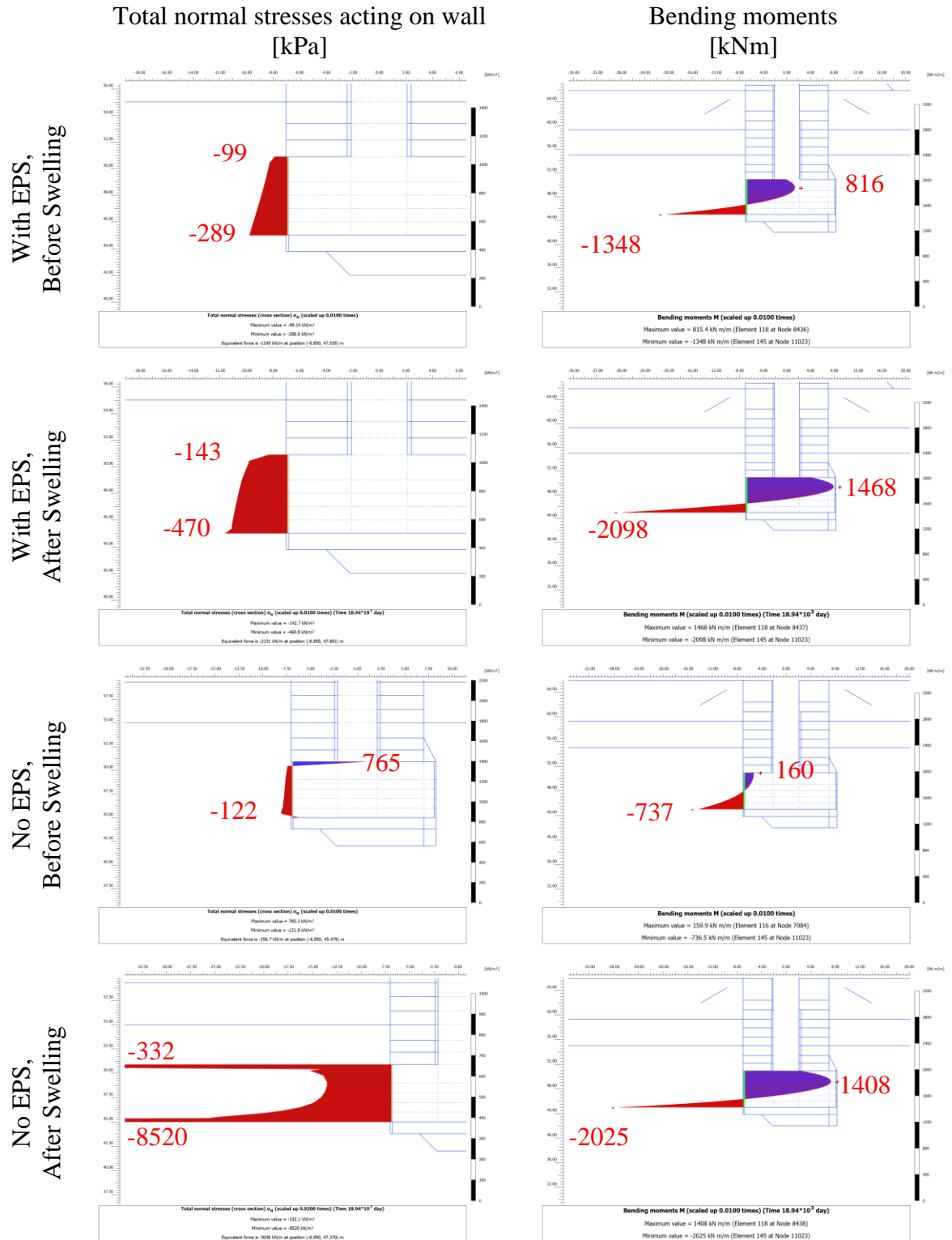


Figure 6.29. Normal stress and bending moments for Case 3.

## Chapter 7

### 7 Summary and conclusions

There were three objectives of this research:

1. Develop a swelling constitutive model for practicing engineers. The model is to be a streamlined implementation of the Lo and Hefny (1996) swelling model for rocks in southern Ontario, and purposely limited the swelling parameter inputs. These inputs were chosen based on industry standard swell tests developed at the Geotechnical Research Centre and include a novel implementation of the “pseudo-Poisson’s ratio” to allow for exploration of the effects of PPR without the need for advanced and difficult testing.
2. Explore the behaviour and engineering characteristics of extruded polystyrene foam and light-weight cellular grout for the purpose of mitigating the effects of swelling rock on buried structures. Tests were conducted on EPS 22, EPS39, and cellular grout with a void ratio of 75%.
3. Observe and analyze swelling rock behaviour due to modern excavation tools and techniques. Past case studies available on swelling rock in southern Ontario are limited in scope, with major studies heavily involving drill and blast excavation. Advances in construction capabilities can impact the swelling behaviour by reducing the damage to the rock mass (smaller Excavation Damage Zone) due to excavation.

#### 7.1 Development of a swelling constitutive model

Chapter 3 describes the development of a swelling constitutive model. The model is based off of Lo and Hefny’s model, shown in Figure 2.2. The model considers the stress dependent swelling potential in principal stress space, calculates the resulting swelling strains for the

given time step, and works within the host program (PLAXIS) to solve for elasto-plastic equilibrium.

The model was designed specifically to provide practicing engineers with a streamlined swelling constitutive model, predominantly for swelling rocks in southern Ontario. The swelling inputs have been limited to the inputs required for the Lo and Henfy (1996) model and include the horizontal and vertical free swell potentials (from Free Swell Tests), threshold stresses (from Semi-Confined Swell Tests), and suppression stresses (from Null Swell Tests). The model also includes an adaptation of the “pseudo-Poisson’s ratio” that allows the practicing engineer to evaluate the effects of PPR on rock swelling without having to run non-standard and difficult testing. All input values are derived from testing developed at the Geotechnical Research Centre at the University of Western Ontario and are considered the industry standards for this region.

The model was first validated through a series of analyses simulating the FST, SCST, and NST conditions. The validation analyses considered the ratios of horizontal and vertical free swell potentials, the ratio of horizontal and vertical applied pressures, the effect of the “pseudo-Poisson’s ratio”, the mesh density and aspect ratio, and the first time step. Results all conditions showed acceptable behaviour of the model. The first time step was shown to affect the total magnitude of deformation due to swelling but not the rate of swelling.

The next phase of validation was an analysis of the Heart Lake Tunnel project which is a well-documented project affected by swelling rock. The constitutive model successfully modeled the tangential stresses in the TBM section over time. The model also acceptably matched the in-situ horizontal stress adjacent to the tunnel springline two years after tunnel construction. The model was used to predict the change in stress in the rock mass over 100 years, indicating that the negative effects of swelling stress would continue, resulting in additional damage.

The model was then used to analyze the monitoring results from two projects in different swelling formations. The Zone 1 Water Main project represented a circular excavation in Queenston shale. The model successfully matched the observed deformations and was used to estimate the effects of 2 MPa strength grout or 35 MPa concrete on the steel tunnel. Results indicated that the 35 MPa concrete provides enough suppression pressure to reduce the impact

of swelling rock on the steel tunnel compared to the 2 MPa grout. The analysis relied heavily on the PPR value, which was successfully implemented without the need for advanced swell testing. The second project was the Billy Bishop Pedestrian Tunnel, where the mainland shaft was analyzed. The rectangular shaft experienced significant deformations during excavation and construction, including swelling deformations. The constitutive model was used to conduct a calibration analysis. The results of the calibration analyses were used to explore the effect of EPS 39 foam on protecting the buried shaft structure. Results indicate that the 200 mm thick EPS layer would reduce the structural stresses due to swelling by 39 to 58%.

## 7.2 Swell mitigation material

Two materials were investigated for the purpose of swell mitigation: EPS foam and light-weight cellular grout.

Two weights of EPS foam were tested, EPS 22 and EPS 39. Both types were tested in uniaxial compression at low strain rates. Results from the tests indicate that the strain rate has a small impact elastic modulus and yield strength, but can greatly affect the post peak behaviour. At low strain, the EPS foams behaved nearly as a linear-elastic perfectly plastic material. Strain hardening began at approximately 35%. Current design practice is to limit the strain experienced by the EPS foams to the linear-elastic behaviour, typically dictated by less than 10% strain. However, most applications for EPS foams in geoenvironmental projects are for cyclic loading such as frost protection or light weight fill under roadworks. For this application where the loading is monotonic, significant savings may be realized by increasing the acceptable strain to less than 35%.

EPS foams present favourable behaviour for the purpose of swell mitigation. Additional testing is required to evaluate the effects of confinement and groundwater on the stress-strain behaviour.

A light-weight cellular grout with a 28 day  $f'_c$  of approximately 1 MPa was tested. Varying the strain rate indicated that lower strain rates reduce the unconfined compression strength by approximately 30 % from the ASTM standard test result. As the strain rate decreases, the

elastic modulus of the material increases. In UCS testing, the material showed a clear strain-softening behaviour, which is ideal for mitigation of swelling strains.

Triaxial tests results of the cellular grout were difficult to interpret. Mohr Circle plots of the effective stresses do not provide clear indication of a strength or yield profile. In general, deviatoric stress vs. strain plots showed a linear portion ending at a yield point followed by a sudden drop in strength, then a gradual build-up of stress post-yield. Test results did not provide any recognizable pattern in regards to confining stresses, yield points, or axial strains.

Saturation of the samples proved very difficult. High saturation required backpressures higher than most engineering applications would experience. Lower backpressure values resulted in very low saturation.

### 7.3 Analysis of case studies

Two case studies were investigated, monitored, and analyzed. The first case study, the Zone 1 Water Main project, was located in the Queenston Formation. The second case study, the Billy Bishop Pedestrian Tunnel project, was located in the Georgian Bay Formation. Each project was excavated using modern construction tools and techniques. The Zone 1 Water Main was a circular shaft excavated with a hydraulic hammer and a circular tunnel excavated with a TBM. The Billy Bishop Pedestrian Tunnel project has a rectangular shaft excavated via hydraulic hammer. The tunnel was oval shaped, 10 m wide and 7.5 m high, and was excavated with a combination of TBM and excavator with hydraulic hammer or roto-miller. Between the two projects, a variety of excavation shapes and tools were employed.

The circular shaft at the Zone 1 Water Main experienced minimal deformation. The horizontal in-situ stress was estimated to be 4 MPa based off of inclinometer data. Negligible time-dependent deformations were observed, likely indicating that the rock mass was highly competent and the in-situ stresses were not greatly affected due to the shape of the shaft. As per Lee and Lo (1993) a reduction in stress is a key initiator of swelling. Although the rock face was protected by a thin layer of shotcrete, it was not water proofed in any way. It is not likely that the shotcrete would have prevented atmospheric water from reaching the rock mass to aid swelling. Tunnel monitoring results indicated minimal swelling deformations. The

deformations observed through tape extensometer tunnel convergence readings indicate that the swelling stops approximately 40 days after excavation. This is significantly less than the 90 day period contractual requirement. The TBM excavation provided an ideal shape (circular) while having a minimal impact on the quality of the rock mass. The tunnel monitoring indicated minimal rock deformations – less than 1 mm within the rock mass over three tunnel diameters.

The mainland shaft excavation at the Billy Bishop Pedestrian Tunnel project provided a case study for a non-circular geometry with a rough excavation method. Deformations were significantly larger, even accounting for the difference in volume excavated. When comparing the lower sections between the BBPT and the Z1WM shafts, both were in rock that had a high RQD (>80%), but the BBPT experienced approximately 25 mm while the Z1WM experienced less than 5 mm. The shape of the BBPT shaft allowed for significant changes in the stress regime in the rock, causing a reduction behind the excavation face – a key initiator of swelling rock. In addition, the large volume of water ingress experienced at the shaft supplied all the fresh water needed for swelling to occur freely. The damage done to the rock mass caused observable openings of joints along the excavation face. If this trend continued into the rock mass in any capacity, it would have allowed the fresh water to penetrate farther and more efficiently into the rock mass further aiding the swelling. The BBPT tunnel portion was excavated with TBM along the top portion and finished with roto-milling. The tunnel was located in the highly competent portion of rock mass. The excavation technique and good quality rock prevented the opening of joints or the formation of new discontinuities. The lack of water within the rock was likely a significant reason for the negligible swelling deformation recorded in the borehole extensometers. Since the tunnel was waterproofed with the shaft as part of the final structure, there is a possibility that freshwater will penetrate the rock over time initiating the swelling that didn't occur during active excavation and construction. This may be resisted by high rock competency and stresses around the semi-circular tunnel. Currently, there is no active monitoring of the structure.

From the limited results two preliminary observations can be made. The first is that excavation technique that preserves the rock mass integrity can greatly reduce the amount of swelling observed. A rougher excavation method, such as large hydraulic hammer or drill and blast,

will create a large Excavation Damage Zone, resulting in the extension of joints beyond the excavation face and the creation of new micro- and macro-fractures. This increases the hydraulic conductivity and reduces the rock mass modulus, resulting in a larger area of swelling and a higher magnitude of swelling. Excavation techniques that limit the damage to the rock mass, such as with a TBM or roto-miller, experienced less deformation in general than the rougher methods.

Circular openings, either vertical or horizontal, appear to experience less swelling. The shaft and tunnel at Z1MW and the roughly circular tunnel at BBPT experienced negligible to minimal deformations. Circular excavations have been known to experience adverse deformations, as observed in the Heart Lake Tunnel project (Lo et al. 1979, Lo and Yuen 1981, Hawlader et al. 2005), so caution must be taken by the designing engineer. Consideration for the in-situ stress state is most important, as highly anisotropic stresses will drive rock mass reaction to excavation.

For the design engineer, there are two key takeaways. The first is that circular, low impact excavations will experience less swelling in a shorter period of time than is typically accounted for. With this in mind, and the use of more advanced design tools such as the swelling rock constitutive model developed for this research, construction schedule for the tunnel structure can be reduced. This has the potential for major cost savings. Caution is still required by the design engineer. The rock mass must be carefully investigated and a high quality QA/QC program must be implemented to ensure proper excavation and construction practices are being followed. A monitoring program is highly recommended to verify design assumptions.

Another major consideration for tunnel projects is the presence of rubble zones and calcareous bioherms that have been observed by the author in the rock formations of southern Ontario. These conditions represent areas of low strength and high hydraulic conductivity, often containing significant amounts of water. These areas are hard to identify in a geotechnical investigation and they are limited in area. The poor rock quality of these areas often require a change in tunnel support design, resulting in additional costs and project scheduling delays. The effect of these areas on swelling behaviour is not well known. Since significant amounts of fresh water and open fractures already exist in these poor rock quality areas, swelling within

them is not expected. However, the easy access to a large amount of fresh water and geological conditions leading to the rubble zones may affect the surrounding rock mass.

## 7.4 Future work recommendations

Results from the research provide advances for the design of excavations and structures in swelling rock. Additional investigations are recommended to further develop these tools.

The constitutive model should be expanded into a fully three dimensional finite element software. Complex excavations, such as subway stations, will require a 3D analysis. Although the code has been written to account for 3D stress, it has only been verified in a 2D plane strain case.

The constitutive swelling model developed for this research assumes that the swelling potentials and critical suppression stresses, which are determined in the horizontal and vertical direction, can be rotated into the principal stress space. This assumption has not been verified with laboratory tests. A series of FST, SCST, and NST is recommended to explore the effects of rotation of applied stress on the swelling behaviour, to determine if the assumptions made for the constitutive model are correct.

Compressible or crushable materials require further studying. Cellular grout holds great potential due to the cost and constructability. However, further study is required to identify the three-phase behaviour in practice. The confined behaviour of EPS foams should also be explored.

Al-Maamori et al. (2018) observed a significant reduction in rock strength and stiffness after soaking. A base assumption for swelling is contact with fresh water at all locations where swelling occurs. This implies that soaking leads to reduction in both elastic modulus and compressive strength due to the swelling behaviour. This reduction of rock strength and stiffness with time should be considered in the constitutive model to account for the degradation in stiffness and strength due to soaking in water.

Results from the cellular grout triaxial tests likely indicate that the cellular grout acts as a three-phase material, especially under the expected porewater and stress conditions. In addition, it



is suspected that only a portion of the pores are connected. The behaviour of a three phase material, composed of solids, liquids, and gasses, is complex and requires additional study. A study looking at the effects of varying porosity, average void size, void size distribution, and void interconnectivity is recommended. Yielding of the material was inconsistent between the tested samples, with some showing yield followed by a sudden drop in strength while other continued to experiences a gradual increase in stress. Non-destructive, 3D scanning of the material at various stages of yield would identify the mechanical behaviour of the material during this critical stage of material behaviour.

Finally, when considering excavations and the issues of poor rock quality and rubble zones, three potential topics for future study are i) classifying how often poor rock quality conditions are encountered and creating a risk analysis for such occasions, ii) developing project management tools, such as better Geotechnical Baseline Reports, contractual agreements, pre-designed solutions, etc. for efficient solutions to a possible problem to be experienced in any project with a large footprint, and iii) monitoring the rock mass behaviour due to excavation within and surrounding these areas of poor rock conditions.

## References

- Aglawe, J., & Sinclair, B. (2002). Design of rock support and pressure relief for shafts in Toronto area. *Proceedings of the 55th Canadian Geotechnical Conference*. Niagara Falls, ON: Canadian Geotechnical Society.
- Al-Maamori, H. (2016). Time-dependent behaviour of microtunneling construction in Queenston shale. *PhD Thesis*. London, Ontario, Canada: The School of Graduate and Post-doctoral Studies, The University of Western Ontario.
- Al-Maamori, H., El Naggar, M., & Micic, S. (2014). A compilation of the geo-mechanical properties of rocks in southern Ontario and neighbouring regions. *Open Journal of Geology, Vol. 4*, 210-227.
- Al-Maamori, H., El Naggar, M., & Micic, S. (2018). Numerical modeling of time-dependent deformation and induced stresses in concrete pipes constructed in Queenston shale using micro-tunneling technique. *Journal of Rock Mechanics and Geotechnical Engineering, 10*, 290-309. doi:10.1016/j.jrmge.2017.11.006
- Al-Maamori, H., El Naggar, M., Micic, S., & Lo, K. (2018). Influence of water and lubricant fluids on peak strength of Queenston shale from southern Ontario. *Canadian Geotechnical Journal, Vol. 55*, 455-476.
- Altwegg, P., Cabot, E., Maloney, S., Coulson, A., Malla, S., & Goodman, S. (2017). In-situ stress measurements at the Coxwell Bypass Tunnel along the inner Harbour East and Lower Don River, Toronto, Ontario. *Proceedings of the 70th Canadian Geotechnical Conference, GeoOttawa 2017. Paper #295*. Ottawa, ON: Canadian Geotechnical Society.

- Anagnostou, G. (1993). A Model for Swelling Rock in Tunnelling. *Rock Mechanics and Rock Engineering*, Vol. 26(4), 307-331.
- Armstrong, D., & Carter, T. (2006). *An updated guide to the suburface Paleozoic stratigraphy of southern Ontario*. Ontario Geological Society. Sudbury, ON: Ontario Geological Society.
- Armstrong, D., & Carter, T. (2006). *An updated guide to the subsurface Paleozoic stratigraphy of southern Ontario*. Ontario Geological Survey. Ontario Geological Survey.
- ASTM C203-05a(2012), Standard Test Methods for Breaking Load and Flexural Properties of Block-Type Thermal Insulation. (2012). West Conshohocken, PA: ASTM International. doi:10.1520/C0203-05AR12
- ASTM C495/C495-M, Standard Test Method for Compressive Strength of Lightweight Insulating Concrete. (2012). West Conshohocken, PA, USA: ASTM International. doi:10.1520/C0495\_C0495M-12
- ASTM D1621-16, Standard Test Method for Compressive Properties of Rigid Cellular Plastics. (2016). West Conshohocken, PA: ASTM International. doi:10.1520/D1621-16
- ASTM D6817 / D6817M-17, Standard Specification for Rigid Cellular Polystyrene Geofoam. (2017). West Conshohocken, PA, USA: ASTM International. doi:10.1520/D6817\_D6817M-17
- ASTM D7012-14, Standard Test Methods for Compressive Strength and Elastic Moduli of Intact Rock Core Specimens under Varying States of Stress and

- Temperatures. (2014). West Conshohocken, PA, USA: ASTM International.  
doi:10.1520/D7012-14E01
- ASTM D7181-11, Standard Test Method for Consolidated Drained Triaxial Compression Test for Soils. (2017). West Conshohocken, PA, USA: ASTM International. doi:10.1520/D7181-11
- (2011). *Best Planning Estimates of population, occupied dwelling units and employment, 2011 – 2031*. Regional Municipality of Halton.
- Bieniawski, Z. (1989). *Engineering rock mass classifications: a complete manual for engineers and geologists in mining, civil, and petroleum engineer*. New York: Wiley.
- Bluming, P. B. (2007). The excavation damage zone in clay formations time-dependent behaviour and influence on performance assessment. *Physics and Chemistry of the Earth, Vol. 32*, 588-599.
- Bowen, C. H. (1976). Rock squeeze in Thorold Tunnel. *Canadian Geotechnical Journal, Vol. 13*, 111-126.
- Brinkgreve, R., Kumarswamy, S., & Swolfs, W. (2016). *PLAXIS2D-Version 2016*. Delft University of Technology & Plaxis b.v. doi:ISBN-13 978-90-76016-20-7
- (2017). *Building better lives: Ontario's long-term infrastructure plan 2017*. Ministry of Infrastructure, Government of Ontario, Queen's Printer for Ontario.
- Carvalho, J. (2015). A simple numerical approach for modelling time dependent swelling mechanisms in shales. *13th ISRM International Congress on Rock Mechanics, Paper 348*. Montreal.

- Chen, W. H. (2015). Static and dynamic mechanical properties of expanded polystyrene. *Materials and Design*, Vol. 69, 170-180.
- Cushing, A., Hurt, J., & Carvalho, J. (2016). Time Dependent Deformations of Shafts and Tunnels in the Greater Toronto Area. *World Tunneling Congress*. San Francisco, CA.
- Diederichs, M. (2007). The 2003 Canadian Geotechnical Colloquium: Mechanistic interpretation and practical application of damage and spalling prediction criteria for deep tunnelling. *Canadian Geotechnical Journal*, Vol. 44, 1082-1116.
- Einstein, H. (Ed.). (1994). Comments and recommendations on design and analysis procedures for structures in argillaceous swelling rock. *International Journal of Rock mechanics and Mining Sciences and Geomechanics Abstracts*, Vol. 31(5), 535-546. International Society for Rock Mechanics.
- Elragi, A. (2000). Selected engineering properties and applications of EPS geofoam (Doctoral dissertation). Syracuse, NY, USA: Statue University of New York.
- Gnip, I. J., Vaitkus, S. I., Kersulis, V. I., & Veyelis, S. A. (2007). Deformability of expanded polystyrene under short-term compression. *Mechanics of Composite Materials*, Vol. 43(No. 5), 433-444.
- Gnip, I., Veyelis, S., Kersulis, V., & Vaitkus, S. (2007). Deformability and strength of expanded polystyrene (EPS) under short-term shear loading. *Mechanics of Composite Materials*, Vol. 43(No. 1), 85-94.
- Grob, H. (1972). Schwelldruc im Belchentunnel. *Proceedings of the International Symposium on Underground Openings*, (pp. 99-119). Lucerne, Switzerland.

- Grunicke, U., Ristic, M., & Wood, D. (2013). Overcoming rock squeeze and overbreak in a large diameter TBM excavation. *World tunnel congress 2013*, (pp. 1-8). Geneva.
- Hawladar, B., Lee, Y., & Lo, K. (2003). Three-dimensional stress effects on time-dependent swelling behaviour of shaly rocks. *Canadian Geotechnical Journal*, Vol. 40, 501-511.
- Hawladar, B., Lo, K., & Moore, I. (2005). Analysis of tunnels in shaly rock considering three-dimensional stress effects on swelling. *Canadian Geotechnical Journal*, Vol. 42, 1-12.
- Hefny, A., & Lo, K. (1996). Design of tunnels in rock with long-term time-dependent and nonlinearly stress-dependent deformation. *Canadian Tunnelling 1996*, 179-214.
- Hefny, A., Lo, K., & Huang, J. (1996). Modelling of long-term time-dependent deformation and stress-dependency of Queenston Shale. *Canadian Tunnelling 1996*, 179-214.
- Hilal, A., Thom, N., & Dawson, A. (2015). On void structure and strength of foamed concrete made without/with additives. *Construction and Building Materials*, Vol. 85, 157-164.
- Hoek, E., & Brown, T. (1980). Empirical strength criterion for rock masses. *Journal of Geotechnical Engineering Division*, Vol. 106(GT9), 1013-1035.
- Hoek, E., Kaiser, P., & Bawden, W. (2005). *Support of underground excavations in hard rock*. New York: Taylor & Francis.

- Hosseinzadeh, S. (2012). Numerical assessment and validation of a swelling rock model. *MESc thesis, Section for Geoengineering, Department of Geoscience and Engineering, Delft University of Technology*. The Netherlands.
- Isherwood, B., Brown, T., Earle, J., & Kreycir, P. (2014). Deep excavation support at Toronto's Shangri-La. *Deep Foundations, Mar/Apr 2014, 77-80*.
- Kearsley, E., & Wainwright, P. (2002). The effect of porosity on the strength of foamed concrete. *Cement and Concrete Research, Vol. 32, 233-239*.
- Kramer, G., & Moore, I. (2005). Finite element modelling of tunnels in swelling rock. *K.Y. Lo Symposium*. London: The University of Western Ontario.
- Lardner, T. (2011). Behaviour of the shoring and bedrock during the excavation for The Bow. *MESc Thesis, Department of Civil and Environmental Engineering*. London, Ontario, Canada: School of Graduate and Postdoctoral Studies, University of Western Ontario.
- Laynon, G., Diederichs, M., & Leech, R. (2011). *Excavation Damaged Zone Assessment. OPG's Deep Geologic Repository for Low and Intermediate Level Waste. Report NWMO DGR-TR-2011-21, Revision R000*. Fracture Systems Ltd.
- Lee, C., & Lo, K. (1976). Rock squeeze study of two deep excavations at Niagara Falls. *Rock Engineering, Proc. Specialty Conference for Foundations and Slopes. Vol. 1, pp. 116-140*. Boulder, Colorado: ASCE.
- Lee, S. (2017). Numerical model for shaley rock masses displaying long-term Time Dependent Deformation (TDD) behaviour and its application to a pedestrian

- tunnel constructed under Lake Ontario. *KSCE Journal of Civil Engineering*, Vol. 21(No. 7), 2919-2931.
- Lee, Y., & Lo, K. (1993). The swelling mechanism of Queenston shale. *Tunnelling Association of Canada Annual Publication*, 75-97.
- Lo, K. (1989). Recent advances in design and evaluation of performance of underground structures in rocks. *Tunnelling and Underground Space Technology*, 4(2), 171-183.
- Lo, K., & Hefny, A. (1996). Design of tunnels in rock with long-term time-dependent and nonlinearly stress-dependent deformation. *Canadian Tunnelling 1996*, 179-214.
- Lo, K., & Hefny, A. (1999). Measurements of Residual Expansion Rates Resulting. *ACI Materials*, 96(3), 339-345.
- Lo, K., & Hefny, A. (2001). Basic rock mechanics and testing. In R. Rowe, *Geotechnical and Geoenvironmental Engineering Handbook*. USA: Kluwer Academic Publishers.
- Lo, K., & Lee, Y. (1990). Time-dependent deformation behaviour of Queenston Shale. *Canadian Geotechnical Journal*, Vol. 27, 461-471.
- Lo, K., & Lukajic, B. (1984). Predicted and measured stresses and displacements around the Darlington Intake Tunnel. *Canadian Geotechnical Journal*, Vol. 21, 147-165.
- Lo, K., & Micic, S. (2010). Evaluation of swelling properties of shales for the design of underground Structures. *ITA-AITES 2010 World Tunnel Congress*. Vancouver: TAC.



- Lo, K., & Yuen, C. (1981). Design of tunnel lining for long term time effects. *Canadian Geotechnical Journal*, Vol. 18, 24-39.
- Lo, K., Cooke, B., & Dunbar, D. (1987). Design of buried structures in squeezing rock in Toronto, Canada. *Canadian Geotechnical Journal*, Vol. 24, 232-241.
- Lo, K., Devata, M., & Yuen, C. (1978). Performance of a shallow tunnel in a shaly rock with high horizontal stresses. *Tunnelling '79, Proc. 2nd International Symposium on Tunnelling* (pp. 1-12, Paper 9). London, England: Institution of Mining and Metallurgy.
- Lo, K., Wai, R., Palmer, J., & Quigley, R. (1978). Time-dependent deformation of shaly rocks in Southern Ontario. *Canadian Geotechnical Journal*, Vol. 13, 1-7.
- Micic, S., Gonsalves, S., Lo, K., & Lardner, T. (2016). Billy Bishop Airport Passenger Tunnel, Toronto. *Canadian Geotechnical Conference, GeoVancouver 2016* (p. Paper 3975). Vancouver, B.C.: Canadian Geotechnical Society.
- Mohamed, G., Hegazy, R., & Mohamed, M. (2017). An investigation on the mechanical behaviour of expanded polystyrene (EPS) geofom under different loading conditions. *International Journal of Plastic Technologies*, Vol. 21(No. 1), 123-129.
- Nambiar, E., & Ramamurthy, K. (2007). Air-void characterisation of foam concrete. *Cement and Concrete Research*, Vol. 37(No. 2), 221-230.
- Negussey, D. (2007). Design parameters for EPS geofom. *Soils Foundations*, Vol. 47(No. 1), 161-170.

- Nehdi, M., Khan, A., & Lo, K. (2002). Development of deformable protective system for underground infrastructure using cellular grouts. *ACI Materials Journal*, Vol. 99(5), 490-498.
- Niagara Tunnel Project Technical Facts, updated November 2012.* (n.d.). Retrieved from <https://www.NiagaraFrontier.com>
- Obert, L., & Duvall, W. (1967). *Rock Mechanics and the Design of Structures in Rocks*. New York: Wiley.
- (2018). *Ontario population projections update, 2017-2041*. Ministry of Finance, Government of Ontario, Queen's Printer for Ontario.
- Parras, M. (2014). Understanding and predicting excavation damage in sedimentary rocks: a continuum based approach (PhD thesis). Kingston, ON: Department of Geology and Geological Engineering, Queen's University.
- Perras, M. (2009). Tunnelling in horizontally laminated ground: the influence of lamination thickness on anisotropic behaviour and practical observations from the Niagara Tunnel Project. *Masters of Science and Engineering thesis*. Kingston, ON: Queen's University.
- Perras, M., Wannemacher, H., & Diederichs, M. (2015). Underground excavation behaviour of the Queenston Formation: Tunnel back analysis for application to shaft damage dimension prediction. *Rock Mech Rock Eng*, Vol. 48, 1647-1671.
- Ramamurthy, K., Kunhanandan Nambiar, E., & Indu Siva Ranjani, G. (2009). A classification of studies on properties of foam concrete. *Cement & Concrete Composites*, Vol. 31, 388-396.

- Smakosz, Ł., & Tejchman, J. (2014). Evaluation of strength, deformability and failure model of composite structural insulated panels. *Materials and Design, Vol. 54*, 1068-1082.
- Srirajan, S., Negussey, D., & Anasthas, N. (2006). *Creep behavior of EPS geof foam*. Syracuse University. Syracuse, NY: Geof foam Research Center.
- Timoshenko, S., & Goodier, J. (1970). *Theory of Elasticity*. McGraw-Hill.
- Tiwari, B., Ajmera, B., Maw, R., Cole, R., Villegas, D., & Palmerson, P. (2017). Mechanical Properties of Lightweight Cellular Concrete for Geotechnical Applications. *Technical Note, Journal of Material Civil Engineering, Vol. 29*(No. 7).
- Vancheri, G., & Braczek, M. (2014). Zone 1 Interconnecting Watermain: Proudly tunnelling under the challenges ahead. *North American Tunneling 2014 Proceedings, Society for Mining, Metallurgy and Exploration*, (pp. 510-519).
- Wittke-Gattermann, P., & Wittke, M. (2004). Computation of Strains and Stresss for Tunnels in Swelling Rocks. *Proc. ITA 2004*, (pp. 1-9). Singapore.
- Yuen, C. (1979). Rock-Structure Time Interaction in Lined Circular Tunnels in High Horizontal Stress Field. *PhD Thesis, Civil and Environmental Engineering Department*. London, Ontario, Canada: The University of Western Ontario.
- Yuen, C., Erziclioglu, A., Huang, J., & Somerville, W. (1992). Design of diversion tunnels Niagara River hydroelectric development. *Proceedings 4th Canadian Geotechnical Conference. Paper 106*. Toronto, ON: Canadian Geotechnical Society.

Zhao, H., Yu, H., Yuan, Y., & Zhu, H. (2015). Blast mitigation effect of the foamed cement-base sacrificial cladding for tunnel structures. *Construction and Building Materials*, Vol. 94, 710-718.

Zienkiewicz, O. (1967). *The finite element method in structural and continuum mechanics*. London, UK: McGrawHill.

# Appendices

## Appendix A: Fortran Code for Swelling Subroutine

All code shown in this Appendix was developed by the author.

```
subroutine TDD_Strain(Sig,Props,DE,Time0,dTime,iEl,Int,iStep,iTer,  
*dSig_ctdd)
```

```
!-----  
!   This subroutine uses the principle stresses at the start of the  
!   step to determine the TDD strains.  
!-----
```

```
Implicit Double Precision (A-H, O-Z)
```

```
!-----  
!  
!   Variables used:  
!   Name           I/O    Type   Description  
!  
!   dSig           I       R/M    Stresses from recent step  
!   E_frh          I       R      Horizontal free swell rate  
!   Sig_thh        I       R      Horizontal threshold pressure  
!   Sig_sph        I       R      Horizontal suppression pressure  
!   E_frv          I       R      Vertical free swell rate  
!   Sig_thv        I       R      Vertical threshold pressure  
!   Sig_spv        I       R      Vertical suppression pressure  
!   DE             I       R/M    Effective material stiffness matrix  
!   Time0          I       R      Time at start of step  
!   dTime          I       R      Time increment  
!   S1             R       R      Major principal stress magnitude  
!   S2             R       R      Secondary principal stress mag.  
!   S3             R       R      Minor principal stress mag.  
!   xN1            R       R      Major principal stress direction  
!   xN2            R       R      Secondary principal stress dir.  
!   xN3            R       R      Minor principal stress dir.  
!   Angle_s1       R       R      Angle from horizontal to S1  
!   Angle_s2       R       R      Angle from horizontal to S2  
!   E_f11          R       R      Free swell in S1 direction  
!   Sig_th1        R       R      Threshold pressure in S1 dir.  
!   Sig_sp1        R       R      Suppression pressure in S1 dir.  
!   K_1            R       R      Swelling potential in S1 dir.  
!   E_sw1          R       R      Swelling rate in S1 dir.  
!   dE_1           R       R      Strain due to swell in S1 dir.  
!   E_f22          R       R      Free swell in S2 direction  
!   Sig_th2        R       R      Threshold pressure in S2 dir.  
!   Sig_sp2        R       R      Suppression pressure in S2 dir.  
!   K_2            R       R      Swelling potential in S2 dir.  
!   E_sw2          R       R      Swelling rate in S2 direction  
!   dE_2           R       R      Strain due to swell in S2 dir.  
!   dE_tdd         R/M    R/M    Swelling strain matrix
```

```

!      dSig_ptdd          R/M   Swelling stress matrix (princ)
!      S_tdd1            R      Swelling pressure in S1 dir.
!      S_tdd2            R      Swelling pressure in S2 dir.
!      S_tdd3            R      Swelling pressure in S3 dir.
!      dSig_ctdd        0      R/M   Swelling stress matrix (cart)
!
!
!-----

Dimension Sig(*), DE(6,6), Props(*)

!--- Local variables
Dimension xN1(3),xN2(3),xN3(3), yN1(3), yN2(3), yN3(3)
Dimension dE_tdd(3,3),dE_xyz(3,3),dE_xy(6),dSig_ctdd(6)
Dimension e_fr(3,3),sig_th(3,3),sig_sp(3,3)
Dimension Prne_fr(3,3),Prnsig_th(3,3),Prnsig_sp(3,3)

! Get principal stresses
iOpt = 1
Call PrnSig(iOpt, Sig, xN1, xN2, xN3, S1, S2, S3, P, Q)
Data PI/3.14159 26535 89793 23846 26433 83279 50288 41971 69399d0/

! Set up swelling parameters as matrices

e_fr(1,1) = Props(7) !horizontal
e_fr(2,2) = Props(10) !vertical
e_fr(3,3) = Props(7) !out of plane

sig_th(1,1) = Props(8)
sig_th(2,2) = Props(11)
sig_th(3,3) = Props(8)

sig_sp(1,1) = Props(9)
sig_sp(2,2) = Props(12)
sig_sp(3,3) = Props(9)

Call rotate(e_fr,xN1,xN2,xN3,Prne_fr)
Call rotate(sig_th,xN1,xN2,xN3,Prnsig_th)
Call rotate(sig_sp,xN1,xN2,xN3,Prnsig_sp)

! Flip signs on principal stresses
S1 = -S1
S2 = -S2
S3 = -S3

! Sigma_11 direction
dlog_s11 = log10(Prnsig_th(1,1)/Prnsig_sp(1,1))

if (S1.ge.Prnsig_sp(1,1)) then
  E_pot11 = 0.0
elseif (S1.le.Prnsig_th(1,1)) then
  E_pot11 = Prne_fr(1,1)
else
  E_pot11 = Prne_fr(1,1)*log10(S1/Prnsig_sp(1,1))/dlog_s11
endif

```

```

!--- Sigma_22 swell potential

dlog_s22 = log10(Prnsig_th(2,2)/Prnsig_sp(2,2))

if (S2.ge.Prnsig_sp(2,2)) then
    E_pot22 = 0.0
elseif (S2.le.Prnsig_th(2,2)) then
    E_pot22 = Prne_fr(2,2)
else
    E_pot22 = Prne_fr(2,2)*log10(S2/Prnsig_sp(2,2))/dlog_s22
endif

!--- Sigma_33 swell potential

dlog_s33 = log10(Prnsig_th(3,3)/Prnsig_sp(3,3))

if (S3.ge.Prnsig_sp(3,3)) then
    E_pot33 = 0.0
elseif (S3.le.Prnsig_th(3,3)) then
    E_pot33 = Prne_fr(3,3)
else
    E_pot33 = Prne_fr(3,3)*log10(S3/Prnsig_sp(3,3))/dlog_s33
endif

!-----
! Pseudo-Poisson's Ratio
!-----

PPR = Props(13)
if (PPR.lt.0.001) then
    PPR = 0.0
elseif (PPR.gt.1.0) then
    PPR = 1.0
endif

Ratio_s11 = E_pot11/Prne_fr(1,1)
Ratio_s22 = E_pot22/Prne_fr(2,2)
Ratio_s33 = E_pot33/Prne_fr(3,3)

! --- Find minimum in-plane Ratio
if(xN1(3).gt.0.0)then !Sigma_11 out of plane
    if(Ratio_s22.le.Ratio_s33) then
        Ratio_sw = Ratio_s22
        E_sw11 = E_pot11
        E_sw22 = Prne_fr(2,2)*(Ratio_s22-PPR*(Ratio_s22-Ratio_sw))
        E_sw33 = Prne_fr(3,3)*(Ratio_s33-PPR*(Ratio_s33-Ratio_sw))
    else
        Ratio_sw = Ratio_s33
        E_sw11 = E_pot11
        E_sw22 = Prne_fr(2,2)*(Ratio_s22-PPR*(Ratio_s22-Ratio_sw))
        E_sw33 = Prne_fr(3,3)*(Ratio_s33-PPR*(Ratio_s33-Ratio_sw))
    endif
elseif(xN2(3).gt.0.0) then !Sigma_22 out of plane
    if(Ratio_s11.le.Ratio_s33) then

```

```

Ratio_sw = Ratio_s11
E_sw11 = Prne_fr(1,1)*(Ratio_s11-PPR*(Ratio_s11-Ratio_sw))
E_sw22 = E_pot22
E_sw33 = Prne_fr(3,3)*(Ratio_s33-PPR*(Ratio_s33-Ratio_sw))
else
Ratio_sw = Ratio_s33
E_sw11 = Prne_fr(1,1)*(Ratio_s11-PPR*(Ratio_s11-Ratio_sw))
E_sw22 = E_pot22
E_sw33 = Prne_fr(3,3)*(Ratio_s33-PPR*(Ratio_s33-Ratio_sw))
endif
elseif(xN3(3).gt.0.0) then ! Sigma_33 is out of plane
if(Ratio_s11.le.Ratio_s22) then
Ratio_sw = Ratio_s11
E_sw11 = Prne_fr(1,1)*(Ratio_s11-PPR*(Ratio_s11-Ratio_sw))
E_sw22 = Prne_fr(2,2)*(Ratio_s22-PPR*(Ratio_s22-Ratio_sw))
E_sw33 = E_pot33
else
Ratio_sw = Ratio_s22
E_sw11 = Prne_fr(1,1)*(Ratio_s11-PPR*(Ratio_s11-Ratio_sw))
E_sw22 = Prne_fr(2,2)*(Ratio_s22-PPR*(Ratio_s22-Ratio_sw))
E_sw33 = E_pot33
endif
endif
endif

```

! --- Set shear swell potentials.

```

E_sw12 = Prne_fr(1,2)*Ratio_sw
E_sw13 = Prne_fr(1,3)*Ratio_sw
E_sw21 = Prne_fr(2,1)*Ratio_sw
E_sw23 = Prne_fr(2,3)*Ratio_sw
E_sw31 = Prne_fr(3,1)*Ratio_sw
E_sw32 = Prne_fr(3,2)*Ratio_sw

```

```

!   if(PPR.ge.0.005)then
!       if (xN1(3).eq.0.0d+15) then
!           if(xN2(3).eq.0.0d+15) then !S3 is out of plane
if(PPR.ge.0.005)then
if (xN1(3).eq.0.0d+15) then
if(xN2(3).eq.0.0d+15) then !S3 is out of plane

If (Ratio_s11.gt.Ratio_s22) then
E_sw11 = (Ratio_s11-PPR*(Ratio_s11-Ratio_s22))*Prne_fr(1,1)
elseif (Ratio_s22.gt.Ratio_s11) then
E_sw22 = (Ratio_s22-PPR*(Ratio_s22-Ratio_s11))*Prne_fr(2,2)
endif

else !S2 is out of plane

If (Ratio_s11.gt.Ratio_s33) then
E_sw11 = (Ratio_s11-PPR*(Ratio_s11-Ratio_s33))*Prne_fr(1,1)
elseif (Ratio_s33.gt.Ratio_s11) then
E_sw33 = (Ratio_s33-PPR*(Ratio_s33-Ratio_s11))*Prne_fr(3,3)
endif
endif

```



```

endif

else ! S1 is out of plane

If (Ratio_s22.gt.Ratio_s33) then
  E_sw22 = (Ratio_s22-PPR*(Ratio_s22-Ratio_s33))*Prne_fr(2,2)
elseif (Ratio_s33.gt.Ratio_s22) then
  E_sw33 = (Ratio_s33-PPR*(Ratio_s33-Ratio_s22))*Prne_fr(3,3)
endif

endif

endif

!-- determine strain increments

if (Time0 .eq. 0.0d+15) then

  dE_tdd(1,1) = E_sw11*log10(dTime) !Strain in S1 dir
  dE_tdd(2,2) = E_sw22*log10(dTime) !Strain in S2 dir
  dE_tdd(3,3) = E_sw33*log10(dTime) !Strain in S3 dir
  dE_tdd(1,2) = E_sw12*log10(dTime) ! Strain in 12 shear
  dE_tdd(1,3) = E_sw13*log10(dTime) ! Strain in 13 shear
  dE_tdd(2,1) = E_sw21*log10(dTime) ! Strain in 21 shear
  dE_tdd(2,3) = E_sw23*log10(dTime) ! Strain in 23 shear
  dE_tdd(3,1) = E_sw31*log10(dTime) ! Strain in 31 shear
  dE_tdd(3,2) = E_sw32*log10(dTime) ! Strain in 32 shear

else

  dE_tdd(1,1) = E_sw11*log10((Time0 + dTime)/Time0) !Strain in S1 dir
  dE_tdd(2,2) = E_sw22*log10((Time0 + dTime)/Time0) !Strain in S2 dir
  dE_tdd(3,3) = E_sw33*log10((Time0 + dTime)/Time0) !Strain in S3 dir
  dE_tdd(1,2) = E_sw12*log10((Time0 + dTime)/Time0) ! Strain in 12 shear
  dE_tdd(1,3) = E_sw13*log10((Time0 + dTime)/Time0) ! Strain in 13 shear
  dE_tdd(2,1) = E_sw21*log10((Time0 + dTime)/Time0) ! Strain in 21 shear
  dE_tdd(2,3) = E_sw23*log10((Time0 + dTime)/Time0) ! Strain in 23 shear
  dE_tdd(3,1) = E_sw31*log10((Time0 + dTime)/Time0) ! Strain in 31 shear
  dE_tdd(3,2) = E_sw32*log10((Time0 + dTime)/Time0) ! Strain in 32 shear

endif

! Rotate strains to cartesean
call MatInv(iE1,Int,xN1,xN2,xN3,yN1,yN2,yN3) !Need inverse eigenvector matrix
call rotate(dE_tdd,yN1,yN2,yN3,dE_xyz) !Rotate

!Transfer strains from xyz maxtrix to array (3x3 to 6 value array)
dE_xy(1) = dE_xyz(1,1) !xx
dE_xy(2) = dE_xyz(2,2) !yy
dE_xy(3) = dE_xyz(3,3) !zz
dE_xy(4) = dE_xyz(1,2) !xy
dE_xy(5) = 0.0 !yz Switch to dE_xyz(2,3) for 3D
dE_xy(6) = 0.0 !zx Switch to dE_xyz(3,1) for 3D

```

```
Call MatVec( DE, 6, dE_xy, 6, dSig_ctdd)
```

```
!flip signs  
do i=1,6  
    dSig_ctdd(i) = -1.0*dSig_ctdd(i)  
end do
```

```
Return  
end subroutine TDD_Strain
```

```
!-----  
subroutine rotate(xmat,V1,V2,V3,rotmat)
```

```
! This subroutine rotates parameters using the eigenvectors  
!-----
```

```
Implicit Double Precision (A-H,O-Z)  
Dimension xmat(3,3),V1(*),V2(*),V3(*),rot(3,3),rotT(3,3)  
Dimension ymat(3,3),rotmat(3,3)
```

```
! fill rotation matrix
```

```
Do i=1,3  
    rot(1,i) = V1(i)  
    rot(2,i) = V2(i)  
    rot(3,i) = V3(i)  
end do
```

```
! fill transervse rotation matrix
```

```
Do i=1,3  
    rotT(1,i) = rot(i,1)  
    rotT(2,i) = rot(i,2)  
    rotT(3,i) = rot(i,3)  
end do
```

```
! rot X mat
```

```
call MatxMat(rot,xmat,ymat)
```

```
! xmat X rotT
```

```
call MatxMat(ymat,rotT,rotmat)
```

```
return  
end subroutine Rotate
```

```
!-----  
subroutine MatxMat(xmatA,xmatB,outmat)
```

```
! Multiplies two square 3x3 matrices
```

```
Implicit Double Precision (A-H,O-Z)
```

```
Dimension:: xmatA(3,3),xmatB(3,3),outmat(3,3)
```

```
do i=1,3  
    do j=1,3  
        x = 0.0
```

```

        do k=1,3
            x = x + xmatA(i,k)*xmatB(k,j)
        end do
        outmat(i,j) = x
    end do
end do

return
end subroutine MatxMat

```

```

!-----
subroutine MatInv(iEl,Int,xV1,xV2,xV3,yV1,yV2,yV3)
! Finds the inverse of a 3x3 matrix using Gauss-Jordan elimination
Implicit Double Precision (A-H,O-Z)
Dimension:: xV1(3),xV2(3),xV3(3) ! Inputs
Dimension:: xmatA(3,3),outmat(3,3),yV1(3),yV2(3),yV3(3) ! Internal and outputs
Dimension:: tempA(3), tempout(3)

!Fill xmatA with eigenvectors
do i = 1,3
    xmatA(1,i) = xV1(i)
    xmatA(2,i) = xV2(i)
    xmatA(3,i) = xV3(i)
end do

! Fill outmat with identity matrix
do i=1,3
    do j=1,3
        if(i.eq.j) then
            outmat(i,j) = 1.0
        else
            outmat(i,j) = 0.0
        endif
    enddo
enddo

! Organize matrices to ensure pivot points are non-zero
if (xmatA(1,1).eq.0.0d+15) then ! Organize row 1
    if(xmatA(2,1).eq.0.0d+15) then
        do i = 1,3
            tempA(i) = xmatA(1,i)
            tempout(i) = outmat(1,i)
            xmatA(1,i) = xmatA(3,i)
            outmat(1,i) = outmat(3,i)
            xmatA(3,i) = tempA(i)
            outmat(3,i) = tempout(i)
        end do
    else
        do i = 1,3
            tempA(i) = xmatA(1,i)
            tempout(i) = outmat(1,i)
            xmatA(1,i) = xmatA(2,i)
            outmat(1,i) = outmat(2,i)
            xmatA(2,i) = tempA(i)
            outmat(2,i) = tempout(i)
        end do
    end if

```

```

end if

if (xmatA(2,2).eq.0.0d15) then ! Organize row 2
  do i = 1,3
    tempA(i) = xmatA(2,i)
    tempout(i) = outmat(2,i)
    xmatA(2,i) = xmatA(3,i)
    outmat(2,i) = outmat(3,i)
    xmatA(3,i) = tempA(i)
    outmat(3,i) = tempout(i)
  end do
end if

!Make the pivot in cell 1,1
pivot = xmatA(1,1)
do i = 1,3
  xmatA(1,i) = xmatA(1,i)/pivot
  outmat(1,i) = outmat(1,i)/pivot
enddo

!eliminate 1st column
elim2 = xmatA(2,1)
elim3 = xmatA(3,1)
do i=1,3
  xmatA(2,i) = xmatA(2,i)-elim2*xmatA(1,i)
  outmat(2,i) = outmat(2,i)-elim2*outmat(1,i)
  xmatA(3,i) = xmatA(3,i)-elim3*xmatA(1,i)
  outmat(3,i) = outmat(3,i)-elim3*outmat(1,i)
end do

!make pivot in cell 2,2
pivot = xmatA(2,2)
do i = 1,3
  xmatA(2,i) = xmatA(2,i)/pivot
  outmat(2,i) = outmat(2,i)/pivot
end do

!eliminate 2nd column
elim1 = xmatA(1,2)
elim3 = xmatA(3,2)
do i = 1,3
  xmatA(1,i) = xmatA(1,i)-elim1*xmatA(2,i)
  outmat(1,i) = outmat(1,i)-elim1*outmat(2,i)
  xmatA(3,i) = xmatA(3,i)-elim3*xmatA(2,i)
  outmat(3,i) = outmat(3,i)-elim3*outmat(2,i)
end do

!make the pivot in cell 3,3
pivot = xmatA(3,3)
do i = 1,3
  xmatA(3,i) = xmatA(3,i)/pivot
  outmat(3,i) = outmat(3,i)/pivot
end do

!eliminate 3rd column
elim1 = xmatA(1,3)
elim2 = xmatA(2,3)

```

```
do i = 1,2
  xmatA(1,i) = xmatA(1,i)-elim1*xmatA(3,i)
  outmat(1,i) = outmat(1,i)-elim1*outmat(3,i)
  xmatA(2,i) = xmatA(2,i)-elim2*xmatA(3,i)
  outmat(2,i) = outmat(2,i)-elim2*outmat(3,i)
end do

!Fill new vectors
do i=1,3
  yV1(i) = outmat(1,i)
  yV2(i) = outmat(2,i)
  yV3(i) = outmat(3,i)
end do

return

end subroutine MatInv
```

## Appendix B: Zone 1 Water Main borehole logs

### Explanation of core log terms

#### Discontinuity types:

BD	Bedding
JN	Joint
FR	Fracture

#### Discontinuity roughness and shape:

VR	Very rough
Ro	Rough
SM	Smooth
PL	Planar
IR	Irregular
CI	Inclined

#### Discontinuity weathering:

CL	Clean
SO	Slight weathering
HW	Heavily weathered

CORE LOG RECORD FOR BH: <u>INCL 1 PARTIAL LOG</u>														
PROJECT: <u>Zone 1 Watermain</u>				DRILLING DATA				Page: <u>1 of 8</u>						
CLIENT: <u>RVA</u>				DRILL: <u>TRUCK MOUNTED</u>										
LOCATION: <u>MAIN SHAFT SE CORNER of QUEEN/BUCKLEAK</u>				METHOD: <u>ROTARY, H<sub>2</sub>O FLUSH</u>										
DATE: <u>2015/08/13 to 2015/08/14</u>				DIAMETER: <u>HQ</u>										
				INCLINATION: <u>-90°</u>										
ELEV/DEPTH (m)	SYMBOL	ROCK DESCRIPTION	GROUND WATER CONDITIONS	RUN NUMBER	CORE SIZE	TOTAL CORE RECOVERY (%)	SOLID CORE RECOVERY (%)	RQD (%)	FRACTURE FREQUENCY (per 0.3m)	DISCONTINUITY DIP (degrees)	DISCONTINUITIES AND WEATHERING	SAMPLE	TEST	NOTES
-114														
-113														
-112		LEAN MIX												
-111														
-110														
-109.2		CONCRETE SLAB												
-109														
-108		QUEENSTON SHALE Predominantly red with grey layers Some limestone lenses												No RECORDS
-107														

GENERAL NOTES:

**CORE LOG RECORD FOR BH: INCL 1 PARTIAL LOGS** Page: 2 of 8

PROJECT: \_\_\_\_\_ DRILLING DATA \_\_\_\_\_

CLIENT: \_\_\_\_\_ DRILL: \_\_\_\_\_

LOCATION: \_\_\_\_\_ METHOD: \_\_\_\_\_

DATE: \_\_\_\_\_ DIAMETER: \_\_\_\_\_

INCLINATION: \_\_\_\_\_

ELEV/ DEPTH (m)	SYMBOL	ROCK DESCRIPTION	GROUND WATER CONDITIONS	RUN NUMBER	CORE SIZE	TOTAL CORE RECOVERY (%)	SOLID CORE RECOVERY (%)	RCD (%)	FRACTURE FREQUENCY (per 0.3m)	DISCONTINUITY DIP (degrees)	DISCONTINUITIES AND WEATHERING	SAMPLE	TEST	NOTES
99.6														
100														
101														
102														
105														
106														
108														

No RECORDS

GENERAL NOTES: No core recorded - off site getting sampling supplies.



CORE LOG RECORD FOR BH: INCL 1 PARTIAL LOG														
PROJECT:			DRILLING DATA						Page: 3 of 8					
CLIENT:			DRILL:											
LOCATION:			METHOD:											
DATE:			DIAMETER:											
			INCLINATION:											
ELEV/DEPTH (m)	SYMBOL	ROCK DESCRIPTION	GROUND WATER CONDITIONS	RUN NUMBER	CORE SIZE	TOTAL CORE RECOVERY (%)	SOLID CORE RECOVERY (%)	ROD (%)	FRACTURE FREQUENCY (per 0.3m)	DISCONTINUITY DIP (degrees)	DISCONTINUITIES AND WEATHERING	SAMPLE	TEST	NOTES
99.6														
99														
98														
97.5														
97				1	HQ	95%	95%	94%	0	0.80	ED, PL, SA BD, PL, SA BD, PL FR, PL FR, PL, RO, SA			
96									1		FR, PL, RO, SA			
95				2	HQ	100%	100%	99%	0		FR, PL, RO			Handling fracture.
94									1		BD, PL, SM, CL			
94				3	HQ	100%	100%	100%	0		FR, IR			Handling fracture.
93									0					
92.4									1	25	FR, PL, SM, CL			

GENERAL NOTES:

CORE LOG RECORD FOR BH: <u>Incl 1 PARTIAL LOG</u>															
PROJECT:			DRILLING DATA						Page: <u>4 of 8</u>						
CLIENT:			DRILL:												
LOCATION:			METHOD:												
DATE:			DIAMETER:												
			INCLINATION:												
ELEV/ DEPTH (m)	SYMBOL	ROCK DESCRIPTION	GROUND WATER CONDITIONS	RUN NUMBER	CORE SIZE	TOTAL CORE RECOVERY (%)	SOLID CORE RECOVERY (%)	RQD (%)	FRACTURE FREQUENCY (per 0.3m)	DISCONTINUITY DIP (degrees)	DISCONTINUITIES AND WEATHERING	SAMPLE	TEST	NOTES	
-92.4				4	HQ	100%	100%	98%	0						
-92									0						
-91.5									1		BD, PL, SM, CL				
-91						5	HQ	100%	100%	100%	0				
-90									0		FR, PL				
-89						6	HQ	100%	100%	100%	0				
-88.5									1		FR, PL, SM, CL				
-88									0						
-87					7	HQ	100%	100%	97%	0					
-87								0	0°	FR, PL, BD, PL, SM, CL					
-86					8	HQ	98%	96%	92%	0					
-85.5								0							
-85.2								2	0°						
								0	0°						

GENERAL NOTES:

CORE LOG RECORD FOR BH: <u>INCL   PARTIAL LOG</u>															
PROJECT:				DRILLING DATA				Page: <u>5 of 8</u>							
CLIENT:				DRILL:											
LOCATION:				METHOD:											
DATE:				DIAMETER:											
				INCLINATION:											
ELEV/DEPTH (m)	SYMBOL	ROCK DESCRIPTION	GROUND WATER CONDITIONS	RUN NUMBER	CORE SIZE	TOTAL CORE RECOVERY (%)	SOLID CORE RECOVERY (%)	ROD (%)	FRACTURE FREQUENCY (per 0.3m)	DISCONTINUITY DIP (degrees)	DISCONTINUITIES AND WEATHERING	SAMPLE	TEST	NOTES	
85.2				9	HQ	98%	98%	98%	0						
85									0						
84									0						
84					10	HQ	100%	100%	96%	1	0	BD, PL, SM, CL			
83									0						
82.5									1	0	FR, PL			Handling fracture	
82									0						
82					11	HQ	94%	94%	94%	0					
81									0	0	BD, PL, SM, CL				
81			Weathered						3		FR, IR, SA BD, PL, SA BD, PL, Ro, SA				
80					12	HQ	100%	95%	72%	0		BD, PL, Ro, SA BD, PL, Ro, IM, CL FR, PL, SM, SO FR, PL, Ro FR, PL, SM, CL			
79.5									2						
79									3						
79				13	HQ	61%	61%	37%	1	0	FR, PL, Ro, CL			Lost upper portion during casing removal	
78								1	0	FR, PL FR, PL, IM FR, PL, SM					
78								3	0	FR, PL, SM					

GENERAL NOTES:

CORE LOG RECORD FOR BH: INCL PARTIAL LOG										Page: 6 of 8				
PROJECT:			DRILLING DATA											
CLIENT:			DRILL:											
LOCATION:			METHOD:											
DATE:			DIAMETER:											
			INCLINATION:											
ELEV/DEPTH (m)	SYMBOL	ROCK DESCRIPTION	GROUND WATER CONDITIONS	RUN NUMBER	CORE SIZE	TOTAL CORE RECOVERY (%)	SOLID CORE RECOVERY (%)	ROD (%)	FRACTURE FREQUENCY (per 0.3m)	DISCONTINUITY DIP (degrees)	DISCONTINUITIES AND WEATHERING	SAMPLE	TEST	NOTES
78				14	HQ	100%	100%	92%	1	0°	FR, PL, SM, CL			Top of core damaged
77									2	10°	FR, PL, SO			Overdrilled to make up for lost run in 13
76.5									1	0°	BD, PL, SM, SO			
76				15	HQ	100%	100%	91%	0	0°	FR, IR, SO, CL			
75									1	0°	BD, PL, SM, SO			
74									1	0°	BD, PL, SM, CL			
73.5									1	0°	FR, PL, i			
73									3	0°	FR, IR, CL			
72									15	15°	BD, PL, SM, CL			
71				16	HQ	100%	100%	92%	2	15°	FR, PL, SM, CL			Bottom of Shaft @ 72.5m.
70.5									2	15°	FR, PL, SM, CL			
70									1	15°	FR, PL, SM, CL			
69.5									0	0°	BD, PL, SM, CL			
69									1	0°	FR, PL, SO, CL			
68				17	HQ	99%	99%	99%	0	0°	BD, PL, SM, SO			
67.5									1	0°	BD, PL, SM			
67									1	0°	BD, PL, SM			
66		Slightly weathered							1	0°	FR, PL, SO, IN, CL			
65				18	HQ	100%	100%	100%	1	0°	BD, PL, SM, SA			
64		Slightly weathered							2	0°	BD, PL, SM, SO			
63									1	0°	BD, PL, SM, CL			
62									1	0°	BD, PL, SM, CL			




GENERAL NOTES:

CORE LOG RECORD FOR BH: <u>INCL 1 PARTIAL LOG</u>														
PROJECT:			DRILLING DATA						Page: <u>7 of 8</u>					
CLIENT:			DRILL:											
LOCATION:			METHOD:											
DATE:			DIAMETER:											
			INCLINATION:											
ELEV/DEPTH (m)	SYMBOL	ROCK DESCRIPTION	GROUND WATER CONDITIONS	RUN NUMBER	CORE SIZE	TOTAL CORE RECOVERY (%)	SOLID CORE RECOVERY (%)	RCD (%)	FRACTURE FREQUENCY (per 0.3m)	DISCONTINUITY DIP (degrees)	DISCONTINUITIES AND WEATHERING	SAMPLE	TEST	NOTES
70.8									2		BD, PL, R <sub>0</sub> , SA			
70.5									2		BD, PL, R <sub>0</sub> , SO			
70		Gouge & Weather		19	HQ	95%	85%	77%	3		See photos			No signs of slickens or other movement
69		Gouge 100nick Weathering							5					
69		Weathering							4					
68				20	HQ	98%	94%	94%	2	0°	BD, PL, SM, CL			
68									0	0°	BD, PL, R <sub>0</sub> , SA			
67.5									1	0°	BD, PL			
67		Gouge & Weathering		21	HQ	100%	95%	79%	2		FR, IR, R <sub>0</sub> , CL			Handling fractures
66									0		FR, IR, R <sub>0</sub> , CL			
66									5		SEE PHOTOS			
66									0		BD, PL, SM, CL			
65									2		BD, PL, SM, CL			
64.8									0					
64.5		GEORGIAN BAY FORMATION							1					
64		Limestone		23	HQ	100%	100%	94%	0		BD, PL, SO			
63.6									2	0°	FR, PL, R <sub>0</sub> , SA			

GENERAL NOTES:

CORE LOG RECORD FOR BH: <u>INCL 1 PARTIAL LOG</u>														
PROJECT:			DRILLING DATA						Page: <u>7 of 8</u>					
CLIENT:			DRILL:											
LOCATION:			METHOD:											
DATE:			DIAMETER:											
			INCLINATION:											
ELEV/DEPTH (m)	SYMBOL	ROCK DESCRIPTION	GROUND WATER CONDITIONS	RUN NUMBER	CORE SIZE	TOTAL CORE RECOVERY (%)	SOLID CORE RECOVERY (%)	RCD (%)	FRACTURE FREQUENCY (per 0.3m)	DISCONTINUITY DIP (degrees)	DISCONTINUITIES AND WEATHERING	SAMPLE	TEST	NOTES
70.8									2		BD, PL, R <sub>0</sub> , SA			
70.5									2		BD, PL, R <sub>0</sub> , SO			
70		Gouge & Weather		19	HQ	95%	85%	77%	3		See photos			No signs of slickens or other movement
69		Gouge 100nick Weathering							5					
69		Weathering							4					
68				20	HQ	98%	94%	94%	2	0°	BD, PL, SM, CL			
68									0	0°	BD, PL, R <sub>0</sub> , SA			
67.5									1	0°	BD, PL			
67		Gouge & Weathering		21	HQ	100%	95%	79%	2		FR, IR, R <sub>0</sub> , CL			Handling fractures
67									0		FR, IR, R <sub>0</sub> , CL			
66									5		SEE PHOTOS			
66									0		BD, PL, SM, CL			
66									2		BD, PL, SM, CL			
65				22	HQ	96%	96%	95%	0					
64.8									1					
64.5		GEORGIAN BAY FORMATION							0					
64		Limestone		23	HQ	100%	100%	94%	0		BD, PL, SO			
63.6									2	0°	FR, PL, R <sub>0</sub> , SA			

GENERAL NOTES:

CORE LOG RECORD FOR BH: <u>INCL</u>   <u>PARTIAL LOG</u>														
PROJECT:				DRILLING DATA				Page: <u>8 of 8</u>						
CLIENT:				DRILL:										
LOCATION:				METHOD:										
DATE:				DIAMETER:										
				INCLINATION:										
ELEV/DEPTH (m)	SYMBOL	ROCK DESCRIPTION	GROUND WATER CONDITIONS	RUN NUMBER	CORE SIZE	TOTAL CORE RECOVERY (%)	SOLID CORE RECOVERY (%)	RCD (%)	FRACTURE FREQUENCY (per 0.3m)	DISCONTINUITY DIP (degrees)	DISCONTINUITIES AND WEATHERING	SAMPLE	TEST	NOTES
-63		Cobble							0.0	00°	PL, SM, CL BD, PL, SM, CL BD, PL, SM, CL			
-62		Limestone							0.0	0°	BD, PL, SM, CL			-61.5m bottom of incl.
-61.5		Thin layers of limestone		24	HQ	100%	100%	100%	0.0	0°	BD, PL, SM, CL			End of hole
-61														
-60														
-59														
-58														
-57														

GENERAL NOTES:

Date: 2015/08/21

Zone 1 Watermain

Main Shaft

Inclinometer 1 - Borehole Photos

Drilled 2015/08/13 – 2015/08/14

Final inclinometer depth/elevation: 51.5m/62.5m

Final drilled depth elevation 52.5m/ 61.5m.

Photos from approximate elevations 97.5 to 61.5m.



Figure 1. Run 1 from approximate elevation 97.5 to 96.6m.



Figure 2. Run 1 from approximate elevation 96.9 to 96.0m.



Figure 3. Run 2 from approximate elevation 96.0 to 94.5m.



Figure 4. Run 3 from approximate elevation 94.5 to 93.0m.





Figure 5. Run 4 from approximate elevation 93.0 to 91.5m.



Figure 6. Run 5 from approximate elevation 91.5 to 90.0m.



Figure 7. Run 6 from approximate elevation 90.0 to 88.5m.



Figure 8. Run 7 from approximate elevation 88.5 to 87.0m.



Figure 9. Run 8 from approximate elevation 87.0 to 85.5m.



Figure 10. Run 9 from approximate elevation 85.5 to 84.0m.



Figure 11. Run 10 from approximate elevation 84.0 to 82.5m.



Figure 12. Run 11 from approximate elevation 82.5 to 81.0m



Figure 13. Run 12 from approximate elevation 81.0 to 79.5m.



Figure 14. Run 13 from approximate elevation 79.5 to 78.0m.



Figure 15. Run 14 from approximate elevation 78.0 to 76.5m.



Figure 16. Run 15 from approximate elevation 76.5 to 75.0m.



Figure 17. Run 16 from approximate elevation 75.0 to 73.5m.



Figure 18. Run 17 from approximate elevation 73.5 to 72.0m.



Figure 19. Run 18 from approximate elevation 72.0 to 70.5m.



Figure 20. Run 19 from approximate elevation 70.5 to 69.0m.



Figure 21. Run 20 from approximate elevation 69.0 to 67.5m.



Figure 22. Run 21 from approximate elevation 67.5 to 66.0m.



Figure 23. Run 22 from approximate elevation 66.0 to 64.5m.



Figure 24. Run 23 from approximate elevation 64.5 to 63.0m.



Figure 25. Run 24 from approximate elevation 63.0 to 61.5m.

CORE LOG RECORD FOR BH: INCL 2 PARTIAL LOG														
PROJECT: ZONE 1 WM			DRILLING DATA						Page: 1					
CLIENT: RVA			DRILL: TRUCK MOUNTED											
LOCATION: MAIN SHAFT SE CORNER QEW/BURLOAK			METHOD: ROTARY, H <sub>2</sub> O FLUSH											
DATE: 2015/08/14 to 2015/08/15			DIAMETER: HQ											
			INCLINATION: -90											
ELEV/DEPTH (m)	SYMBOL	ROCK DESCRIPTION	GROUND WATER CONDITIONS	RUN NUMBER	CORE SIZE	TOTAL CORE RECOVERY (%)	SOLID CORE RECOVERY (%)	RQD (%)	FRACTURE FREQUENCY (per 0.3m)	DISCONTINUITY DIP (degrees)	DISCONTINUITIES AND WEATHERING	SAMPLE	TEST	NOTES
-114														Ground SURFACE
-113														Augered thru lean mix
-112		Lean MIX												
-111														
-110														
-109.2														Begin Coring
-108.9		QUEENSTON SHALE							1	40	FR, PL, RO, CL			
		Predominantly red to grey layers		1	HQ	100%	100%	99%	1	0	BD, PL, RO, CL			
		Some limestone lenses.							1	0	BD, PL, RO, CL			
-108									2	0	FR, PL, RO, CL			
									2	0	FR, PL, RO, CL			
-107.4									2	0	FR, PL, RO, CL			
-107		WEATHERED		2	HQ				2	0	FR, PL, RO, CL			
											BD, PL, IN, CI			

GENERAL NOTES: Augered ~ 9.6m (15ft) thru lean mix prior to coring.

**CORE LOG RECORD FOR BH: INCL 2 PARTIAL LOG** Page: 2

PROJECT: DRILLING DATA  
 CLIENT: DRILL:  
 LOCATION: METHOD:  
 DATE: DIAMETER:  
 INCLINATION:

ELEV/DEPTH (m)	SYMBOL	ROCK DESCRIPTION	GROUND WATER CONDITIONS	RUN NUMBER	CORE SIZE	TOTAL CORE RECOVERY (%)	SOLID CORE RECOVERY (%)	RQD (%)	FRACTURE FREQUENCY (per 0.3m)	DISCONTINUITY DIP (degrees)	DISCONTINUITIES AND WEATHERING	SAMPLE	TEST	NOTES
107		CLAY GOUGE 25 mm thick		2	HQ	100%	97%	89%	2	0°	Weathered rock with thin			
106.5									1	0°	FR, VR, CL			
105.9									1	0°	BD, PL, SM, CL			
105				3	HQ	100%	100%	88%	0	0°	FR, PL, SM, CL			
104.4									1	0°	FR, PL, SM, CL			
104				4	HQ	100%	100%	97%	0	0°	FR, IR, PL, CL			
103.9									1	0°	FR, PL, SM, CL			
102				5	HQ	88%	88%	88%	0	100°	FR, PL, SM, CL			
101				6	HQ	100%	100%	100%	0	0°	BD, PL, SM, CL			No photo for run 6

GENERAL NOTES:

CORE LOG RECORD FOR BH: INCL 2 PARTIAL LOG														
PROJECT:				DRILLING DATA				Page: 3						
CLIENT:				DRILL:										
LOCATION:				METHOD:										
DATE:				DIAMETER:										
				INCLINATION:										
ELEV/ DEPTH (m)	SYMBOL	ROCK DESCRIPTION	GROUND WATER CONDITIONS	RUN NUMBER	CORE SIZE	TOTAL CORE RECOVERY (%)	SOLID CORE RECOVERY (%)	RQD (%)	FRACTURE FREQUENCY (per 0.3m)	DISCONTINUITY DIP (degrees)	DISCONTINUITIES AND WEATHERING	SAMPLE	TEST	NOTES
97.9				7	HQ	100%	100%	100%	0	0°	FR, IR, VR, CL			
99									0	0°	FR, PL, SM, CL			
98.4									0	0°	BD, CL			
98				8	HQ	98%	98%	98%	0	0°	BD, CL			
97.6									0	0°	BD, CL			
96				9	HQ	98%	98%	98%	0	0°				
95.2									0	0°				
95				10	HQ	100%	100%	100%	0	0°	BD, PL, SM, CL			
94.1									0	0°				
93.7									0	0°				
93				11	HQ	100%	100%	100%	0	0°	BD, PL, SM, CL GYP SUM LAYER			
92.9									0	0°				

GENERAL NOTES:



**CORE LOG RECORD FOR BH: INCL 2 PARTIAL LOG** Page: 4

PROJECT: \_\_\_\_\_ DRILLING DATA \_\_\_\_\_

CLIENT: \_\_\_\_\_ DRILL: \_\_\_\_\_

LOCATION: \_\_\_\_\_ METHOD: \_\_\_\_\_

DATE: \_\_\_\_\_ DIAMETER: \_\_\_\_\_

INCLINATION: \_\_\_\_\_

ELEV/DEPTH (m)	SYMBOL	ROCK DESCRIPTION	GROUND WATER CONDITIONS		RUN NUMBER	CORE SIZE	TOTAL CORE RECOVERY (%)	SOLID CORE RECOVERY (%)	ROD (%)	FRACTURE FREQUENCY (per 0.3m)	DISCONTINUITY DIP (degrees)	DISCONTINUITIES AND WEATHERING	SAMPLE	TEST	NOTES	
92.8										0						
92		CLAY GOUGE 40mm thick			12	HQ	94%	92%	78%	1	0°	FR, IR, Ro, SA ED, PL, SM, CL FR, IR, Ro, SA FR, IR, Ro, SA				
-91										0						
-90.7										0						Mech fractures @ end of run due to removal
-90					13	HQ	100%	100%	99%	0	0°	ED, PL, SM, CL				
-89.2										0						
-89.1										1	0°	FR, IR, Ro, CL				Lost core in barrel. Had to remove casing.
-89										0	0°	FR, PL, Ro, CL				
-89										2	0°	FR, PL, Ro, CL				
-89										0	0°	FR, IR, Ro, CL				
-89.6										2	0°	FR, IR, Ro, CL				
-88					15	HQ	92%	92%	89%	2						No photo available
-88										0						
-88										0						
-88.1										0						
-88		CLAY GOUGE 10mm thick								1						
-88.7																

GENERAL NOTES:

**CORE LOG RECORD FOR BH: INCL 2 PARTIAL LOG** Page: 5

PROJECT: DRILLING DATA  
 CLIENT: DRILL:  
 LOCATION: METHOD:  
 DATE: DIAMETER:  
 INCLINATION:

ELEV/DEPTH (m)	SYMBOL	ROCK DESCRIPTION	GROUND WATER CONDITIONS	RUN NUMBER	CORE SIZE	TOTAL CORE RECOVERY (%)	SOLID CORE RECOVERY (%)	ROD (%)	FRACTURE FREQUENCY (per 0.3m)	DISCONTINUITY DIP (degrees)	DISCONTINUITIES AND WEATHERING	SAMPLE	TEST	NOTES
85.7				16	HQ	100%	76%		1					No photo available
85									0					
84.3				17	HQ	93%	93%	87%	1	0	BD, PL, SM, CL			
84									1	0	BD, PL, SM, CL			
83									2	5	FR, PL, CL			
82.8									1	0	BD, PL, SM, CL			
82				18	HQ	100%	100%	100%	1	0	BD, PL, SM, SO			
81.3									1	0	BD, PL, SM, SO			
81									0		BD, PL, SM, CL			
80				19	HQ	98%	98%	83%	4		FR, IR, SO			
79.8									1		FR, IR, SO			
79									1		FR, PL, SM, CL			
78.6									1		BD, PL, SM, CL			
									1		FR, IR, SO			
				20	HQ	91%	91%	76%	3	0	BD, PL, SO, SA			
									2	0	FR, IR, SO			
									1	20	FR, IR, SO			
									0		FR, PL, SO			
									0		JN, PL, SM, CL			

GENERAL NOTES:

**CORE LOG RECORD FOR BH: InCL 2 PARTIAL LOG** Page: 6


PROJECT: \_\_\_\_\_ DRILLING DATA \_\_\_\_\_

CLIENT: \_\_\_\_\_ DRILL: \_\_\_\_\_

LOCATION: \_\_\_\_\_ METHOD: \_\_\_\_\_

DATE: \_\_\_\_\_ DIAMETER: \_\_\_\_\_

INCLINATION: \_\_\_\_\_

ELEV/DEPTH (m)	SYMBOL	ROCK DESCRIPTION	GROUND WATER CONDITIONS	RUN NUMBER	CORE SIZE	TOTAL CORE RECOVERY (%)	SOLID CORE RECOVERY (%)	ROD (%)	FRACTURE FREQUENCY (per 0.3m)	DISCONTINUITY DIP (degrees)	DISCONTINUITIES AND WEATHERING	SAMPLE	TEST	NOTES
78.6				21	HQ	100%	100%	100%	2					Mostly handling breaks.
78.3									1	0°	FR, PL, RO, CL			
78									1	0°	FR, IR, SA			
77									1	0°	FR, PL, RO, SA			
76.8									2	0°	FR, PL, RO, CL			
76														
75														

GENERAL NOTES: FINAL INCL DEPTH = 49m ⇒ BOTTOM ELEV = 65.7m

Date: 2015/08/21

Zone 1 Watermain

Main Shaft

Inclinometer 2 - Borehole Photos

Drilled 2015/08/14 – 2015/08/15

Final inclinometer depth/elevation 49m/65.7m.

Photos from approximate elevations 108.9 to 76.8m.



Figure 26. Run 1 from elevation 108.9 to 107.4m.



Figure 27. Run 2 from elevation 107.4 to 105.9m.



Figure 28. Run 3 from elevation 105.9 to 104.4m



Figure 29. Run 4 from elevation 104.4 to 102.9m.



Figure 30. Run 5 from elevation 102.9 to 101.4m



Figure 31. Run 6 from elevation 101.4 to 99.9m.



Figure 32. Run 7 from elevation 99.9 to 98.4m.



Figure 33. Run 8 from elevation 98.4 to 96.9m.



Figure 34. Run 9 from 96.9 to 95.2m.



Figure 35. Run 10 from elevation 95.2 to 93.7m.



Figure 36. Run 11 from elevation 93.7 to 92.2m.



Figure 37. Run 12 from elevation 92.2 to 90.7m.



Figure 38. Run 13 from elevation 90.7 to 89.2m.



Figure 39. Run 14 from elevation 89.2 to 87.6m.

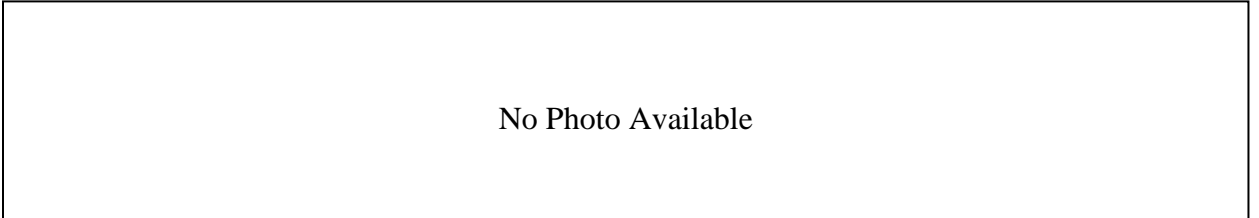


Figure 40. Run 15 from elevation 87.6 to 86.1m.

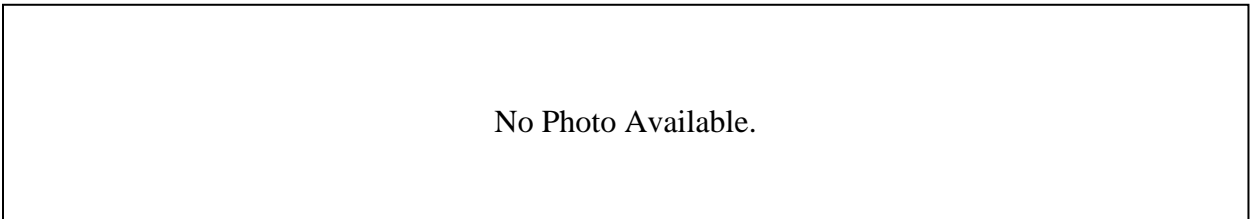


Figure 41. Run 16 from elevation 86.1 to 84.3.

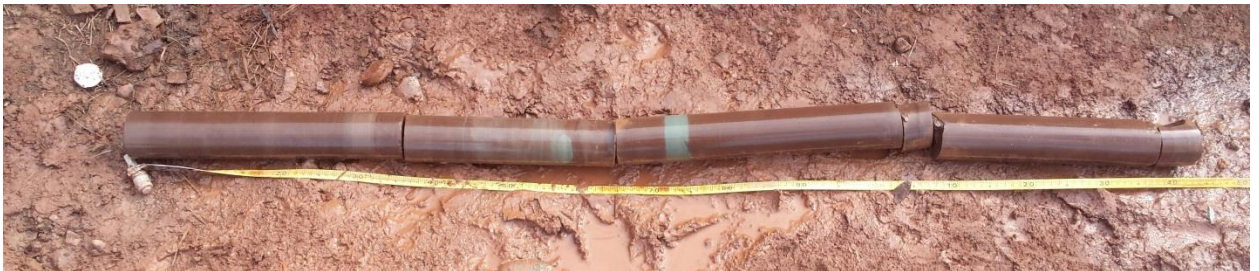


Figure 42. Run 17 from elevation 84.3 to 82.8m.

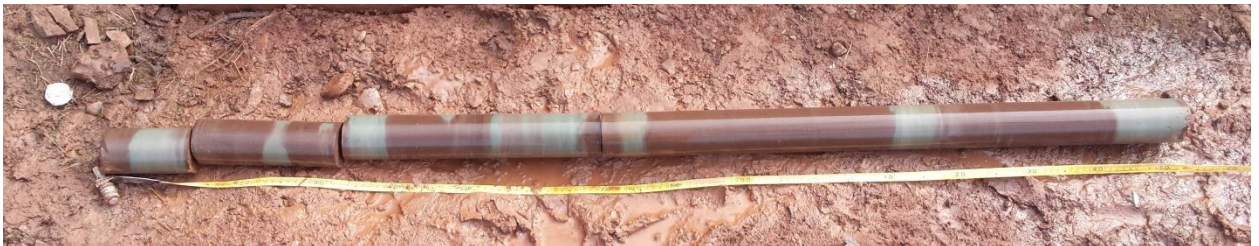


Figure 43. Run 18 from elevation 82.8 to 81.3m.



Figure 44. Run 19 from elevation 81.3 to 79.8m.



Figure 45. Run 20 from elevation 79.8 to 78.3m.



Figure 46. Run 21 from elevation 78.3 to 76.8m.



**CORE LOG RECORD FOR BH: INCL 3 PARTIAL LOG**

PROJECT: ZONE 1 WATERMAIN DRILLING DATA Page: 1 of 6

CLIENT: RVA DRILL: TRUCK MOUNTED

LOCATION: MAIN SHAFT SW CORNER CREW/BULWARK METHOD: ROTARY, H<sub>2</sub>O FLUSH

DATE: 2015/08/15 DIAMETER: HQ

INCLINATION: -90°

ELEV/ DEPTH (m)	SYMBOL	ROCK DESCRIPTION	GROUND WATER CONDITIONS	RUN NUMBER	CORE SIZE	TOTAL CORE RECOVERY (%)	SOLID CORE RECOVERY (%)	ROD (%)	FRACTURE FREQUENCY (per 0.3m)	DISCONTINUITY DIP (degrees)	DISCONTINUITIES AND WEATHERING	SAMPLE	TEST	NOTES
114														
113.7														
115														
112														
111														No RECORDS AVAILABLE
110														
109														
108														
107														
106														

GENERAL NOTES:

**CORE LOG RECORD FOR BH: INCL 3 PARTIAL LOG** Page: 2 of 6

PROJECT: \_\_\_\_\_ DRILLING DATA \_\_\_\_\_

CLIENT: \_\_\_\_\_ DRILL: \_\_\_\_\_

LOCATION: \_\_\_\_\_ METHOD: \_\_\_\_\_

DATE: \_\_\_\_\_ DIAMETER: \_\_\_\_\_

INCLINATION: \_\_\_\_\_

ELEV/DEPTH (m)	SYMBOL	ROCK DESCRIPTION	GROUND WATER CONDITIONS	RUN NUMBER	CORE SIZE	TOTAL CORE RECOVERY (%)	SOLID CORE RECOVERY (%)	RCD (%)	FRACTURE FREQUENCY (per 0.3m)	DISCONTINUITY DIP (degrees)	DISCONTINUITIES AND WEATHERING	SAMPLE	TEST	NOTES
106.8														
106														No RECORDS AVAILABLE
105														
104														
103														
102		QUEENSTON SHALE Predominantly red with grey layers. Some limestone												
101														
100				1	HQ	100%	100%	100%	1	0	FR, PL, SM			
99.6														

GENERAL NOTES:

CORE LOG RECORD FOR BH: INCL 3 PARTIAL LOG														
PROJECT:			DRILLING DATA						Page: 3 of 6					
CLIENT:			DRILL:											
LOCATION:			METHOD:											
DATE:			DIAMETER:											
			INCLINATION:											
ELEV/DEPTH (m)	SYMBOL	ROCK DESCRIPTION	GROUND WATER CONDITIONS	RUN NUMBER	CORE SIZE	TOTAL CORE RECOVERY (%)	SOLID CORE RECOVERY (%)	RCD (%)	FRACTURE FREQUENCY (per 0.3m)	DISCONTINUITY DIP (degrees)	DISCONTINUITIES AND WEATHERING	SAMPLE	TEST	NOTES
-99.5									0					
-99				2	HQ	100%	100%	94%	1	0°	BD, PL, SM, CL			
-98									3	0°	BD, PL, SM, CL FR, PL, SM BD, PL, SM, CL			Bottom fracture from handling
-97				3	HQ	100%	100%	100%	1	0°	BD, PL, SM, CL			
-96.5									1	15°	FR, PL, SM, SO			
-96				4	HQ	100%	100%	100%	0					
-95		Gouge							0					
-94				5	HQ	93%	93%	93%	1	0°	BD, PL, SM, CL			
-93.5									1	0°	BD, PL, SM, CL			
-93									1	0°	FR, PL, SM, SA			
-92.4				6	HQ	100%	100%	100%	1	0°	BD, PL, SM, CL			

GENERAL NOTES:

CORE LOG RECORD FOR BH: INCL 3 PARTIAL LOG														
PROJECT:			DRILLING DATA						Page: 4 of 6					
CLIENT:			DRILL:											
LOCATION:			METHOD:											
DATE:			DIAMETER:											
			INCLINATION:											
ELEV/ DEPTH (m)	SYMBOL	ROCK DESCRIPTION	GROUND WATER CONDITIONS	RUN NUMBER	CORE SIZE	TOTAL CORE RECOVERY (%)	SOLID CORE RECOVERY (%)	RCD (%)	FRACTURE FREQUENCY (per 0.3m)	DISCONTINUITY DIP (degrees)	DISCONTINUITIES AND WEATHERING	SAMPLE	TEST	NOTES
92.4									0					
-92									1	0°	BD, PL, SM, CL			Handling break
-91				7	HQ	100%	100%	95%	0					
-90.5									0					
-90				8	HQ	100%	100%	100%	0		BD, PL, SM, CL			
-89									0					
-88				9	HQ	100%	100%	95%	0	0.00°	FR, IR FR, IR FR, IR			
-87.5									0					
-87									1		BD, PL, R, CL			
-86				10	HQ	97%	97%	97%	0		BD, PL, SM, CL			
-85.7									0					

GENERAL NOTES:

**CORE LOG RECORD FOR BH: INU 3 PARTIAL LOG**


PROJECT: DRILLING DATA Page: 5 of 6  
 CLIENT: DRILL:  
 LOCATION: METHOD:  
 DATE: DIAMETER:  
 INCLINATION:

ELEV/DEPTH (m)	SYMBOL	ROCK DESCRIPTION	GROUND WATER CONDITIONS	RUN NUMBER	CORE SIZE	TOTAL CORE RECOVERY (%)	SOLID CORE RECOVERY (%)	ROD (%)	FRACTURE FREQUENCY (per 0.3m)	DISCONTINUITY DIP (degrees)	DISCONTINUITIES AND WEATHERING	SAMPLE	TEST	NOTES
80.2				11	HQ	99%	99%	99%	0	0				
81.5				12	HQ	100%	100%	100%	0	0	BD, PL, SM, CL			
83				13	HQ	100%	100%	100%	0	0	BD, PL, SM, CL			
84.5									0	0	BD, PL, SM, CL			
86				14	HQ	79%	79%	66%	0	0	BD, PL, SM, CL FR, PL, SM, CL FR, PL, CL BD, PL, RO, CL			Bottom of core lost during drilling. Top crushed due to drilling
87.5				15	HQ	100%	100%	78%	2	0	FR, RO, SO FR, RO, FR, RO			Top crushed due to drilling
89									0	0	FR, IR, RO			

GENERAL NOTES:

**CORE LOG RECORD FOR BH: Incl 3 PARTIAL LOG** Page: 6 of 6

PROJECT: DRILLING DATA  
 CLIENT: DRILL:  
 LOCATION: METHOD:  
 DATE: DIAMETER:  
 INCLINATION:

ELEV/ DEPTH (m)	SYMBOL	ROCK DESCRIPTION	GROUND WATER CONDITIONS	RUN NUMBER	CORE SIZE	TOTAL CORE RECOVERY (%)	SOLID CORE RECOVERY (%)	RCD (%)	FRACTURE FREQUENCY (per 0.3m)	DISCONTINUITY DIP (degrees)	DISCONTINUITIES AND WEATHERING	SAMPLE	TEST	NOTES
78				16	HQ	100%	100%	100%	1	0°	BD, PL, CL	<input checked="" type="checkbox"/>		
77										0°	BD, PL, SM, CL	<input checked="" type="checkbox"/>		End of records
76										0°	BD, PL, SM, CL			
75														
74														
73														
72.5														
72														Bottom of shaft
71														

GENERAL NOTES:

Date: 2015/08/21

Zone 1 Watermain

Main Shaft

Inclinometer 3 - Borehole Photos

Drilled 2015/08/15

Final inclinometer depth/elevation: 52.5m/61.8m

Photos from approximate elevations 101.0 to 77.0m.



Figure 47. Run 1 from approximate elevation 101.0 to 99.5m.



Figure 48. Run 2 from approximate elevation 99.5 to 98.0m.



Figure 49. Run 3 from approximate elevation 98.0 to 96.5m.



Figure 50. Run 4 from approximate elevation 96.5 to 95.0m.



Figure 51. Run 5 from approximate elevation 95.0 to 93.5m.



Figure 52. Run 6 from approximate elevation 93.5 to 92.0m.



Figure 53. Run 7 from approximate elevation 92.0 to 90.5m.



Figure 54. Run 8 from approximate elevation 90.5 to 89.0m.



Figure 55. Run 9 from approximate elevation 89.0 to 87.5m.





Figure 56. Run 10 from approximate elevation 87.5 to 86.0m.



Figure 57. Run 11 from approximate elevation 86.0 to 84.5m.



Figure 58. Run 12 from approximate elevation 84.5 to 83.0m.



Figure 59. Run 13 from approximate elevation 83.0 to 81.5m.



Figure 60. Run 14 from approximate elevation 81.5 to 80.0m.



Figure 61. Run 15 from approximate elevation 80.0 to 78.5m.



Figure 62. Run 16 from approximate elevation 78.5 to 77.0m.

# Curriculum Vitae

**Name:** Thomas Lardner

**Post-secondary Education and Degrees:** Queen's University  
Kingston, Ontario, Canada  
2002 – 2006 BSc – Geological engineering.

The University of Western Ontario  
London, Ontario, Canada  
2009 – 2011 MEng

**Honours and Awards:** LG Soderman Award  
Department of Civil and Environmental Engineering  
July 2011

2017 Graduate Student Teaching Assistant Award  
UWO School of Graduate and Post-doctoral Studies  
May 2017

2016 Michael Bozozuk National Graduate Scholarship  
Canadian Foundation for Geotechnique  
October 2016

**Related Work Experience** Teaching Assistant  
The University of Western Ontario  
2012 – 2016

Undergraduate Lecturer  
The University of Western Ontario  
Fall Semester 2018

Geotechnical engineer and project manager  
Isherwood Geotechnical Engineers  
Mississauga, ON, Canada  
2006 – 2018

**Publications:**

Micic, S., Gonsalves, S., Lo, K.Y., and Lardner, T., 2016. Billy Bishop Toronto Airport Passenger Tunnel, Toronto – Geotechnical Aspect of Design. Proceedings of the 69 Canadian Geotechnical Conference GeoVancouver 2016, Vancouver, British Columbia, Canada, paper # 3975.

Lardner, T., Lo, K.Y., and Isherwood, B., 2014. Performance analysis of deep excavations in rock. Proceedings of the 67 Canadian Geotechnical Conference, GeoRegina 2014, Regina, Saskatchewan, Canada.